Functional renormalization group for frustrated quantum magnetism: method extension and material applications

Dissertation

zur Erlangung des Grades eines

Doktors der Naturwissenschaften

am Fachbereich Physik

der Freien Universität Berlin

vorgelegt von

Vincent Noculak

Berlin, 2024

Erstgutachter: Prof. Dr. Johannes Reuther

Zweitgutachter: Prof. Dr. Piet Brouwer

Tag der Disputation: 06.11.2024

Abstract

The field of highly frustrated magnetism harbors a wide variety of exotic phases that sustain interest in the field with no end in sight. Competing interactions yield models that often remain highly fluctuating down to zero temperature, have long-range entangled ground states, or exhibit fractionalized excitations. The study of these frustrated models presents a challenge for experimental and theoretical methods alike, driving their development in the process. As a contribution to the field, this thesis both further develops the pseudo-fermion functional renormalization group and applies the method in collaborative studies involving complementary methods to reveal low-temperature properties of a selection of frustrated spin models with relevance to spin compound families of recent interest.

In the first chapters of the thesis, the pseudo-fermion functional renormalization group is extended to enable the treatment of spin models with broken time-reversal symmetry. Newly accessible applications include models with finite magnetic fields in the form of site-dependent Zeeman terms. While previous formulations of the method could investigate magnetically ordered models only in their paramagnetic regime, often achieved by a finite renormalization group parameter in the model, the new scheme further allows the study of magnetic phases in absence of this parameter. In an exploratory study across a selection of Heisenberg and XXZ models, magnetic order parameters and magnetization plateaus will be compared with literature results to reveal for which newly accessible applications the method is best suited.

In addition to method development, a major emphasis of the thesis is placed on the study of nearest-neighbor spin models on the pyrochlore lattice. It is argued that the $S = 1/2$ and $S = 1$ Heisenberg models assume nematic ground states that break either only C_3, or both C_3 and lattice inversion symmetry. Quantum and classical phase diagrams of the model with Heisenberg and Dzyaloshinskii-Moriya interactions, and of non-Kramers pyrochlores are computed as well. In this context, an in-depth study of the so-called Γ_5 phase will resolve subtle order-by-disorder selections from quantum or thermal fluctuations at both zero and critical temperatures. Furthermore, a model contained in both phase diagrams will be presented that exhibits a temperature-dependent spin liquid to spin liquid transition driven by entropic selections between ground state submanifolds in the case of classical spins. While the intermediate-temperature spin liquid can be described by coexisting vector and matrix gauge fields, spin degrees of freedom associated with the matrix gauge field depopulate as the temperature is lowered, realizing a spin-ice phase in the process. Emphasis is put on the study of the corresponding quantum model and its vicinity in the phase diagrams. This model is found to be best described in analogy to the intermediate-temperature classical spin liquid.

In the last part of the thesis, the pseudo-fermion functional renormalization group is applied in collaboration with classical Monte Carlo and inelastic neutron scattering to resolve the low-temperature behavior and magnetic order of the three-dimensional tetra-trillium compound and spin liquid candidate $K_2Ni_2(SO_4)_3$. The phase diagram of a Heisenberg model on the tetra-trillium lattice contextualizes the strongly fluctuating behavior of $K_2Ni_2(SO_4)_3$ by hosting a large paramagnetic region close to the density functional theory model of $K_2Ni_2(SO_4)_3$. In a broader scope, this region establishes compounds of the langbeinite family, which are described by Heisenberg models on the tetra-trillium lattice, as a promising platform in the future search for three-dimensional quantum spin-liquid phases.

Zusammenfassung

Auf dem Forschungsgebiet des stark frustrierten Magnetismus sorgen eine Vielfalt an exotischer Phasen für andauerndes Interesse. Durch konkurrierende Wechselwirkungen kommen Modelle zustande, die oft bis zum Temperaturnullpunkt stark fluktuierend bleiben, weitreichig verschränkte Grundzustände aufweisen oder fraktionale Anregungen beherbergen. Die Erforschung dieser frustrierten Modelle stellt hohe Anforderungen an experimentelle und theoretische Methoden gleichermaßen und treibt deren Entwicklung voran. In dieser Arbeit wird die Pseudofermion-basierte funktionale Renormalisierungsgruppe weiterentwickelt und in Kollaboration mit komplementären Methoden angewendet, um die Tieftemperatureigenschaften verschiedener frustrierter Spinmodelle, die für Spinmaterialien relevant sind, aufzuklären.

In den ersten Kapiteln der Arbeit wird die Pseudofermion-basierte funktionale Renormalisierungsgruppe erweitert, um die Behandlung von Spinmodellen mit gebrochener Zeitumkehrsymmetrie zu ermöglichen. Zu den neu zugänglichen Anwendungen zählt die Behandlung von Modellen mit endlichen Magnetfeldern in Form von gitterstellenabhängigen Zeeman-Termen. Während frühere Formulierungen der Methode magnetisch geordnete Modelle nur in ihren paramagnetischen Regimen untersuchen konnten, die häufig durch einen endlichen Renormierungsgruppenparameter im Modell realisiert wurden, ermöglicht das neue Schema darüber hinaus die Untersuchung magnetischer Phasen bei Nulltemperatur in Abwesenheit dieses Parameters. Im Rahmen einer explorativen Studie werden mit der Methode magnetische Ordnungsparameter und Magnetisierungsplateaus für eine Auswahl von Heisenberg- und XXZ-Modellen mit Literaturergebnissen verglichen, um zu untersuchen, für welche der neuen Anwendungsgebiete die Methode am besten geeignet ist.

Neben der Methodenentwicklung liegt ein weiterer Schwerpunkt der Arbeit auf der Untersuchung von Spinmodellen auf dem Pyrochlor-Gitter mit Wechselwirkungen zwischen nächsten Nachbarn. Es wird argumentiert, dass die $S = 1/2$ und $S = 1$ Heisenberg-Modelle nematische Grundzustände annehmen, die entweder nur C_3 oder sowohl C_3 als auch Gitterinversionssymmetrie brechen. Des Weiteren werden Quanten- und klassische Phasendiagramme des Modells mit Heisenberg- und Dzyaloshinskii-Moriya-Wechselwirkungen sowie von nicht-Kramers-entarteten Pyrochlore-Verbindungen berechnet. Eine in diesem Zusammenhang durchgeführte Untersuchung der sogenannten Γ_5-Phase wird subtile, durch Quanten- oder thermische Fluktuationen hervorgerufene Selektionen von Ordnungen sowohl bei Null als auch bei kritischer Temperatur auflösen. Darüber hinaus wird ein Modell vorgestellt, das in beiden Phasendiagrammen enthalten ist und im Falle klassischer Spins einen temperaturabhängigen Phasenübergang zwischen zwei Spinflüssigkeiten aufweist, der durch die entropische Selektionen zwischen Grundzustandsmannigfaltigkeiten stabilisiert wird. Während die Spinflüssigkeit bei mittleren Temperaturen durch koexistierende Vektor- und Matrix-Eichfelder beschrieben werden kann, depopulieren die dem Matrix-Eichfeld zugeordneten Spin-Freiheitsgrade mit abnehmender Temperatur. Dies resultiert in der Realisierung einer Spin-Eis-Phase. Ein Schwerpunkt liegt auf der Untersuchung des entsprechenden Quantenmodells und seiner Umgebung in den Phasendiagrammen. Die Ergebnisse legen nahe, dass das Modell am besten in Analogie zur klassischen Spinflüssigkeit bei mittleren Temperaturen beschrieben werden kann.

Im letzten Teil der Arbeit wird die Pseudofermion-basierte funktionale Renormalisierungsgruppe zusammen mit klassischen Monte-Carlo-Simulationen und inelastischer Neutronenstreuung angewendet, um das Tieftemperaturverhalten und die magnetische Ordnung der dreidimensionalen Tetra-Trillium-Verbindung und des Spinflüssigkeitskandidaten $K_2Ni_2(SO_4)_3$ zu untersuchen. Das Phasendiagramm eines Heisenberg-Modells auf dem Tetra-Trillium-Gitter kontextualisiert das stark fluktuierende Tieftemperaturverhalten von $K_2Ni_2(SO_4)_3$, indem es einen großen paramagnetischen Bereich in der Nähe des Dichtefunktionaltheorie-basierten Modells von $K_2Ni_2(SO_4)_3$ enthüllt. Damit etablieren sich die Verbindungen der Langbeinit-Familie, die Heisenberg-Modelle auf dem Tetra-Trillium-Gitter realisieren, als vielversprechende Plattform für die zukünftige Suche nach dreidimensionalen Quantenspinflüssigkeiten.

List of publications

1. Ivica Živković, Virgile Favre, Catalina Salazar Mejia, Harald O. Jeschke, Arnaud Magrez, Bhupen Dabholkar, Vincent Noculak, Rafael S. Freitas, Minki Jeong, Nagabhushan G. Hegde, Luc Testa, Peter Babkevich, Yixi Su, Pascal Manuel, Hubertus Luetkens, Christopher Baines, Peter J. Baker, Jochen Wosnitza, Oksana Zaharko, Yasir Iqbal, Johannes Reuther, and Henrik M. Rønnow, *Magnetic Field Induced Quantum Spin Liquid in the Two Coupled Trillium Lattices of $K_2Ni_2(SO_4)_3$*, Phys. Rev. Lett. 127, 157204 (2021).

2. Max Hering, Vincent Noculak, Francesco Ferrari, Yasir Iqbal, Johannes Reuther, *Dimerization tendencies of the pyrochlore Heisenberg antiferromagnet: A functional renormalization group perspective*, Phys. Rev. B 105, 054426 (2022).

3. Imre Hagymási, Vincent Noculak, Johannes Reuther, *Enhanced symmetry-breaking tendencies in the S=1 pyrochlore antiferromagnet*, Phys. Rev. B 106, 235137 (2022).

4. Vincent Noculak, Daniel Lozano-Gómez, Jaan Oitmaa, Rajiv R. P. Singh, Yasir Iqbal, Michel J. P. Gingras, Johannes Reuther, *Classical and quantum phases of the pyrochlore S=1/2 magnet with Heisenberg and Dzyaloshinskii-Moriya interactions*, Phys. Rev. B 107, 214414 (2023).

5. Vincent Noculak, Johannes Reuther, *Pseudo-fermion functional renormalization group with magnetic fields*, Phys. Rev. B 109, 174414 (2024).

6. Matías G. Gonzalez, Vincent Noculak, Aman Sharma, Virgile Favre, Jian-Rui Soh, Arnaud Magrez, Robert Bewley, Harald O. Jeschke, Johannes Reuther, Henrik M. Rønnow, Yasir Iqbal, Ivica Živković, *Dynamics of $K_2Ni_2(SO_4)_3$ governed by proximity to a 3D spin liquid model*, Nature Communications 15, 7191 (2024), this article is distributed under Creative Commons Attribution-NonCommercial-NoDerivatives License 4.0 (CC BY-NC-ND), reproduced with permission from Springer Nature.

7. Daniel Lozano-Gómez, Vincent Noculak, Jaan Oitmaa, Rajiv R. P. Singh, Yasir Iqbal, Johannes Reuther, Michel J. P. Gingras, *Competing gauge fields and entropically driven spin liquid to spin liquid transition in non-Kramers pyrochlores*, Proceedings of the National Academy of Sciences 121 (36), e2403487121 (2024), this article is distributed

Contents

Chapter 1

Introduction

Frustration is a major motif that has steadily been guiding research on spin models throughout the last decades [1]. The term describes the scenario in which multiple local interactions of a model cannot be minimized simultaneously. Different mechanisms exist to enforce this competition between interactions. As a starting point for discussing the phenomenon, one may consider the lattice model

$$\mathcal{H} = \frac{1}{2} \sum_{ij} \boldsymbol{S}_i^T \boldsymbol{J}_{ij} \boldsymbol{S}_j, \tag{1.1}$$

which contains 3×3 interaction matrices $\boldsymbol{J}_{ij}$ only between pairs of classical spin vectors $\boldsymbol{S}_i$ and $\boldsymbol{S}_j$ located on lattice sites i and j. In the case of so-called geometrical frustration, competition between interactions $\boldsymbol{J}_{ij}$ on nearest-neighbor lattice bonds $\langle i, j \rangle$ is caused by the underlying lattice structure itself. E.g., the energies of nearest-neighbor antiferromagnetic Heisenberg interactions $J \boldsymbol{S}_i \cdot \boldsymbol{S}_j$, with $J > 0$, on a square lattice of spins can classically be minimized on each bond $\langle i, j \rangle$ by antiferromagnetically aligning spins, i.e., spins fulfill $\boldsymbol{S}_i = -\boldsymbol{S}_j$ for nearest-neighbor bonds $\langle i, j \rangle$. Thus, the Heisenberg interactions do not cause frustration by themselves in this example. In contrast, the same type of nearest-neighbor interaction results in geometrically frustrated spins on a triangular lattice. In this case, the lattice model assumes a minimum classical energy by arranging neighboring spin at angles of 120°. Alternative routes to enforce frustration consist of including interactions between further neighbors, as is achieved by the J_1-J_2 square lattice Heisenberg model that has nearest-neighbor interactions of size J_1 and second-nearest-neighbor interactions of size J_2 [2], or include anisotropic interactions $\boldsymbol{J}_{ij} \not\propto \mathbb{1}$, as done by the Kitaev model, which has nearest-neighbor interactions $S_i^{\mu_{ij}} S_j^{\mu_{ij}}$, with bond-dependent $\mu_{ij} \in \{x, y, z\}$ [3].

The world of frustration-induced phenomena is rich in exotic phases that harbor in-

triguing properties. As an important prerequisite for these phases, frustration often results in an accidentally degenerate ground state manifold in classical spin models, i.e., a degenerate manifold of states that are not related by symmetries of the model. In cases of strong frustration, the degeneracy can even become extensive and allow for local spin degrees of freedom within the ground state manifold [4]. However, for a ground state manifold (and its environment) to serve as a framework for the realization of frustration-induced phenomena, another ingredient is still often required in addition to frustration: fluctuations. In classical spin models, thermal fluctuations are induced by a finite temperature, with the size of the temperature tuning the strength of the fluctuations. Since the degeneracy between states of the ground state manifold is generally accidental, fluctuations distinguish between these states. It follows that thermal fluctuations entropically favor particular states within the manifold, often enabling the selection of a magnetic order despite the presence of an accidental degeneracy in absence of fluctuations, a phenomenon known as order-by-disorder [5]. Alternatively, fluctuations may fail to select a state within the ground state manifold such that the spins remain strongly fluctuating for any finite temperature. In this case, the model may remain paramagnetic down to $T = 0$. However, the low-temperature liquid-like phase may exhibit a hidden structure that can lead to properties not found in the freely fluctuating gas-like paramagnetic phase at high temperatures. A prominent example of such a classical spin-liquid phase is given by the spin-ice phase found in the nearest-neighbor Ising model on the pyrochlore lattice. In this phase, single spin-flip excitations fractionalize into deconfined pairs of excitations with characteristics analogous to magnetic monopoles (see Sec. 5.1.1).

The effect of quantum fluctuations on state selection can often be understood in analogy to thermal fluctuations. Similar to the thermal order-by-disorder effect, quantum fluctuations can energetically favor states in the classical ground state manifold, leading to the selection of a magnetic order from quantum order-by-disorder. However, the quantum nature of spins can further lead to frustration-induced phenomena with no classical analogue, as superpositions of states with classical interpretations can result in non-classical states with favorable energies. A minimalistic example is given by the ground state of the antiferromagnetic Heisenberg model on a dimer, described by the Hamiltonian $\hat{\mathcal{H}} = J\hat{\boldsymbol{S}}_0 \cdot \hat{\boldsymbol{S}}_1$ with $J > 0$. In this model, the antiferromagnetic coupling between two spins yields a singlet ground state. In lattice models, the entanglement between classical states can assume more sophisticated structures. Resulting paramagnetic ground states can be nematic by spontaneously breaking lattice symmetries or spin rotation symmetries, as is achieved in a valence bond crystal by the dimerization of spins. Alternatively, a long-range entangled quantum spin liquid can be realized, as is the case in a resonating valence bond spin liquid [1]. Returning to the earlier

example of spin ice, the highly entangled structure of the quantum spin-ice version, obtained by allowing tunneling processes between different classical spin-ice ground states, is reflected by the emergence of additional ground state excitations in comparison to classical spin ice. These are described as gapped electric monopole and gapless photon excitations, and coexist with the magnetic monopole excitations of the classical model, i.e., the quantum spin-ice phase realizes emergent electromagnetism [4].

In this thesis, we study a variety of frustrated spin models that realize the aforementioned frustration-induced phenomena of order-by-disorder or $T = 0$ paramagnetic phases. These models are effective descriptions of recently synthesized spin compounds, as is the case in the study of Chapter 6 on the three-dimensional spin liquid candidate $K_2Ni_2(SO_4)_3$, or of high relevance to spin compound families, as is the case for the phase diagram of non-Kramers pyrochlore compounds studied in Chapter 5. An emphasis is placed on the study of highly frustrated three-dimensional models on either the pyrochlore or tetra-trillium lattice. Sites of both lattices are arranged in corner-sharing tetrahedra, resulting in a strong geometrical frustration. Models on the pyrochlore lattice will include only interactions between nearest neighbors that can either be of Heisenberg type or anisotropic, e.g., Dzyaloshinskii-Moriya interactions. In contrast, models considered on the tetra-trillium lattice will contain competing Heisenberg interactions from first up to fifth-nearest neighbors.

Obtaining a comprehensive understanding of these models and their relevant spin compounds is a challenging endeavor and usually requires close collaboration between experimental and theoretical approaches. On the theoretical side, methods with diverse strengths have been developed to access properties of spin models. Approaches such as mean-field theory, linear spin-wave analysis, and exact diagonalization have successfully been applied for many decades [1]. More recent approaches can especially benefit from, or are made possible by, the over the years rapidly increasing magnitude of numerical resources available. Prominent among these numerically demanding methods are functional renormalization group (FRG), quantum Monte Carlo, and density matrix renormalization group (DMRG) approaches. However, all newer and older methods have in common that they are limited in their range of applicability. E.g., mean-field approximations are accurate only if fluctuations around the mean-field solution are weak. Similarly, linear spin-wave theory requires a magnetically ordered ground state and assumes that quantum fluctuations on top the classical ground state are small [6, 7]. Exact diagonalization suffers from a Hilbert space dimension that grows exponentially with the number of spins, allowing only for the treatment of small system sizes as a consequence. DMRG allows for larger system sizes by effectively reducing the Hilbert space dimension, but often struggles with the treatment of two- and three-dimensional systems [8, 9]. Quantum Monte Carlo applications are highly limited in their range

of applications on frustrated models by the infamous sign problem [10]. Finally, FRG approaches are limited in the observables they can compute. More specifically, the pseudo-fermion functional renormalization group (PFFRG), a FRG variant formulated for the treatment of spin models, only allows to access observables that are linear or quadratic in spin operators [11, 12].

The study of models in this thesis will be centered around the PFFRG approach. To account for the weaknesses of individual methods as summarized above, and to overcome limitations of the PFFRG itself, the method will generally be applied in collaboration with complementary theoretical and experimental techniques. These include DMRG, classical Monte Carlo, high-temperature series expansion or inelastic neutron scattering. The collaborative studies of models on the pyrochlore and tetra-trillium lattices will reveal the diverse underlying properties of the considered systems, not only answering previous questions about their state selection, but also guiding future research in the field of frustrated magnetism.

In addition to the study of spin models by PFFRG, a second major subject of the thesis is the further development of the PFFRG method. While the application of the PFFRG had previously been limited to spin models that do not break time-reversal symmetry [12], we will extend the method in this thesis to allow for the treatment of models with broken time-reversal symmetry as well. A generalized method formulation will enable a variety of new applications, such as the treatment of models with spins coupled to finite magnetic fields via site-dependent Zeeman terms. Furthermore, the previous methodological formulation only allowed the study of magnetic phases beyond their critical point in an adjacent paramagnetic regime. In contrast, the extended method allows to regularize susceptibility divergences at the critical point of a magnetic phase transition, thereby allowing a model to transition into its magnetically ordered phase via the flow of a renormalization group parameter, corresponding to a frequency cutoff. This enables the PFFRG study of magnetic phases in the physically relevant cutoff-free limit at $T = 0$. An exploratory study on newly available method applications will be performed, which uncovers strengths and limitations of the extended method and provides the groundwork for future applications on models with broken time-reversal symmetry. Under investigation are capabilities of the method to qualitatively and quantitatively resolve magnetic order parameters, and to correctly resolve magnetization curves. In the latter application, an emphasis is placed on the resolution of magnetization plateaus. Due to the nature of the study, efforts are mostly restricted to previously studied models with well-known behavior, enabling the comparison of PFFRG results with literature values. The considered models are given by nearest-neighbor Heisenberg models on the square, honeycomb, and triangular lattices. Magnetization curves are studied on the Heisenberg model on a dimer, on a pyrochlore

lattice, and on the triangular lattice XXZ model.

The thesis is structured as follows. Chapter 2 introduces field-theoretical concepts that pose a prerequisite for establishing the functional renormalization group. Chapter 3 treats the methodological contribution of the thesis, namely the extension of the pseudo-fermion functional renormalization group (PFFRG) to treat spin models with broken time-reversal symmetry. The derivation of the generalized so-called flow equations, on which the method is based, will be the highlight of the chapter. A subsequent discussion and extensive review on the method will be provided. The following Chapter 4 explores the PFFRG extension by applying the method to a variety of spin models with broken time-reversal symmetry. A comparison with literature results will provide insight into which newly accessible applications the PFFRG is best suited for. While the first chapters of the thesis have a methodological focus, the following chapters will focus on the treatment of frustrated spin models of recent interest. Nearest-neighbor models on the pyrochlore lattice are treated in Chapter 5. After investigating symmetry properties of the paramagnetic ground states in the $S = 1/2$ and $S = 1$ Heisenberg models, models with additional anisotropic interactions are considered. In this context, the quantum and classical phase diagrams of the pyrochlore model with Heisenberg and Dzyaloshinskii-Moriya interactions are studied with an emphasis on order-by-disorder selections. The last part of the chapter is centered around a model described by so-called non-Kramers pyrochlores that realizes a novel entropically-driven spin liquid to spin liquid transition in case of classical spins. A study of the phase diagram treating the general nearest-neighbor non-Kramers pyrochlore model will reveal the effect of quantum fluctuation on the classical model. The study of Chapter 6 is inspired by the newly synthesized three-dimensional spin-liquid candidate on the tetra-trillium lattice $K_2Ni_2(SO_4)_3$ [13]. A collaboration between PFFRG, classical Monte Carlo simulations, inelastic neutron scattering experiments, and density functional theory will reveal the low-temperature behavior of the compound. A PFFRG study of the closely related J_3-J_4-J_5 Heisenberg model on the tetra-trillium lattice will discover a paramagnetic regime that contextualizes the highly fluctuating low-temperature behavior of $K_2Ni_2(SO_4)_3$ and suggests langbeinite compounds as a future platform in the search for three-dimensional spin liquids. Finally, we end the thesis with a conclusion in Chapter 7.

Chapter 2

Quantum field theoretical foundations towards the functional renormalization group

In the theory of quantum mechanics, the properties of a system are encoded by its Hamiltonian. Depending on the structure of the Hamiltonian, different strategies for extracting these properties, which are often expressed via observables, can be successful. In presence of weak interactions, the behavior of a model may already be captured well by the noninteracting model or by a perturbative expansion around the noninteracting model. Such is the conservative approach, generally introduced early in any quantum mechanics textbook, to determine a model's energy spectrum and eigenstates, which in turn can be applied for the computation of observables [14]. For strongly interacting models, perturbation theory fails and alternative strategies for accessing observables have to be applied. E.g., the behavior of some models is approximated well by a mean-field approximation, as is the case with the BCS mean-field theory for conventional superconductivity [15]. Fundamentally different strategies for accessing observables compared to those of the early mathematical framework of quantum mechanics are found in quantum field theory. In the quantum field theoretical framework, observables are often expressed in terms of Green functions instead, shifting the problem from finding a quantum state to the problem of determining Green functions. Alternatively, one can go a step further by expressing the Green functions, and by extension observables, in terms of vertex functions. A model is then solved by the determination of vertex functions. This is the approach pursued by FRG methods [16].

FRG methods give a hierarchy of coupled differential equations for vertex functions [16]. These functions are known in a quantum field theoretical context as being built

from Feynman diagrams that satisfy the properties of being amputated, connected and one-particle irreducible [17]. It follows that knowledge on some concepts of quantum field theory, such as Green functions, vertex functions or Feynman diagrams, is recommended before getting involved with the FRG. It is the aim of this chapter to introduce the quantum field theoretical foundation on which the FRG method is built. Introduced concepts, including the above-mentioned vertex functions and their relations to Green functions, will then be applied in the next chapter to further develop the PFFRG method.

In order to achieve a simple and intuitive introduction of quantum field theoretical concepts, we will pursue a diagrammatic approach that goes beyond the sole manipulation of analytic formulas. As supplementary material to this chapter, we refer to quantum field theory textbooks such as Refs. [17, 18]. The chapter is structured as follows. It will begin by introducing the building blocks of Feynman diagrams in Sec. 2.1, those being single-particle Green functions (commonly known as propagators) and two-particle interactions. The former objects will also be referred to as particle lines if they are mentioned in the context of Feynman diagrams. From the classification, manipulation and structural subdivision of diagrams, vertex functions (including the self-energy) will arise as a class of diagrams exhibiting characteristic properties. The diagrammatic structure of vertex functions will then be considered further to derive relations between Green and vertex functions. The parquet equations will be introduced in Sec. 2.2. Together with the Schwinger-Dyson equation for the self-energy and the parquet approximation, a fully self-consistent set of equations for the computation of the self-energy and two-particle vertex will be obtained. From these equations, the FRG differential equations for the self-energy and two-particle vertex can be derived [19], as will be shown in the following chapter. The chapter will end with a summary in Sec. 2.3

2.1 Green and vertex functions

2.1.1 Green functions

We now first aim at introducing Green functions. For this purpose, a general Hamiltonian is defined for which the Green functions will be considered. More specifically, we consider a fermionic lattice Hamiltonian given by

$$\hat{\mathcal{H}} = \hat{\mathcal{H}}_0 + \hat{\mathcal{V}}, \tag{2.1}$$

which can be subdivided in an exactly solvable term $\hat{\mathcal{H}}_0$ describing noninteracting particles, and a term $\hat{\mathcal{V}}$ corresponding to a two-body interaction of the form

$$\hat{\mathcal{V}} = \frac{1}{2} \sum_{\bar{1}',\bar{2}',\bar{1},\bar{2}} \hat{f}^\dagger_{\bar{1}'} \hat{f}^\dagger_{\bar{2}'} V(\bar{1}',\bar{2}'|\bar{1},\bar{2}) \hat{f}_{\bar{2}} \hat{f}_{\bar{1}} \tag{2.2}$$

$$= \frac{1}{2} \sum_{\alpha\beta\gamma\delta} \sum_{\boldsymbol{r}\boldsymbol{r}'} d\boldsymbol{r} d\boldsymbol{r}' \hat{f}^\dagger_\alpha(\boldsymbol{r}) \hat{f}^\dagger_\beta(\boldsymbol{r}') V_{\alpha\beta\gamma\delta}(\boldsymbol{r},\boldsymbol{r}') \hat{f}_\delta(\boldsymbol{r}') \hat{f}_\gamma(\boldsymbol{r}), \tag{2.3}$$

with arguments such as $\bar{1} = \{\alpha_1, \boldsymbol{r}_1\}$ being composed of a spin α_1 and real space coordinates $\boldsymbol{r}_1$, and $\hat{f}^{(\dagger)}_\alpha(\boldsymbol{r})$ being a fermionic field operator annihilating (creating) a fermion with spin α at coordinates $\boldsymbol{r}$. In the Heisenberg or interaction picture, the imaginary-time-dependent two-body interaction can be written as

$$\hat{\mathcal{V}}(\tau) = \frac{1}{2} \int_0^{1/T} d\tau' \sum_{\alpha\beta\gamma\delta} \sum_{\boldsymbol{r}\boldsymbol{r}'} d\boldsymbol{r} d\boldsymbol{r}' \hat{f}^\dagger_\alpha(\boldsymbol{r},\tau) \hat{f}^\dagger_\beta(\boldsymbol{r}',\tau') V_{\alpha\beta\gamma\delta}(\boldsymbol{r},\boldsymbol{r}') \delta(\tau-\tau') \hat{f}_\delta(\boldsymbol{r}',\tau') \hat{f}_\gamma(\boldsymbol{r},\tau). \tag{2.4}$$

We use the convention of $\hbar = k_B = 1$, with k_B being the Boltzmann constant. T corresponds to the temperature. Note that the arguments of $V(1',2'|1,2)$ gain an imaginary time dependence τ in the Heisenberg or interaction picture, i.e., $1 = \{\alpha_1, \boldsymbol{r}_1, \tau_1\}$. Note that the two-body interaction matrix elements fulfill the relations $V(1',2'|1,2) = V(2',1'|2,1)$ and $V(1',2'|1,2) = -V(1',2'|2,1)$.

The model of Eq. (2.1) can be characterized by n-particle Green functions defined as

$$\begin{aligned} G(1',2',\ldots,n'|1,2,\ldots,n) = \langle \mathcal{T}_\tau \big[& \hat{f}_{\alpha_{1'}}(\mathbf{r}_{1'},\tau_{1'}) \hat{f}_{\alpha_{2'}}(\mathbf{r}_{2'},\tau_{2'}) \ldots \hat{f}_{\alpha_{n'}}(\mathbf{r}_{n'},\tau_{n'}) \\ & \hat{f}^\dagger_{\alpha_n}(\mathbf{r}_n,\tau_n) \ldots \hat{f}^\dagger_{\alpha_2}(\mathbf{r}_2,\tau_2) \hat{f}^\dagger_{\alpha_1}(\mathbf{r}_1,\tau_1) \big] \rangle, \end{aligned} \tag{2.5}$$

with the time evolution being given in the Heisenberg picture. $\mathcal{T}_\tau$ is the time-ordering operator, which orders the operators to its right-hand side with decreasing imaginary time arguments from left to right and adds a prefactor $(-1)^l$, with l being the number of permutations required for this operation [17]. The n-particle Green function is specified by $2n$ sets of arguments, one for each fermion operator on the right-hand side of the equation. Each set of arguments $m \in \{1',2',\ldots,n',n,\ldots,2,1\}$ is composed of a spin α_m, imaginary time τ_m and real space coordinates $\boldsymbol{r}_m$. For clarity, Green function arguments for creation and annihilation operators are separated by a vertical line. This convention will be applied for the later introduced vertex functions as well. The special case of a single-particle Green function is given by

$$G(1'|1) = \langle \mathcal{T}_\tau \big[\hat{f}_{\alpha_{1'}}(\mathbf{r_{1'}},\tau_{1'}) \hat{f}^\dagger_{\alpha_1}(\mathbf{r_1},\tau_1) \big] \rangle. \tag{2.6}$$

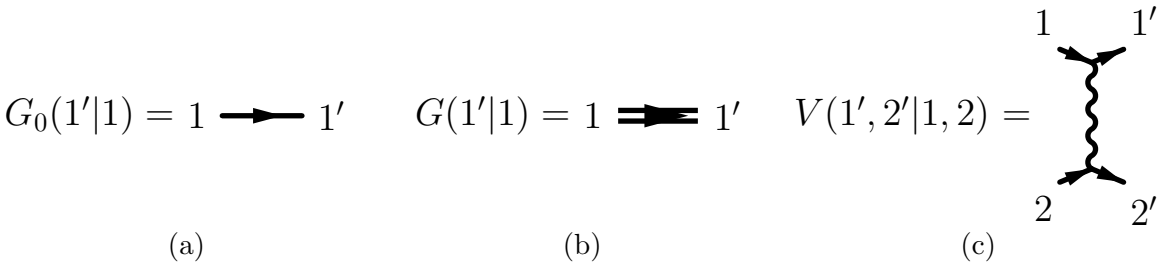

(a) (b) (c)

Figure 2.1: Display of building blocks of Feynman diagrams. The free and full single-particle Green functions $G_0(1'|1)$ and $G(1'|1)$, as well as the two-body interaction $V(1', 2'|1, 2)$ are shown. Positions for in and outgoing particle lines are indicated for the two-body interaction line.

The magnitude of $G(1'|1)$ gives the expectation value of the overlap between the state to which a fermion (hole), inserted into the system at specified time and state given by the set of arguments 1 ($1'$), propagates to at time $\tau_{1'}$ (τ_1), and the state specified by the remaining arguments $\{\boldsymbol{r_{1'}}, \alpha_{1'}\}$ ($\{\boldsymbol{r_1}, \alpha_1\}$). The imaginary-time evolution of the system is performed in the grand canonical ensemble. In the Heisenberg picture, the imaginary-time-dependence of fermion operators is given by

$$\hat{f}_\alpha(\mathbf{r}, \tau) = e^{\hat{K}\tau} \hat{f}_\alpha(\mathbf{r}) e^{-\hat{K}\tau} \tag{2.7}$$

with $\tau \in \mathbb{R}$ and $\hat{K} = \hat{\mathcal{H}} - \mu\hat{N}$, involving the chemical potential μ and particle number operator $\hat{N}$. We will only consider the case $\hat{K} = \hat{\mathcal{H}}$, since only the case of a vanishing chemical potential will be relevant in this thesis.

Green functions can be applied to access properties of a Hamiltonian. They allow the computation of expectation values of observables, including the thermal average of a model's energy [17]. E.g., in case of a general one-body observable $\hat{O}$, its expectation value can be reformulated in terms of the equal-time single-particle Green function as

$$\begin{aligned} \langle \hat{O} \rangle &= \sum_{\alpha\beta} \sum_{\boldsymbol{r}\boldsymbol{r'}} O_{\alpha\beta}(\boldsymbol{r}, \boldsymbol{r'}) \langle \hat{f}^\dagger_\alpha(\boldsymbol{r}) \hat{f}_\beta(\boldsymbol{r'}) \rangle \\ &= \sum_{\alpha\beta} \sum_{\boldsymbol{r}\boldsymbol{r'}} O_{\alpha\beta}(\boldsymbol{r}, \boldsymbol{r'}) G(\{\alpha, \boldsymbol{r}, \tau^+\} | \{\beta, \boldsymbol{r'}, \tau\}), \end{aligned} \tag{2.8}$$

with τ^+ being infinitesimally larger than τ. I.e., the expectation value of any one-body observable can be computed once the single-particle Green function $G(1'|1)$ of a model is determined. The computation of n-body observables with $n > 1$ usually requires knowledge of n-particle Green functions with $n > 1$. For a single-particle Green function, one distinguishes between a free Green function $G_0(1'|1)$, which is obtained by evaluating Eq. (2.6) with respect to the free Hamiltonian $\hat{\mathcal{H}}_0$, and the full Green function $G(1'|1)$ obtained by using the full Hamiltonian of Eq. (2.1) instead. While the computation of $G_0(1'|1)$ can be carried out analytically, $G(1'|1)$ generally has

to be approximated. An approach to such an approximation consists of formulating a perturbative series about the known solution of $G_0(1'|1)$. This strategy will be elaborated in the following, leading to the introduction of Feynman diagrams as a visualization of analytical terms in the perturbative series.

Feynman diagrams

The general inability to analytically compute full Green functions from Eq. (2.5) is caused by the two-body interaction $\hat{\mathcal{V}}$, which is implicitly contained in the time-evolution operator $e^{-\tau\hat{\mathcal{H}}}$ and the Boltzmann weight $e^{-\hat{\mathcal{H}}/T}$. While the former operator gives the time dependence of the fermion creation and annihilation operators [see Eq. (2.7)], the latter operator is included in the thermal average

$$\langle \dots \rangle = \frac{\mathrm{tr}(e^{-\hat{\mathcal{H}}/T} \dots)}{\mathrm{tr}(e^{-\hat{\mathcal{H}}/T})}. \tag{2.9}$$

A perturbative expansion around the exactly solvable noninteracting model $\hat{\mathcal{H}}_0$, whose derivation we will briefly sketch here, is accessed by switching to the interaction picture for time evolution. Such a reformulation can be achieved by rewriting previous time-evolution operators of the Heisenberg picture as

$$e^{-\tau\hat{\mathcal{H}}} = e^{-\tau\hat{\mathcal{H}}_0}\hat{\mathcal{U}}(\tau, 0). \tag{2.10}$$

The analogous reformulation, obtained by exchanging τ and $1/T$ in the above equation, is applied to the Boltzmann constant $e^{-\hat{\mathcal{H}}/T}$. By extending $\hat{\mathcal{U}}(\tau, \tau')$ in an infinite series as

$$\hat{\mathcal{U}}(\tau, \tau') = \sum_{i=0}^{\infty} \frac{1}{i!} \int_{\tau'}^{\tau} d\tau_1 \cdots \int_{\tau'}^{\tau} d\tau_i \mathcal{T}_\tau[\hat{\mathcal{V}}(\tau_1) \dots \hat{\mathcal{V}}(\tau_i)], \tag{2.11}$$

the n-particle Green function can be expressed by an infinite series in turn after setting in Eqs. (2.10) and (2.11) in Eq. (2.5). The resulting expression is given by

$$\begin{aligned} G(1', 2', \dots, n'|1, 2, \dots, n) = &\sum_{i=0}^{\infty} \frac{1}{i!} \int_{\tau'}^{\tau} d\tau_1 \cdots \int_{\tau'}^{\tau} d\tau_i \\ &\times \langle \mathcal{T}_\tau \big[\hat{\mathcal{V}}(\tau_1) \dots \hat{\mathcal{V}}(\tau_i) \hat{f}_{\alpha_{1'}}(\mathbf{r}_{1'}, \tau_{1'}) \hat{f}_{\alpha_{2'}}(\mathbf{r}_{2'}, \tau_{2'}) \dots \hat{f}_{\alpha_{n'}}(\mathbf{r}_{n'}, \tau_{n'}) \\ &\times \hat{f}^\dagger_{\alpha_n}(\mathbf{r}_n, \tau_n) \dots \hat{f}^\dagger_{\alpha_2}(\mathbf{r}_2, \tau_2) \hat{f}^\dagger_{\alpha_1}(\mathbf{r}_1, \tau_1) \big] \rangle_0 \langle \hat{\mathcal{U}}(\beta, 0) \rangle_0^{-1}. \end{aligned} \tag{2.12}$$

The term $\langle \hat{\mathcal{U}}(\beta, 0) \rangle_0^{-1}$ corresponds to the inverse partition sum. Operators in Eqs. (2.11) and (2.12) are given in the interaction picture, including $\hat{\mathcal{V}}(\tau)$, which is given by Eq. (2.4). $\langle \dots \rangle_0$ are expectation values under $\hat{\mathcal{H}}_0$. For further information on the derivation of the perturbative expansions we refer to Sec. 24 of Ref. [18]. For our

purposes, it is important to emphasize that while each individual term occurring in Eq. (2.12) can be computed in principle [18], terms of higher order i quickly become sophisticated in their structure.

The perturbative series Eq. (2.12) becomes more accessible by visualizing its terms as Feynman diagrams [17], as will be specified later. Each Feynman diagram uniquely translates to a unique analytical expression. Based on this property, this diagrammatic approach allows us to treat properties of quantum field theoretical concepts without bothering with underlying sophisticated analytical expressions. To keep the following discussions of Green and vertex functions simple and accessible, we will focus on their diagrammatic properties. Furthermore, connections between Green, connected Green, and vertex functions will mostly be established through their diagrammatic properties.

The general structure of Feynman diagrams will be explained in the following. Elemental building blocks of Feynman diagrams are free single-particle Green functions $G_0(1'|1)$ and interaction lines corresponding to two-body interaction matrix elements $V(1', 2'|1, 2)$. They are visualized in Feynman diagrams as shown in Fig. 2.1. $G_0(1'|1)$ is visualized by a thin particle line, orientated by an arrow. The line's beginning is associated with the set of arguments 1 for the ingoing particle, whereas the endpoint corresponds to the set of arguments $1'$ of the outgoing particle. In other words, the direction of the particle line is given such that either the propagating fermion is created or hole is annihilated at the beginning of the line. In contrast to $G_0(1'|1)$, $G(1'|1)$ is often visualized by a double line. In some cases, we will omit arrows for propagator lines if they are not required. Two-body interaction matrix elements $V(1', 2'|1, 2)$ are visualized by wiggly lines, as shown in Fig. 2.1(c). At each endpoint of the interaction line, each one ingoing and outgoing particle line can attach. Arguments $1'$ and 1 ($2'$ and 2) are always located at the same endpoint of the interaction line corresponding to $V(1', 2'|1, 2)$. Examples of simple Feynman diagrams that contribute to the full single- or two-particle Green functions, are shown in Fig. 2.2. Diagrams of Fig. 2.2(a)-(d) contribute to $G(1'|1)$. Fig. 2.2(a) corresponds to a free single-particle Green function, Fig. 2.2(b) shows the so-called Hartree diagram, and Fig. 2.2(c) shows the so-called Fock diagram. Diagrams of Fig. 2.2(e)-(f) contribute to $G(1', 2'|1, 2)$.

The structure of Feynman diagrams has now been given. Next, we state the rules to evaluate n-particle Green functions $G(1', 2', \ldots, n'|1, 2, \ldots, n)$ from a series of Feynman diagrams. The rules will be formulated as done in Ref. [17] and are shown in the gray box below. Notations and phrasings are adjusted to be in agreement with our conventions for notations.

1. Draw all distinct diagrams composed of n external points $1, \ldots, n$, n external points $1', \ldots, n'$, and r interaction lines connected by directed particle lines in which all components are connected to external points. Two diagrams are distinct if, holding the external points fixed, vertices of the Feynman diagrams and internal propagators cannot be deformed so as to coincide complete1y including the direction of arrows on propagators. The contribution for each distinct diagram is evaluated as follows:

2. Each external point corresponds to a specified state and imaginary time given by an argument of the n-particle Green function to which the Feynman diagram contributes. For each particle line running from 1 to $1'$, as shown in Fig. 2.1(a), include the factor $G_0(1'|1)$.

3. For each interaction line with ingoing particle lines of arguments 1 and 2, and outgoing particle lines of arguments $1'$ and $2'$, as shown in Fig. 2.1(c), include the factor $V(1', 2'|1, 2)$.

4. Sum over all internal single-particle variables (spins and real space coordinates) and integrate the internal imaginary times τ_i over the interval $[0, 1/T]$.

5. Multiply the result by the factor $(-1)^{r+n_P+n_L}$ where n_L is the number of closed particle line loops and n_P is the number of permutations needed for external Green function arguments $1, \ldots, n, 1', \ldots, n'$ such that each particle line originating at the external point j terminates at the external point j', with $j \in \{1, \ldots, n\}$.

Note that in our visualizations of Feynman diagrams, we will mark vertices that contain summations over variables by black dots. As expressions for both $G_0(1'|1)$ and $V(1', 2'|1, 2)$ are generally known, all Feynman diagrams that they construct can in principle be computed. However, the evaluation of diagrams with internal loops can lead to divergences. The reason becomes clear if the diagrams are expressed in frequency space, as will be explained in the following (see Ref. [18] for the rules to compute Feynman diagrams in frequency and momentum space).

Since previous dependencies have been formulated in imaginary time, frequency dependencies will be given by fermionic Matsubara frequencies $\omega_m = (2m + 1)T\pi$, with $m \in \mathbb{Z}$. The frequency-dependent single-particle Green function $\bar{G}(1'|1)$ (with arguments $1(') = \{\alpha_{1(')}, \mathrm{r}_{1(')}, \omega_{1(')}\}$) is related to the time-dependent version $G(1'|1)$ (with

arguments $1(') = \{\alpha_{1(')}, \mathrm{r}_{1(')}, \tau_{1(')}\}$) by the Fourier transformation

$$G(1'|1) = T \sum_m e^{-i\omega_1(\tau_1 - \tau_{1'})} \bar{G}(1'|1), \tag{2.13}$$

with $\bar{G}(1'|1) \sim \delta_{\omega_{1'}\omega_1}$. Note that at a later point we will use the simplified notation $G(1'|1)$ for frequency-dependent Green functions as well, once time-dependent Green functions will not be applied anymore. Similarly, the imaginary time-dependent two-body interaction, given in Eq. (2.4), is related to its (frequency-independent) Fourier transform by

$$V_{\alpha\beta\gamma\delta}(\boldsymbol{r}, \boldsymbol{r'})\delta(\tau' - \tau) = T \sum_m e^{-i\omega(\tau' - \tau)} V_{\alpha\beta\gamma\delta}(\boldsymbol{r}, \boldsymbol{r'}). \tag{2.14}$$

By inserting Eqs. (2.13) and (2.14) into the analytical expression of any Feynman diagram, previous imaginary-time integrals at internal vertices are repurposed as frequency conservation laws. More precisely, each internal vertex comes with a factor $\int_0^{1/T} d\tau_j e^{-i(\omega_m - \omega_{m'} + \omega_{m''})} = T\delta_{(\omega_m - \omega_{m'} + \omega_{m''})0}$, with ω_m corresponding to the frequency of the ingoing particle line, $\omega_{m'}$ of the outgoing particle line, and $\omega_{m''}$ of the interaction line. Each resulting Kronecker delta $\delta_{(\omega_m - \omega_{m'} + \omega_{m''})0}$ allows for the evaluation of one frequency summation. However, for each closed loop in the diagram, one frequency summation will remain after the evaluation of all Kronecker deltas. These remaining summations can lead to divergences in the evaluation of Feynman diagrams. The above argument can be performed analogously for Fourier transformations to momentum space. Note that one strategy to regularize divergent Feynman diagrams consists of introducing a renormalization group parameter [16].

Connected Green functions

In individual Feynman diagrams of the single-particle Green function, all components are connected to each other. In contrast, different components of Feynman diagrams that contribute to n-particle Green functions with $n > 1$ are often disconnected. Note that each component still has to be connected to external particle lines. The simplest example of a Feynman diagram with disconnected components contributing to $G(1', 2'|1, 2)$ is given by simply two disconnected particle lines. It can be useful to separate the fully connected diagrams of a Green function by defining the connected Green functions $G_c(1', 2', \ldots, n'|1, 2, \ldots, n)$ obtained from the full Green function $G(1', 2', \ldots, n'|1, 2, \ldots, n)$ by only summing over its connected Feynman diagrams. In case of the two-particle Green function, the relation between connected and full

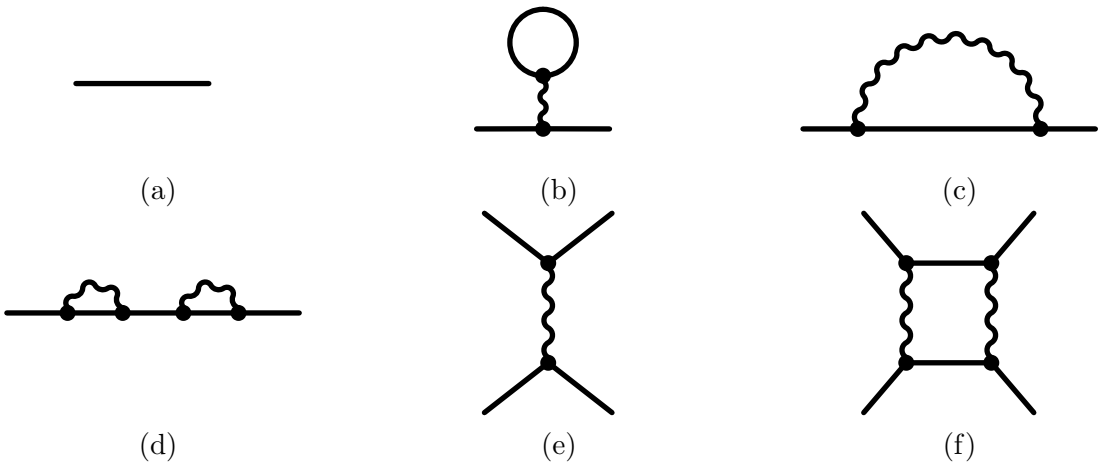

Figure 2.2: Display of simple Feynman diagrams that contribute to the single- and two-particle Green functions $G(1'|1)$ and $G(1', 2'|1, 2)$. Directions of particle lines and external arguments are omitted for simplicity. Internal vertices are highlighted by black dots.

Green function is given by [17]

$$G_c(1', 2'|1, 2) = G(1', 2'|1, 2) - G(1'|1)G(2'|2) + G(2'|1)G(1'|2). \tag{2.15}$$

A diagrammatic visualization of the equation is given by

$G_c(1', 2'|1, 2)$ =

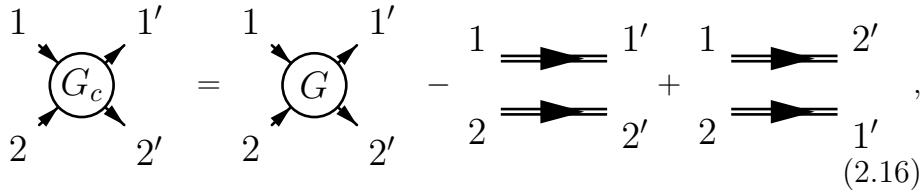

, (2.16)

in which the external arguments are labeled. The equation shows that the disconnected diagrams of $G(1', 2'|1, 2)$ can be reorganized in terms of single-particle Green functions. Note that the last two terms of the equation differ in that two external arguments are exchanged. This leads to a change in prefactor for one term due to the Pauli principle. While we have simply stated the relation between the two-particle connected and full Green functions here, the relations between any n-particle connected and full Green function can be derived analytically as well by manipulating the so-called generating functional for connected Green functions, as shown in [17]. Since the given diagrammatic relation between $G_c(1', 2'|1, 2)$ and $G(1', 2'|1, 2)$ is quite intuitive, and because we are not interested in connected n-particle Green functions with $n > 2$, we do not bother with the analytic derivation of these relations.

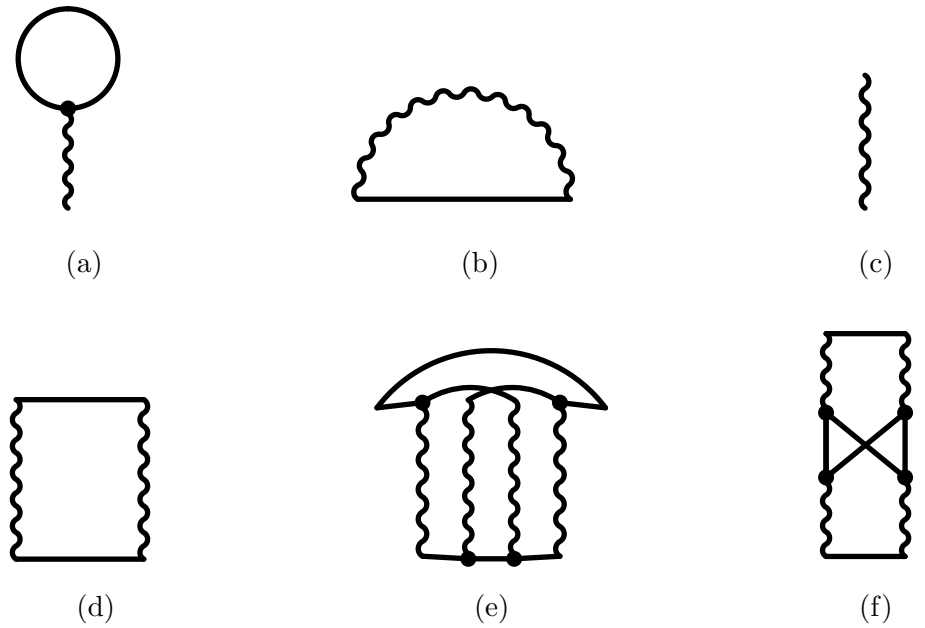

Figure 2.3: Display of simple Feynman diagrams that are single-particle irreducible and amputated. The shown diagrams contribute to the self-energy $\Sigma(1'|1)$ and two-particle vertex function $\Gamma(1', 2'|1, 2)$. Directions of particle lines and external arguments are omitted for simplicity. Internal vertices are highlighted by black dots. In contrast, vertices that coincide with an external point are absent of a black dot. All diagrams from Fig. 2.2 that contribute to vertex functions once they are amputated are shown in (a)-(d).

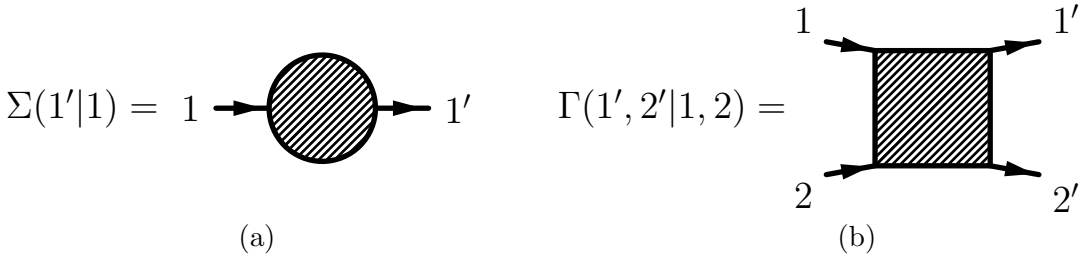

Figure 2.4: The Feynman diagrams of the self-energy $\Sigma(1'|1)$ and two-particle vertex function $\Gamma(1', 2'|1, 2)$ are shown. The position of an argument in $\Sigma(1'|1)$ and $\Gamma(1', 2'|1, 2)$ uniquely corresponds to a direction from which the corresponding particle line connects to a Feynman diagram of the corresponding vertex function. Particle lines always enter the vertex diagrams from the left and leave them to the right. Particle lines of arguments 1 and $1'$ connect to upper corners of $\Gamma(1', 2'|1, 2)$ diagrams, whereas particle lines of arguments 2 and $2'$ connects to lower corners.

2.1.2 Vertex functions

We now continue by introducing vertex functions, which will occasionally be referred to solely as vertices. They are the objects that are computed in FRG methods, and thus are of central importance to this thesis [16]. An emphasis will be put on the single and two-particle vertex functions, such as their relation to Green functions. It was previously argued that full Green functions can be formulated as a sum over Feynman

diagrams that are build from free single-particle Green functions and two-particle interaction lines. However, different choices for elemental building blocks of the diagrams can be made as well by summarizing subsets of Feynman diagrams with distinct properties into novel well-defined objects. The determination of those objects then implicitly gives the sum over an infinite subset of Feynman diagrams, and consequently, may constitute a more efficient approach to the evaluation of the Green function diagrammatic perturbation series. One choice of reorganizing Feynman diagrams was already given previously by the introduction of connected Green functions. A more relevant concept in the context of the FRG are the so-called vertex functions. In fact, one can argue that vertex functions are a concept on equal footing as Green functions in the sense that they can be applied to access the same properties of a model. Accordingly, the same observables of a model can be accessed by either expressing them through vertex or Green functions. From a diagrammatic perspective this is clear from the fact that all Green functions can be reconstructed from only vertex functions and free particle lines [17]. On the other hand, from an analytical perspective this is apparent by the fact that generating functionals of connected Green and vertex functions are related by a Legendre transformation with respect to the source field (see Sec. 2.1.3).

In a diagrammatic approach, the n-particle vertex function is defined by the sum over all amputated, connected and one-particle irreducible diagrams with each n in and outgoing particle lines [17]. Amputated diagrams are obtained from Green function diagrams by removing all particle lines that are attached to external points. External points of the resulting diagrams directly connect to interaction lines. One-particle irreducible diagrams cannot become disconnected by removing a single internal particle line. An example of a one-particle reducible diagram is given by Fig. 2.2(d). All remaining diagrams of Fig. 2.2 are one-particle irreducible. Examples of diagrams contributing to single and two-particle vertex functions are given in Fig. 2.3. Diagrams in Fig. 2.3(a)-(b) contribute to the single-particle vertex function, whereas diagrams in Fig. 2.3(c)-(f) contribute to the two-particle vertex function. The simplest diagram in the latter set is given by the bare interaction.

In context of this thesis' FRG implementation, we will mostly be interested in the single-particle vertex, corresponding to the self-energy $\Sigma(1'|1)$, and the two-particle vertex $\Gamma(1', 2'|1, 2)$. These are the only vertex functions that will be determined by the method. They are visualized as shown in Fig. 2.4. As a convention, further specified in the same figure, diagrams of vertices will be drawn such that external points will always be assigned to the same vertex function argument depending on their location. E.g., particle lines will always enter from the left and leave to the right-hand side of the diagram. In case of the two-particle vertex $\Gamma(1', 2'|1, 2)$, external points of arguments $1^{(\prime)}$ are located on the upper and external points of arguments $2^{(\prime)}$ are located on the

lower edge of a diagram.

2.1.3 Relating Green and vertex functions

Full Green functions can be constructed from Feynman diagrams whose building elements are only vertex functions and free single-particle Green functions. The resulting diagrams do not contain any closed propagator loops and are called tree diagrams because of this property [17]. Vice versa, all Green function diagrams with internal loops will be isolated in vertex functions if such a construction is pursued.

Relations between Green and vertex functions can be derived analytically by manipulating generating functionals for Green and vertex functions, as shown in Ref. [17]. We will skip these derivations in the following and put an emphasis on the diagrammatic expressions of the relations between single and two-particle Green and vertex functions. Complementary analytical equations will often be written in matrix notation to keep them clean and simple. In matrices of $G_{(0)}(1'|1)$ or $\Sigma(1'|1)$, arguments $1'$ specify the row and 1 the column. Generating functionals for Green and vertex functions will be introduced near the end of this section for completeness.

We first consider the relation between $G_c(1',2'|1,2)$ and $\Gamma(1',2'|1,2)$. As follows from the above-mentioned diagrammatic definitions of connected Green and vertex functions, in order to exactly obtain all Feynman diagrams of $\Gamma(1',2'|1,2)$ from the full set of $G_c(1',2'|1,2)$ diagrams, one first has to remove all one-particle reducible diagrams. Subsequently, the remaining diagrams have to be amputated. E.g., the latter operations will transform the diagram of Fig. 2.2(e) into that of Fig. 2.3(c), and the diagram of Fig. 2.2(f) into that of 2.3(d). Vice versa, all diagrams of $G_c(1',2'|1,2)$ are obtained from $\Gamma(1',2'|1,2)$ by attaching full single-particle Green functions to each of its external points [17]. Diagrammatically, this relation corresponds to the equation

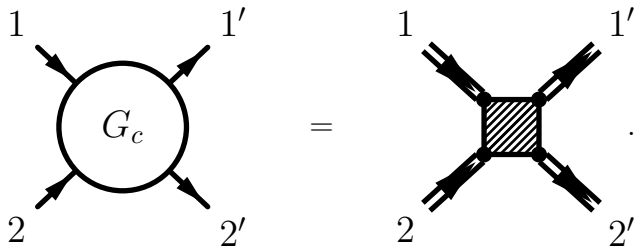

(2.17)

The corresponding analytic equation is given by

$$G_c(1',2'|1,2) = \sum_{3',4',3,4} G(1'|3')G(2'|4')G(3|1)G(4|2)\Gamma(3',4'|3,4). \tag{2.18}$$

Dyson's equation

To describe single- and two-particle properties of a model via vertex instead of Green functions, we still need to express $G(1'|1)$ in terms of the self-energy $\Sigma(1'|1)$. The sought-after relation is given by Dyson's equation, which expresses the full single-particle Green function $\boldsymbol{G}$ via the self-energy $\boldsymbol{\Sigma}$ and free propagator $\boldsymbol{G_0}$ [17]. The equation can be derived from simple diagrammatic arguments, as presented in the following.

The strategy for deriving Dyson's equation consists of classifying each diagram contributing to $G(1'|1)$ as n-fold one-particle reducible, with $n \in \mathbb{N}$ giving the maximum number of times by which a diagram is subsequently one-particle reducible. E.g., the diagram of Fig. 2.2(d) is one-fold one-particle reducible. Since $\Sigma(1'|1)$ is given by the sum over all single-particle *irreducible* diagrams that are amputated, connected and have two external points, one obtains all one-particle irreducible diagrams contained in $G(1'|1)$, except for the diagram of $G_0(1'|1)$, by attaching particle lines on both ends of the self-energy Feynman diagram. All one-fold one-particle reducible diagrams of $G(1'|1)$ are generated by connecting two self-energies by a particle line and dressing the resulting diagram with two particle lines as well. Continuing this construction, each non-amputated n-fold single-particle reducible connected diagram, except for the bare free Green function, is obtained by constructing an open chain of $n+1$ self-energies, with each self-energy being dressed and connected by particle lines. By summing up such chains over all lengths $n \geq 0$ and adding the diagram of the bare free propagator $G_0(1'|1)$, one sums up each connected single-particle Feynman diagram and thus constructs the full single-particle Green function. The diagrammatic equation reads as

(2.19)

or, expressed analytically, as

$$\begin{aligned}\boldsymbol{G} =& \boldsymbol{G}_0 + \boldsymbol{G}_0\boldsymbol{\Sigma}\boldsymbol{G}_0 + \boldsymbol{G}_0\boldsymbol{\Sigma}\boldsymbol{G}_0\boldsymbol{\Sigma}\boldsymbol{G}_0 + ... \\ =& \sum_{i=0}^{\infty} (\boldsymbol{G}_0\boldsymbol{\Sigma})^i \boldsymbol{G}_0,\end{aligned} \tag{2.20}$$

in which internal summations over vertices are left implicit by writing the Green functions and self-energy as matrices. The full Green function can be identified on the

right-hand side of the equation by reformulating

$$\begin{aligned}\boldsymbol{G} =& \sum_{i=0}^{\infty} (\boldsymbol{G}_0 \boldsymbol{\Sigma})^i \boldsymbol{G}_0 \\ =& \boldsymbol{G}_0 + \sum_{i=0}^{\infty} (\boldsymbol{G}_0 \boldsymbol{\Sigma})^i \boldsymbol{G}_0 \boldsymbol{\Sigma} \boldsymbol{G}_0 \\ \overset{(2.20)}{=}& \boldsymbol{G}_0 + \boldsymbol{G} \boldsymbol{\Sigma} \boldsymbol{G}_0. \end{aligned} \tag{2.21}$$

The equation is solved by matrix inversion, giving Dyson's equation

$$\boldsymbol{G} = (\boldsymbol{G}_0 - \boldsymbol{\Sigma})^{-1}. \tag{2.22}$$

Generating functionals for Green and vertex functions

In the previous sections, Green functions were established, based on their definition Eq. (2.5), as a summation over Feynman diagrams. Vertex and connected Green functions were then introduced and related to Green functions on the basis of their diagrammatic properties. As an alternative approach, Green, connected Green and vertex functions, and the relations between them, can be established from their respective generating functionals. Here, we give a brief introduction on these functionals and state their relations. The equations will be given in the path integral formulation of quantum field theory, similar to their formulations in Ref. [17].

The generating functional for n-particle Green functions has a functional dependence on source fields J_m and J_m^*, with $m = \{\alpha_m, \boldsymbol{r}_m, \tau_m\}$, and is defined as

$$\mathcal{G}[J_m^*, J_m] = \frac{1}{\mathcal{Z}} \int D[\phi_m^*, \phi_m] \exp\Big\{ i\mathcal{S}[\phi_m^*, \phi_m] - \sum_m [J_m^* \phi_m + \phi_m^* J_m] \Big\}, \tag{2.23}$$

with the grand canonical partition sum $\mathcal{Z}$, and the action being given by

$$\mathcal{S}[\phi_m^*, \phi_m] = i\Big(\sum_m \phi_m^* (\partial_{\tau_m} - \mu) \phi_m + \mathcal{H}[\phi_m^*, \phi_m] \Big). \tag{2.24}$$

The definition of $\mathcal{G}[J_m^*, J_m]$ involves a functional integral over fields ϕ_m and ϕ_m^* that can be understood as a source-field-dependent partition sum

$$\mathcal{Z}[J_m^*, J_m] = \int D[\phi_m^*, \phi_m] \exp\Big\{ i\mathcal{S}[\phi_m^*, \phi_m] - \sum_m [J_m^* \phi_m + \phi_m^* J_m] \Big] \Big\}, \tag{2.25}$$

with the property $\mathcal{Z}[J_m^* = 0, J_m = 0] = \mathcal{Z}$. The notation $\sum_m$ denotes an implicit imaginary time integral over τ_m, and summations over spin α_m and real space coordi-

nate variables $\boldsymbol{r}_m$. The involved fields ϕ_m and J_m act as Grassmann variables fulfilling $\phi_m\phi_n + \phi_n\phi_m = 0$. $\mathcal{H}[\phi_m^*, \phi_m]$ denotes the Hamiltonian of Eq. (2.1) with fermionic annihilation operators $\hat{f}_m$ replaced by fields ϕ_m and creation operators $\hat{f}_m^\dagger$ replaced by conjugated fields ϕ_m^*. Green functions are obtained from $\mathcal{G}[J_m^*, J_m]$ by taking derivatives with respect to the source fields and setting all source fields to zero afterwards. The equation is given by

$$G(1', 2', \ldots, n'|1, 2, \ldots, n) = (-1)^n \frac{\delta^{2n}\mathcal{G}[J_m^*, J_m]}{\delta J_{1'}^* \ldots \delta J_{n'}^* \delta J_n \ldots \delta J_1}\bigg|_{J_m = J_m^* = 0}. \tag{2.26}$$

The generating functional for connected Green functions $\mathcal{G}_c[J_m^*, J_m]$ is obtained by taking the logarithm of $\mathcal{G}[J_m^*, J_m]$, i.e.,

$$\mathcal{G}_c[J_m^*, J_m] = \ln(\mathcal{G}[J_m^*, J_m]). \tag{2.27}$$

Connected Green functions are obtained from $\mathcal{G}_c[J_m^*, J_m]$ analogously to Green functions from $\mathcal{G}[J_m^*, J_m]$ via the equation

$$G_c(1', 2', \ldots, n'|1, 2, \ldots, n) = (-1)^n \frac{\delta^{2n}\mathcal{G}_c[J_m^*, J_m]}{\delta J_{1'}^* \ldots \delta J_{n'}^* \delta J_n \ldots \delta J_1}\bigg|_{J_m = J_m^* = 0}. \tag{2.28}$$

At last, we introduce the generating functional for vertex functions $\mathcal{V}[\psi_m^*, \psi_m]$, which is obtained from $\mathcal{G}_c[J_m^*, J_m]$ via a Legendre transformation with respect to the source fields. The relation is given by

$$\mathcal{V}[\psi_m^*, \psi_m] = -\mathcal{G}_C[J_m^*, J_m] - \sum_m (\psi_m^* J_m + J_m^* \psi_m) + \sum_{m',m} \psi_{m'}^* (\boldsymbol{G}_0)^{-1}(m'|m)\psi_m, \tag{2.29}$$

in which the last term was added in order for the single-particle vertex to be equal to the self-energy [17]. The new source fields of $\mathcal{V}[\psi_m^*, \psi_m]$ are given by

$$\begin{aligned} \psi_n &= -\frac{\delta}{\delta J_n^*}\mathcal{G}_C[J_m^*, J_m] = \langle \hat{f}_n \rangle, \\ \psi_n^* &= \frac{\delta}{\delta J_n}\mathcal{G}_C[J_m^*, J_m] = \langle \hat{f}_n^* \rangle. \end{aligned} \tag{2.30}$$

Any n-particle vertex function $\Gamma(1', 2', \ldots, n'|1, 2, \ldots, n)$ is obtained from $\mathcal{V}[\psi_m^*, \psi_m]$ by taking derivatives with respect to the source fields ψ_m and ψ_m^*, i.e.,

$$\Gamma(1', 2', \ldots, n'|1, 2, \ldots, n) = (-1)^n \frac{\delta^{2n}\mathcal{V}[\psi_m^*, \psi_m]}{\delta\psi_{1'}^* \ldots \delta\psi_{n'}^* \delta\psi_n \ldots \delta\psi_1}\bigg|_{\psi_m = \psi_m^* = 0}. \tag{2.31}$$

2.1.4 Schwinger-Dyson equations

The previous sections provided relationships between Green and vertex functions. The relation between $G(1',2'|1,2)$ and $\Gamma(1',2'|1,2)$ was expressed diagrammatically in form of a simple tree diagram, see Eq. (2.17). Furthermore, the relation between $G(1'|1)$ and $\Sigma(1'|1)$ was given by Dyson's equation (2.22), which could be derived from simple diagrammatic arguments. However, no nonperturbative scheme to either determine Green or vertex functions has been given at this point. In order to provide equations for vertex functions, we will introduce the Schwinger-Dyson equations (SDE) and parquet equations. While the former will be introduced to obtain an expression for $\Sigma(1'|1)$, the latter will give access to $\Gamma(1',2'|1,2)$. If considered together, these equations allow for a fully self-consistent scheme to determine both $\Sigma(1'|1)$ and $\Gamma(1',2'|1,2)$. As will be argued in the following chapter, the SDE and parquet equations can be utilized to derive the FRG equations for $\Sigma(1'|1)$ and $\Gamma(1',2'|1,2)$.

The Schwinger-Dyson equations can be derived from the assumption that the source-field-dependent partition sum $\mathcal{Z}[J^*_m, J_m]$, as defined in Eq. (2.25), stays invariant under an infinitesimal transformation of the path integral fields $\phi_m \to \phi_m + \delta\phi_m$, i.e., the resulting transformation $\mathcal{Z}[J^*_m, J_m] \to \mathcal{Z}[J^*_m, J_m] + \delta\mathcal{Z}[J^*_m, J_m]$ satisfies $\delta\mathcal{Z}[J^*_m, J_m] = 0$ [20]. This ansatz is closely reminiscent of the classical stationary-action principle, which states that the fields ϕ_m of a classical model are arranged such that the action is stationary under a derivative with respect to them, i.e., $\frac{\partial\mathcal{S}[\phi_m]}{\partial\phi_n} = 0$. While the Euler-Lagrange equations follow from the classical stationary-action principle, the above ansatz for a quantum path integral leads to an infinite set of coupled differential equations for n-particle Green functions instead, the so-called Schwinger-Dyson equations.

In principle SDEs can be formulated for any n-particle Green function. However, we will solely be interested in the SDE of the self-energy, which is obtained from the SDE of $G(1'|1)$ by applying Dyson's equation (2.22) [21]. The SDE of the self-energy is given by

$$\begin{aligned}\Sigma(1'|1) = &-\sum_{2',2} G(2|2')V(1',2'|1,2) \\ &-\frac{1}{2}\sum_{\substack{2',3',4',\\2,3,4}} G(2|2')G(3|3')G(4|4')V(3',4'|1,2)\Gamma(1',2'|3,4),\end{aligned} \tag{2.32}$$

and is visualized diagrammatically as

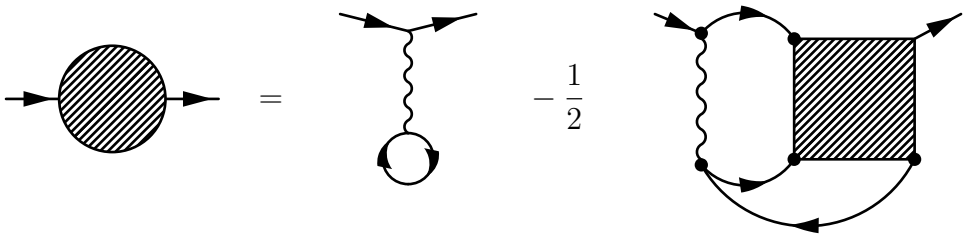

(2.33)

For simplicity, in Eq. (2.33) and for the rest of the thesis we change the conventions for Feynman diagrams such that $G(1'|1)$ will be visualized by thin lines. The following Feynman diagrams will not contain any free Green functions such that no ambiguity in the interpretation of thin lines remains. On the right-hand side of Eq. (2.33), $G(1'|1)$ can be computed from $\Sigma(1'|1)$ via Dyson's equation. The second term reveals that the self-consistent computation of $\Sigma(1'|1)$ from a SDE requires a scheme that provides the two-particle vertex $\Gamma(1', 2'|1, 2)$. Different strategies for a self-consistent computation of $\Sigma(1'|1)$ from Eq. (2.32) can be pursued. A simple approximation consists of neglecting the second term, which involves $\Gamma(1', 2'|3, 4)$. The resulting formula is fully self-consistent and corresponds to the so-called Hartree-Fock approximation, which gives a mean-field single-particle potential [17].

A self-energy beyond mean-field approximation is obtained by incorporating $\Gamma(1', 2'|1, 2)$ into the solution of Eq. (2.33). In this case, a scheme for computing $\Gamma(1', 2'|1, 2)$ has to be applied as well. For this purpose, one may consider the SDE for the two-particle Green function. However, this equation will couple to n-particle Green functions with $n > 2$ in turn. In the next section, the parquet equations will be introduced as another approach of computing $\Gamma(1', 2'|1, 2)$. They possess the advantageous property that they are self-consistent if $\Sigma(1'|1)$ is known, i.e., the approach does not involve any n-particle vertices with $n > 2$.

2.2 Parquet equations

The parquet equations enable the self-consistent computation of $\Gamma(1', 2'|1, 2)$ with only $G(1'|1)$ [or $\Sigma(1'|1)$ and $G_0(1'|1)$], and the so-called totally irreducible two-particle vertex $R(1', 2'|1, 2)$ as input [22]. We will proceed by deriving the parquet equations from simple diagrammatic arguments.

$\Gamma(1', 2'|1, 2)$ has four sets of arguments. In a diagrammatic visualization, two of these sets (1 and 2) are associated with each one ingoing particle line, whereas the remaining sets ($1'$ and $2'$) are associated with each one outgoing particle line. In total, there are

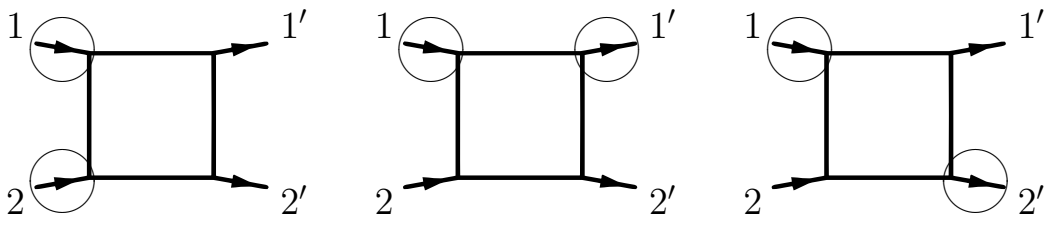

(a) s-channel (b) t-channel (c) u-channel

Figure 2.5: Showcase of the possible pairings for external particle lines in Feynman diagrams with each two in and outgoing particle lines. Paired-up particle lines are circled. Choices of pairing specify whether one considers the s, t, or u channel of the diagram. The subfigures are labeled accordingly. Blank squares represent unspecified two-particle diagrams.

three possible choices to pair the four sets of arguments up, as visualized in Fig. 2.5. Depending on the choice of pairing, one can consider different channels through which Feynman diagrams contributing to $\Gamma(1', 2'|1, 2)$ are traversed. The choice of pairing 1 and 2 (or $1'$ and $2'$) corresponds to entering a diagram through a particle-particle channel, whereas the two remaining channels are of particle-hole type.

In order to label the different channels, we consider the frequency dependencies of diagrams that contribute to $\Gamma(1', 2'|1, 2)$. As a consequence of energy conservation in presence of a time-independent Hamiltonian,

$$\omega_{1'} + \omega_{2'} = \omega_1 + \omega_2 \tag{2.34}$$

is fulfilled for the frequency arguments of each $\Gamma(1', 2'|1, 2)$ diagram. It follows that the frequency dependence of $\Gamma(1', 2'|1, 2)$ can alternatively be expressed by three bosonic so-called transfer frequencies given by

$$\begin{aligned} s =& \omega_{1'} + \omega_{2'}, \\ t =& \omega_{1'} - \omega_1, \\ u =& \omega_{1'} - \omega_2, \end{aligned} \tag{2.35}$$

which fulfill Eq. (2.34) for any combination of values they assume. Vice versa, the frequencies for the individual in and outgoing particle lines are obtained from the relations

$$\begin{aligned} \omega_{1'} =& \frac{1}{2}(s + t + u), \qquad \omega_{2'} = \frac{1}{2}(s - t - u), \\ \omega_1 =& \frac{1}{2}(s - t + u), \qquad \omega_2 = \frac{1}{2}(s + t - u). \end{aligned} \tag{2.36}$$

Depending on through which channel a diagram is traversed, the corresponding in or

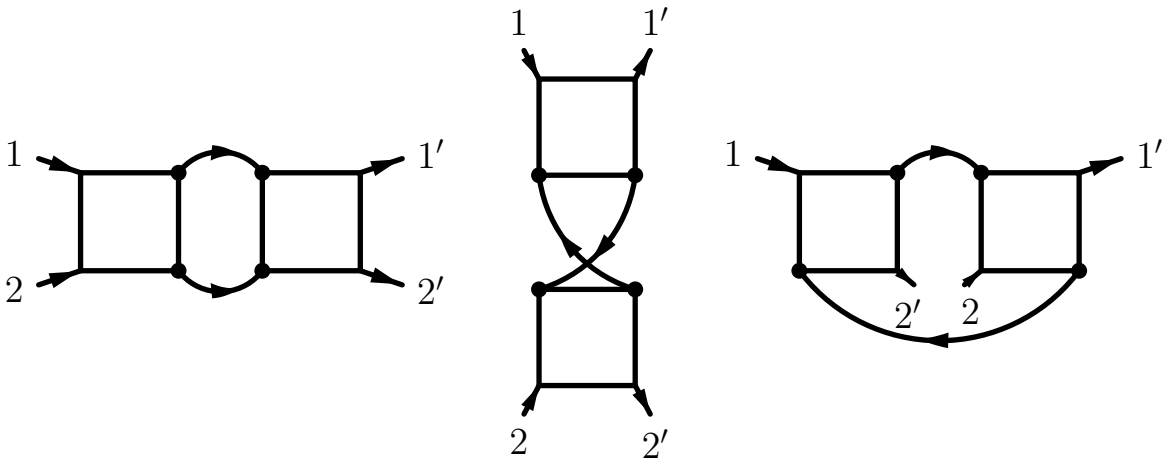

(a) s-channel (b) t-channel (c) u-channel

Figure 2.6: Visualizations of reducible two-particle diagrams with respect to each channel. Subfigure labels specify the channel in which the shown diagrams are two-particle reducible. In and outgoing particle lines are indicated by in and outgoing lines. Blank squares represent unspecified two-particle diagrams.

outgoing paired-up particle lines, either of particle-particle or particle-hole type, allow for a different single transfer frequency to be determined. The channels are labeled accordingly in dependence on the choice of pairing as either s-, t- or u-channel. The allocations are specified in Fig. 2.5. The channels s, t and u introduced here will be conceptually important in the following to subdivide diagrams of $\Gamma(1', 2'|1, 2)$ into smaller diagrams with distinct properties.

During the derivation of Dyson's equation, single-particle diagrams that contribute to $G(1'|1)$ were subdivided into one-particle irreducible sections. The sum over all one-particle irreducible, amputated and connected single-particle diagrams was then identified as the self-energy. Analogously, one can subdivide each diagram that contributes to $\Gamma(1', 2'|1, 2)$ into sections that are irreducible with respect to removing two particle lines in a specified channel. Depending on through which channel a diagram can be cut apart by the removal of a propagator pair, we label the diagram as either (two-particle) reducible in the s-, t- or u-channel. E.g., the Feynman diagram of Fig. 2.3(d) is two-particle reducible in the s-channel. The sum over all one-particle irreducible, amputated and connected two-particle diagrams that are reducible in the r-channel, with $r \in \{s, t, u\}$, gives the two-particle vertex $\gamma_r(1', 2'|1, 2)$ reducible in the r-channel. Visualizations of reducible diagrams with respect to each channel are shown in Fig. 2.6. Similarly, there exist diagrams of $\Gamma(1', 2'|1, 2)$ that are not reducible in any channel. The sum of all such diagrams gives the totally irreducible vertex $R(1', 2'|1, 2)$. Examples of diagrams contributing to $R(1', 2'|1, 2)$ are given by Fig. 2.3(c), 2.3(e) and 2.3(f). Approximating $R(1', 2'|1, 2)$ as the bare interaction $V(1', 2'|1, 2)$ [shown in Fig. 2.3(c)] corresponds to the so-called parquet approximation. Note that the FRG

implementation of this thesis will not generate vertex function diagrams beyond this approximation. A profound insight fundamental to the derivation of the parquet equations is the nonexistence of diagrams contributing to $\Gamma(1', 2'|1, 2)$ that are reducible in more than one channel [22]. In other words, there is no overlap in diagrams between $R(1', 2'|1, 2)$ and $\gamma_r(1', 2'|1, 2)$ for different $r \in \{s, t, u\}$. It follows that one can obtain the full two-particle vertex by summing over all $\gamma_r(1', 2'|1, 2)$, with $r \in \{s, t, u\}$, and R. The analytic formula in matrix notation is given by

$$\boldsymbol{\Gamma} = \boldsymbol{R} + \sum_{r=s,t,u} \boldsymbol{\gamma}_r. \tag{2.37}$$

As counterparts to the reducible vertices, one can introduce the in r-channel irreducible vertex $I_r(1', 2'|1, 2)$, whose individual diagrams cannot be disconnected by removing a single propagator pair in the r-channel. The relations to full and reducible vertices are given by

$$\boldsymbol{I}_r = \boldsymbol{\Gamma} - \boldsymbol{\gamma}_r, \tag{2.38}$$

$$= \boldsymbol{R} + \sum_{\bar{r} \neq r} \boldsymbol{\gamma}_{\bar{r}}. \tag{2.39}$$

2.2.1 Bethe-Salpeter equation

The previous insight, which states that connected and amputated two-particle diagrams can only be reducible in one channel, leads to another simple equation that relates $\gamma_r(1', 2'|1, 2)$ to the full vertex $\Gamma(1', 2'|1, 2)$. The equation is self-consistent under knowledge of $R(1', 2'|1, 2)$, $G_0(1'|1)$, and $\Sigma(1'|1)$, and the parquet relations of Eqs. (2.37)-(2.39). This so-called Bethe-Salpeter equation (BSE) can be considered as the two-particle vertex-function analogue to Dyson's equation and is given in different formulations by

$$\boldsymbol{\Gamma} = \boldsymbol{I}_r + \boldsymbol{I}_r \circ \boldsymbol{\Pi}_r \circ \boldsymbol{\Gamma}, \tag{2.40}$$

$$\boldsymbol{\Gamma} = (1 - \boldsymbol{I}_r \circ \boldsymbol{\Pi}_r)^{-1} \circ \boldsymbol{I}_r, \tag{2.41}$$

$$\boldsymbol{\gamma}_r = \boldsymbol{I}_r \circ \boldsymbol{\Pi}_r \circ \boldsymbol{\Gamma}. \tag{2.42}$$

$\boldsymbol{\Pi}_r$ is a free propagator pair that connects vertices through the r channel, and $\circ$ stands for a matrix multiplication (the formulations of the BSE are chosen similar as in Ref. [19]). Matrix definitions are dependent on the channel r for which the BSE is formu-

lated. The explicit versions of Eq. (2.42) are given for each channel by [19]

$$\gamma_s(1',2'|1,2) = -\frac{1}{2}\sum_{3',4',3,4} I_s(3',4'|1,2)G(3|3')G(4|4')\Gamma(1',2'|3,4), \tag{2.43}$$

$$\gamma_t(1',2'|1,2) = \sum_{3',4',3,4} I_t(1',4'|1,3)G(3|3')G(4|4')\Gamma(3',2'|4,2), \tag{2.44}$$

$$\gamma_u(1',2'|1,2) = -\sum_{3',4',3,4} I_u(3',2'|1,4)G(3|3')G(4|4')\Gamma(1',4'|3,2). \tag{2.45}$$

The diagrammatic representation of Eq. (2.40) is given by

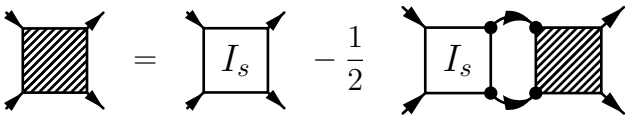

(2.46)

if $r = s$ is considered. Note that the factor $\frac{1}{2}$ in Eq. (2.43) and the second term of Eq. (2.46) appears due to the double counting of diagrams.

The BSE (2.42) has to be solved for each channel $r \in \{s,t,u\}$ simultaneously in order to obtain a solution for the full two-particle vertex function $\Gamma(1',2'|1,2)$. This is typically done by solving the equation across each channel iteratively until a convergent solution is achieved in all channels [23, 24]. The classification of the diagrammatic contributions to $\mathbf{\Gamma}$ into two-particle reducible components $\boldsymbol{\gamma}_r$ and two-particle irreducible components $\boldsymbol{I}_r$ and $\boldsymbol{R}$ [see Eqs. (2.37)-(2.39)], together with the BSE [see Eqs. (2.40)-(2.42)], are known as the parquet equations [22].

In analogue to Dyson's equation, one can derive the BSE by classifying diagrams contributing to $\Gamma(1',2'|1,2)$ into sets of diagrams that are n-fold reducible in the r-channel [22]. $\boldsymbol{I}_r$ then takes the analogue role of $\mathbf{\Sigma}$ in Dyson's equation. I.e., all in the r-channel n-fold reducible two-particle vertex diagrams are obtained by constructing a chain of r-channel irreducible vertices $\boldsymbol{I}_r$ connected by free propagator pairs $\mathbf{\Pi}$ though the r channel. In the form of a matrix equation, this statement is formulated as

$$\mathbf{\Gamma} = \boldsymbol{I}_r + \boldsymbol{I}_r \circ \mathbf{\Pi}_r \circ \boldsymbol{I}_r + \boldsymbol{I}_r \circ \mathbf{\Pi}_r \circ \boldsymbol{I}_r \circ \mathbf{\Pi}_r \circ \boldsymbol{I}_r ..., \tag{2.47}$$

which is of analogue form to Eq. (2.20). Expressed diagrammatically, the same equation reads as

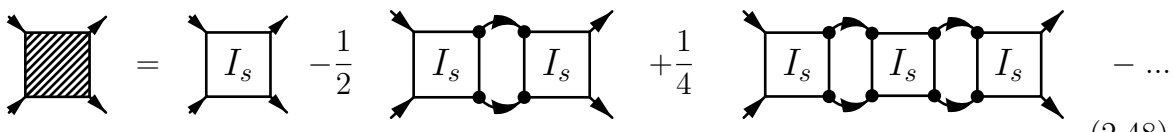

(2.48)

if $r = s$ is considered. Identifying the full vertex on the right-hand side of Eq. (2.47) [or Eq. (2.48)] leads to Eq. (2.40) [or Eq. (2.46)]. Solving this equation via matrix

inversion gives Eq. (2.41). Alternatively, applying Eq. (2.38) instead leads to Eq. (2.42).

Crossing symmetries

The crossing symmetries state the behavior of the two-particle vertex under the exchange of two in or outgoing particle lines [22]. The symmetries follow from the Pauli principle and are given by

$$\Gamma(1',2';1,2) = -\Gamma(2',1';1,2), \tag{2.49}$$
$$\gamma_s(1',2';1,2) = -\gamma_s(2',1';1,2), \tag{2.50}$$
$$\gamma_t(1',2';1,2) = -\gamma_u(2',1';1,2) \tag{2.51}$$

in case of fermionic particle lines. Note that the symmetry operation of exchanging external particle lines exchanges the t and u-channel in Eq. (2.51). One can exchange each both in and outgoing particles as well, which leaves the vertices invariant, i.e.,

$$\Gamma(1',2';1,2) = \Gamma(2',1';2,1), \tag{2.52}$$
$$\gamma_s(1',2';1,2) = \gamma_s(2',1';2,1), \tag{2.53}$$
$$\gamma_t(1',2';1,2) = \gamma_t(2',1';2,1), \tag{2.54}$$
$$\gamma_u(1',2';1,2) = \gamma_u(2',1';2,1). \tag{2.55}$$

2.3 Summary

The theoretical foundation for the following treatment of the PFFRG has been provided in this chapter. Field theoretical concepts, such as Green and vertex functions, were introduced with an emphasis being put on their diagrammatic properties. Furthermore, relations between Green and vertex functions were provided. The relation between the single-particle Green function and self-energy is given by Dyson's equation. In case of the two-particle Green function, the relation to the two-particle vertex function can be presented in form of a tree diagram.

At last, self-consistent schemes for the computation of vertex functions were presented. The first such scheme involves the Schwinger-Dyson equations, which are fixed-point equations for any n-particle Green function. An explicit expression of the Schwinger-Dyson equation for the self-energy was given. As a set of equations for the determination of the two-particle vertex, the parquet equations were diagrammatically derived

by utilizing the reducibility properties of two-particle vertex Feynman diagrams with respect to pairs of particle lines. Together with the Schwinger-Dyson equation for the self-energy and the parquet approximation, a fully self-consistent scheme for the computation of the self-energy and two-particle vertex is obtained. Numerical solutions of these equations are difficult to converge. This issue is lifted by the introduction of a renormalization group parameter, leading to the derivation of the FRG flow equations, as will be shown in the next chapter.

Chapter 3

The pseudo-fermion functional renormalization group

The previous chapter established Green and vertex functions as two quantum field theoretical concepts through which quantum models can be accessed. Furthermore, two nonperturbative approaches to compute these functions were presented by introducing the Schwinger-Dyson and parquet equations. In practice, solving these equations poses a challenge. Expressions may prevent an evaluation by harboring singular behavior, as may be the case for the BSE frequency integral, which will be evaluated in mean-field approximation in Sec. 3.7. In this example, a phenomenological pseudo-fermion lifetime is introduced to the single-particle Green function to regularize the integral. But even in presence of convergent integrals, obtaining convergent solutions for Green or vertex functions is not guaranteed. E.g., previous efforts to iteratively solve the parquet equations (often applied together with the SDE of the self-energy in a self-consistent solving scheme for the self-energy and two-particle vertex) for variants of the Hubbard model have failed in obtaining convergent solutions in presence of strong interactions, whereas solutions were successfully obtained in presence of weak interactions [23, 24].

A regularization of singular expressions and a reliable solution scheme for vertex functions can be obtained from the SDE or parquet equations by introducing a renormalization group parameter Λ to the single-particle Green function that cuts off low-energy degrees of freedom [21, 19]. The introduction of a cutoff parameter is the approach pursued by function renormalization group (FRG) methods [16]. As a nonperturbative approach, the FRG is suited for the study of a wide variety of strongly interacting models. Previous applications of the FRG include the study of Hubbard models [16], quantum chromodynamics [25], nonequilibrium systems [26] and spin models [12]. As a method that fixes the above-mentioned shortcomings of the SDE and parquet equations, a variant of the FRG will be the main approach applied to study highly frustrated

spin models in this thesis.

The study of spin models by means of the FRG is made possible by a selection of method variants. The first FRG formulation for spin models, the pseudo-fermion FRG (PFFRG), maps spin operators onto pseudo fermions (also known as Abrikosov fermions) [12]. The mapping yields models of strongly interacting fermions that are treatable by the standard FRG formalism. As a more recent FRG variant, the pseudo-Majorana functional renormalization group (PMFRG) applies an alternative pseudo-Majorana fermion mapping onto the spin operators, which, in contrast to the previous pseudo-fermion mapping, does not introduce any unphysical states [27, 28]. Another recent approach, the spin FRG (SFRG), does not rely on a spin mapping at all and applies the FRG formalism directly to the spin models of interest [29, 30].

Out of these FRG formulations for spin models, the PFFRG is the variant that will be applied in this thesis and, in its current state, is most well established and developed in the range of spin models that it can treat [12]. While the PFFRG had first been formulated in 2010 for the treatment of $S = 1/2$ Heisenberg models $\hat{\mathcal{H}}_{\text{Heisenberg}} = 1/2 \sum_{ij} J_{ij} \hat{\boldsymbol{S}}_i \cdot \hat{\boldsymbol{S}}_j$ at $T = 0$ [11], with Heisenberg interactions $J_{ij} \in \mathbb{R}$ and $\hat{\boldsymbol{S}}_i = (\hat{S}_i^x, \hat{S}_i^y, \hat{S}_i^z)$ being spin-1/2 vectors acting on a lattice site i, the scope of treatable spin models has been extended since then, as will be summarized in the following. In the method's recent formulation of Ref. [31], spin models $\hat{\mathcal{H}} = 1/2 \sum_{ij} \sum_{\mu,\nu=x,y,z} J_{ij}^{\mu\nu} \hat{S}_i^\mu \hat{S}_j^\nu$ with any anisotropic bilinear spin interaction $J_{ij}^{\mu\nu}$ are treatable. Furthermore, quantum spins of arbitrary spin length $S = M/2$ with $M \in \mathbb{N}$ can be considered, with the method replicating the Luttinger-Tisza approximation in the large-S limit [32]. Similarly, SU(N) spins are treatable for any $N \in \mathbb{N}$ up to the large-N limit [33, 34]. Since the methodologically inherent mapping from spins to pseudo fermions introduces additional unphysical states with no analogue physical state in the original spin Hamiltonian for each lattice site, the method is generally applied at $T = 0$ to keep the influence of unphysical states to a minimum. However, the recent implementation of the Popov-Fedotov trick [35] allows to remove the weight of unphysical states from any thermodynamic average and, as a consequence, opens the door to finite temperature applications. Efforts to qualitatively improve results of the PFFRG by implementing more advanced approximation schemes have been made as well and resulted in the implementation of so-called multiloop truncation schemes [36, 37]. The numerical stability required for such schemes drove further improvements in numerical PFFRG implementations [36, 38]. Furthermore, to emphasize the range of applicability that the PFFRG has in the treatment of spin models, it should be noted that methodologically intrinsic to the PFFRG is the ability to treat models with many frustrated or longer-range interactions at no additional numerical cost. This property makes the method suited for the treatment of highly frustrated spin models with many competing inter-

actions (as will be demonstrated in Chapter 6 by the treatment of a three-dimensional Heisenberg model with many geometrically frustrated interactions).

While a lot of progress has been made in the development of the PFFRG since its initial formulation, some desired use cases were still out of reach since recently [39]. One such use case was the PFFRG application to models with broken time-reversal symmetry (TRS), which had not been explored previously due to an assumed large numerical cost and sophistication in numerical implementation [31]. As such, couplings between spins and external magnetic fields were not treated in previous PFFRG applications. To fix this blind spot in use cases, a central subject of this thesis is the PFFRG method extension towards spin models with broken TRS. In this context, a generalized PFFRG formulation has recently been published in Ref. [39] that allows for the treatment of spin models with arbitrary interactions linear and bilinear in spin operators, given by

$$\hat{\mathcal{H}} = \frac{1}{2}\sum_{ij}\sum_{\mu\nu} J_{ij}^{\mu\nu}\,\hat{S}_i^{\mu}\,\hat{S}_j^{\nu} - \sum_{i}\sum_{\mu} h_i^{\mu}\,\hat{S}_i^{\mu}. \tag{3.1}$$

Such models include sites i and j dependent interactions $J_{ij}^{\mu\nu}$ with $\mu,\nu \in \{x,y,z\}$, which may correspond to Heisenberg or anisotropic interaction interactions, such as Dzyaloshinskii-Moriya interactions. Additionally, arbitrary site-dependent magnetic fields h_i^{μ} can be included that couple linearly to spin operators.

It is the subject of this methodologically focused chapter to introduce and explore the generalized PFFRG formulation of Ref. [39]. For this purpose, we will begin in Sec. 3.1 by offering a high-level introduction to the FRG method. The so-called truncated flow equations of the cutoff parameter Λ dependent self-energy $\Sigma^{\Lambda}(1'|1)$ and two-particle vertex $\Gamma^{\Lambda}(1',2'|1,2)$ will be presented, and their relations to the self-energy SDE and parquet equations will be clarified, as was done in Ref. [19], giving straightforward connections to already known schemes for the computation of $\Sigma(1'|1)$ and $\Gamma(1',2'|1,2)$. The mapping from spins to pseudo fermions will be introduced subsequently in Sec. 3.2 as a prerequisite to the introduction of the PFFRG. The following sections will treat the resulting general pseudo-fermion model obtained by applying the pseudo-fermion mapping to the spin model given by Eq. (3.1), and the general $T = 0$ PFFRG formulation will be derived along a similar path as done in our recent publication Ref. [39]. To this end, symmetries of the pseudo-fermion Hamiltonian will be gathered and their restrictions on the Green and vertex functions will be derived in Sec. 3.3. Based on these symmetry restrictions, appropriate Green and vertex function parameterizations will be introduced in Sec. 3.4 that will allow for a numerically efficient evaluation of the flow equations. The parameterizations are then inserted into the general truncated flow equations of $\Sigma^{\Lambda}(1'|1)$ and $\Gamma^{\Lambda}(1',2'|1,2)$ in Sec. 3.5 to obtain parameterized flow equations. Due to their complexity, the parameterized flow equations will be presented in

detail and their characteristic properties and simplifications for models with additional symmetries, such as TRS or continuous spin rotation symmetries, will be treated. At this point, we will have covered the PFFRG formulation of Ref. [39]. An alternative route towards the implementation of magnetic fields in the PFFRG without breaking TRS will be explored in Sec. 3.6. Subsequently, some general considerations towards the solution of the parquet equations for a pseudo-fermion Hamiltonian are presented in Sec. 3.7. Finally, we end the chapter with a summary in Sec. 3.8.

3.1 Approaches to the FRG

The FRG gives an infinite set of coupled differential equations for the exact n-particle vertex functions [16]. These so-called flow equations can be derived from the generating functional for Green and vertex functions by taking a derivative with respect to a frequency or momentum cutoff Λ of choice after introducing it to the free single-particle Green function, giving it a Λ dependence as $G_0(1'|1) \to G_0^\Lambda(1'|1)$, such that it vanishes in the infinite (infrared) cutoff limit, i.e., $G_0^{\Lambda\to\infty}(1'|1) = 0$ [16]. In this thesis, a sharp frequency cutoff will be applied that modifies

$$G_0(1'|1) \to \theta(|\omega_1| - \Lambda) G_0(1'|1) \equiv G_0^\Lambda(1'|1), \tag{3.2}$$

$$\text{with} \quad \theta(\omega) = \begin{cases} 1, \omega \geq 0 \\ 0, \omega < 0 \end{cases} \tag{3.3}$$

being the Heaviside step function. Accordingly, n-particle vertex functions $\Gamma^\Lambda(1', \ldots, n'|1, \ldots, n)$, each obtained from a separate flow equation, obtain an implicit Λ dependence as well, as can be understood from the fact that their Feynman diagrams are built from free single-particle Green functions. The flow equations are coupled to each other since the flow equation for each n-particle vertex function always contains a term involving the $(n+1)$-particle vertex. While the solution of the infinite set of flow equations gives the exact n-particle vertex functions for each $n \in \mathbb{N}$, obtaining such a solution is generally not feasible. Instead, a truncation scheme has to be applied to obtain a self-consistent finite set of flow equations that is numerically solvable. The truncation is often applied above the two-particle level, i.e, only flow equations for $\Sigma^\Lambda(1'|1)$ and $\Gamma^\Lambda(1', 2'|1, 2)$ have to be solved after the truncation is applied. In this case, the truncation has to handle the term in the flow equation of $\Gamma^\Lambda(1', 2'|1, 2)$ that couples to the unknown three-particle vertex $\Gamma^\Lambda(1', 2', 3'|1, 2, 3)$. A trivial truncation would consist of neglecting this term completely. More advanced truncation schemes partially capture Feynman diagrams of this term self-consistently by constructing them from two-particle vertices. Once the truncated flow equations are obtained, they can

be solved from the known infrared limit $\Lambda \to \infty$ towards the physically relevant cutoff-free limit $\Lambda = 0$, giving a cutoff-dependent flow of vertices in the process. Note that vertices in the limit $\Lambda \to \infty$ can be determined from the simple argument that single-particle Green functions vanish in this limit. Since $G_0^{\Lambda\to\infty}(1'|1) = 0$, the only Feynman diagram contributing to $\Gamma^{\Lambda\to\infty}(1', 2'|1, 2)$ is the Feynman diagram of the two-particle vertex that does not contain any particle lines, corresponding to the bare two-body interaction, i.e., $\Gamma^{\Lambda\to\infty}(1', 2'|1, 2) = V(1', 2'|1, 2)$.

In this thesis, we apply the so-called Katanin truncation scheme. Within this truncation, the flow equations for self-energy and two-particle vertex are given by

$$\frac{d}{d\Lambda}\Sigma^\Lambda(1'|1) = -\sum_{2',2} \Gamma^\Lambda(1', 2'|1, 2)\mathcal{S}^\Lambda(2|2'), \tag{3.4}$$

$$\begin{aligned}\frac{d}{d\Lambda}\Gamma^\Lambda(1', 2'|1, 2) = \sum_{\substack{3',4',\\3,4}} \Big[&\Gamma^\Lambda(1', 2'|3, 4)\Gamma^\Lambda(3', 4'|1, 2) \\ &+ \Gamma^\Lambda(2', 4'|1, 3)\Gamma^\Lambda(3', 1'|4, 2) + \Gamma^\Lambda(2', 3'|1, 4)\Gamma^\Lambda(4', 1'|3, 2) \\ &- \Gamma^\Lambda(1', 4'|1, 3)\Gamma^\Lambda(3', 2'|4, 2) - \Gamma^\Lambda(1', 3'|1, 4)\Gamma^\Lambda(4', 2'|3, 2)\Big] \\ &\times G^\Lambda(3|3')\tilde{\mathcal{S}}^\Lambda(4|4').\end{aligned} \tag{3.5}$$

$\mathcal{S}^\Lambda(1|1') = -\frac{d}{d\Lambda}G^\Lambda(1|1')|_{\Sigma^\Lambda=\text{const}}$ is the so-called single-scale propagator. Upgrading the trivial truncation, corresponding to the full neglection of the three-particle vertex, to a Katanin truncation amounts to upgrading the single-scale propagator $\mathcal{S}^\Lambda(1|1')$ in the two-particle vertex flow equation to $\tilde{\mathcal{S}}^\Lambda(1|1') = -\frac{d}{d\Lambda}G^\Lambda(1|1')$, i.e., the derivative now accounts for the implicit Λ dependence of $\Sigma^\Lambda(1'|1)$. In a diagrammatic visualization, the flow equations are given by

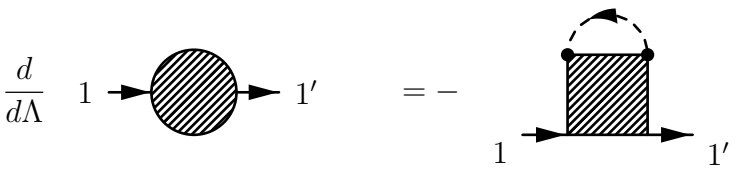

, (3.6)

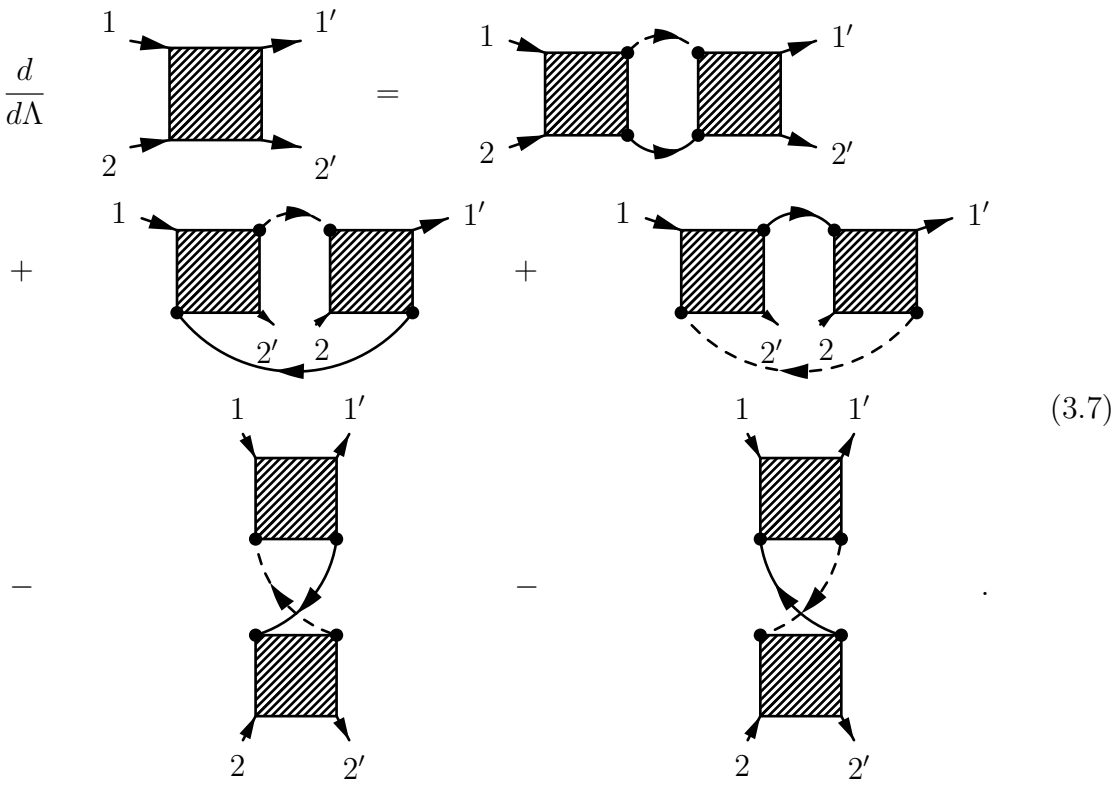

(3.7)

Single-scale propagators $\mathcal{S}^{\Lambda}(1'|1)$ in the self-energy flow equation and $\tilde{\mathcal{S}}^{\Lambda}(1'|1)$ in the two-particle vertex flow equation are shown as dashed particle lines.

The general flow equations within Katanin truncation have now been presented. Before we continue to apply these equations in the PFFRG, we will first take a closer look on how these equations can be derived. There exist different strategies of deriving the truncated FRG flow equations. As mentioned above, the original derivation, which derives the infinite hierarchy of flow equations, manipulates generating functionals of Green and vertex functions [16]. Later, it was shown that the FRG flow equations can be reproduced from the SDEs by introducing a cutoff dependence in the free single-particle Green function. The flow equations of $\Sigma^{\Lambda}(1'|1)$ and $\Gamma^{\Lambda}(1',2'|1,2)$ within Katanin truncation are then replicated from the SDEs of the same functions by neglecting terms higher than quadratic order in $\Gamma^{\Lambda}(1',2'|1,2)$ [21]. A newer approach reveals that the truncated flow equation of $\Gamma^{\Lambda}(1',2'|1,2)$ can be reproduced from the parquet equations by introducing a cutoff to the free single-particle Green function as well [19]. While the standard (one-loop) Katanin truncated flow equation of $\Gamma^{\Lambda}(1',2'|1,2)$ amounts to an incomplete replication of two-particle vertex Feynman diagrams generated from the parquet equations with parquet approximation, a so-called multiloop truncation scheme allows for an extrapolation towards the full equivalence of the FRG flow equation for $\Gamma^{\Lambda}(1',2'|1,2)$ and parquet equations in the infinite loop limit [19]. Note that the parquet formalism only involves single-particle and two-particle vertices. Hence, a replication of n-particle vertex flow equations with $n > 2$ is not possible by this

approach. However, this does not pose a problem for our purposes, since the numerical solution of n-particle vertex flow equations with $n > 2$ is generally not feasible at the time of writing due to the large amount of numerical resources required and, as such, has not been pursued in context of the PFFRG. The same paper of Ref. [19] shows that the self-energy flow equation can be replicated from the self-energy SDE or from the functional derivative of the self-energy with respect to the full single-particle Green function. Both approaches differ from the standard FRG flow equation derivation [16]. We will highlight the connection between the $\Sigma^\Lambda(1'|1)$ flow equation and self-energy SDE, such as the $\Gamma^\Lambda(1',2'|1,2)$ flow equation and parquet equations in the following, based on the derivations of Ref. [19].

3.1.1 From the parquet equations to the two-particle vertex flow equation

We begin by following along the argumentation of Ref. [19] to show how the flow equation of $\Gamma^\Lambda(1',2'|1,2)$ within Katanin truncation can be obtained from the parquet equations. The introduction of a cutoff parameter Λ in $G_0^\Lambda(1'|1)$ results in an implicit Λ dependence of vertex and Green functions since $G_0^\Lambda(1'|1)$ acts as a building block of their respective Feynman diagrams. In the parquet formalism, Feynman diagrams of $\Gamma^\Lambda(1',2'|1,2)$ are organized with respect to their two-particle reducibility. Accordingly, $\Gamma^\Lambda(1',2'|1,2)$ is given by a summation over the reducible vertices $\gamma_r^\Lambda(1',2'|1,2)$ and the totally irreducible vertex $R(1',2'|1,2)$ [see Eq. (2.37)]. Importantly, within parquet approximation, $R(1',2'|1,2)$ does not exhibit a Λ dependence since it is given by the bare two-body interaction $V(1',2'|1,2)$ whose Feynman diagram does not include any Λ-dependent particle lines. The relation of the BSE and two-particle vertex flow equation is revealed by taking the derivative with respect to Λ in Eq. (2.42), giving an equation for $\dot{\boldsymbol{\gamma}}_r^\Lambda = \frac{d\boldsymbol{\gamma}_r^\Lambda}{d\Lambda}$. For the sake of clarity, we apply the previous matrix notation for vertices. By applying some algebra, one arrives at the equations

$$\dot{\boldsymbol{\gamma}}_r^\Lambda = \boldsymbol{\Gamma}^\Lambda \circ \dot{\boldsymbol{\Pi}}_r^\Lambda \circ \boldsymbol{\Gamma}^\Lambda + \dot{\boldsymbol{I}}_r^\Lambda \circ \boldsymbol{\Pi}_r^\Lambda \circ \boldsymbol{\Gamma}^\Lambda + \boldsymbol{\Gamma}^\Lambda \circ \boldsymbol{\Pi}_r^\Lambda \circ \dot{\boldsymbol{I}}_r^\Lambda + \boldsymbol{\Gamma}^\Lambda \circ \boldsymbol{\Pi}_r^\Lambda \circ \dot{\boldsymbol{I}}_r^\Lambda \circ \boldsymbol{\Pi}_r^\Lambda \circ \boldsymbol{\Gamma}^\Lambda, \quad (3.8)$$

$$\overset{(2.39)}{=} \boldsymbol{\Gamma}^\Lambda \circ \dot{\boldsymbol{\Pi}}_r^\Lambda \circ \boldsymbol{\Gamma}^\Lambda + \sum_{r' \neq r} \left(\dot{\boldsymbol{\gamma}}_{r'}^\Lambda \circ \boldsymbol{\Pi}_r^\Lambda \circ \boldsymbol{\Gamma}^\Lambda + \boldsymbol{\Gamma}^\Lambda \circ \boldsymbol{\Pi}_r^\Lambda \circ \dot{\boldsymbol{\gamma}}_{r'}^\Lambda + \boldsymbol{\Gamma}^\Lambda \circ \boldsymbol{\Pi}_r^\Lambda \circ \dot{\boldsymbol{\gamma}}_{r'}^\Lambda \circ \boldsymbol{\Pi}_r^\Lambda \circ \boldsymbol{\Gamma}^\Lambda \right). \quad (3.9)$$

Expressed diagrammatically for the $r = s$ channel, Eq. (3.8) is given by

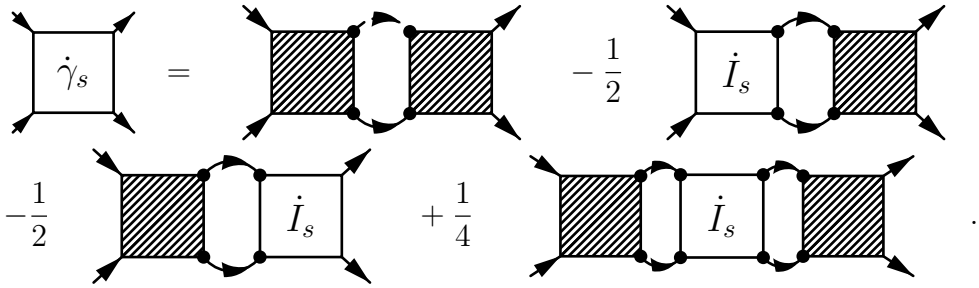

(3.10)

$\tilde{\mathcal{S}}^\Lambda(1|1')$, which appears in the first term, is visualized by a dashed particle line. Note that we applied the crossing symmetry of Eq. (2.50) to arrive at the diagrammatic expression. Since we will refer to it later, we define the last term of Eq. (3.8) as

$$\dot{\boldsymbol{\gamma}}^\Lambda_{r(C)} = \boldsymbol{\Gamma}^\Lambda \circ \boldsymbol{\Pi}^\Lambda_r \circ \dot{\boldsymbol{I}}^\Lambda_r \circ \boldsymbol{\Pi}^\Lambda_r \circ \boldsymbol{\Gamma}^\Lambda. \tag{3.11}$$

The standard two-particle vertex flow equation within (one-loop) Katanin truncation (3.5) is obtained by only considering the first term on the right-hand side of Eq. (3.9) and then summing up the reducible vertices $\dot{\boldsymbol{\gamma}}^\Lambda_r$ over each channel r to obtain the derivative of the full two-particle vertex given by

$$\dot{\boldsymbol{\Gamma}} = \sum_{r=s,t,u} \dot{\boldsymbol{\gamma}}_r \approx \sum_{r=s,t,u} \boldsymbol{\Gamma} \circ \dot{\boldsymbol{\Pi}}_r \circ \boldsymbol{\Gamma}. \tag{3.12}$$

In this step, we applied the parquet approximation, under which $\dot{\boldsymbol{R}} = \boldsymbol{0}$. Note that a so-called two-loop truncation scheme of the FRG can be obtained by iteratively reinserting the one-loop $\dot{\boldsymbol{\gamma}}_r = \boldsymbol{\Gamma}^\Lambda \circ \dot{\boldsymbol{\Pi}}^\Lambda_r \circ \boldsymbol{\Gamma}^\Lambda$ on the right-hand side of Eq. (3.9). Higher loop truncations are obtained analogously by further iterative insertion. Since multiloop truncations will not be applied in this thesis, we refer for further information regarding their implementation in the FRG to Ref. [19].

3.1.2 From the self-energy Schwinger-Dyson equation to the self-energy flow equation

The evaluation of the Green function pair $\boldsymbol{\Pi}^\Lambda_r$ in Eq. (3.9) requires knowledge of $\Sigma^\Lambda(1'|1)$ [see Dyson's Eq. (2.22)], which is not covered by the BSE. Among other approaches, the flow equation of $\Sigma^\Lambda(1'|1)$ can be replicated from the SDE (2.32) [19]. Again, the derivation can be carried out by introducing an explicit cutoff parameter dependence Λ to G^Λ_0 and subsequently taking a derivative with respect to it in the SDE of $\Sigma^\Lambda(1'|1)$. Since the corresponding derivation carried out in Ref. [19] is quite involved, it will not be replicated here. Instead, the end result that is obtained by

taking the Λ derivative of the self-energy SDE will be simply stated. Note that the derivation assumes the parquet approximation at some point. Otherwise, additional terms would emerge in the final expression given below. Starting from the SDE for the self-energy given by Eq. (2.32), one arrives at the expression [19]

$$\dot{\Sigma}^{\Lambda}(1'|1) = -\sum_{2,2'} \Gamma^{\Lambda}(1',2'|1,2)\mathcal{S}^{\Lambda}(2|2') + \dot{\Sigma}^{\Lambda}_{\bar{t}}(1'|1) + \dot{\Sigma}^{\Lambda}_{t}(1'|1), \tag{3.13}$$

with

$$\dot{\Sigma}^{\Lambda}_{\bar{t}}(1'|1) = -\sum_{2,2'} \dot{\gamma}^{\Lambda}_{\bar{t}(C)}(1',2'|1,2)G^{\Lambda}(2|2'), \tag{3.14}$$

$$\dot{\Sigma}^{\Lambda}_{t}(1'|1) = -\sum_{2,2',3,3'} \Gamma^{\Lambda}(1',2'|1,2)G^{\Lambda}(2|3')\dot{\Sigma}^{\Lambda}_{\bar{t}}(3'|3)G^{\Lambda}(3|2'), \tag{3.15}$$

and [see Eq. (3.11)]

$$\dot{\gamma}^{\Lambda}_{\bar{t}(C)}(1',2'|1,2) = \dot{\gamma}^{\Lambda}_{s(C)}(1',2'|1,2) + \dot{\gamma}^{\Lambda}_{u(C)}(1',2'|1,2). \tag{3.16}$$

The diagrammatic representation of Eq. (3.13) is given by

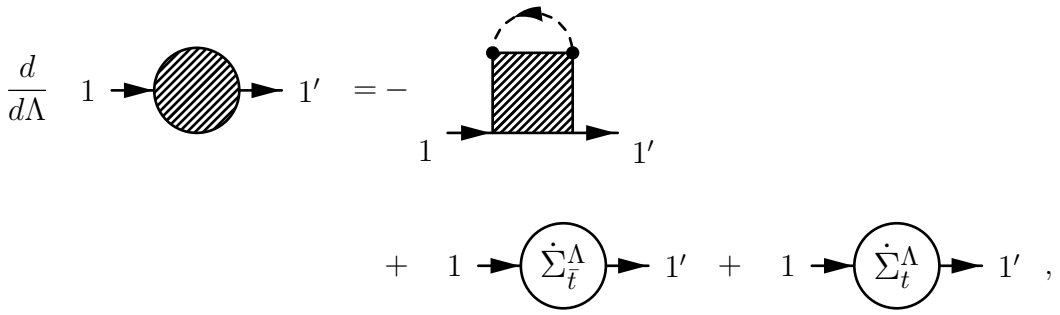

(3.17)

with $\mathcal{S}^{\Lambda}$ being visualized by a dashed particle line.

The standard self-energy flow equation (3.4) is replicated by only considering the first term of Eq. (3.13). Note that in absence of any truncation scheme for the infinite hierarchy of FRG flow equations, the standard flow equation of $\Sigma^{\Lambda}(1'|1)$ gives the exact self-energy. However, because we apply a truncation scheme in the flow equation of $\Gamma^{\Lambda}(1',2'|1,2)$, the insertion of $\Gamma^{\Lambda}(1',2'|1,2)$ into the self-energy flow equation no longer generates all Feynman diagrams of $\Sigma^{\Lambda}(1'|1)$, resulting in an approximation of $\Sigma^{\Lambda}(1'|1)$ [19]. In a multiloop truncation scheme, $\dot{\gamma}^{\Lambda}_{\bar{t}(C)}(1',2'|1,2)$ is assumed as finite in Eq. (3.9). In this case, the terms $\dot{\Sigma}_{t}(1'|1)$ and $\dot{\Sigma}_{\bar{t}}(1'|1)$ have to be taken into account to correctly generate all multiloop Feynman diagrams of $\Sigma^{\Lambda}(1'|1)$ [40]. However, an implementation of a multiloop truncation is beyond the scope of this thesis.

3.2 Introducing the pseudo fermion to the FRG

Methods not applicable to spin models may become feasible once a corresponding fermion or bosonic model is considered. As such, the mapping to fermionic or bosonic models, while keeping the underlying physics unchanged by conserving the spin algebra, poses a powerful tool in the study of quantum spin models. E.g., while mean-field theory is straightforwardly applied to spin models such as that of Eq. (3.1), its solution becomes trivial in a paramagnetic phase due to the vanishing expectation values of single-spin operators. A parton approach, which splits spin operators up into pairs of fermionic (or bosonic) operators, lifts this problem and allows to pair up the resulting fermion or boson operators into expectation values of finite size. The resulting mean-field theories and their classification have become a widespread tool in the study of quantum spin liquids [41].

Relevant to us is the possibility to apply a spin-to-particle mapping in order to apply the FRG formalism to spin models. Such a mapping will be introduced in the following[1]. The PFFRG applies the mapping from spin-1/2 operators to pseudo fermions given by [42]

$$\hat{S}_i^\mu \to \frac{1}{2} \sum_{\alpha,\beta=\uparrow,\downarrow} \sigma^\mu_{\alpha\beta} \hat{f}^\dagger_{i\alpha} \hat{f}_{i\beta}, \tag{3.18}$$

or, rewritten, by

$$\hat{S}_i^\mu \to \frac{1}{4} \mathrm{tr}(\hat{\boldsymbol{F}}_i^\dagger \boldsymbol{\sigma}^\mu \hat{\boldsymbol{F}}_i), \tag{3.19}$$

with spin components $\mu = \{x, y, z\}$, spin quantum numbers $\alpha, \beta = \{\uparrow, \downarrow\}$ and site i dependent matrices of fermion operators

$$\hat{\boldsymbol{F}}_i \coloneqq \begin{pmatrix} \hat{f}_{i\uparrow} & \hat{f}^\dagger_{i\downarrow} \\ \hat{f}_{i\downarrow} & -\hat{f}^\dagger_{i\uparrow} \end{pmatrix}. \tag{3.20}$$

$\sigma^\mu_{\alpha\beta}$ are Pauli matrix elements, and $\hat{f}^\dagger_{i\uparrow}$ ($\hat{f}_{i\downarrow}$) creates (annihilates) a fermion on site i with spin up (down). Applying the pseudo-fermion mapping to the spin Hamiltonian of Eq. (3.1) results in the fermionic model

$$\hat{\mathcal{H}}_{\mathrm{PF}} = \frac{1}{8} \sum_{i,j} \sum_{\mu,\nu} J^{\mu\nu}_{ij} \sum_{\substack{\alpha,\beta,\\ \alpha',\beta'}} \sigma^\mu_{\alpha\beta} \sigma^\nu_{\alpha'\beta'} \hat{f}^\dagger_{i\alpha} \hat{f}_{i\beta} \hat{f}^\dagger_{j\alpha'} \hat{f}_{j\beta'} - \frac{1}{2} \sum_i \sum_\mu h^\mu_i \sum_{\alpha,\beta} \sigma^\mu_{\alpha\beta} \hat{f}^\dagger_{i\alpha} \hat{f}_{i\beta}. \tag{3.21}$$

Note that we will often consider the case of vanishing magnetic fields h^μ_i, i.e., the strongly interacting limit of the model.

[1] Note that field theoretical approaches, including the FRG framework, can also be applied to spin models directly without applying a mapping from spin to fermion or boson operators, as is done in the SFRG [30, 29]. However, the involved formalism might be more difficult to work with.

The latter expression of the pseudo-fermion mapping, given by Eq. (3.19), reveals that the mapping introduces a local SU(2) gauge freedom that acts on site i as a right-multiplication on the matrices $\hat{\boldsymbol{F}}_i$ as

$$\hat{\boldsymbol{F}}_i \longrightarrow \hat{\boldsymbol{F}}_i \boldsymbol{W}_i. \tag{3.22}$$

We will denote the site-dependent unitary symmetry operation matrix as $\boldsymbol{W}_i$. As is implied by the local gauge freedom, the pseudo-fermion mapping increases the Hilbert space dimension of the model. For each site, two unphysical states are created in addition to pseudo-fermion equivalents of the previous two physical spin-up and spin-down states. In the pseudo-fermion Hamiltonian, the local unphysical states correspond to sites j with fermion occupation numbers $n_j = 0$ and $n_j = 2$, whereas the physical states fulfill $n_j = 1$. In other words, unphysical states of a site are characterized by a vanishing local spin. Thus, each of them effectively acts as an empty site in the spin model that neither interacts with spins of other sites via interactions $J_{ij}^{\mu\nu}$ nor with an external magnetic field h_i^{μ}.

In order for the fermionic system to behave as the original spin system, a constraint of one fermion per site

$$\sum_{\alpha=\uparrow,\downarrow} \hat{f}_{i\alpha}^{\dagger} \hat{f}_{i\alpha} \stackrel{!}{=} 1 \tag{3.23}$$

would have to be applied on every site i. The standard PFFRG procedure is to fulfill only the soft constraint

$$\sum_{\alpha=\uparrow,\downarrow} \langle \hat{f}_{i\alpha}^{\dagger} \hat{f}_{i\alpha} \rangle = 1 \tag{3.24}$$

instead. Because both unphysical states of a single site j, which have local fermion occupation numbers $n_j = 0$ and $n_j = 2$, result in the same energy contributions to the model due to a vanishing local spin, the soft constraint is fulfilled by default for any $J_{ij}^{\mu\nu}$ and h_i^{μ} in Eq. (3.1). Generally, the PFFRG is applied at zero temperature to keep the influence of unphysical states at a minimum. Importantly, h_i^{μ} only couples to the local physical spin-1/2 states and energetically favors a ground state with a maximum local magnetizations $|\langle \boldsymbol{S}_i \rangle|$. Since a maximum local magnetization implies the fulfillment of the strong constraint Eq. (3.23), this constraint is approached in case of large magnetic fields.

Other strategies to approach the strong constraint within PFFRG exist as well. E.g., one can introduce a term in the Hamiltonian that energetically penalizes unphysical states for each site, as done in Refs. [32, 43]. While one would like to choose the size of this term and the corresponding energy cost of unphysical states as large as possible, a stable numerical implementation of the PFFRG flow equations may become

more difficult in the case where terms of largely different prefactors are present in the Hamiltonian. A newer approach implements the Popov-Fedotov scheme, which introduces an imaginary chemical potential in order for the weights of unphysical states to cancel out in thermodynamic averages [35]. Although this approach is more elegant, it is not without disadvantages. Its implementation increases the numerical complexity of the PFFRG fourfold and only allows the method to be applied at finite temperatures. Finally, it turns out that the truncation of flow equations negates an exact fulfillment of the strong constraint Eq. (3.23), even with the Popov-Fedotov scheme being applied.

3.3 Symmetries of Green and vertex functions

The PFFRG flow equations conserve symmetries of a Hamiltonian on an exact level throughout the vertex flow. These symmetries manifest themselves in the Green and vertex functions, restricting their argument dependencies in turn. Solving the flow equations is a numerically intensive task. While it is in principle possible to straightforwardly solve them for every set of arguments for $\Sigma(1'|1)$ and $\Gamma(1',2'|1,2)$, such an approach is numerically inefficient and would therefore require strong numerical approximations (e.g., regarding the resolution of continuous frequency dependencies) due to a limited amount of numerical resources available. In order to solve the flow equations efficiently, it is crucial to take advantage of each symmetry of $\hat{\mathcal{H}}_{\mathrm{PF}}$. The implementation of these symmetries allows to decrease the required numerical resources for solving the flow equations by a multiple.

In this section, we provide the prerequisite to consider vertex symmetries in the flow equations by demonstrating how the symmetries of the pseudo-fermion Hamiltonian $\hat{\mathcal{H}}_{\mathrm{PF}}$ manifest themselves in the single and two-particle Green and vertex functions. For this purpose, symmetry-based Green function restrictions will be derived along a path similar to that taken in Refs. [31, 39, 12]. Green and vertex function symmetries will be gathered in Table 3.1. Furthermore, Green and vertex functions will be expressed such that their arguments, such as $1 = \{\omega_1, \alpha_1, i_1\}$, consist of a Matsubara frequency ω_1, spin $\alpha_1 = \pm 1$, and lattice site i_1.

Symmetries of $\hat{\mathcal{H}}_{\mathrm{PF}}$ are twofold in origin. On the one hand, the original spin Hamiltonian $\hat{\mathcal{H}}$ has physical symmetries. On the other hand, we had shown in Sec. 3.2 that the mapping to pseudo fermions introduces a local SU(2) gauge freedom. In addition to those symmetries, the two-particle Green and vertex functions have additional symmetries as a consequence of fermion statistics. More precisely, an exchange of in or outgoing particle lines in $G(1',2'|1,2)$ corresponds to the switching of arguments

$1 \leftrightarrow 2$, $1' \leftrightarrow 2'$, or both, with each pairwise permutation of arguments leading to a minus sign in front of $G(1', 2'|1, 2)$. The resulting symmetries are shown in Table 3.1.

In order to derive how symmetries of $\hat{\mathcal{H}}_{\mathrm{PF}}$ manifest themselves in Green and vertex functions, we consider a general symmetry operation $\hat{w}$, i.e.,

$$[\hat{\mathcal{H}}_{\mathrm{PF}}, \hat{w}] = 0. \tag{3.25}$$

Inserting this unitary operation in between the fermion operators in the Green function definition Eq. (2.5) by making use of the property $\hat{w}^\dagger \hat{w} = 1$ and applying $[e^{-\hat{\mathcal{H}}_{\mathrm{PF}}/T}, \hat{w}] = 0$ leads to the transformation of fermion operators

$$\hat{f}_i^{(\dagger)}(\tau) \to \hat{w} \hat{f}_i^{(\dagger)}(\tau) \hat{w}^\dagger. \tag{3.26}$$

The resulting n-particle Green function symmetry restriction is obtained by requiring the Green function to be invariant under such a transformation. Vertex function symmetries can be inferred subsequently by applying the equations that relate Green and vertex functions. In case of the self-energy, this relation is given by Dyson's equation (2.22). In case of the two-particle vertex, one can apply the tree diagram analytically expressed by Eq. (2.18). Note that an alternative approach to deriving vertex function symmetries consists of performing an induction proof in which the induction step consists of inserting the assumed vertex symmetry transformation for the vertex on the left-hand side of the flow equation and verifying that the resulting expression on the right-hand side can be transformed back to its previous expression under application of the assumed symmetry transformations (see Appendix B of Ref. [31]). If this is the case, then the symmetry fulfilled at any finite cutoff Λ is fulfilled at infinitesimally smaller $\Lambda - \delta\Lambda$ as well and, consequently, for any smaller Λ. In case of $\hat{\mathcal{H}}_{\mathrm{PF}}$, n-particle Green and vertex function symmetry transformations are found not to differ for $n = 1$ and $n = 2$, as can be verified by applying Eqs. (2.22) and (2.18). Consequently, we can discuss only the symmetry restrictions from $\hat{\mathcal{H}}_{\mathrm{PF}}$ along Green functions, and the vertex functions symmetries follow trivially. More specifically, we will continue by first treating the Green function restrictions from gauge symmetries and, subsequently, treat the restrictions based on symmetries of the spin Hamiltonian.

3.3.1 Gauge symmetries

It was shown in Sec. 3.2 that the local SU(2) gauge freedom on site j acts as a right-multiplication with a unitary 2×2 matrix $\boldsymbol{W}_j$ on matrices $\hat{\boldsymbol{F}}_j$ of pseudo-fermion operators defined by Eq. (3.20), and leaves fermion operators of the remaining sites

Symmetry	$G(1'\|1)$	$G(1',2'\|1,2)$
Particle exchange	Not applicable	$G(1',2'\|1,2) = -G(1',2'\|2,1) = -G(2',1'\|1,2)$ $= -G(2',1'\|1,2)$
$\boldsymbol{W} = i\boldsymbol{\sigma}^z$ (gauge transformation)	$G(1'\|1) \sim \delta_{i_{1'}i_1}$	$G(1',2'\|1,2) = G_{\|\|}(1',2'\|1,2)\delta_{i_{1'}i_1}\delta_{i_{2'}i_2}$ $+ G_{\times}(1',2'\|1,2)\delta_{i_{2'}i_1}\delta_{i_{1'}i_2}$
$\boldsymbol{W} = i\boldsymbol{\sigma}^x$ or $\boldsymbol{W} = i\boldsymbol{\sigma}^y$ (gauge transformation)	$G(1'\|1) = -\alpha_1\alpha_{1'}G(-\bar{1}\|-\bar{1}')$	$G_{\|\|}(1',2'\|1,2) = -\alpha_1\alpha_{1'}G_{\|\|}(-\bar{1},2'\|-\bar{1}',2)$ $= -\alpha_2\alpha_{2'}G_{\|\|}(1',-\bar{2}\|1,-\bar{2}')$
Hermiticity	$G(1'\|1) = G(-1\|-1')^*$	$G(1',2'\|1,2) = G(-1,-2\|-1',-2')^*$
Time-translational invariance	$G(1'\|1) \sim \delta(\omega_{1'} - \omega_1)$	$G(1',2'\|1,2) \sim \delta(\omega_{1'} + \omega_{2'} - \omega_1 - \omega_2)$
Time-reversal	$G(1'\|1) = \alpha_{1'}\alpha_1 G(-\bar{1}'\|-\bar{1})^*$	$G(1',2'\|1,2) = \alpha_{1'}\alpha_{2'}\alpha_1\alpha_2 G(-\bar{1}',-\bar{2}'\|-\bar{1},-\bar{2})^*$

Table 3.1: Symmetry properties of the pseudo-fermion single-particle Green function $G(1'|1)$ (second column) and two-particle Green function $G(1',2'|1,2)$ (third column) enforced by the symmetries listed in the first column. Number arguments denote a set of variables, containing the Matsubara frequency ω, spin α and site i, i.e., $1 = \{\omega_1, \alpha_1, i_1\}$. Spin variables take values $\alpha = \pm 1$, which is used interchangeably with $\alpha = \uparrow, \downarrow$. Furthermore, we define $-1 = \{-\omega_1, \alpha_1, i_1\}$ and $\bar{1} = \{\omega_1, -\alpha_1, i_1\}$. The corresponding symmetry relations for the self-energy Σ and the two-particle vertex Γ are obtained by simply replacing $G \leftrightarrow \Sigma$ and $G \leftrightarrow \Gamma$ in the second and third columns, respectively. The table and its caption are replicated from Ref. [39]

invariant. For the derivation of Green function symmetries, we restrict ourselves to the cases in which the symmetry operation can be written as $\boldsymbol{W}_j = i\boldsymbol{\sigma}^\mu$.

In case $\boldsymbol{W}_j = i\boldsymbol{\sigma}^z$ is applied, fermion operators of site j transform as

$$\begin{pmatrix} \hat{f}_{j\alpha} \\ \hat{f}^\dagger_{j\alpha} \end{pmatrix} \longrightarrow i \begin{pmatrix} \hat{f}_{j\alpha} \\ -\hat{f}^\dagger_{j\alpha} \end{pmatrix}. \tag{3.27}$$

Green functions $G(1',2',...,N'|1,2,...,N)$ only stay invariant under any choice of successively applying such local transformations if the site arguments of incoming fermion lines $\{i_1, i_2,...,i_N\}$ are given by a permutation of site arguments of outgoing fermion lines $\{i_{1'}, i_{2'},...,i_{N'}\}$. It follows that the n-particle Green function only depends on n site arguments. In case of the single-particle Green function, this fact is expressed analytically by $G(1'|1) \propto \delta_{i_{1'}i_1}$. By construction, the dependence of $G(1',2'|1,2)$ on the two site arguments i_1 and i_2 is fulfilled by the parameterization

$$\begin{aligned} G(1',2'|1,2) =& G_{||}(1',2'|1,2)\delta_{i_{1'}i_1}\delta_{i_{2'}i_2} \\ &+ G_{\times}(1',2'|1,2)\delta_{i_{2'}i_1}\delta_{i_{1'}i_2}. \end{aligned} \tag{3.28}$$

The application of particle-exchange symmetry reveals the relation

$$G_{\times}(1',2'|1,2) = -G_{||}(1',2'|2,1). \tag{3.29}$$

We continue with the remaining gauge transformations $\boldsymbol{W}_j^x = i\boldsymbol{\sigma}^x$ and $\boldsymbol{W}_j^y = i\boldsymbol{\sigma}^y$, which transform fermion operators on site j as

$$\begin{pmatrix} \hat{f}_{j\alpha} \\ \hat{f}^{\dagger}_{j\alpha} \end{pmatrix} \longrightarrow i \begin{pmatrix} \alpha \hat{f}^{\dagger}_{j\bar{\alpha}} \\ \bar{\alpha} \hat{f}_{j\bar{\alpha}} \end{pmatrix} \tag{3.30}$$

and

$$\begin{pmatrix} \hat{f}_{j\alpha} \\ \hat{f}^{\dagger}_{j\alpha} \end{pmatrix} \longrightarrow -\alpha \begin{pmatrix} \hat{f}^{\dagger}_{j\bar{\alpha}} \\ \hat{f}_{j\bar{\alpha}} \end{pmatrix}. \tag{3.31}$$

Both transformations involve a particle-hole exchange. Note that the equations use the spin argument as a scalar $\alpha = \pm 1$, with $\bar{\alpha} = -\alpha$. The implied single and two-particle Green function restrictions are equivalent for both transformations and are given in Table 3.1. They are formulated in terms of $G_{||}(1',2'|1,2)$, for which it is known that $i_{1'} = i_1$ and $i_{2'} = i_2$. Note that since the gauge transformations are local, they can be applied either on one or both sites involved as arguments in $G_{||}(1',2'|1,2)$.

3.3.2 Physical symmetries

The pseudo-fermion Hamiltonian $\hat{\mathcal{H}}_{\mathrm{PF}}$ exhibits hermiticity and time-translational invariance. Hermiticity leads to a Green function invariance under a combined operation of complex conjugation, exchanging all incoming with outgoing particle lines, and changing the sign of all Matsubara frequencies (see Table 3.1). Time-translational invariance leads to energy conservation, which allows to reduce the number of Green function frequency arguments by one. It follows that $G(1'|1)$ depends on one frequency argument, whereas $G(1',2'|1,2)$ depends on three. For two-particle Green and vertex functions, energy conservation will be implemented by expressing their Matsubara frequency dependencies in terms of transfer frequencies s, t and u, given by Eq. (2.35). Note that the frequency dependencies become nondiscrete at $T = 0$.

While this chapter is dedicated to presenting the generalized PFFRG method for systems with broken TRS, the following chapters will mainly consider models with TRS intact. As such, we here consider the effect of TRS on Green functions as well. Since TRS flips the spins of a model ($\hat{\boldsymbol{S}} \to -\hat{\boldsymbol{S}}$), terms of a spin model that are odd in spin operators break TRS. Within the framework of the PFFRG, only spin Hamiltonians with terms linear or bilinear in spin operators can be treated due to the truncation of

flow equations. Hence, we only consider TRS-breaking terms that are linear in spin operators. These terms can be interpreted as the Zeeman coupling to an external magnetic field. In the pseudo-fermion model $\hat{\mathcal{H}}_{\mathrm{PF}}$, the analogue to the TRS transformation of the spin Hamiltonian ($\sum_{\alpha\beta=\uparrow\downarrow} \sigma^{\mu}_{\alpha\beta} \hat{f}^{\dagger}_{i\alpha} \hat{f}_{i\beta} \rightarrow -\sum_{\alpha\beta=\uparrow\downarrow} \sigma^{\mu}_{\alpha\beta} \hat{f}^{\dagger}_{i\alpha} \hat{f}_{i\beta}$ instead of $\hat{\boldsymbol{S}} \rightarrow -\hat{\boldsymbol{S}}$) is achieved by an antiunitary operator $\hat{w}$ that transforms fermion operators of each site as

$$\begin{pmatrix} \hat{f}_{j\alpha} \\ \hat{f}^{\dagger}_{j\alpha} \end{pmatrix} \longrightarrow \begin{pmatrix} e^{i\pi\alpha/2} \hat{f}_{j\bar{\alpha}} \\ e^{-i\pi\alpha/2} \hat{f}^{\dagger}_{j\bar{\alpha}} \end{pmatrix} \tag{3.32}$$

and applies complex conjugation to Pauli matrix elements $\sigma^{\mu}_{\alpha\beta}$. The resulting Green function symmetries are given in Table 3.1.

Considered models, such as Heisenberg models, may exhibit global spin rotation symmetries. Those symmetry transformations solely transform the spin arguments of Green functions and therefore restrict their spin dependencies. We will go further into the implications of pure spin rotation symmetries on the spin dependencies of vertex functions in Sec. 3.5.3 once we have formulated vertex parameterizations.

Finally, lattice symmetries can be applied to relate Green functions of different site arguments. In presence of anisotropic interactions $J^{\mu\nu}_{ij}$ or site-dependent finite magnetic fields h^{μ}_{i}, point group symmetries of a lattice generally have to be applied together with global spin rotations in order to constitute a symmetry operation of $\hat{\mathcal{H}}$ [2]. As such, the lattice symmetries of a model generally not only transform site arguments of Green functions but spin arguments as well. Note that in case of broken TRS, the action of spin rotations on $G(1'|1)$ has to be considered, whereas in presence of TRS $G(1'|1)$ remains invariant under any spin rotations. This property will be discussed in more detail in Sec. 3.4. In the simplest symmetry case, all sites of a model are symmetry equivalent, i.e., translation and combined point group and spin rotation symmetries allow for each site to be mapped onto every other site. In this case, $G(1'|1)$ is known for each site argument i_1 once it is known for a reference site. Similarly, one site argument of $G_{||}(1', 2'|1, 2)$, e.g., i_1, can always be set to a reference site. For a fixed i_1, point group symmetries reduce the set of sites i_2 for which $G_{||}(1', 2'|1, 2)$ is independent further. In case a model has multiple symmetry-inequivalent sites (as is the case in the $K_2Ni_2(SO_4)_3$ compound treated in Chapter 6), Green functions $G(1'|1)$ and $G_{||}(1', 2'|1, 2)$ of each reference site i_1 are independent.

[2] In spin models based on physical systems, this is a consequence of spin-orbit coupling.

3.4 Parameterization of vertex functions

All single and two-particle Green and vertex function symmetries relevant to $\hat{\mathcal{H}}_{\mathrm{PF}}$ have been gathered now. In the following, they will be applied as the foundation for a numerically efficient vertex parameterization. It will be shown that previous parameterizations of Refs. [11, 31] can be extended in order to capture vertex components that become finite upon breaking TRS. In fact, in the extended parameterization, only $G(1'|1)$ and $\Sigma(1', 1)$ will gain additional components once TRS is broken, whereas the parameterization of $\Gamma(1', 2'|1, 2)$ remains invariant upon breaking TRS. Most importantly, the introduced parameterizations will make use of the reduced site argument dependencies of vertex functions, making the solution of flow equations in real space the numerically most efficient choice. Furthermore, it will follow from the parameterizations that vertices will not be computed for each possible combination of spin-up and spin-down arguments separately in the parameterized flow equations. Instead, the spin dependency of vertices will be expressed in a new basis based on Pauli matrices and the identity matrix. These matrices will be abbreviated as $\boldsymbol{\sigma}^{\rho}$ with $\rho \in \{0, x, y, z\}$, where $\boldsymbol{\sigma}^{0}$ corresponds to the 2×2 identity matrix and $\boldsymbol{\sigma}^{\mu}$ with $\mu \in \{x, y, z\}$ corresponds to Pauli matrices. While $\Sigma(1'|1)$ will be expressed as a linear combination of $\boldsymbol{\sigma}^{\rho}$ matrices, $\Gamma(1', 2'|1, 2)$ will be written in terms bilinear in them. The advantage of this choice of expression is two-fold: In the new basis for spin arguments, the vertex parameters will be either purely real or imaginary. Furthermore, if the underlying Hamiltonian exhibits continuous global spin rotation symmetries or TRS, the vertices will simplify straightforwardly such that the ρ for which the terms proportional to $\boldsymbol{\sigma}^{\rho}$ are finite is restricted to a reduced set of values. In the following, we will use the convention of $\mu, \nu \in \{x, y, z\}$ and $\rho, \varphi \in \{0, x, y, z\}$.

3.4.1 Self-energy parameterization

We begin by proposing a parameterization for $\Sigma(1'|1)$. The presence of a $\boldsymbol{W} = i\boldsymbol{\sigma}^{z}$ gauge freedom and time-translational invariance reduces the number of independent site and frequency arguments of the self-energy and therefore allows for a parameterization given by

$$\Sigma(1'|1) = \Sigma_{i_1}(\omega_1, \alpha_{1'}, \alpha_1)\delta_{i_{1'} i_1}\delta(\omega_{1'} - \omega_1). \tag{3.33}$$

A further expansion of the spin dependence as

$$\Sigma_{i_1}(\omega_1, \alpha_{1'}, \alpha_1) = \sum_\rho \Sigma^\rho_{i_1}(\omega_1)\sigma^\rho_{\alpha_{1'}\alpha_1} \tag{3.34}$$

$$= \big(- i\gamma^0_{i_1}(\omega_1)\delta_{\alpha_{1'}\alpha_1} + \sum_\mu \gamma^\mu_{i_1}(\omega_1)\sigma^\mu_{\alpha_{1'}\alpha_1}\big) \tag{3.35}$$

separates the self-energy into components with distinct symmetry properties and organizes all spin dependencies in matrices $\boldsymbol{\sigma}^\rho$. The $\boldsymbol{W} = i\boldsymbol{\sigma}^{x(y)}$ gauge freedom leads to even and odd frequency dependencies for self-energy components

$$\begin{aligned} \gamma^0_i(\omega) &= -\gamma^0_i(-\omega), \\ \gamma^\mu_i(\omega) &= \gamma^\mu_i(-\omega), \end{aligned} \tag{3.36}$$

and hermiticity enforces all components to be purely real, i.e.,

$$\gamma^\rho_i(\omega) \in \mathbb{R}. \tag{3.37}$$

Likewise, one can parameterize $G(1'|1)$ as

$$G(1'|1) = G_{i_1}(\omega_1, \alpha_{1'}, \alpha_1)\delta_{i_{1'}i_1}\delta(\omega_{1'} - \omega_1) \tag{3.38}$$

$$= \sum_\rho G^\rho_{i_1}(\omega_1)\sigma^\rho_{\alpha_{1'}\alpha_1}\delta_{i_{1'}i_1}\delta(\omega_{1'} - \omega_1) \tag{3.39}$$

$$= \big(- ig^0_{i_1}(\omega_1)\delta_{\alpha_{1'}\alpha_1} + \sum_\mu g^\mu_{i_1}(\omega_1)\sigma^\mu_{\alpha_{1'}\alpha_1}\big)\delta_{i_{1'}i_1}\delta(\omega_{1'} - \omega_1), \tag{3.40}$$

with $g^\rho_i(\omega)$ fulfilling the same symmetries as $\gamma^\rho_i(\omega)$ for equal ρ.

For a pseudo-fermion Hamiltonian $\hat{\mathcal{H}}_{\mathrm{PF}}$ based on the spin model of Eq. (3.1), $\Sigma(1'|1)$ and $G(1'|1)$ are not diagonal in spin arguments. This has to be considered when relating both functions by applying a matrix inversion in Dyson's equation (2.22). By inserting the parameterizations of Eqs. (3.35) and (3.40), the relations between components

$$\begin{aligned} g^0(\omega) &= \frac{\omega + \gamma^0(\omega)}{[\omega + \gamma^0(\omega)]^2 + \sum_\nu [\gamma^\nu(\omega)]^2}, \\ g^\mu(\omega) &= \frac{-\gamma^\mu(\omega)}{[\omega + \gamma^0(\omega)]^2 + \sum_\nu [\gamma^\nu(\omega)]^2} \end{aligned} \tag{3.41}$$

are obtained.

Under the application of TRS and the symmetry of Eq. (3.36), γ^μ_i and g^μ_i solely change sign, whereas γ^0_i and g^0_i remain invariant. It follows that γ^μ_i and g^μ_i can only be finite in case of broken TRS. Components with $\mu \in \{x, y, z\}$ and $\rho = 0$ further differ in their transformation properties under spin rotations. Components g^0_i and γ^0_i transform as a

scalar, i.e., they remain invariant under spin rotations. In contrast, g_i^μ and γ_i^μ transform inversely to the Cartesian components of a pseudovector. Under a spin rotation, which transforms spins by a 3×3 rotation matrix $\boldsymbol{R}$ as $\hat{S}^\mu \to \sum_\nu R^{\mu\nu}\hat{S}^\nu$, they transform as $\gamma_i^\mu \to \sum_\nu R^{\nu\mu}\gamma_i^\nu$ and $g_i^\mu \to \sum_\nu R^{\nu\mu}g_i^\nu$. It follows that for a specified $\mu = x, y, z$ g_i^μ (γ_i^μ) can differ on two symmetry-equivalent sites if the symmetry operation relating both sites involves a spin rotation. It is worth highlighting that in case a model with TRS is considered, $g_i^\mu = 0$ ($\gamma_i^\mu = 0$). Hence, in this case γ_i^ρ (g_i^ρ) is always equal on symmetry-equivalent sites.

3.4.2 Two-particle vertex parameterization

The parameterization of $\Gamma(1', 2'|1, 2)$ is carried out in two steps. First, we apply the property that the vertex only depends on two site arguments by expressing it as

$$\begin{aligned}\Gamma(1', 2'|1, 2) = \big(&\Gamma_{||i_1 i_2}(1', 2'|1, 2)\delta_{i_{1'} i_1}\delta_{i_{2'} i_2} \\ &- \Gamma_{||i_2 i_1}(1', 2'|2, 1)\delta_{i_{1'} i_2}\delta_{i_{2'} i_1}\big)\delta(\omega_1 + \omega_2 - \omega_{1'} - \omega_{2'}).\end{aligned} \tag{3.42}$$

As shown in Sec. 3.3, this form follows from particle exchange and the local $\boldsymbol{W} = i\boldsymbol{\sigma}^z$ gauge freedom. Furthermore, energy conservation, following from time-translational invariance, has been applied by inserting the term $\delta(\omega_1 + \omega_2 - \omega_{1'} - \omega_{2'})$. The next step consists of expressing $\Gamma_{||i_1 i_2}(1', 2'|1, 2)$ in terms that are bilinear in elements of matrices $\boldsymbol{\sigma}^\rho$. The parameterization is given by

$$\Gamma_{||i_1 i_2}(1', 2'|1, 2) = \sum_{\rho\varphi} \Gamma^{\rho\varphi}_{i_1 i_2}(s, t, u)\sigma^\rho_{\alpha_{1'}\alpha_1}\sigma^\varphi_{\alpha_{2'}\alpha_2}, \tag{3.43}$$

in which we transitioned to expressing the frequency dependencies via transfer frequencies, which are defined by Eq. (2.35) and fulfill energy conservation $\omega_{1'} + \omega_{2'} = \omega_1 + \omega_2$ by construction. Similar to the parameterization of the self-energy $\Sigma(1'|1)$, the parameterization of $\Gamma^\Lambda_{||i_1 i_2}(1', 2'|1, 2)$ separates vertex components $\Gamma^{\rho\varphi}_{i_1 i_2}(s, t, u)$ with distinct symmetry properties and organizes all spin dependencies in matrices $\boldsymbol{\sigma}^\rho$. Note that all components $\Gamma^{\rho\varphi}$ can become finite regardless of whether TRS is present or not. This is in contrast to the self-energy where the presence of TRS enforces $\gamma^\mu = 0$.

The $\boldsymbol{W} = i\boldsymbol{\sigma}^{x(y)}$ gauge freedom together with hermiticity restricts each component in the complex plane as

$$\Gamma^{\rho\varphi}_{i_1 i_2}(s, t, u) \in \begin{cases} \mathbb{R} & \text{if } \rho, \varphi = 0 \text{ or } \rho, \varphi \neq 0 \\ i\mathbb{R} & \text{otherwise.} \end{cases} \tag{3.44}$$

Symmetries of $\Gamma^{\rho\varphi}_{i_1 i_2}(s,t,u)$ that transform frequency arguments are straightforwardly derived from Table 3.1 by insertion of the vertex parameterizations given by Eqs. (3.42)-(3.43). The resulting frequency symmetries of the parameterized two-particle vertex are given by

$$\begin{aligned}\Gamma^{\rho\varphi}_{i_1 i_2}(s,t,u) =& \Gamma^{\rho\varphi}_{i_1 i_2}(-s,t,-u)^* && (3.45)\\ =& \Gamma^{\varphi\rho}_{i_2 i_1}(s,-t,-u) && (3.46)\\ =& (-1)^{\delta_{\varphi 0}}\Gamma^{\rho\varphi}_{i_1 i_2}(u,t,s). && (3.47)\end{aligned}$$

If TRS is assumed, the additional symmetry

$$\Gamma^{\rho\varphi}_{i_1 i_2}(s,t,u) = \Gamma^{\rho\varphi}_{i_1 i_2}(-s,-t,-u) \tag{3.48}$$

is present [31]. In this case, the symmetries of $\Gamma^{\rho\varphi}_{i_1 i_2}(s,t,u)$ can be written as

$$\begin{aligned}\Gamma^{\rho\varphi}_{i_1 i_2}(s,t,u) =& \Gamma^{\rho\varphi}_{i_2 i_1}(-s,t,u) && (3.49)\\ =& \Gamma^{\rho\varphi}_{i_1 i_2}(s,-t,u)^* && (3.50)\\ =& \Gamma^{\rho\varphi}_{i_2 i_1}(s,t,-u)^* && (3.51)\\ =& (-1)^{\delta_{\varphi 0}}\Gamma^{\rho\varphi}_{i_1 i_2}(u,t,s). && (3.52)\end{aligned}$$

In this formulation, the first three symmetries each only transform a single transfer frequency.

To summarize, broken TRS generates additional components Σ^{ρ} in the self-energy. This is the main reason for the increase in complexity in solving the flow equations upon breaking TRS. On the other hand, no additional two-particle vertex components are generated by broken TRS. Instead, the frequency arguments for which $\Gamma^{\rho\varphi}_{i_1 i_2}(s,t,u)$ is independent double. Note that spin rotation symmetries can restrict which components Σ^{ρ} and $\Gamma^{\rho\varphi}$ can become finite as well. We will return to this property and discuss it in the next section in context of the flow equations.

3.5 Flow equations

The derivation of vertex symmetries and the subsequent introduction of suitable vertex parameterizations allow us to now write down a numerically efficient formulation of the flow equations within Katanin truncation for a general pseudo-fermion Hamiltonian obtained from the spin model given by Eq. (3.1). In the following, the previously proposed vertex parameterizations will be inserted into the unparameterized flow equa-

tions (3.4) and (3.5). Since the resulting equations are quite complex in structure, they will be discussed in sufficient detail afterwards. Note that the self-energy, two-particle vertex, single-particle Green function, and single-scale propagator exhibit a Λ dependence in the flow equations that was often omitted in the previous sections for reasons of simplicity.

The fully parameterized flow equations are obtained in two steps. First, the vertex parameterizations given by Eqs. (3.33) and (3.42), which state the locality and bilocality of the self-energy and two-particle vertex respectively, are inserted into the flow equations (3.4) and (3.5). In the second step, spin argument dependencies of vertices will be taken advantage of by inserting the parameterizations of Eqs. (3.35) and (3.43). The flow equations will be formulated for models at $T = 0$. It follows that Matsubara frequency summations, which are discrete for $T \neq 0$, are given by continuous frequency integrals instead.

The flow equations that apply the local and bilocal parameterizations are given by

$$\begin{aligned}\frac{d}{d\Lambda}\Sigma^{\Lambda}_{i_1}(\omega_1,\alpha_{1'},\alpha_1) = &-\frac{1}{2\pi}\int_{-\infty}^{\infty}d\omega_2\sum_{\alpha_{2'}\alpha_2}\Big[\sum_j \Gamma^{\Lambda}_{||i_1j}(1',2'|1,2)\mathcal{S}^{\Lambda}_j(\omega_2,\alpha_2,\alpha_{2'})\\ &-\Gamma^{\Lambda}_{||i_1i_1}(1',2'|2,1)\mathcal{S}^{\Lambda}_{i_1}(\omega_2,\alpha_2,\alpha_{2'})\Big]\\ &\times\delta(\omega_1+\omega_2-\omega_{1'}-\omega_{2'}),\end{aligned} \tag{3.53}$$

$$\begin{aligned}\frac{d}{d\Lambda}\Gamma^{\Lambda}_{||i_1i_2}(1',2'|1,2) = &\frac{1}{2\pi}\int_{-\infty}^{\infty}d\omega_4\int_{-\infty}^{\infty}d\omega_3\sum_{\substack{\alpha_{3'}\alpha_{4'}\\ \alpha_3\alpha_4}}\\ &\Big[\Gamma^{\Lambda}_{||i_1i_2}(1',2'|3\,,4\,)\Gamma^{\Lambda}_{||i_1i_2}(3',4'|1,2)\Pi^{\Lambda}_{i_1i_2}(3,4|3',4')\\ &-\sum_j\Gamma^{\Lambda}_{||i_1j}(1',4'|1,3)\Gamma^{\Lambda}_{||ji_2}(3',2'|4,2)\Pi^{\Lambda}_{jj}(3,4|3',4')\\ &+\Gamma^{\Lambda}_{||i_1i_2}(1',4'|1,3)\Gamma^{\Lambda}_{||i_2i_2}(3',2'|2,4)\Pi^{\Lambda}_{i_1i_1}(3,4|3',4')\\ &+\Gamma^{\Lambda}_{||i_1i_1}(1',4'|3,1)\Gamma^{\Lambda}_{||i_1i_2}(3',2'|4,2)\Pi^{\Lambda}_{i_2i_2}(3,4|3',4')\\ &+\Gamma^{\Lambda}_{||i_2i_1}(2',4'|3,1)\Gamma^{\Lambda}_{||i_2i_1}(3',1'|2,4)\Pi^{\Lambda}_{i_2i_1}(3,4|3',4')\Big]\\ &\times\delta(\omega_1+\omega_2-\omega_{1'}-\omega_{2'}),\end{aligned} \tag{3.54}$$

with

$$\begin{aligned}\Pi^{\Lambda}_{i_3i_4}(3,4|3',4') = &\,G^{\Lambda}_{i_3}(\omega_3,\alpha_3,\alpha_{3'})\tilde{\mathcal{S}}^{\Lambda}_{i_4}(\omega_4,\alpha_4,\alpha_{4'})\\ &+G^{\Lambda}_{i_4}(\omega_4,\alpha_4,\alpha_{4'})\tilde{\mathcal{S}}^{\Lambda}_{i_3}(\omega_3,\alpha_3,\alpha_{3'}).\end{aligned}$$

Before the second parameterization step is performed, we discuss aspects of this intermediate version of the flow equations first. The frequency-dependent Dirac delta functions that originate from the vertices on the right-hand side of the equation were neglected for clarity. They will become obsolete in the next step, in which we express

the vertex frequency dependencies via transfer frequencies. In the partially parameterized flow equations, terms of different structures emerge. The self-energy flow equation consists of a Hartree and a Fock term. While the Hartree term contains a site summation $\sum_j$, the Fock term is purely local and only contains the site i_1 of the left-hand side self-energy as site argument. In the two-particle vertex flow equation, five terms emerge. With all these terms being quadratic in two-particle vertices and propagators [i.e., $G^\Lambda(1'|1)$ and $\tilde{\mathcal{S}}^\Lambda(1'|1)$] each, they differ in their internal vertex argument structures and cannot be transformed into each other under the application of vertex symmetries. Considering the structure of site arguments, in four of the five flow equation terms, vertices and propagators contain only site arguments i_1 and i_2. Only one term involves an internal site summation $\sum_j$, which therefore requires by far the most computational resources to evaluate. This term is known as the random phase approximation (RPA) channel. Importantly, if one considers a reduced version of the flow equations that only takes into account the RPA channel and the Hartree term, standard spin mean-field theory is reproduced [11, 32]. These are exactly the only terms that involve a site summation. The resulting mean-field $\Sigma^\Lambda(1'|1)$ is computed within Hartree approximation, whereas the resulting mean-field $\Gamma^\Lambda(1',2'|1,2)$ is computed within RPA. However, note that in presence of TRS, $\Sigma^\Lambda(1'|1) = 0$ for these reduced flow equations such that the RPA channel itself fully replicates mean-field theory. The inclusion of the remaining terms in the flow equations results in a vertex flow that goes beyond mean-field theory and captures the effect of quantum fluctuations.

Finally, we set in the parameterizations of Eqs. (3.35) and (3.43), which express the self-energy and two-particle vertex spin dependencies in terms Σ^ρ and $\Gamma^{\rho\varphi}$. The resulting flow equations of the general spin lattice Hamiltonian given by Eq. (3.1) read as

$$\begin{aligned}\frac{d}{d\Lambda}\Sigma_i^{\rho,\Lambda}(\omega) = \frac{1}{4\pi}\int_{\mathbb{R}} d\omega' \Big[&- 4\sum_j \sum_a \Gamma_{ij}^{\rho a,\Lambda}(\omega+\omega',0,\omega-\omega')\mathcal{S}_j^{a,\Lambda}(\omega') \\ &+ \sum_{abc} \Gamma_{ii}^{ab,\Lambda}(\omega+\omega',\omega-\omega',0)\mathcal{S}_i^{c,\Lambda}(\omega')\mathrm{tr}(\boldsymbol{\sigma}^a\boldsymbol{\sigma}^c\boldsymbol{\sigma}^b\boldsymbol{\sigma}^\rho)\Big],\end{aligned} \tag{3.55}$$

$$
\begin{aligned}
&\frac{d}{d\Lambda}\Gamma^{\rho\varphi,\Lambda}_{i_1 i_2}(s,t,u) = \frac{1}{8\pi}\int_{\mathbb{R}} d\omega' \sum_{abcdef} \\
&\Big[\Gamma^{ab,\Lambda}_{i_1 i_2}(s,-\omega'-\omega_{2'},\omega_{1'}+\omega')\Gamma^{cd,\Lambda}_{i_1 i_2}(s,\omega_2+\omega',\omega_1+\omega') \\
&\quad\times\left[G^{e,\Lambda}_{i_1}(s+\omega')S^{f,\Lambda}_{i_2}(\omega')^* + G^{f,\Lambda}_{i_2}(\omega')^* S^{e,\Lambda}_{i_1}(s+\omega')\right] \\
&\quad\times \mathrm{tr}\big(\boldsymbol{\sigma}^a\boldsymbol{\sigma}^e\boldsymbol{\sigma}^c\boldsymbol{\sigma}^\rho\big)\mathrm{tr}\big(\boldsymbol{\sigma}^b\boldsymbol{\sigma}^f\boldsymbol{\sigma}^d\boldsymbol{\sigma}^\varphi\big) \\
&-4\sum_j \Gamma^{ab,\Lambda}_{i_1 j}(\omega_{1'}+\omega',t,\omega_1-\omega')\Gamma^{cd,\Lambda}_{j i_2}(\omega_2+\omega',t,-\omega_{2'}+\omega')\Pi^{ef,\Lambda}_{jj}(t+\omega',\omega') \\
&\quad\times \mathrm{tr}(\boldsymbol{\sigma}^b\boldsymbol{\sigma}^e\boldsymbol{\sigma}^c\boldsymbol{\sigma}^f)\delta_{a\rho}\delta_{d\varphi} \\
&+2\Gamma^{ab,\Lambda}_{i_1 i_2}(\omega_{1'}+\omega',t,\omega_1-\omega')\Gamma^{cd,\Lambda}_{i_2 i_2}(\omega_2+\omega',-\omega_{2'}+\omega',t)\Pi^{ef,\Lambda}_{i_2 i_2}(t+\omega',\omega') \\
&\quad\times \mathrm{tr}\big(\boldsymbol{\sigma}^d\boldsymbol{\sigma}^f\boldsymbol{\sigma}^b\boldsymbol{\sigma}^e\boldsymbol{\sigma}^c\boldsymbol{\sigma}^\varphi\big)\delta_{a\rho} \\
&+2\Gamma^{ab,\Lambda}_{i_1 i_1}(\omega_{1'}+\omega',\omega_1-\omega',t)\Gamma^{cd,\Lambda}_{i_1 i_2}(\omega_2+\omega',t,-\omega_{2'}+\omega')\Pi^{ef,\Lambda}_{i_1 i_1}(t+\omega',\omega') \\
&\quad\times \mathrm{tr}\big(\boldsymbol{\sigma}^a\boldsymbol{\sigma}^e\boldsymbol{\sigma}^c\boldsymbol{\sigma}^f\boldsymbol{\sigma}^b\boldsymbol{\sigma}^\rho\big)\delta_{d\varphi} \\
&+\Gamma^{ab,\Lambda}_{i_1 i_2}(\omega_{2'}-\omega',-\omega_1-\omega',u)\Gamma^{cd,\Lambda}_{i_1 i_2}(\omega_2-\omega',\omega_{1'}+\omega',u)\Pi^{ef,\Lambda}_{i_2 i_1}(u+\omega',\omega')^* \\
&\quad\times \mathrm{tr}\big(\boldsymbol{\sigma}^c\boldsymbol{\sigma}^f\boldsymbol{\sigma}^a\boldsymbol{\sigma}^\rho\big)\mathrm{tr}\big(\boldsymbol{\sigma}^b\boldsymbol{\sigma}^e\boldsymbol{\sigma}^d\boldsymbol{\sigma}^\varphi\big)\Big],
\end{aligned}
\tag{3.56}
$$

with

$$\Pi^{ef,\Lambda}_{i_3,i_4}(\omega_3,\omega_4) = G^{e,\Lambda}_{i_3}(\omega_3)\tilde{\mathcal{S}}^{f,\Lambda}_{i_4}(\omega_4) + G^{f,\Lambda}_{i_4}(\omega_4)\tilde{\mathcal{S}}^{e,\Lambda}_{i_3}(\omega_3).$$

Within the chosen parameterizations, the single-scale propagator within Katanin truncation is given by

$$\tilde{\mathcal{S}}^{\rho,\Lambda}_i(\omega) = -\frac{dG^{\rho,\Lambda}_i(\omega)}{d\Lambda} = \mathcal{S}^{\rho,\Lambda}_i(\omega) - \frac{1}{2}\sum_{abc} G^{a,\Lambda}_i(\omega)\frac{d\Sigma^{b,\Lambda}_i(\omega)}{d\Lambda}G^{c,\Lambda}_i(\omega)\mathrm{tr}(\boldsymbol{\sigma}^a\boldsymbol{\sigma}^b\boldsymbol{\sigma}^c\boldsymbol{\sigma}^\rho). \tag{3.57}$$

We will explore various aspects of the parameterized flow equations in the following. On the right-hand side of the flow equations, indices that specify the spin-dependent vertex components are given roman letters $a,\ldots,f \in \{0,x,y,z\}$ if they are summed over, whereas indices of the left-hand side vertices are given by Greek letters $\rho,\varphi \in \{0,x,y,z\}$. Note that the first and last term of the $\Gamma^{\rho\varphi,\Lambda}_{i_1 i_2}(s,t,u)$ flow equation contain complex conjugations of $G^\Lambda(1'|1)$ or $\tilde{\mathcal{S}}^\Lambda(1'|1)$. Since the components $G^{\rho,\Lambda}_i$ and $S^{\rho,\Lambda}_i$ are either purely real or imaginary, the complex conjugation either leaves the components invariant ($G^{\mu,\Lambda *}_i = G^{\mu,\Lambda}_i$ for $\mu \in \{x,y,z\}$) or alternates their sign ($G^{0,\Lambda *}_i = -G^{0,\Lambda}_i$ for $\rho = 0$). The origin of the complex conjugations lies in the fact that besides setting in the self-energy and vertex parameterizations from Eqs. (3.53)-(3.54) to Eqs. (3.55)-(3.56), vertex symmetries were applied in order to arrive at the presented expressions of flow equations.

Previous summations over spin arguments α in the unparameterized flow equations (3.53)-(3.54) manifest themselves as products of matrices $\mathrm{tr}(\boldsymbol{\sigma}^{a_1}\cdots\boldsymbol{\sigma}^{a_n})$ once the vertex

parameterizations are set in and matrix indices $a_1, \ldots, a_n \in \{0, x, y, z\}$ are summed over instead [see Eqs. (3.55)-(3.56)]. In case a trace only contains a product of two matrices, we write it as a Kronecker delta instead [$\mathrm{tr}(\boldsymbol{\sigma}^{a_1}\boldsymbol{\sigma}^{a_2}) = 2\delta_{a_1 a_2}$]. Note that each trace and Kronecker delta vanishes for 3/4 of all summands over its internal matrix indices $a_1, \ldots, a_n$. Of particular interest is the RPA channel due to its large numerical complexity and its solution that reproduces mean-field theory. The RPA channel has one trace and two Kronecker delta. Consequently, $1/4^3$ of its terms do not vanish by evaluating the summation over indices $a, \ldots, f$. Since the remaining channels each either contain a total of two traces, or one trance and one Kronecker delta, only $1/4^2$ of their terms vanish instead.

The number of terms in the RPA channel that need to be evaluated can be reduced even further, as will be explained in the following. Two-particle vertex products in the RPA channel are of the form $\Gamma^{ab}_{i_1 j}\Gamma^{cd}_{j i_2}$, in which we neglect the frequency arguments. After the evaluation of Kronecker deltas and traces, for fixed values of indices a, b, c, d the same product appears exactly in four terms. Since the site summation over each two-particle vertex product has to be performed only once, the numerical resources required to evaluate the RPA channel can be reduced by computing the site summation over each of the 4^4 combinations of products $\Gamma^{ab}_{i_1 j}\Gamma^{cd}_{j i_2}$ only once and reusing it in terms needed. Note that for a model with global U(1) spin rotation symmetry and broken TRS, flow equations simplify (see Sec. 3.5.3) and each finite product $\Gamma^{ab}_{i_1 j}\Gamma^{cd}_{j i_2}$ with fixed indices a, b, c, d appears twice. Furthermore, in presence of TRS the flow equations further simplify such that each finite product only appears once.

3.5.1 Initial conditions

The flow equations can be solved from the known infrared cutoff limit $\Lambda \to \infty$ down to smaller Λ. Since $G_0^\Lambda(1'|1)$ vanishes in this limit, only Feynman diagrams devoid of particle lines contribute to the two-particle vertex at $\Lambda \to \infty$. Only one such diagram exists, which is given by the bare interaction. It follows that the initial condition of the two-particle vertex, in case of a general spin Hamiltonian $\hat{\mathcal{H}}$ given by Eq. (3.1) [and corresponding to Eq. (3.21) after the pseudo-fermion mapping], is given by

$$\Gamma^{\mu\nu,\Lambda\to\infty}_{ij}(s,t,u) = \frac{1}{4} J^{\mu\nu}_{ij}. \tag{3.58}$$

Next, we consider the initial condition of $\Sigma_i^{\mu,\Lambda}(\omega)$. $\hat{\mathcal{H}}$ includes magnetic fields h_i^μ that couple linearly to spin operators. After the pseudo-fermion mapping, the corresponding terms are quadratic in fermion operators and thus modify $G_0^\Lambda(1'|1)$. This modification

can be recast as a finite self-energy at $\Lambda \to \infty$, which will then be given by

$$\Sigma_i^{\mu,\Lambda\to\infty}(\omega) = -\frac{1}{2}h_i^\mu. \tag{3.59}$$

Note that in a numerical implementation, the initial cutoff $\Lambda \to \infty$ for which the vertices are known is often approximated as large but finite. Alternatively, the parquet equations and the SDE for the self-energy can be solved at a large Λ to obtain the initial values for vertices of a PFFRG flow [36].

3.5.2 Observables

Once $\Sigma^\Lambda(1'|1)$ and $\Gamma^\Lambda(1',2'|1,2)$ are determined by solving the flow equations, they can be applied to compute observables of the original spin Hamiltonian such as the magnetization or spin correlations. Since the PFFRG treats symmetries on an exact level, the computation of a finite magnetization requires a Hamiltonian that breaks TRS, as is achieved by including a finite magnetic field. In the spin Hamiltonian, the μ component of the magnetization on site i is given by

$$M_i^\mu = \langle \hat{S}_i^\mu \rangle. \tag{3.60}$$

To compute the corresponding expression in the pseudo-fermion Hamiltonian, we first apply the pseudo-fermion mapping given by Eq. (3.18) and then apply the Green function definition Eq. (2.5). The formula

$$M_i^\mu = \frac{1}{2\pi}\int_{\mathbb{R}} d\omega g_i^\mu(\omega). \tag{3.61}$$

is obtained after inserting the Green function parameterization of Eq. (3.40).

A computation of spin correlations via vertex functions is more involved. The spin correlation between sites i and j, and depending on imaginary time τ is defined as

$$\chi_{ij}^{\mu\nu}(\tau) = \langle \mathcal{T}_\tau[\hat{S}_i^\mu(\tau)\hat{S}_j^\nu(0)]\rangle - \langle \hat{S}_i^\mu(\tau)\rangle\langle \hat{S}_j^\nu(0)\rangle. \tag{3.62}$$

A Fourier transformation at $T = 0$ leads to the static correlation

$$\chi_{ij}^{\mu\nu}(\omega) = \int_0^\infty d\tau e^{i\omega\tau}[\langle \hat{S}_i^\mu(\tau)\hat{S}_j^\nu(0)\rangle - \langle \hat{S}_i^\mu(\tau)\rangle\langle \hat{S}_j^\nu(0)\rangle]. \tag{3.63}$$

Unless stated otherwise, only the static PFFRG correlations will be studied in this thesis. After mapping the spin operators onto pseudo fermions, one can rewrite the resulting expression in terms of single and two-particle Green functions $G^\Lambda(1'|1)$ and

$G^\Lambda(1',2'|1,2)$ by applying their definition given by Eqs. (2.5)-(2.6). Afterwards, the application of Eqs. (2.15) and (2.18) allows the expression of $G^\Lambda(1',2'|1,2)$ via the $G^\Lambda(1'|1)$ and $\Gamma^\Lambda(1',2'|1,2)$. Finally, Green and two-particle vertex function parameterizations of Eqs. (3.40), (3.42) and (3.43) are applied to arrive at the expression for spin correlations

$$\begin{aligned}\chi_{ij}^{\mu\nu}(\omega) = &-\frac{1}{8\pi}\delta_{ij}\sum_{ab}\int_{\mathbb{R}} d\omega' G_i^a(\omega')G_i^b(\omega+\omega')\mathrm{tr}(\boldsymbol{\sigma}^\mu\boldsymbol{\sigma}^a\boldsymbol{\sigma}^\nu\boldsymbol{\sigma}^b)\\ &-\frac{1}{16\pi^2}\sum_{\substack{abc\\dgh}}\int_{\mathbb{R}^2} d\omega' d\omega'' G_i^a(\omega')G_j^b(\omega+\omega'')G_i^c(\omega+\omega')G_j^d(\omega'')\\ &\times[\Gamma_{ij}^{gh}(\omega+\omega'+\omega'',\omega,\omega'-\omega'')\mathrm{tr}(\boldsymbol{\sigma}^\mu\boldsymbol{\sigma}^c\boldsymbol{\sigma}^g\boldsymbol{\sigma}^a)\mathrm{tr}(\boldsymbol{\sigma}^\nu\boldsymbol{\sigma}^d\boldsymbol{\sigma}^h\boldsymbol{\sigma}^b)\\ &-\delta_{ij}\Gamma_{ii}^{gh}(\omega+\omega'+\omega'',\omega'-\omega'',\omega)\mathrm{tr}(\boldsymbol{\sigma}^\mu\boldsymbol{\sigma}^c\boldsymbol{\sigma}^g\boldsymbol{\sigma}^b\boldsymbol{\sigma}^\nu\boldsymbol{\sigma}^d\boldsymbol{\sigma}^h\boldsymbol{\sigma}^a)].\end{aligned} \tag{3.64}$$

It is apparent that the evaluation of the sum over indices $a\ldots h$ in the equation would generate a lot of terms. Like in the flow equations, TRS and spin rotation symmetries of the Hamiltonian may reduce the number of finite terms that will be generated by such an evaluation, as these symmetries allow the restriction of indices μ, ν, and $a...h$ for which the vertices and single-particle Green function are finite.

Generally more useful than $\chi_{ij}^{\mu\nu}(\omega)$ in the study of magnetism are magnetic susceptibilities $\chi^{\mu\nu}(\boldsymbol{q},\omega)$. They are obtained straightforwardly from $\chi_{ij}^{\mu\nu}(\omega)$ by applying a Fourier transformation in order to introduce a momentum dependence $\boldsymbol{q}$. To study the ground states of different spin models, we will often compute the static (i.e., $\omega = 0$) susceptibility given by

$$\bar{\chi}^{\mu\nu}(\boldsymbol{q}) = \frac{1}{N}\sum_{ij} e^{i\boldsymbol{q}(\boldsymbol{r}_i-\boldsymbol{r}_j)}\chi_{ij}^{\mu\nu}(\omega=0), \tag{3.65}$$

with N being the number of lattice sites and the summation indices i and j going over all lattice sites, with lattice vectors $\boldsymbol{r}_i$ and $\boldsymbol{r}_j$.

Structure factors

We now introduce the magnetic structure factor (SF), which is measured in neutron scattering experiments [1] and can be computed from spin correlations. It will become relevant in Chapter 5, where PFFRG results on spin models will be linked to the properties of pyrochlore compounds. In polarized neutron scattering experiments, two components of the SF can be distinguished by filtering the scattered neutrons according to their polarization [44]. The so-called spin-flip channel $\chi_{\mathrm{sf}}(\boldsymbol{q},\omega)$ is measured by neutrons that change their polarization during the scattering process, whereas

the non-spin-flip channel $\chi_{\mathrm{nsf}}(\boldsymbol{q},\omega)$ is measured by neutrons that do not change their polarization. The total SF is given by

$$\chi_{\mathrm{total}}(\boldsymbol{q},\omega) = \chi_{\mathrm{sf}}(\boldsymbol{q},\omega) + \chi_{\mathrm{nsf}}(\boldsymbol{q},\omega). \tag{3.66}$$

The expressions for the static components $\bar{\chi}_{\mathrm{sf}}(\boldsymbol{q})$ and $\bar{\chi}_{\mathrm{nsf}}(\boldsymbol{q})$ will be formulated similarly as in Ref. [45] in the following. They employ a coordinate frame that is dependent on the scattering vector $\boldsymbol{q}$. Its normalized axis vectors are labeled as $\boldsymbol{x}_{\mathrm{s}}$, $\boldsymbol{y}_{\mathrm{s}}$ and $\boldsymbol{z}_{\mathrm{s}}$. Neutrons of a neutron scattering experiment are polarized along the direction $\boldsymbol{z}_{\mathrm{s}} \perp \boldsymbol{q}$. If SFs are measured along a plane in $\boldsymbol{q}$, $\boldsymbol{z}_{\mathrm{s}}$ is orthogonal to that plane. The second axis vector is given by $\boldsymbol{x}_{\mathrm{s}} = \boldsymbol{q}/|\boldsymbol{q}|$, and the remaining vector is given by $\boldsymbol{y}_{\mathrm{s}} = \boldsymbol{z}_{\mathrm{s}} \times \boldsymbol{x}_{\mathrm{s}}$. Expressed using the axis vectors, the static SF channels are given by

$$\bar{\chi}_{\mathrm{sf}}(\boldsymbol{q}) = \frac{1}{N}\sum_{ij} e^{i\boldsymbol{q}(\boldsymbol{r}_i-\boldsymbol{r}_j)} \sum_{\mu\nu} y_{\mathrm{s}}^{\mu} y_{\mathrm{s}}^{\nu} \chi_{c,ij}^{\mu\nu}(\omega=0), \tag{3.67}$$

$$\bar{\chi}_{\mathrm{nsf}}(\boldsymbol{q}) = \frac{1}{N}\sum_{ij} e^{i\boldsymbol{q}(\boldsymbol{r}_i-\boldsymbol{r}_j)} \sum_{\mu\nu} z_{\mathrm{s}}^{\mu} z_{\mathrm{s}}^{\nu} \chi_{c,ij}^{\mu\nu}(\omega=0), \tag{3.68}$$

with the spin correlation

$$\chi_{c,ij}^{\mu\nu}(\omega) = \int_0^{\infty} d\tau e^{i\omega\tau} \langle \hat{S}_i^{\mu}(\tau) \hat{S}_j^{\nu}(0) \rangle. \tag{3.69}$$

While $\bar{\chi}_{\mathrm{sf}}(\boldsymbol{q})$ only detects spin components perpendicular to the neutron polarization axis $\boldsymbol{z}_{\mathrm{s}}$, spin components measured by $\bar{\chi}_{\mathrm{nsf}}(\boldsymbol{q})$ are parallel to $\boldsymbol{z}_{\mathrm{s}}$.

The above equations still neglect that the effective spins realized by magnetic compounds possess a g tensor, which quantifies the magnetic moments of spin degrees of freedom $\hat{S}_i^{\mu}$. Furthermore, this tensor $\boldsymbol{g}_i$, with components $g_i^{\mu\nu}$, can be dependent on a lattice site argument i. Under consideration of $\boldsymbol{g}_i$, spin components are replaced by $\hat{S}_i^{\mu} \to \sum_{\nu} g_i^{\mu\nu} \hat{S}_i^{\nu}$. In this case, Eqs. (3.67)-(3.68) have to be adjusted by substituting $\chi_{c,ij}^{\mu\nu} \to \sum_{ab} g_i^{\mu a} g_j^{\nu b} \chi_{c,ij}^{ab}$, with $a, b \in \{x, y, z\}$.

3.5.3 Symmetry-based flow equation simplifications

The flow equations [Eqs. (3.55)-(3.56)], static spin correlation [Eq. (3.64)], and magnetization [Eq. (3.61)] have been formulated for a general spin Hamiltonian, given by Eq. (3.1), without any continuous spin rotation symmetry or TRS. In the following, it will be discussed how the flow equations simplify once such symmetries are assumed. Simplifications of expressions for observables follow analogously.

Interaction	TRS	$\boldsymbol{\Sigma}$	$\boldsymbol{\Gamma}$
Heisenberg	Yes	$\begin{pmatrix}\Sigma^0\\0\\0\\0\end{pmatrix}$	$\begin{pmatrix}\Gamma^{\mathrm{d}} & 0 & 0 & 0\\0 & \Gamma^{\mathrm{s}} & 0 & 0\\0 & 0 & \Gamma^{\mathrm{s}} & 0\\0 & 0 & 0 & \Gamma^{\mathrm{s}}\end{pmatrix}$
XYZ	Yes	$\begin{pmatrix}\Sigma^0\\0\\0\\0\end{pmatrix}$	$\begin{pmatrix}\Gamma^{00} & 0 & 0 & 0\\0 & \Gamma^{xx} & 0 & 0\\0 & 0 & \Gamma^{yy} & 0\\0 & 0 & 0 & \Gamma^{zz}\end{pmatrix}$
U(1) symmetric (about z axis)	Yes	$\begin{pmatrix}\Sigma^0\\0\\0\\0\end{pmatrix}$	$\begin{pmatrix}\Gamma^{00} & 0 & 0 & \Gamma^{0z}\\0 & \Gamma^{xx} & \Gamma^{xy} & 0\\0 & -\Gamma^{xy} & \Gamma^{xx} & 0\\\Gamma^{z0} & 0 & 0 & \Gamma^{zz}\end{pmatrix}$
Unconstrained	Yes	$\begin{pmatrix}\Sigma^0\\0\\0\\0\end{pmatrix}$	$\begin{pmatrix}\Gamma^{00} & \Gamma^{0x} & \Gamma^{0y} & \Gamma^{0z}\\\Gamma^{x0} & \Gamma^{xx} & \Gamma^{xy} & \Gamma^{xz}\\\Gamma^{y0} & \Gamma^{yx} & \Gamma^{yy} & \Gamma^{yz}\\\Gamma^{z0} & \Gamma^{zx} & \Gamma^{zy} & \Gamma^{zz}\end{pmatrix}$
U(1) symmetric (about z axis)	No	$\begin{pmatrix}\Sigma^0\\0\\0\\\Sigma^z\end{pmatrix}$	$\begin{pmatrix}\Gamma^{00} & 0 & 0 & \Gamma^{0z}\\0 & \Gamma^{xx} & \Gamma^{xy} & 0\\0 & -\Gamma^{xy} & \Gamma^{xx} & 0\\\Gamma^{z0} & 0 & 0 & \Gamma^{zz}\end{pmatrix}$
Unconstrained	No	$\begin{pmatrix}\Sigma^0\\\Sigma^x\\\Sigma^y\\\Sigma^z\end{pmatrix}$	$\begin{pmatrix}\Gamma^{00} & \Gamma^{0x} & \Gamma^{0y} & \Gamma^{0z}\\\Gamma^{x0} & \Gamma^{xx} & \Gamma^{xy} & \Gamma^{xz}\\\Gamma^{y0} & \Gamma^{yx} & \Gamma^{yy} & \Gamma^{yz}\\\Gamma^{z0} & \Gamma^{zx} & \Gamma^{zy} & \Gamma^{zz}\end{pmatrix}$

Table 3.2: Finite spin components of the self-energy Σ^ρ (third column) and the two-particle vertex $\Gamma^{\rho\varphi}$ (fourth column) for $\rho, \varphi \in \{0, x, y, z\}$ for different types of spin models with distinct symmetries. The considered spin models are characterized by their types of two-body spin interactions or by their spin rotation symmetries (first column), and whether they possess TRS (second column). An XYZ interaction is of the form $J_x \hat{S}_i^x \hat{S}_j^x + J_y \hat{S}_i^y \hat{S}_j^y + J_z \hat{S}_i^z \hat{S}_j^z$. Frequency and site arguments are omitted for brevity. Components that are equal by symmetry are labeled identically. The table and its caption are replicated from Ref. [39]

The presence of TRS or continuous spin rotation symmetries restricts the components $\Gamma^{\rho\varphi}$ and Σ^ρ (G^ρ) that can be finite [46, 31, 39]. As a consequence, simplified flow equations can be obtained by restricting the values that the indices ρ, φ, and $a, \ldots, f$ can assume in Eqs. (3.55)-(3.56). Simplified vertex structures for a variety of different spin models, with and without TRS, are provided in Table 3.2. The expressions are straightforwardly obtained by applying the assumed symmetry transformations and using the property that Pauli matrices $\boldsymbol{\sigma}^\mu$ in the vertex parameterizations of Eqs.

(3.39) and (3.43) transform in the same ways as the Pauli matrix representations of corresponding spin components $\hat{S}^\mu$ under a spin rotation symmetry, whereas $\boldsymbol{\sigma}^0$ stays invariant under spin rotations. Note that while TRS transforms $\boldsymbol{\sigma}^\mu$ in the same way as Pauli matrix representations of $\hat{S}^\mu$ as well, i.e., $\boldsymbol{\sigma}^\mu \to -\boldsymbol{\sigma}^\mu$ (and $\boldsymbol{\sigma}^0 \to \boldsymbol{\sigma}^0$) under the application of TRS, it additionally applies a complex conjugation to vertex components $\Sigma^\rho(\omega)$ and $\Gamma^{\rho\varphi}_{i_1 i_2}(s,t,u)$, and changes the sign of their vertex frequency arguments (e.g., $\Sigma^\mu(\omega_1)\sigma^\mu_{\alpha_{1'}\alpha_1} \to \Sigma^\mu(-\omega_1)^*(-\sigma^\mu_{\alpha_{1'}\alpha_1})$ and $\Sigma^0(\omega_1)\sigma^0_{\alpha_{1'}\alpha_1} \to \Sigma^0(-\omega_1)^*\sigma^0_{\alpha_{1'}\alpha_1}$ under the application of TRS). As argued in Sec. 3.4, this leads to the restriction $\Sigma^\mu(\omega) = 0$ and the previously stated symmetry transformation of Eq. (3.48) for $\Gamma^{\rho\varphi}_{i_1 i_2}(s,t,u)$.

We now continue by discussing some explicit symmetry scenarios as examples. Structures of the self-energy and the two-particle vertex for the considered scenarios are summarized in Table 3.2. For the self-energy, a global U(1) spin rotation symmetry about the z axis enforces vanishing components $\Sigma^x = \Sigma^y = 0$. The presence of TRS always enforces each component Σ^μ with $\mu \in \{x, y, z\}$ to vanish, regardless of whether any rotation symmetry is present. In contrast, TRS does not restrict any components $\Gamma^{\rho\varphi}$ of the two-particle vertex, whereas rotation symmetries do. In case of a Heisenberg model (i.e., a global SU(2) spin rotation symmetry exists), the two-particle vertex only contains two independent components Γ^{00} and $\Gamma^{xx} = \Gamma^{yy} = \Gamma^{zz}$, usually labeled as Γ^d and Γ^s [11]. In an XYZ model with TRS, the two-particle vertex contains four finite and independent components $\Gamma^{\rho\varphi}$, even though the model does generally not contain any continuous rotation symmetry. A more involved two-particle vertex structure is obtained for a general model with a global $U(1)$ spin rotation symmetry, which we again assume about the z axis. In this case, different finite components $\Gamma^{\rho\varphi}$ become dependent on each other, i.e., $\Gamma^{xy} = -\Gamma^{yx}$ and $\Gamma^{xx} = \Gamma^{yy}$ for equal frequency and site arguments, resulting in a total number of 6 independent two-particle vertex components $\Gamma^{\rho\varphi}$ [46]. Finally, in absence of any continuous rotation symmetries, all 16 components $\Gamma^{\rho\varphi}$ can become finite and independent throughout the PFFRG flow [31]. Since studies on Heisenberg models are frequent, we present the simplified expressions for flow equations and observables that are obtained if a Heisenberg model is considered in Appendix A.

Simplified vertex structures in presence of additional symmetries are reflected in the computational resources required to solve the flow equations. Since the RPA channel mostly determines the computational resources required to solve the flow equations, we now consider how vertex structure simplifications affect the number of finite and independent two-particle vertex products $\Gamma^{ab}\Gamma^{cd}$ for unconstrained indices $a, b, c, d \in \{0, x, y, z\}$ in the RPA channel. The numbers of such independent terms are given in Table 3.3 for the previously considered models with different symmetry properties. With the exception of the XYZ model, the number of terms generally increases for each

Interactions	TRS	Relative number of products $\Gamma^{ab}\Gamma^{cd}$
Heisenberg	Yes	1
XYZ	Yes	2
U(1) symmetric	Yes	6
Unconstrained	Yes	32
U(1) symmetric	No	10
Unconstrained	No	128

Table 3.3: Relative number of independent and finite two-particle vertex products $\Gamma^{ab}\Gamma^{cd}$ in the RPA channel for unconstrained indices $a, b, c, d \in \{0, x, y, z\}$ (frequency and site arguments are kept implicit and differ between Γ^{ab} and Γ^{cd}). The same type of models as in Table 3.2 are considered, i.e., systems with and without TRS. The table and its caption are replicated from Ref. [39]

broken spin rotation symmetry. Furthermore, the absence of TRS increases the number of terms fourfold in absence of any continuous rotation symmetries. In contrast, the number is less than doubled by breaking TRS in a U(1) symmetric model. Notably, a U(1) symmetric model without TRS still contains fewer independent terms in the RPA channel than a model with TRS and without any continuous rotation symmetries. Note that the vertex frequency symmetry of Eq. (3.48) is not present in case of broken TRS, doubling the number of frequency arguments for which the two-particle vertex is independent. It follows that the absence of TRS additionally doubles the number of frequency arguments for which the flow equation of the two-particle vertex has to be evaluated. Note that the exact computational complexity of solving the flow equations is difficult to estimate, since it depends on additional subtle but nevertheless resource-heavy computational processes, such as efficiently reading out vertex components from an array.

3.5.4 Cutoff parameter as an effective temperature

We will now explore the analogy between a temperature T and an applied cutoff parameter Λ, which can be considered to obtain an intuitive understanding of PFFRG flows. Both the T and Λ flow of a model start in a trivial paramagnetic phase at $T \to \infty$ or $\Lambda \to \infty$, and may transition into a magnetically ordered or nontrivial paramagnetic phase (such as a spin liquid or nematic phase) as the flow parameter is lowered towards $T = 0$ or $\Lambda = 0$. In presence of a sharp frequency cutoff, given by Eq. (3.2), the analogy can be made explicit in the mean-field limit. For this cutoff, the RPA solutions of a model for a finite T and for a finite Λ are related by a simple rescaling $\Lambda = 2T/\pi$ in case no finite magnetic fields are present [32]. However, as will be shown

in the following, the cutoff and temperature analogy should generally be applied with caution, as it can break apart at small Λ and T. For the analytically solvable model of a free spin in a magnetic field, it will be shown that the exact expressions of observables involve qualitatively different functions, depending on whether T or Λ is applied as a parameter. Additionally, the solutions will inform us which PFFRG flow behavior is to be expected in spin models exposed to large magnetic fields.

Assuming a magnetic field of size h^z along the z axis, the considered model is given by

$$\hat{\mathcal{H}} = -h^z \hat{S}^z. \tag{3.70}$$

Due to the absence of interaction terms, the flow equations become trivial, i.e., all vertices remain unchanged from their initial conditions throughout the Λ flow. The single-particle Green function can be solved analytically and is given by

$$G^\Lambda(1'|1) = G_0^\Lambda(1'|1) = \theta(|\omega_1| - \Lambda)\delta(\omega_{1'} - \omega_1) \left(i\omega_1 \boldsymbol{\sigma}^0 + \frac{h}{2}\boldsymbol{\sigma}^z \right)^{-1}_{\alpha_{1'}\alpha_1}. \tag{3.71}$$

The resulting cutoff-dependent magnetization is obtained from Eq. (3.61) and is given by

$$M^\Lambda(T=0) = \frac{1}{2} - \frac{1}{\pi}\arctan(\frac{2\Lambda}{h}). \tag{3.72}$$

In contrast, the temperature-dependent magnetization for a single spin in a magnetic field is straightforwardly obtained as

$$M^{\Lambda=0}(T) = \frac{1}{2}\tanh(\frac{h}{2T}). \tag{3.73}$$

Both magnetization functions are shown in Fig. 3.1(a), which makes the qualitative difference of both functions at small T and Λ apparent. While $\frac{dM^{\Lambda=0}(T)}{dT}$ vanishes at $T=0$, $\frac{dM^\Lambda(T=0)}{d\Lambda}$ remains finite at $\Lambda = 0$, and instead $\frac{d^2M^\Lambda(T=0)}{d\Lambda^2}$ vanishes.

Relevant to the PFFRG are the suseptibility flows as well. They are obtained by taking the derivative of the magnetization with respect to the global external field, i.e.,

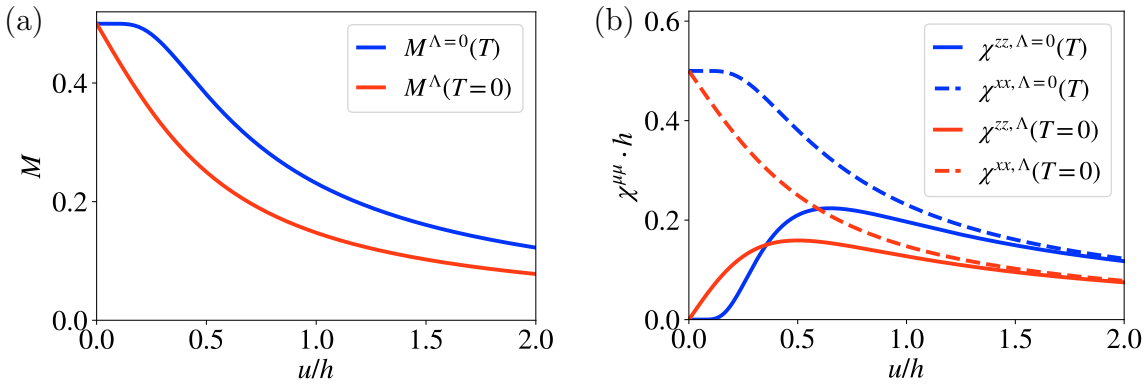

Figure 3.1: Analytic flows of the temperature T and sharp frequency cutoff Λ dependent magnetization $M^{\Lambda}(T)$ and susceptibility $\chi^{\mu\mu,\Lambda}(T)$ for a spin-$\frac{1}{2}$ in a magnetic field of size h, described by the Hamiltonian of Eq. (3.70). The observables are either shown in dependence on T or Λ, represented by the variable u, while the remaining parameter is set as zero. (a) Analytic magnetization flows are shown. The functions are given by Eqs. (3.72) and (3.73). (b) Static susceptibility flows are shown. The functions are given by Eqs. (3.75) and (3.74). The subfigures are replicated from Ref. [39].

$\chi^{\mu\mu,\Lambda}(T) = \frac{\partial M^{\mu,\Lambda}(T)}{\partial h^{\mu}}$. The analytical solutions are given by

$$\chi^{zz,\Lambda}(T=0) = \frac{1}{\pi h}\frac{1}{(\frac{2\Lambda}{h}) + (\frac{2\Lambda}{h})^{-1}}, \tag{3.74}$$

$$\chi^{xx,\Lambda}(T=0) = \frac{1}{2h}\big[1 - \frac{2}{\pi}\arctan(\frac{2\Lambda}{h})\big], \tag{3.75}$$

$$\chi^{zz,\Lambda=0}(T) = \frac{1}{4T\cosh(\frac{h}{2T})^2}, \tag{3.76}$$

$$\chi^{xx,\Lambda=0}(T) = \frac{1}{2h}\tanh(\frac{h}{2T}). \tag{3.77}$$

They are shown in Fig. 3.1(b). Note that $\chi^{zz,\Lambda}(T=0)$ has a maximum of $\chi^{zz}_{\max} = (2\pi h)^{-1}$ at $\Lambda = h/2$, and $\chi^{xx,\Lambda}(T=0)$ reaches its maximum value of $\chi^{xx}_{\max} = (2h)^{-1}$ at $\Lambda = 0$.

3.5.5 Mean-field approximation

Within the PFFRG, spin models with spins of length $S = \frac{M}{2} > \frac{1}{2}$, with $M \in \mathbb{N}$, are treated by introducing M copies of spin-$\frac{1}{2}$ degrees of freedom on each lattice site [32]. As a consequence of this implementation, terms in the flow equation with an internal site summation $\sum_j$ gain a prefactor M, such that only these terms remain relevant in the limit $S \to \infty$. Terms with a site summation are given by the Hartree term in the self-energy flow equation and the RPA term in the two-particle vertex flow equation. It is known that the PFFRG reproduces the Hartree and RPA approximation if only

those terms are considered [47]. Hence, PFFRG transitions to mean-field theory in the limit $S \to \infty$. In the following, we will further investigate the $S \to \infty$ limit of the PFFRG by solving the Hartree approximation analytically in presence of magnetic fields and in dependence on a sharp frequency cutoff. In this context, we will highlight qualitatively different expressions of the Hartree magnetization depending on whether it is solved as a function of a sharp frequency cutoff Λ or a temperature T.

In the absence of any magnetic field, the Hartree self-energy and local magnetization remain zero for any Λ. The RPA susceptibility can then be obtained by solving the two-particle vertex flow equation considering only the RPA channel and treating the remaining terms as zero, or by solving the BSE self-consistency equation solely considering the RPA term, which contributes to the reducible vertex $\gamma_t(1', 2'|1, 2)$ (note that the RPA flow equation is obtained from the RPA BSE by taking a derivative with respect to Λ). Note that the latter approach will be demonstrated in Sec. 3.7.

If a model with a finite magnetic field h^μ is considered, the Hartree magnetization M^μ is finite. In this case, one can analytically solve the Hartree magnetization from the corresponding Hartree self-consistency equation, as shown below. The RPA susceptibility is then obtained straightforwardly by taking the derivative with respect to an external magnetic field, i.e., $\chi^{\mu\mu,\Lambda} = \frac{\partial M^{\mu,\Lambda}}{\partial h^\mu}$. It follows that knowledge of the two-particle vertex is not required to determine the RPA susceptibility if h^μ is incorporated into the model. For simplicity, a nearest-neighbor Heisenberg model in a magnetic field h along the z axis, given by the Hamiltonian

$$\hat{\mathcal{H}} = J \sum_{\langle ij \rangle} \hat{\boldsymbol{S}}_i \cdot \hat{\boldsymbol{S}}_j - h \sum_i \hat{S}_i^z, \tag{3.78}$$

will be considered in the following calculation of a Hartree magnetization.

The Hartree self-consistency equation of the self-energy [18] is given by

$$\Sigma^\Lambda(1', 1) = \sum_{2,2'} \frac{J_{||}(1', 2'|1, 2)}{4} G^\Lambda(2|2'), \tag{3.79}$$

with

$$J_{||}(1', 2'|1, 2) = J_{i_1 i_2} \sum_\mu \sigma^\mu_{\alpha_{1'}\alpha_1} \sigma^\mu_{\alpha_{2'}\alpha_2} \delta(\omega_{1'} + \omega_{2'} - \omega_1 - \omega_2) \delta_{i_{1'} i_1} \delta_{i_{2'} i_2}. \tag{3.80}$$

The self-consistent Hartree self-energy is frequency independent. By inserting the self-

energy and Green function parameterizations of Eqs. (3.35) and (3.40), the equation

$$\gamma_i^{z,\Lambda} = \frac{1}{4\pi} \sum_j J_{ij} \int_{-\infty}^{\infty} d\omega g_j^{z,\Lambda}(\omega) \tag{3.81}$$

is obtained, which can be further simplified to

$$\gamma^{z,\Lambda} = \frac{cJM^{\Lambda}}{2} \tag{3.82}$$

by comparison to the magnetization expression of Eq. (3.61). The constant c is the coordination number of the lattice. A self-consistency equation for the Hartree magnetization is obtained by inserting Eq. (3.82) into the Green function in Eq. (3.61) after applying Dyson's Eq. (3.41). An evaluation of the frequency integral leads to

$$M^{\Lambda} = \frac{1}{2}\mathrm{sgn}(h - cJM^{\Lambda}) - \frac{1}{\pi}\arctan(\frac{2\Lambda}{h - cJM^{\Lambda}}). \tag{3.83}$$

The equation replicates the exact solution of a free spin in case $J = 0$, which is given by Eq. (3.72). At finite h, the Hartree mean-field solution becomes qualitatively different depending on whether a sharp frequency cutoff or a temperature is considered as a variable, as is reflected by the respective mean-field self-consistency equations. While the self-consistency equation of M^{Λ} is characterized by an arctan function, the temperature-dependent solution $M(T)$ involves a tanh function.

3.5.6 Cutoff function

The FRG formalism leaves much freedom in the choice of a cutoff parameter. Possible choices include the parameter to be a momentum, frequency, interaction, or temperature [16]. PFFRG applications generally apply a frequency cutoff function $R(\Lambda, \omega)$ that modifies the free Green function as

$$G_{0,i}^{\mu}(\omega) \to R(\Lambda, \omega) G_{0,i}^{\mu}(\omega). \tag{3.84}$$

However, a momentum cutoff had previously been applied as well [34]. As already mentioned, we only apply a sharp frequency cutoff $R(\Lambda, \omega) = \theta(|\omega| - \Lambda)$ in this thesis, which modifies the free single-particle Green function via the Heaviside step function

$$\theta(\omega) = \begin{cases} 1, \omega \geq 0 \\ 0, \omega < 0 \end{cases} . \tag{3.85}$$

The cutoff dependencies of the full single-particle Green function and single-scale propagator follow as

$$G_i^{\mu,\Lambda}(\omega) = \theta(|\omega| - \Lambda) G_i^{\mu}(\omega), \tag{3.86}$$

$$\mathcal{S}_i^{\mu,\Lambda}(\omega) = -\frac{d}{d\Lambda} G_i^{\mu,\Lambda}(\omega)|_{\Sigma^\Lambda=\text{const}} = \delta(|\omega| - \Lambda) G_i^{\mu}(\omega). \tag{3.87}$$

Note that $\tilde{\mathcal{S}}_i^{\mu,\Lambda}(\omega)$, given by Eq. (3.57), does not include a Dirac delta dependence. Instead, $\tilde{\mathcal{S}}_i^{\mu,\Lambda}(\omega) \propto \theta(|\omega| - \Lambda)$. A sharp cutoff simplifies a numerical PFFRG implementation as it simplifies the frequency integrals of the flow equations straightforwardly. While the Dirac delta function of $\mathcal{S}_i^{\mu,\Lambda}(\omega)$ eliminates one frequency integral, the Heaviside function of $G_i^{\mu,\Lambda}(\omega)$ changes boundaries of frequency integrals in the two-particle vertex flow equation. As a disadvantage, the sharp frequency cutoff, combined with the numerically necessary discretization of vertex frequency dependencies, leads to oscillatory numerical artifacts in the frequency resolutions of $\Sigma^\Lambda(1'|1)$ and $\Gamma^\Lambda(1', 2'|1, 2)$ [36]. Such oscillatory features are often visible in the PFFRG susceptibility flow as well.

The oscillatory numerical artifacts can be circumvented by more sophisticated numerical implementations of the PFFRG that apply continuous cutoff functions $R(\Lambda, \omega)$ [38, 36]. Two examples of continuous $R(\Lambda, \omega)$, used in Refs. [36] and [28], are given by

$$\begin{aligned} R(\omega) &= 1 - e^{-\omega^2/\Lambda^2}, \\ R(\omega) &= \frac{\omega^2}{\omega^2 + \Lambda^2}. \end{aligned} \tag{3.88}$$

3.5.7 Detection of magnetic phases

We now continue with a discussion on how the PFFRG is applied to investigate $T = 0$ phases of spin models. Symmetries of a spin model with TRS are spontaneously broken at a magnetic phase transition. This is reflected by a divergence of the magnetic susceptibility. Experimentally, a magnetic phase transition typically occurs by lowering the temperature of a system. In context of the PFFRG, a magnetic phase is entered through a Λ flow instead, and the corresponding divergence of the magnetic susceptibility usually manifests itself as a flow breakdown in the form of a kink at a critical cutoff Λ_c in an otherwise smooth susceptibility flow at $\Lambda > \Lambda_c$. Since the flow equations are solved from the infrared $\Lambda \to \infty$ towards the $\Lambda = 0$ limit, flows at cutoffs below a breakdown at $\Lambda < \Lambda_c$ are unphysical. As a consequence, the manifestation of a flow breakdown at Λ_c enforces the treatment of a spin model at cutoffs $\Lambda > \Lambda_c$ above a magnetic phase transition. Properties of a magnetically ordered phase at $\Lambda < \Lambda_c$ can

partially be inferred from the magnetic susceptibility at cutoffs just above Λ_c. E.g., the magnetic Bragg peaks that emerge in the magnetic susceptibility near Λ_c can often be identified with a magnetic order. As an alternative scenario, a PFFRG flow may not encounter any flow breakdown at all down to $\Lambda = 0$. This implies the absence of any spontaneous symmetry breaking that leads to the onset of magnetic order, since these spontaneously broken symmetries would have resulted in a flow breakdown. If a model with TRS is considered, such a fully stable flow implies the presence of a nonmagnetic phase at $T = 0$ as a consequence. Note that the absence of flow breakdowns is found in flows into nematic paramagnetic phases as well, even though they spontaneously break symmetries. In this case, no flow breakdown is detected due to the truncation of flow equations above the two-particle vertex. To detect a phase transition into a nematic order, one could employ a truncation scheme that does not truncate the flow equations of the n-particle vertex functions with $n > 2$ that are able to detect the diverging susceptibility of a nematic phase transition. However, at the time of writing, such a truncation scheme is not feasible with the computational resources available.

A selection of exemplary PFFRG flows is provided in Fig. 3.2. The corresponding models are treated in Chapters 5 and 6 respectively. The nearest-neighbor antiferromagnetic Heisenberg model on the pyrochlore lattice remains paramagnetic down to $T = 0$ [48]. Accordingly, the PFFRG flow of the maximum susceptibility $\chi^{zz,\Lambda}_{\max}$, shown in red, remains smooth down to $\Lambda \to 0$. In contrast, the flow of the ferromagnetic model on the same lattice, shown in green, experiences a magnetic phase transition that manifests itself as a clear flow breakdown in form of a sharp susceptibility peak at $\Lambda \approx 0.6$. A softer flow breakdown is observed in the blue-colored flow corresponding to the density-functional-theory model of the compound $K_2Ni_2(SO_4)_3$, again caused by a magnetic phase transition. In this case, the breakdown manifests itself as a kink in the susceptibility flow. At cutoffs below the breakdown, oscillatory features are observed to be enhanced. These features are numerical artifacts caused by a sharp frequency cutoff in combination with finite frequency grids on which vertices are computed. These artifacts can be cured by an advanced numerical implementation as done in [36]. Softer flow breakdowns are often observed in highly frustrated models that are close to a paramagnetic phase transition [49]. Thus, soft flow breakdowns are often associated with weak magnetic order. E.g., as interactions of a model are continuously changed for it to transition from a magnetically ordered to a nonmagnetic phase at $T = 0$, the PFFRG flow of the model evolves such that the flow breakdown continuously becomes softer until it disappears completely once the model turns nonmagnetic. This continuous behavior can lead to an uncertainty in the interaction parameter space in question over which a paramagnetic phase extends in a $T = 0$ phase diagram.

In order for the PFFRG to access properties of a model within its magnetically ordered

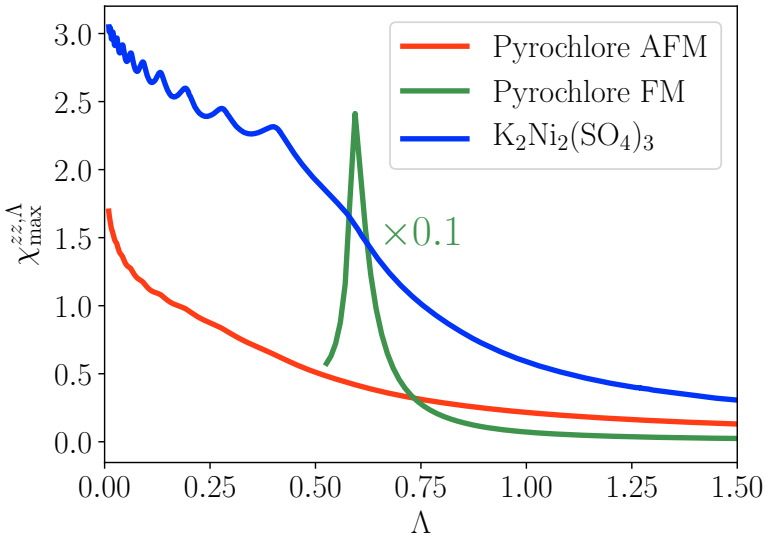

Figure 3.2: Exemplary PFFRG flows of the maximum static susceptibility $\chi^{zz,\Lambda}_{\max}$. Flows both with and without a flow breakdown caused by a magnetic phase transition are shown. The flows of the $S = 1/2$ nearest-neighbor antiferromagnetic ("Pyrochlore AFM") and ferromagnetic ("Pyrochlore FM") Heisenberg model on the pyrochlore lattice, obtained with the PFFRG implementation of Sec. 5.2, are shown in red and green respectively. The intensity of the latter flow is multiplied by a factor of 0.1. The flow of the highly geometrically frustrated $S = 1$ Heisenberg model of the three-dimensional tetra-trillium compound $K_2Ni_2(SO_4)_3$, with interactions obtained by density functional theory, is shown in blue. The latter flow is obtained from the PFFRG implementation of Chapter 6.

phase, the susceptibility divergence at a magnetic phase transition has to be regularized. This can be achieved by breaking symmetries of a model by the introduction of a perturbative (possibly site-dependent) magnetic seed field that would otherwise be broken spontaneously by a magnetic order. Such a strategy was previously used in the fermionic FRG [50, 51]. The seed field suppresses a susceptibility divergence at Λ_c. Instead, a maximum in susceptibility emerges and a smooth susceptibility flow down to the cutoff-free limit is enabled. Subsequently, properties of the magnetic ground state can be studied by computing the susceptibility or (site-dependent) magnetization in the $\Lambda = 0$ limit. An in-depth study of PFFRG flows into magnetically ordered phases will be provided in Chapter 4, which covers contents of our recent paper Ref. [39].

3.5.8 Detection of nematic phases

The previous section discussed how magnetic and paramagnetic phases are detected within PFFRG. Furthermore, it was argued that the magnetic susceptibility can be investigated just above Λ_c to further characterize a magnetically ordered phase. As the

next step, we now consider the question how PFFRG can be applied to characterize $T = 0$ nonmagnetic phases as well. More specifically, we will be interested in the characterization of nematic phases, i.e., phases that do not spontaneously break TRS but break spin rotation or lattice rotation symmetries [1]. While nematic phases that break spin rotation symmetries are referred to as spin nematic phases, those that break lattice rotation symmetries are referred to as lattice nematic phases [52]. In this thesis, we will study nonmagnetic phases by PFFRG only with respect to the presence of lattice nematic order. However, in principle they can be studied by PFFRG with respect to the presence of spin nematic order as well, as shown in Ref. [52]. It will turn out that compared to the characterization of magnetic order, the characterization of nematic phases is challenging within PFFRG.

The susceptibilities that are able to detect nematic phases are often obtained from spin correlations that are of quartic or higher order in spin operators. E.g., finite long-range dimer correlations $\chi_{\mathrm{VB}} = \langle(\hat{\boldsymbol{S}}_i \cdot \hat{\boldsymbol{S}}_j)(\hat{\boldsymbol{S}}_k \cdot \hat{\boldsymbol{S}}_l)\rangle - \langle(\hat{\boldsymbol{S}}_i \cdot \hat{\boldsymbol{S}}_j)\rangle\langle(\hat{\boldsymbol{S}}_k \cdot \hat{\boldsymbol{S}}_l)\rangle$ are expected for a valence-bond solid that has dimers on bonds $\langle i, j\rangle$ and $\langle k, l\rangle$ [53]. A computation of these correlations would require a flow equation truncation above the four-particle vertex or higher, which is not numerically feasible at the time of writing. Instead, the PFFRG is generally applied with a truncation above the two-particle vertex, which highly limits the capability of the method to detect nematic phases. This limitation is apparent by the lack of flow breakdowns in nematically ordered models that should follow from the spontaneously broken symmetries of their nematic phases [52].

Nevertheless, an approach to detecting nematic phases with PFFRG exists, which does not require the computation of spin correlations that are of higher than quadratic order in spin operators. The approach measures the response of a model to a perturbation that breaks the same symmetries as a proposed nematic phase does spontaneously. Note that this approach introduces an a priori bias, since spontaneously broken symmetries that are probed for have to be decided on before the perturbation is applied. This issue is not present in the detection of ordered phases via susceptibilities. The PFFRG strategy for detecting nematic phases will be described in the following. We will first give a general description of the approach before making it mathematically concrete.

Magnetic orders can be detected via the magnetic susceptibility χ, which can be accessed theoretically either by evaluating spin correlations [see Eq. (3.62)], or from the response of a magnetic order parameter M to an infinitesimal magnetic field h ($\chi = \frac{\partial M}{\partial h}|_{h=0}$). Similarly, one can access the susceptibility to a nematic order either from spin correlations (given by χ_{VB} in case of a valence bond solid) or by considering the response of a nematic order parameter to a symmetry-breaking perturba-

tion (the corresponding so-called dimer response function will be introduced at a later point). E.g., in case of a valence bond solid, an order parameter would be given by $\langle(\hat{\boldsymbol{S}}_i \cdot \hat{\boldsymbol{S}}_j)\rangle - \langle(\hat{\boldsymbol{S}}_k \cdot \hat{\boldsymbol{S}}_l)\rangle$, where $\langle i,j\rangle$ is a bond with a dimer being present and $\langle k,l\rangle$ is a bond without a dimer [54]. Only the latter approach for detecting nematic order is applicable within the PFFRG truncation. While the PFFRG is not able to observe a divergence in the response function of a nematic order, large response values in the limit $\Lambda \to 0$ indicate that a model assumes a nematic phase at zero temperature. E.g., such an approach was applied in Ref. [52] on the square lattice Heisenberg model with further-neighbor interactions to investigate the model with respect to nematic ground states with broken spin rotation symmetry, lattice rotation symmetry, or a combination of both. In Sec. 5.1 of this thesis, the same strategy to detect nematic phases is applied to study the paramagnetic ground state of the antiferromagnetic Heisenberg model on the pyrochlore lattice with respect to lattice symmetry breaking.

We now specify the approach used in the latter study. In order to probe a nearest-neighbor Heisenberg model

$$\hat{\mathcal{H}} = J \sum_{\langle ij \rangle} \hat{\boldsymbol{S}}_i \hat{\boldsymbol{S}}_j \tag{3.89}$$

with respect to lattice symmetry breaking, e.g., in form of a valence bond solid ground state, Heisenberg interactions $J\hat{\boldsymbol{S}}_i\hat{\boldsymbol{S}}_j$ will be either strengthened or weakened on different bonds by perturbing $J \to J \pm \delta$, with $\delta \ll J$. Different perturbation patterns allow one to investigate the responses with respect to different lattice symmetry breaking scenarios. The responses of the system to the respective perturbations are captured by the dimer response function $\chi^{\Lambda}_{D,ijkl}$, which is defined on the bonds $\langle i,j\rangle$ and $\langle k,l\rangle$, and is given by

$$\chi^{\Lambda}_{D,ijkl} = \left| \frac{J}{\delta} \frac{\chi^{\Lambda}_{ij} - \chi^{\Lambda}_{kl}}{\chi^{\Lambda}_{ij} + \chi^{\Lambda}_{kl}} \right| , \text{where } J_{ij} = J + \delta,\ J_{kl} = J - \delta \ , \tag{3.90}$$

with $\chi^{\Lambda}_{ij} = \chi^{xx,\Lambda}_{ij} + \chi^{yy,\Lambda}_{ij} + \chi^{zz,\Lambda}_{ij}$. In the limit $\Lambda \to \infty$ the response function is normalized, i.e., $\chi^{\Lambda\to\infty}_{D,ijkl} = 1$. A large increase to values $\chi^{\Lambda}_{D,ijkl} \gg 1$ in the cutoff-free limit $\Lambda \to 0$ hints at a phase in which the lattice symmetry, that maps the two bonds $\langle i,j\rangle$ and $\langle k,l\rangle$ onto each other, is broken.

3.6 Alternative implementation of magnetic fields within PFFRG

This section explores an alternative strategy for accessing observables of models with broken TRS within PFFRG. Importantly, the presented approach circumvents the direct treatment of models with broken TRS. Instead, models with TRS will be treated

for which observables such as spin correlations or local magnetizations can be related to observables of similar models with broken TRS by taking a partial trace. As such, this approach is numerically efficient in principle, since the breaking of TRS is associated with an increase in the numerically required resources for solving the flow equations. However, upon closer inspection, we will reveal that the approach exhibits properties that make it impractical for a PFFRG implementation. The technique will be described in the following. Note that this approach had been formulated before the general PFFRG formulation for models with broken TRS was derived. At that point, it was thought that the treatment of models with broken TRS requires high computational costs [31], which justified the persuasion of this numerically efficient trick.

For the purpose of this section, we aim at solving the $S = 1/2$ Hamiltonian

$$\hat{\mathcal{H}}(h) = J \sum_{\langle ij \rangle} \boldsymbol{S}_i^T \boldsymbol{S}_j - h \sum_i \hat{S}_i^z \tag{3.91}$$

of a nearest-neighbor Heisenberg model that is coupled to an external magnetic field h in the following. Broken TRS can be circumvented by considering both $\hat{\mathcal{H}}(h)$ and $\hat{\mathcal{H}}(-h)$, i.e., the Hamiltonian before and after the application of time-reversal, simultaneously. The resulting model can be interpreted as a spin model in which each lattice site i is coupled to an external site i_{ext} by an Ising interaction of size $2h$. The model is given by

$$\hat{\mathcal{H}}_h = \hat{\mathcal{H}}_L + \hat{\mathcal{H}}_{\text{ext}} = J \sum_{\langle ij \rangle} \boldsymbol{S}_i \cdot \boldsymbol{S}_j - 2h \sum_{i \in \text{Lattice}} \hat{S}_i^z \hat{S}_{i_{\text{ext}}}^z \tag{3.92}$$

and does not break TRS. Note that the interactions of $\hat{\mathcal{H}}_h$ are treatable within PFFRG in principle. The Hamiltonian can be split up into $\hat{\mathcal{H}}_L$, which is the Heisenberg Hamiltonian of the lattice, and $\hat{\mathcal{H}}_{\text{ext}}$ being the Ising coupling between the lattice and external spin.

$\hat{\mathcal{H}}(h)$ is obtained from $\hat{\mathcal{H}}_h$ by performing a partial projection onto the up state $|\uparrow_{i_{\text{ext}}}\rangle$ of the external spin operator $\hat{S}_{i_{\text{ext}}}^z$, which fulfills $\hat{S}_{i_{\text{ext}}}^z |\uparrow_{i_{\text{ext}}}\rangle = \frac{1}{2} |\uparrow_{i_{\text{ext}}}\rangle$, i.e.,

$$\hat{\mathcal{H}}(h) = \langle \uparrow_{i_{\text{ext}}} | \, \hat{\mathcal{H}}_h \, | \uparrow_{i_{\text{ext}}} \rangle \, . \tag{3.93}$$

Since $[\hat{\mathcal{H}}_h, \hat{S}_{i_{\text{ext}}}^z] = 0$, $\hat{S}_{i_{\text{ext}}}^z$ and $\hat{\mathcal{H}}_h$ share the same eigenvectors. It is straightforward to confirm that

$$\begin{aligned} \langle \uparrow_{i_{\text{ext}}} | \, e^{-\beta \hat{\mathcal{H}}_h} \, | \uparrow_{i_{\text{ext}}} \rangle &= e^{-\beta \hat{\mathcal{H}}(h)}, \\ \langle \downarrow_{i_{\text{ext}}} | \, e^{-\beta \hat{\mathcal{H}}_h} \, | \downarrow_{i_{\text{ext}}} \rangle &= e^{-\beta \hat{\mathcal{H}}(-h)}, \end{aligned} \tag{3.94}$$

with $\hat{S}_{i_{\text{ext}}}^z |\downarrow_{i_{\text{ext}}}\rangle = -\frac{1}{2} |\downarrow_{i_{\text{ext}}}\rangle$.

We now consider a spin correlation $\langle \hat{S}^z_{i_{\text{ext}}} \hat{S}^z_i \rangle_h$ of $\hat{\mathcal{H}}_h$ between the external spin and a spin of the lattice and show that the correlation is equal to twice the magnetization $\langle \hat{S}^z_i \rangle(h)$ of $\hat{\mathcal{H}}(h)$. For this purpose, an explicit evaluation of the trace over the eigenstates of $\hat{S}^z_{i_{\text{ext}}}$ will be performed in the following. $\text{tr}_h(\dots)$ denotes the trace over states of $\hat{\mathcal{H}}_h$ and $\text{tr}_L(\dots)$ is the trace over states of the lattice Hamiltonian $\hat{\mathcal{H}}_L$. Furthermore, Z_h is the partition sum of $\hat{\mathcal{H}}_h$, whereas $Z(h)$ is the partition sum of $\hat{\mathcal{H}}(h)$.

$$
\begin{aligned}
&\langle \hat{S}^z_{i_{\text{ext}}} \hat{S}^z_i \rangle_h \\
=&\frac{1}{Z_h} \text{tr}_h\big(e^{-\beta \hat{\mathcal{H}}_h} \hat{S}^z_{i_{\text{ext}}} \hat{S}^z_i\big) \\
=&\frac{1}{Z_h} \text{tr}_L\big(\langle \uparrow_{i_{\text{ext}}} | \, e^{-\beta \hat{\mathcal{H}}_h} \hat{S}^z_{i_{\text{ext}}} \hat{S}^z_i \, | \uparrow_{i_{\text{ext}}} \rangle \big) + \text{tr}_L\big(\langle \downarrow_{i_{\text{ext}}} | \, e^{-\beta \hat{\mathcal{H}}_h} \hat{S}^z_{i_{\text{ext}}} \hat{S}^z_i \, | \downarrow_{i_{\text{ext}}} \rangle \big) \\
\overset{(3.94)}{=}&\frac{1}{Z(h)+Z(-h)} \frac{1}{2} \big[\text{tr}_L\big(e^{-\beta \hat{\mathcal{H}}(h)} \hat{S}^z_i\big) - \text{tr}_L\big(e^{-\beta \hat{\mathcal{H}}(-h)} \hat{S}^z_i\big) \big] \\
=&\frac{1}{Z(h)+Z(-h)} \frac{1}{2} \big[\langle \hat{S}^z_i \rangle(h) - \langle \hat{S}^z_i \rangle(-h) \big] \\
=&\frac{1}{2} \langle \hat{S}^z_i \rangle(h).
\end{aligned} \tag{3.95}
$$

$Z(h) = Z(-h)$ and $\langle \hat{S}^z_i \rangle(-h) = -\langle \hat{S}^z_i \rangle(h)$ was applied in the last step . Furthermore, we can compute spin correlations of $\hat{\mathcal{H}}_h$ between spins of the lattice and show their equality to spin correlations of $\hat{\mathcal{H}}(h)$.

$$
\begin{aligned}
&\langle \hat{S}^z_i \hat{S}^z_j \rangle_h \\
=&\frac{1}{Z_h} \text{tr}_h\big(e^{-\beta \hat{\mathcal{H}}_h} \hat{S}^z_i \hat{S}^z_j\big) \\
=&\frac{1}{Z_h} \text{tr}_L\big(\langle \uparrow_{i_{\text{ext}}} | \, e^{-\beta \hat{\mathcal{H}}_h} \hat{S}^z_i \hat{S}^z_j \, | \uparrow_{i_{\text{ext}}} \rangle \big) + \text{tr}_L\big(\langle \downarrow_{i_{\text{ext}}} | \, e^{-\beta \hat{\mathcal{H}}_h} \hat{S}^z_i \hat{S}^z_j \, | \downarrow_{i_{\text{ext}}} \rangle \big) \\
\overset{(3.94)}{=}&\frac{1}{Z(h)+Z(-h)} \big[\text{tr}_L\big(e^{-\beta \hat{\mathcal{H}}(h)} \hat{S}^z_i \hat{S}^z_j\big) + \text{tr}_L\big(e^{-\beta \hat{\mathcal{H}}(-h)} \hat{S}^z_i \hat{S}^z_j\big) \big] \\
=&\frac{1}{Z(h)+Z(-h)} \big[\langle \hat{S}^z_i \hat{S}^z_j \rangle(h) + \langle \hat{S}^z_i \hat{S}^z_j \rangle(-h) \big] \\
=&\langle \hat{S}^z_i \hat{S}^z_j \rangle(h).
\end{aligned} \tag{3.96}
$$

The last step applies $\langle \hat{S}^z_i \hat{S}^z_j \rangle(h) = \langle \hat{S}^z_i \hat{S}^z_j \rangle(-h)$.

To summarize, we have shown that by coupling spins of a spin model $\hat{\mathcal{H}}_L$ to an external spin $\hat{S}^z_{i_{\text{ext}}}$ via an Ising interaction, we can relate spin correlations of the combined lattice and external spin model $\hat{\mathcal{H}}_h$ to spin correlations and local magnetizations of the lattice model coupled to a magnetic field $\hat{\mathcal{H}}(h)$. Once $\hat{\mathcal{H}}_h$ is solved, observables of $\hat{\mathcal{H}}(h)$ can be calculated straightforwardly. Note that the Ising interaction involving the external spin is global in contrast to the local interactions within the lattice. Ultimately, this is the reason why this approach of treating magnetic fields fails within PFFRG. The

explanation for this failure will be summarized in the following.

The Hartree term of the self-energy flow equation and the RPA term of the two-particle vertex flow equation both contain a site summation $\sum_j$. Since $\hat{S}^z_{i_{\text{ext}}}$ is coupled nonlocally in $\hat{\mathcal{H}}_h$ to each lattice site, these site summations generate a prefactor N, being the number of unit cells in the lattice, in front of the Hartree and RPA terms if site arguments of the computed vertices $\Sigma(1'|1)$ and $\Gamma(1',2'|1,2)$ fulfill $i_1 = i_{\text{ext}}$ or $i_2 = i_{\text{ext}}$. Since the PFFRG assumes a lattice of infinite extend $N \to \infty$, the two-particle vertex has to be rescaled if it contains i_{ext} at least once as an argument in order to obtain a convergent PFFRG solution. The rescaling is given by

$$\tilde{\Gamma}^{\rho\rho,\Lambda}_{i_{\text{ext}}i_{\text{ext}}} = N\Gamma^{\rho\rho,\Lambda}_{i_{\text{ext}}i_{\text{ext}}}, \tag{3.97}$$

$$\tilde{\Gamma}^{\rho\rho,\Lambda}_{i_{\text{ext}}i_L} = N\Gamma^{\rho\rho,\Lambda}_{i_{\text{ext}}i_L}, \tag{3.98}$$

$$\tilde{\Gamma}^{\rho\rho,\Lambda}_{i_Li_{\text{ext}}} = N\Gamma^{\rho\rho,\Lambda}_{i_Li_{\text{ext}}}, \tag{3.99}$$

with i_L being an arbitrary lattice site. This rescaling approach is similar to the approach that was pursued to compute the large S or large N solution of the PFFRG [32, 33]. At the beginning of the flow, the rescaled vertices are given by

$$\tilde{\Gamma}^{\rho\rho,\Lambda\to\infty}_{i_{\text{ext}}i_{\text{ext}}} = 0, \tag{3.100}$$

$$\tilde{\Gamma}^{\rho\rho,\Lambda\to\infty}_{i_{\text{ext}}i_L} = \frac{Nh}{2}\delta_{\rho z}, \tag{3.101}$$

$$\tilde{\Gamma}^{\rho\rho,\Lambda\to\infty}_{i_Li_{\text{ext}}} = \frac{Nh}{2}\delta_{\rho z}. \tag{3.102}$$

Since $N \to \infty$, the flow equations can only be solved for infinitesimal magnetic fields $h = \tilde{h}/N$. However, the response of a system to an infinitesimal magnetic field is already contained in its magnetic susceptibility at $h = 0$. One can conclude that the approach of this section to treat models with broken TRS does not allow the computation of any observables at finite magnetic fields if a lattice of infinite size is considered.

3.7 Considerations on the pseudo-fermion parquet equations

It was shown in Sec. 3.1.1 that the truncated FRG flow equation of $\Gamma^{\Lambda}(1',2'|1,2)$ can be understood as a simplification of the parquet equations. It is hence reasonable to ask whether one can circumvent the FRG scheme altogether and instead compute the pseudo-fermion self-energy and two-particle vertex at zero cutoff self-consistently to begin with by using the parquet equations and the self-energy SDE. We will explore this

question in the following and point out some hurdles that such an approach includes.

In order to compute $\Sigma(1'|1)$ and $\Gamma(1',2'|1,2)$ self-consistently, the BSE (2.42) has to be solved for each reducible vertex $\gamma_r(1',2'|1,2)$, with $r \in \{s,t,u\}$, and $\Sigma(1'|1)$ has to be obtained from another self-consistency equation, e.g., the SDE (2.32), in a combined scheme. Each, the self-consistency equations of γ_r and Σ, couple between each other since γ_r and Σ are both required as input in the SDE and BSE, i.e., the SDE requires γ_r, and the BSE of channel r requires Σ and $\gamma_{\bar{r}}$, with $\bar{r} \neq r$, as input. A strategy for obtaining a simultaneous solution for the SDE and BSE is to apply an algorithm that solves these equations iteratively until convergence is obtained for each solution [23, 24].

We continue by exploring how a BSE solution of a single channel $r \in \{s,t,u\}$ can be obtained under the assumption that $\Sigma(1'|1)$ is known. There are different approaches to solving the BSE for γ_r. As an approach, one may choose to iteratively set in γ_r on the right-hand side of Eq. (2.42). This leads to a series, as given by Eq. (2.47), which however may not converge. Alternatively, one can solve the BSE of a single channel r directly by applying a matrix inversion, starting from the matrix formulation of the BSE given by Eq. (2.42). This equation can be solved after setting in $\boldsymbol{\Gamma} = \boldsymbol{\gamma}_r + \boldsymbol{I}_r$ as

$$\boldsymbol{\gamma}_r = \frac{\boldsymbol{I}_r \circ \boldsymbol{\Pi}_r \circ \boldsymbol{I}_r}{\mathbb{1} - \boldsymbol{I}_r \circ \boldsymbol{\Pi}_r}. \tag{3.103}$$

Due to the matrix inversion, the numerical implementation for a solution of Eq. (3.103) is more involved than the previous iterative approach and requires numerically efficient matrix definitions for vertices. A trivial matrix notation, e.g., for $\gamma_t(1',2'|1,2)$ in the t-channel BSE of $\gamma_t(1',2'|1,2)$, would involve assigning a unique row index for each tuple $(1',1)$ of vertex arguments and a unique column index for each tuple $(2',2)$ (at $T = 0$ the frequency arguments have to be discretized for such a procedure). Note that valid matrix definitions differ between BSEs of different channels [compare Eq. (2.42) and Eqs. (2.43)-(2.45)]. More efficient matrix definitions that result in smaller matrix dimensions exist and make use of energy conservation and conservation of the transfer frequency r throughout the BSE Feynman diagrams of the r channel [55]. Furthermore, matrices may be defined even more efficiently within PFFRG by making use of the bilocality of γ_r.

Even though an implementation of the matrix inversion approach to solving the BSE is numerically demanding, we show in the following that it can allow for convergent solutions in cases where the alternative procedure of iteratively inserting γ_r into the BSE leads to a divergence. For this purpose, the analytical solution of the sole RPA channel will be considered.

RPA solution of the Bethe-Salpeter equation

The RPA self-consistency equation is obtained by only considering the RPA channel of the BSE and is given by

$$\begin{aligned}\gamma^{\rho\varphi}_{t,i_1i_2}(s,t,u) =& \frac{1}{2\pi}\int_{-\infty}^{\infty} d\omega' \sum_{abcdef} \\ &\times \sum_j I^{ab}_{t,i_1j}(\omega_{1'}+\omega', t, \omega_1-\omega')\Gamma^{cd}_{ji_2}(\omega_2+\omega', t, -\omega_{2'}+\omega') \\ &\times G^e_j(\omega'+t)G^f_j(\omega')\mathrm{tr}(\boldsymbol{\sigma}^b\boldsymbol{\sigma}^e\boldsymbol{\sigma}^c\boldsymbol{\sigma}^f)\delta_{a\rho}\delta_{d\varphi}. \end{aligned} \tag{3.104}$$

Since the s and u channels are neglected within the RPA, $\gamma_s = 0$ and $\gamma_u = 0$. The two-particle vertex solution obtained from Eq. (3.104) only exhibits a t frequency dependence. For simplicity, we will consider a Heisenberg model at zero magnetic field in the following. In this case, only diagonal vertex components $\gamma^{\rho\rho}_t$, $I^{\rho\rho}_t$ and $\Gamma^{\rho\rho}_t$ are finite. In case of the single-particle Green function, only the component $G^{\rho=0}$ is finite (see Table 3.2). It follows that Eq. (3.104) simplifies to

$$\gamma^{\rho\rho}_{t,i_1i_2}(t) = \frac{1}{\pi}\int_{-\infty}^{\infty} d\omega \sum_j I^{\rho\rho}_{t,i_1j}(t)\Gamma^{\rho\rho}_{ji_2}(t)\cdot G^0_j(\omega)G^0_j(\omega+t), \tag{3.105}$$

in which we have carried out the summation over indices $a,\ldots,f$ and simplified the frequency dependencies. From this expression it is apparent that the self-consistency equations for two-particle vertices $\gamma^{\rho\rho}_{t,i_1i_2}(t)$ and $\gamma^{\varphi\varphi}_{t,i_1i_2}(t')$ of different frequency arguments $t \neq t$ and indices $\rho \neq \varphi$ do not couple and hence we are able to continue by solely solving the equation for the static vertex and simplify the notation as $\gamma^{\mu\mu}_{t,i_1i_2}(t=0) \to \gamma_{t,i_1i_2}$. In the absence of a magnetic field, the RPA self-energy vanishes. To still obtain a converging frequency integral, one can introduce a finite pseudo-fermion lifetime constant d to the Green function such that

$$G^0_j(\omega) = \frac{1}{i[\omega + d\cdot\mathrm{sgn}(\omega)]}. \tag{3.106}$$

We assume d as site-independent for simplicity. The RPA self-consistency equation now reads as

$$\gamma_{t,i_1i_2} = -\sum_j I_{ti_1j}\Gamma_{ji_2}\cdot\frac{1}{\pi}\int_{-\infty}^{\infty} d\omega[\omega + d\cdot\mathrm{sgn}(\omega)]^{-2} \tag{3.107}$$

A Fourier transformation leads to the momentum $\boldsymbol{q}$ dependent expression

$$\begin{aligned} \gamma_t(\boldsymbol{q}) &= -CI(\boldsymbol{q})\Gamma(\boldsymbol{q}), \\ \text{with} \quad C &= \frac{1}{\pi}\int_{-\infty}^{\infty} d\omega[\omega + d\cdot\mathrm{sgn}(\omega)]^{-2} = \frac{2}{d}. \end{aligned} \tag{3.108}$$

Finally, application of the parquet decomposition, given by Eq. (2.37), results in the equation

$$\gamma_t(\boldsymbol{q}) = -CR(\boldsymbol{q})[R(\boldsymbol{q}) + \gamma_t(\boldsymbol{q})]. \tag{3.109}$$

Within parquet approximation, $R(\boldsymbol{q})$ is given by the momentum-dependent bare two-body interaction.

We explore the solution of Eq. (3.109) obtained by either "matrix" inversion or iterative insertion of $\gamma_t(\boldsymbol{q})$ in the following. Note that due to the reduced argument dependencies of vertices within RPA, matrix definitions of vertices become diagonal. It follows that the "matrix" inversion approach applied to Eq. (3.109) only has to deal with scalars instead. First, an exact solution obtained by "matrix" inversion is given by

$$\begin{aligned} \gamma_t(\boldsymbol{q}) &= -\frac{CR(\boldsymbol{q})^2}{1+CR(\boldsymbol{q})} \\ \overset{(2.37)}{\Longrightarrow}\ \Gamma(\boldsymbol{q}) &= \frac{1}{C+R(\boldsymbol{q})^{-1}}, \end{aligned} \tag{3.110}$$

which results in the static susceptibility

$$\chi^{zz}(\boldsymbol{q}) = \frac{1}{4[C^{-1}+R(\boldsymbol{q})]} \tag{3.111}$$

by the application of Eq. (3.64). The alternative approach consists of an iterative reinsertion of $\gamma_t(\boldsymbol{q})$ on the right-hand side of Eq. (3.109). Within RPA, this approach is equal to evaluating the geometric series

$$\Gamma(\boldsymbol{q}) = R(\boldsymbol{q})\sum_{n=0}^{\infty}[-CR(\boldsymbol{q})]^n \tag{3.112}$$

with the solution

$$\Gamma(\boldsymbol{q}) = \frac{1}{C+R(\boldsymbol{q})^{-1}} \quad \text{for} \quad |CR(\boldsymbol{q})| < 1. \tag{3.113}$$

Importantly, the iterative solution approach does not converge for $|CR(\boldsymbol{q})| \geq 1$ whereas the "matrix" inversion approach can still give a result. While we have demonstrated the different solution procedures only within RPA, the results show that iterative and "matrix" inversion solution strategies can have different advantages. While the iterative solution procedure is generally easier to numerically implement, one approach may

achieve a convergent solution in situations where the other does not.

Finally, we end the section with some closing remarks on the application of the parquet equations for pseudo-fermion models. It has been observed for Hubbard models that the difficulty in obtaining a simultaneous convergence of the SDE for the self-energy and the parquet equations increases with the interaction strengths of a model [23, 24]. These results suggest that solutions of the pseudo-fermion Hamiltonian of Eq. (3.21) may be difficult to converge as well if it is considered in the strongly interacting limit of small or zero magnetic fields h_i^μ. Indeed, for pseudo-fermion Hamiltonians with TRS ($h_i^\mu = 0$), the parquet equations were previously observed to converge only in presence of a finite cutoff Λ. The convergence is achieved easier for larger Λ. For Λ equal to or below the magnitude of the interactions of a model, convergence becomes challenging and generally not possible in the limit $\Lambda \to 0$ [36]. Thus, the parquet equations themselves are unsuitable for the study of spin models with TRS. However, in context of the PFFRG, the parquet equations still are useful, as they can be solved at large Λ to obtain vertices that can be applied as starting conditions of a PFFRG flow [36]. Furthermore, note that the parquet equations were previously only applied in the PFFRG for models without magnetic fields. Since the process of convergence for parquet-equation solutions has been observed to be improved in systems with weaker interactions [23, 24], it would be reasonable to investigate whether such an effect is observable in pseudo-fermion models as well upon the inclusion of finite magnetic fields.

3.8 Summary

The chapter began with a general introduction of the FRG method and related it to alternative schemes for the calculation of vertex functions, such as the Schwinger-Dyson equations and parquet equations. Afterwards, the PFFRG has been introduced as a FRG variant for the treatment of spin models that maps spins onto pseudo fermions. The mapping results in pseudo-fermion Hamiltonians that exhibit both physical symmetries, which are already present in the original spin model, and gauge symmetries, which are introduced by the pseudo-fermion mapping. The exploitation of these symmetries is crucial to make a numerical solution of the PFFRG flow equations feasible. Vertex function symmetries were derived for a spin model with arbitrary terms linear or bilinear in spin operators. Subsequently, suitable vertex parameterizations were proposed based on the resulting constrained vertex structures, allowing for a numerically efficient evaluation of the flow equations. Most importantly, the presented PFFRG formulation extends previous formulations to allow for the treatment of models with linear spin couplings to external magnetic fields.

The parameterized PFFRG flow equations for $\Sigma^{\Lambda}(1'|1)$ and $\Gamma^{\Lambda}(1', 2'|1, 2)$ were presented and discussed in detail. It was shown that the chosen vertex parameterizations allow simplified flow equations for models with continuous spin rotation symmetries or TRS to be obtained by simply constraining the values that summation indices in the flow equations can assume. The numerical feasibility of the PFFRG for models with broken TRS will be demonstrated in the next Chapter 4 by considering a variety of models with broken TRS. Some of these models will be absent of continuous spin rotation symmetries.

The PFFRG approaches to detect magnetic and nematic orders were discussed. Spontaneously broken symmetries were shown to manifest in susceptibility flow breakdowns at magnetic phase transitions within PFFRG. The type of magnetic order can then be inferred above the critical cutoff from the magnetic susceptibility. In contrast, due to the truncation of flow equations, the detection of nematic phases is only possible by calculating the response of a system to different symmetry breaking perturbations. It was further mentioned that the methodologically new capability to treat magnetic fields unlocks the new paradigm of detecting magnetic phases via their order parameter directly. This approach will be investigated in Chapter 4 for applications on two-dimensional Heisenberg models.

Near the end of the chapter, an alternative approach for treating TRS-breaking models within PFFRG was presented. Ultimately, this approach failed due to the presence of nonlocal interactions. Furthermore, possible solution strategies for the pseudo-fermion parquet equations were investigated. Since the truncated FRG flow equations and the parquet equations are closely related, the PFFRG method extension to treat models with broken TRS can analogously be applied to the pseudo-fermion parquet equations at minimum effort. Importantly, it had been observed in earlier studies that solutions for parquet equations are difficult to converge for strongly interacting models [23, 24]. In agreement with this observation, previous solutions of the pseudo-fermion parquet equations for models without magnetic fields were only achieved in presence of a finite frequency cutoff [36]. In future applications, the implementation of finite magnetic fields may allow to achieve solutions of the pseudo-fermion parquet equations even in absence of any cutoff.

Chapter 4

PFFRG at finite magnetic fields: Zero-field magnetizations, magnetization curves and magnetization plateaus

The theoretical foundation for the application of the PFFRG was provided in the previous chapter. In the remaining chapters of the thesis, the method will be applied to study a variety of spin models. The physical properties of the models considered in Chapters 5 and 6 are of recent interest. The models considered in these chapters are of the general form

$$\hat{\mathcal{H}} = \frac{1}{2}\sum_{ij}\sum_{\mu\nu} J_{ij}^{\mu\nu}\hat{S}_i^{\mu}\hat{S}_j^{\nu}. \tag{4.1}$$

They display high geometrical frustration and often have anisotropic interactions. Moreover, all of them fulfill TRS. Capabilities and limitations of the PFFRG in the study of such models that are given by Eq. (4.1) are well known, and the method is well established in their study [12]. In contrast, the PFFRG has been applied to models with broken TRS that are given by a general Hamiltonian

$$\hat{\mathcal{H}} = \frac{1}{2}\sum_{ij}\sum_{\mu\nu} J_{ij}^{\mu\nu}\hat{S}_i^{\mu}\hat{S}_j^{\nu} - \sum_{i}\sum_{\mu} h_i^{\mu}\hat{S}_i^{\mu} \tag{4.2}$$

just recently [39]. We presented the PFFRG formulation for the treatment of such models in the previous Chapter 3. In this chapter, we will shed light on this so far less explored PFFRG application to models with broken TRS. To this end, the content of this chapter will follow along our recent paper of Ref. [39], which explores $S = 1/2$ applications on models with broken TRS for the general PFFRG formulation given

in Chapter 3. More specifically, the regularization of PFFRG flow breakdowns at magnetic phase transitions will be demonstrated and the resulting flows will be studied. A subsequent study of magnetic order parameters in the limit $\Lambda \to 0$ is thus enabled, allowing for quantitative comparisons with literature values. In addition, the chapter will provide new insights on finite-field applications as well by investigating whether the method is suited for the study of magnetization curves and, in particular, magnetization plateaus.

Throughout the chapter, magnetic fields will be subdivided conceptually into a site-dependent perturbative seed field $\delta \boldsymbol{n}_i$, which is applied for the regularization of a susceptibility divergence caused by a magnetic phase transition, and a nonperturbative global component h oriented along the z axis, which can be interpreted as an external magnetic field. The Hamiltonians of this chapter are of the general form

$$\hat{\mathcal{H}} = \sum_{\langle ij \rangle} J^{\mu\mu} \hat{S}_i^{\mu} \hat{S}_j^{\mu} - h \sum_i \hat{S}_i^z - \delta \sum_i \boldsymbol{n}_i \cdot \hat{\boldsymbol{S}}_i. \tag{4.3}$$

All models considered only contain nearest-neighbor interactions that are either of Heisenberg ($J_{ij}^{xx} = J_{ij}^{yy} = J_{ij}^{zz}$) or XXZ ($J_{ij}^{xx} = J_{ij}^{yy} \neq J_{ij}^{zz}$) type. We use the simplified notation $J^{\mu\mu} = J$ in case a Heisenberg model is considered. The seed field will be applied with normalized vectors $|\boldsymbol{n}_i| = 1$ and with $\delta \ll |J^{\mu\mu}|$. To achieve the regularization of a susceptibility divergence, the seed field is chosen to break all symmetries of a model that would otherwise be broken spontaneously by a magnetic order. To this end, $\delta \boldsymbol{n}_i$ will always be oriented along the site-dependent magnetization of a predicted magnetic ground state unless stated otherwise. E.g., it will be applied colinearly and with an alternating sign in the case of antiferromagnetic order on the square-lattice antiferromagnetic Heisenberg model, and in angles of 120° on the triangular-lattice antiferromagnetic Heisenberg model, which assumes so-called 120° order.

The chapter is structured as follows. Models in absence of global magnetic fields ($h = 0$) will be treated first. Sec. 4.1 will treat magnetically ordered phases on the two-dimensional square, honeycomb and triangular lattices. By applying perturbative seed fields to nearest-neighbor Heisenberg models, flow breakdowns will be regularized, which allows a subsequent study of magnetically ordered phases in the physically relevant limit at $\Lambda \to 0$ and $\delta \to 0$. Zero-field magnetizations will be compared to literature values, and the stability of magnetic orders with respect to different choices of seed fields will be studied. The following Section 4.2 will investigate PFFRG applications at finite magnetic fields h beyond the perturbative regime. As a pedagogical example, the magnetization curve of the antiferromagnetic Heisenberg model on the square lattice will be resolved and compared to literature results. Note that Sec. 4.1 and 4.2 cover content of Ref. [39]. In contrast, Sec. 4.3 goes beyond previously published results and

explores whether the PFFRG can be applied successfully in the study of magnetization plateaus. Such plateaus are stabilized by quantum fluctuations [1] and are predicted in the magnetization curves of the $S = 1/2$ antiferromagnetic Heisenberg models on a dimer and pyrochlore lattice [56, 57], and the $S = 1/2$ XXZ model on the triangular lattice [58, 59]. The conceptually different ground states of these magnetization plateaus will allow for a more comprehensive study of the extent to which magnetization plateaus are captured by PFFRG. While the plateau state of the latter model is given by a classical magnetic order exposed to quantum fluctuations, the plateaus studied in the former two models are not built by states with classical interpretations. Finally, the chapter will be concluded in Sec. 4.4 with a general discussion on the PFFRG treatment of spin models with broken TRS.

The PFFRG is applied with the following specifications in this chapter. Two-particle vertices are computed on a frequency grid with 76^3 transfer frequencies for models on the triangular and pyrochlore lattice. This number changes to 92^3 for the remaining lattice models, and to 200^3 for the antiferromagnetic dimer. For any model, the self-energy is given out for 2000 frequencies. Considered frequencies are distributed exponentially around the zero frequency. If not explicitly stated otherwise, correlations on square and triangular lattice models are neglected beyond distances of $L = 5$ nearest-neighbor spacings. On the pyrochlore lattice, correlations beyond $L = 4$ nearest-neighbor spacings are neglected. An explicit embedded Runge-Kutta $(2, 3)$ method with an adaptive step size, implemented using the library Ref. [60], is applied to solve the flow equations for any model. The numerical PFFRG implementation used for the computation of the magnetization curve of the XXZ model on the triangular lattice is made available in Ref. [61].

4.1 Flow regularization and study of magnetic ground states

To demonstrate and investigate the regularization of PFFRG flows for magnetically ordered models with $h = 0$, the method will be applied to the two-dimensional nearest-neighbor Heisenberg models on the square, honeycomb and triangular lattices. For the square lattice, both the ferromagnetic ($J < 0$) and antiferromagnetic ($J > 0$) models will be considered, whereas only the antiferromagnetic case will be considered for models on the remaining lattices. All models are solved for the quantum case $S = 1/2$. At first, only the square-lattice Heisenberg model will be studied to investigate the flow regularization process in detail. Afterwards, all mentioned Heisenberg models will be considered in a quantitative study of magnetic order parameters in the limit

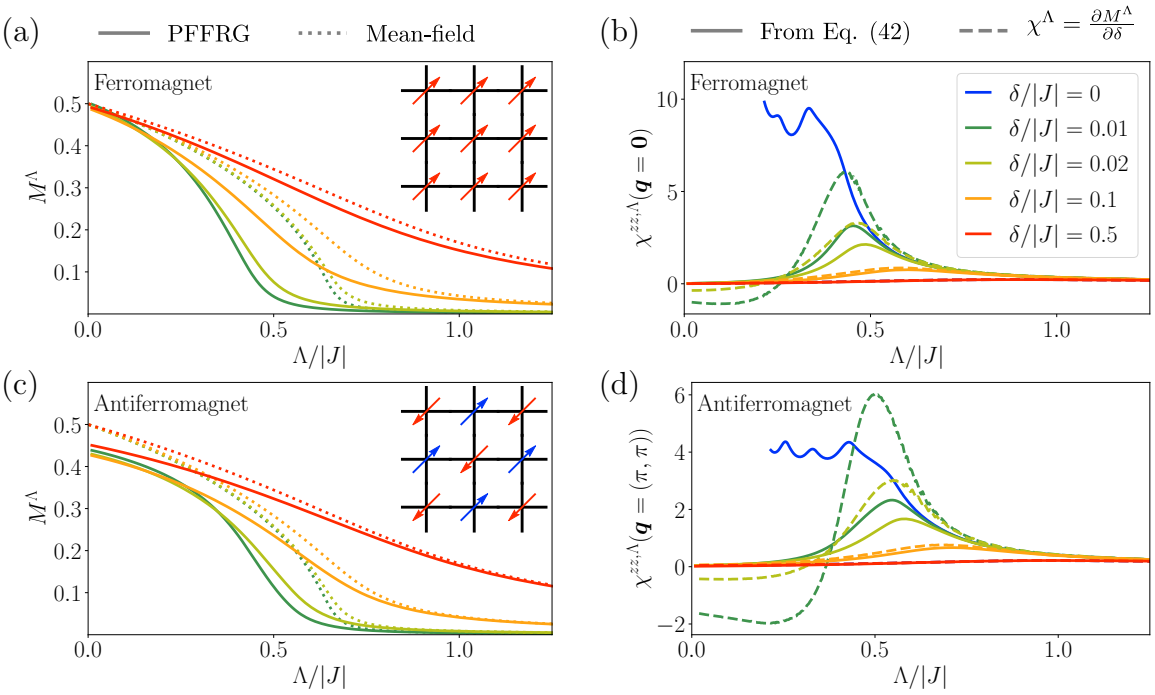

Figure 4.1: (a), (c) Magnetization $M^\Lambda = |\boldsymbol{M}_i^\Lambda|$ as a function of Λ for the (a) ferromagnetic and (c) antiferromagnetic square-lattice Heisenberg model. Full (dotted) lines correspond to PFFRG (mean-field) results. Different colors correspond to different strengths of seed fields ($\delta/|J| = 0$, 0.01, 0.02, 0.1 and 0.5), see legend in subfigure (b), which applies to all subfigures. Seed fields are oriented parallel or antiparallel to the z axis according to the insets. (b), (d) Longitudinal order parameter susceptibilities $\chi^{zz,\Lambda}(\boldsymbol{q})$ as a function of Λ for the (b) ferromagnetic and (d) antiferromagnetic square-lattice Heisenberg model where $\boldsymbol{q} = \boldsymbol{0}$ and $\boldsymbol{q} = (\pi, \pi)$, respectively. Full lines are PFFRG results derived from Eq. (3.64) while dashed lines are derived from $\chi^\Lambda = \partial M^\Lambda / \partial \delta$. In the latter approach, δ-derivatives are approximated by the variation of M^Λ when δ is varied by 10%. The smaller of these δ values is that of the legend of (b). The figure and its caption are replicated from Ref. [39].

$\Lambda \to 0$.

PFFRG magnetization and susceptibility flows for the ferromagnetic and antiferromagnetic Heisenberg models on the square lattice are shown in Fig. 4.1 for different seed field sizes $\delta/|J|$. The flows of susceptibilities $\chi^{zz,\Lambda}(\boldsymbol{q} = \boldsymbol{0})$ and $\chi^{zz,\Lambda}(\boldsymbol{q} = (\pi, \pi))$ are shown in Fig. 4.1(b) and 4.1(d), with $\boldsymbol{q}$ corresponding to the respective position of the magnetic Bragg peak. Flow breakdowns in the form of a kink are caused by a magnetic phase transition in case $\delta/|J| = 0$. At cutoffs below the kink, the flows are unphysical. At finite seed field sizes $\delta/|J| \geq 0.01$, the flows are regularized and a susceptibility maximum is formed at the phase transition instead. Consequently, smooth flows down the $\Lambda \to 0$ are achieved. At smaller but finite seed field sizes $\delta/|J| < 0.01$ (not shown in the figure), numerical instabilities can cause flow breakdowns to reappear. Simultaneously, seed fields of small sizes $\delta/|J|$ are generally desired in the study of magnetic orders, since seed fields introduce an energetic bias that is proportional to

$\delta/|J|$ and favors spin orientations along $\boldsymbol{n}_i$. For this reason, a numerical implementation of the PFFRG with a high stability that allows for small $\delta/|J|$ is desired. The PFFRG implementations of this chapter always achieved a successful flow regularization in case $\delta/|J| \geq 0.02$ for the models considered in Sec. 4.1 and 4.2. Similar to the response of a temperature-dependent susceptibility at a magnetic phase transition to a finite magnetic field $\delta/|J|$, susceptibility peaks in Figs. 4.1(b) and 4.1(d) are suppressed, broadened and shifted to larger Λ if $\delta/|J|$ is increased. However, note that the two-dimensional models considered exhibit a continuous spin rotation symmetry even in presence of a finite $\delta/|J|$. It follows from the Mermin-Wagner theorem that they should not exhibit a magnetic phase transition at finite T or Λ. The presence of a phase transition at finite Λ in the ($T = 0$) PFFRG flow is an artifact resulting from the truncation of flow equations and is therefore inherent to the method.

Flows of the absolute magnetization $M^\Lambda = |\boldsymbol{M}_i|$ are shown in Figs. 4.1(a) and 4.1(c), again for different sizes of $\delta/|J|$. In the limit $\delta/|J| \to 0$, the exact M^Λ is expected to become finite at the critical cutoff Λ_c of the magnetic phase transition. Indeed, such a sharp transition appears to be approached with decreasing $\delta/|J|$. Vice versa, with increasing $\delta/|J|$ the absolute curvature $|\partial^2 M^\Lambda/\partial\Lambda^2|$ of the M^Λ flow at Λ_c decreases and the buildup of M^Λ about Λ_c is extended over a larger interval in Λ. Magnetization flows within the (mean-field) Hartree approximation are shown as dotted lines. A comparison with the PFFRG flows reveals that the presence of quantum fluctuations, which is captured by PFFRG, leads to magnetic phase transitions at smaller cutoffs. Furthermore, quantum fluctuations are observed to reduce $M^{\Lambda\to 0}$ in the antiferromagnetic Heisenberg model from its saturated mean-field value of $M_{\mathrm{mf}} = 1/2$.

At small Λ, the shown flows exhibit artifacts that stem from the numerical PFFRG implementation. The magnetization $M^{\Lambda\to 0}$ is expected to increase monotonically with increasing seed field size $\delta/|J|$. This is not the case in the magnetization flows of Figs. 4.1(a) and 4.1(c). E.g., in magnetization flows of the antiferromagnetic model, a larger $M^{\Lambda\to 0} = 0.438$ is achieved for $\delta/|J| = 0.01$ than for the larger seed field of size $\delta/|J| = 0.1$, in which case $M^{\Lambda\to 0} = 0.426$ is obtained. We interpret this unphysical artifact to be caused by oscillatory artifacts in the frequency dependence of vertex functions, which generally emerge at small Λ of approximately the size of J. If this interpretation is correct, the artifact should be cured by an advanced numerical PFFRG implementation as described in Ref. [36].

While PFFRG applications on models with TRS only allow for the computation of magnetic susceptibilities χ^Λ via the two-particle vertex, the consideration of models with broken TRS enables the computation of χ^Λ from the self-energy alone. While the former approach accesses χ^Λ from spin correlations given by Eq. (3.64), the latter

approach takes the derivative of the magnetization, obtained from the self-energy via Eq. (3.61), with respect to a magnetic field. In our case, this field is given by the seed field $\delta\boldsymbol{n}$, which is aligned with the underlying order. The magnetic susceptibility is then given by $\chi^\Lambda = \partial M^\Lambda/\partial\delta$. Both approaches of computing χ^Λ are compared in Figs. 4.1(b) and 4.1(d). The respective flows are either shown as solid or dashed lines. For an exact solution, which would be obtained by solving the untruncated flow equations, both approaches to computing χ^Λ should give identical results. The same is true for so-called conserving approximations such as the Hartree and random-phase approximation [62, 63]. However, the Katanin truncation scheme applied within PFFRG is not a conserving approximation. As such, it leads to deviating results depending on the scheme by which the susceptibility is computed. It can be observed that the agreement between susceptibility flows improves with increasing δ or Λ, suggesting higher quality results for larger δ or Λ. Vice versa, at small δ/J, the difference between χ^Λ values builds up as Λ flows close to the magnetic phase transition, coming down from large Λ values. This difference remains large down to $\Lambda \to 0$. Note that $\chi^\Lambda = \partial M^\Lambda/\partial\delta$ becomes negative at small δ and Λ as a consequence of the previously mentioned nonmonotonic behavior of M^Λ in δ.

4.1.1 Zero-field magnetizations

The previously demonstrated successful regularization of PFFRG flows by seed fields of size δ enables the computation of $T = 0$ magnetizations in the limit $\Lambda \to 0$. Magnetizations of this limit will be studied in the following for Heisenberg models on the square, honeycomb, and triangular lattice. The aim of the study is to investigate whether PFFRG correctly predicts magnetic order parameters both on a qualitative and quantitative level.

First, it should be noted that PFFRG captures well the saturated magnetization $M^{\Lambda\to 0} = 1/2$ of the ground state of the ferromagnetic Heisenberg model on the square lattice, as shown in Fig. 4.1(a). Furthermore, magnetization flows of the antiferromagnetic model on the same lattice, shown in Fig. 4.1(c), confirm that PFFRG captures the reduction of the magnetization by quantum fluctuations in the antiferromagnetic ground state by measuring a reduced magnetization $M^{\Lambda\to 0} < 1/2$. This qualitative observation provides reason to now quantitatively study to which extent quantum-fluctuation-induced suppressions of magnetizations are captured within PFFRG. A systematic study of this subject is provided by Fig. 4.2, which considers $M^{\Lambda\to 0}$ in dependence on the maximum considered correlation distance L for a variety of two-dimensional nearest-neighbor Heisenberg models. In addition to Heisenberg models on the square lattice, antiferromagnetic Heisenberg models on the honeycomb

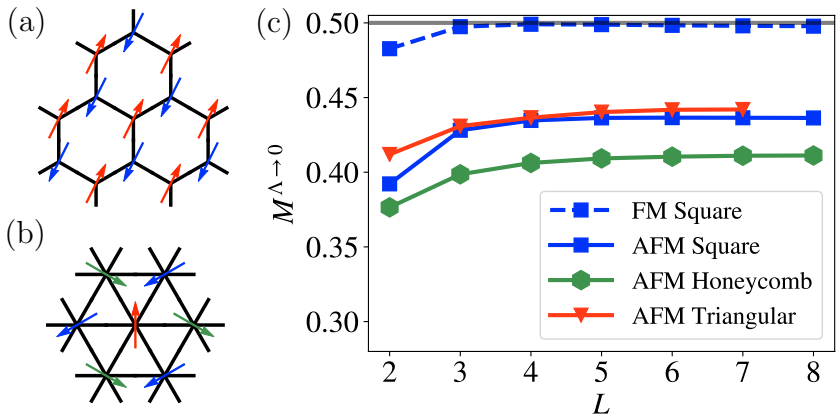

Figure 4.2: (a) Néel order on the honeycomb lattice. (b) Three sublattice 120° Néel order. Different sublattices are distinguished by different colors of the spins. (c) Magnetization $M^{\Lambda\to 0}$ in the small-Λ limit as a function of system size L, for the ferromagnetic Heisenberg model on the square lattice as well as for the antiferromagnetic Heisenberg models on the square, honeycomb and triangular lattices. Here, L is defined as the maximum distance of spin-spin correlations (in units of the lattice constant), while longer distance spin-spin correlations are treated as zero. The magnetizations shown are obtained at cutoffs $\Lambda/J = 0.02$, except for the square lattice ferromagnet where $\Lambda/J = 0.01$ is used. Seed fields are of size $\delta/J = 0.01$ on the square lattice, and of size $\delta/J = 0.02$ on the honeycomb and triangular lattices. The figure and its caption are replicated from Ref. [39].

and triangular lattices are considered as well. Both the antiferromagnetic model on the square and honeycomb lattice realize a colinear Néel ground state due to the bipartite structure of the lattices, as visualized in Figs. 4.1(c) and 4.2(a). In the presence of finite seed fields, these models still exhibit a global U(1) spin rotation symmetry about the magnetization axis, which allows for an efficient numerical treatment via PFFRG. On the other hand, the antiferromagnetic Heisenberg model on the triangular lattice enforces geometrical frustration. As a consequence, the $S = 1/2$ model realizes a coplanar 120° magnetic order in which spins are arranged in angles of 120° on three magnetic sublattices, as visualized in Fig. 4.2(b). A regularized PFFRG flow into this kind of order requires a site-dependent seed field that breaks any continuous spin rotation symmetry of the pure Heisenberg model. Since no continuous global spin rotation symmetry remains in the resulting model, a numerical treatment requires more numerical resources at a similar maximum correlation distance L. For this reason, the point $L = 8$ has not been computed for the Heisenberg model on the triangular lattice in Fig. 4.2(c).

Magnetizations are observed to converge already at numerically accessible maximum correlation distances of $L \approx 5$ for all considered Heisenberg models. At the largest considered correlation distances, a magnetization of $M^{\Lambda\to 0} \approx 0.436$ is found for the antiferromagnetic square lattice, $M^{\Lambda\to 0} \approx 0.411$ for the honeycomb lattice, and $M^{\Lambda\to 0} \approx$

0.442 for the triangular lattice. A comparison with literature values reveals that PFFRG magnetizations are systematically overestimated. On the square and honeycomb lattices, quantum Monte Carlo (qMC) predicts values of $M = 0.3075(25)$ [64] and $M = 0.22(3)$ [65] respectively. On the triangular lattice, the sign problem prevents the application of qMC. A magnetization of $M = 0.205(15)$ is provided by variational Monte Carlo (vMC) and DMRG instead [66, 67, 68]. While the overestimation of PFFRG magnetizations implies an underestimation of quantum fluctuations, such a systematic underestimation is generally not observed in PFFRG applications on spin models with TRS. E.g., paramagnetic regimes obtained by PFFRG show good agreement with competing methods in the Heisenberg-Kitaev model [69], the J_1-J_2 square-lattice Heisenberg model [11], the Shastry-Sutherland model [70] and the non-Kramers nearest-neighbor pyrochlore model [71].

To gain a better understanding of the observed systematic overestimation of $M^{\Lambda\to 0}$ within PFFRG, we take a closer look at the evolution of magnetizations along the PFFRG flows. Of major importance for a correct magnetization at $\Lambda \to 0$ is the correct buildup of M^Λ across the phase transition at $\Lambda \approx \Lambda_c$. The magnetic phase transition causes M^Λ to experience a large increase over a relatively short interval in Λ from values $M^\Lambda \approx 0$ (note that M^Λ is small but finite at $\Lambda > \Lambda_c$ due to finite seed fields $\delta > 0$) towards a size close to $M^{\Lambda\to 0}$. Simultaneously, the spin correlations become long-range at $\Lambda \approx \Lambda_c$. The spreading of correlations results in dominant contributions from the Hartree and RPA channels of the flow equations, since only these terms include a site summation $\sum_j$ [see Eqs. (3.53)-(3.54)]. As a consequence, the flow at $\Lambda \approx \Lambda_c$ is mostly determined by the RPA and Hartree channels. However, these channels are known to reproduce a mean-field approximation if they are considered by themselves (see Sec. 3.5.5). It follows that PFFRG flows across magnetic phase transitions suffer from a mean-field bias, which is known to result in systematically overestimated magnetizations. While the build-in mean-field bias at the phase transition gives a reasonable explanation for systematically overestimated magnetizations, further study is needed to confirm whether this explanation actually holds. Note that the incorrect buildup of M^Λ at $\Lambda \approx \Lambda_c$ is already hinted at by the discrepancies between susceptibility flows in Figs. 4.1(b) and 4.1(d), either computed from $\chi^\Lambda = \partial M^\Lambda / \partial \Lambda$ or from spin correlations, that emerge at $\Lambda \approx \Lambda_c$ as well.

4.1.2 Robustness of magnetic order under different choices of seed fields

We now study the robustness of magnetic order under different choices of seed field configurations $\delta \boldsymbol{n}_i$. In particular, we will consider the robustness of the 120° order of

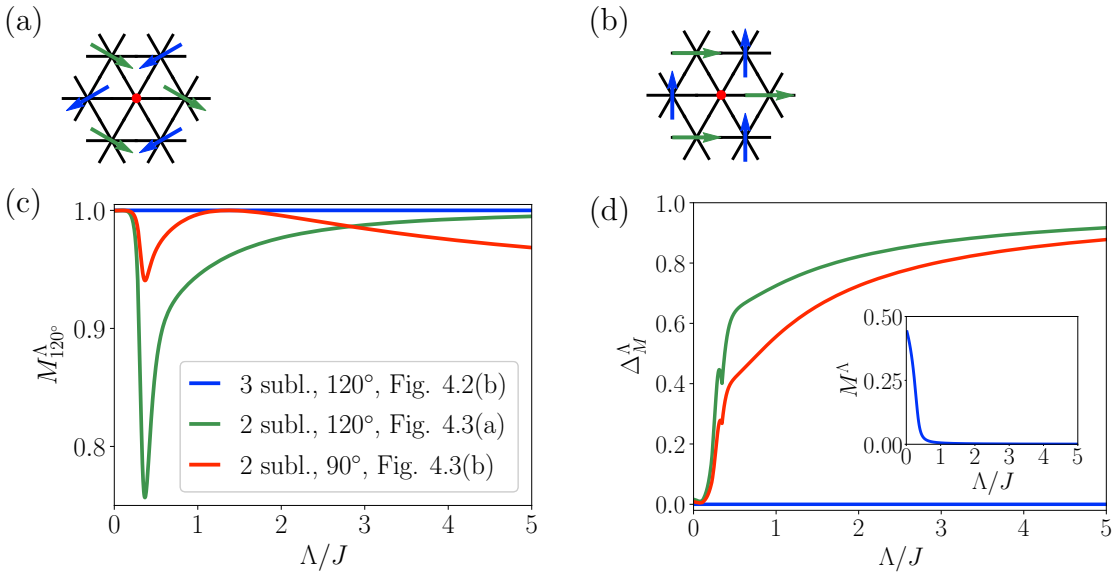

Figure 4.3: (a), (b) Two choices of seed fields $\delta \boldsymbol{n}_i$ deviating from a 120° Néel pattern on the triangular lattice. Red dots indicate vanishing amplitudes δ on this sublattice. On the other two sublattices with identical δ, the arrows depict the directions of $\boldsymbol{n}_i$, which either enclose (a) angles of 120° or (b) angles of 90°. (c) $M^{\Lambda}_{120^\circ}$ defined in Eq. (4.4) as a function of Λ for the two seed fields of the triangular-lattice Heisenberg antiferromagnet in (a) and (b) and for the perfect 120° seed field in Fig. 4.2(b). (d) Δ^{Λ}_{M} defined in Eq. (4.5) as a function of Λ for the same seed fields as considered in (c). The inset in (d) shows the magnetization M^{Λ} of the triangular-lattice Heisenberg antiferromagnet as a function of Λ for the ideal seed fields illustrated in Fig. 4.2(b). The figure and its caption are replicated from Ref. [39].

the antiferromagnetic Heisenberg model on the triangular lattice. In the PFFRG implementation of Fig. 4.2(c), the seed field had been oriented along the spin orientations of the classical 120° order, as visualized in Fig. 4.2(b). However, to regularize flow breakdowns, seed fields generally only need to fulfill the property that they break all symmetries of a model that are otherwise broken spontaneously at its magnetic phase transition. In other words, the regularization of PFFRG flows only requires knowledge of which symmetries the magnetic order of a model breaks, and not knowledge of the magnetic order itself.

We investigate this property of the method along the Heisenberg model on the triangular lattice by applying two alternative seed field choices in Fig. 4.3 that exert a finite δ on only two magnetic sublattices. The orientations $\boldsymbol{n}_i$ on these sublattices either enclose an angle of 90° or 120°, as visualized in Figs. 4.3(a) and 4.3(b). Note that these alternative seed fields break more symmetries than the 120° magnetic order. The site-dependent magnetization along the PFFRG flow is studied for each choice of seed field. For this purpose, two observables are computed that quantify the deviation of the site-dependent magnetization from an ideal magnetization of a 120° order. $M^{\Lambda}_{120^\circ}$ is the first such observable and probes the angles between magnetizations $\boldsymbol{M}^{\Lambda}_{i\in\gamma}$ of different

sublattices $\gamma \in \{A, B, C\}$. It is defined by

$$M^{\Lambda}_{120^\circ} = \frac{2}{3\sqrt{3}} |\boldsymbol{m}^{\Lambda}_{A} \times \boldsymbol{m}^{\Lambda}_{B} + \boldsymbol{m}^{\Lambda}_{B} \times \boldsymbol{m}^{\Lambda}_{C} + \boldsymbol{m}^{\Lambda}_{C} \times \boldsymbol{m}^{\Lambda}_{A}|, \tag{4.4}$$

with the normalized magnetization vector $\boldsymbol{m}^{\Lambda}_{\gamma} = \boldsymbol{M}^{\Lambda}_{i\in\gamma}/|\boldsymbol{M}^{\Lambda}_{i\in\gamma}|$. The quantity $M^{\Lambda}_{120^\circ}$ measures how close $\boldsymbol{m}^{\Lambda}_{\gamma}$ are oriented in accordance with an ideal 120° order, which is coplanar and has spins oriented in angles of 120° on different sublattices. Only in case of a perfect agreement of spin orientations with 120° order does $M^{\Lambda}_{120^\circ}$ assume a maximum value of $M^{\Lambda}_{120^\circ} = 1$. Δ^{Λ}_{M} is the second considered observable and probes differences in magnitude of $\boldsymbol{M}^{\Lambda}_{i\in\gamma}$ for different γ. It is defined by

$$\Delta^{\Lambda}_{M} = \frac{M^{\Lambda}_{\max} - M^{\Lambda}_{\min}}{M^{\Lambda}_{\max}}, \tag{4.5}$$

with the maximum magnetization amplitude $M^{\Lambda}_{\max} = \max\{|\boldsymbol{M}^{\Lambda}_{i\in A}|, |\boldsymbol{M}^{\Lambda}_{i\in B}|, |\boldsymbol{M}^{\Lambda}_{i\in C}|\}$ and minimum magnetization amplitude $M^{\Lambda}_{\min} = \min\{|\boldsymbol{M}^{\Lambda}_{i\in A}|, |\boldsymbol{M}^{\Lambda}_{i\in B}|, |\boldsymbol{M}^{\Lambda}_{i\in C}|\}$. Δ^{Λ}_{M} is given by $\Delta^{\Lambda}_{M} = 0$ for an ideal 120° order with $|\boldsymbol{M}^{\Lambda}_{i\in A}| = |\boldsymbol{M}^{\Lambda}_{i\in B}| = |\boldsymbol{M}^{\Lambda}_{i\in C}|$. In summary, a perfect agreement of site-dependent magnetization with an ideal 120° order is signified by $M^{\Lambda}_{120^\circ} = 1$ and $\Delta^{\Lambda}_{M} = 0$.

PFFRG flows of $M^{\Lambda}_{120^\circ}$ and Δ^{Λ}_{M} are shown in Figs. 4.3(c) and 4.3(d) for the different choices of seed fields. For context, the magnetization flow, which exhibits a magnetic phase transition at $\Lambda/J \approx 0.33$, is shown as an inset in Fig. 4.3(d). Flows of the models with seed fields only applied on two sublattices begin at $\Delta^{\Lambda\to\infty} = 1$. At Λ_c, these flows exhibits a sharp decrease of Δ^{Λ} as it approaches a value of $\Delta^{\Lambda} \approx 0$ in the limit $\Lambda \to 0$. For the same models, ideal values of $M^{\Lambda}_{120^\circ} \approx 1$ are already achieved at $\Lambda > \Lambda_c$ in the flows of $M^{\Lambda}_{120^\circ}$. However, intermediate decreases leading to a local minimum in $M^{\Lambda}_{120^\circ}$ are observed at the phase transition at smaller $\Lambda = \Lambda_c$. These observed minima give another example of error generation at Λ_c in addition to the previously discussed systematic error generation in M^{Λ} corresponding to a mean-field bias. However, values of $M^{\Lambda}_{120^\circ} \approx 1$ are recovered in the limit $\Lambda \to 0$. Regardless of the applied seed field choice, flows of $M^{\Lambda}_{120^\circ}$ and Δ^{Λ} are observed to closely approach values expected for an ideal 120° order in the limit $\Lambda \to 0$. This observation confirms that in a PFFRG study the 120° order of the Heisenberg model on the triangular lattice is robust under the application of different seed fields. More generally, the stability of magnetic order with respect to different seed field choices justifies the application of flow-regularizing seed fields $\delta\boldsymbol{n}$ that do not coincide with $\boldsymbol{M}_i$ orientations of an underlying magnetic order. Instead, the seed fields only have to break the same lattice symmetries as a magnetic order does, and can optionally break additional symmetries as well.

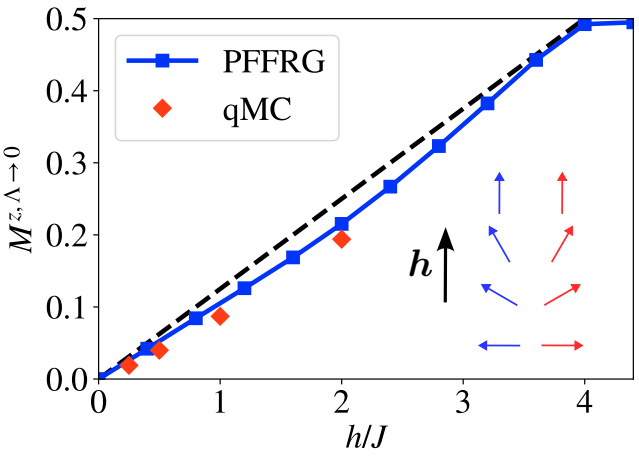

Figure 4.4: Blue squares show the magnetization $M^{z,\Lambda\to 0}$ from PFFRG of the antiferromagnetic Heisenberg model on the square lattice as a function of the homogeneous field strength h, linearly extrapolated to zero seed fields, $\delta \to 0$. For comparison, red diamonds are qMC results from Ref. [72]. The dashed black line is the linear classical magnetization curve. The inset illustrates the magnetization process schematically, where red and blue arrows depict spins on the two sublattices in a field $\boldsymbol{h}$ that increases from bottom to top. The figure and its caption are replicated from Ref. [39].

4.2 Magnetization curve of the antiferromagnetic Heisenberg model on a square lattice

We continue by treating models with finite global magnetic fields of size $h > 0$, again described by the Hamiltonian of Eq. (4.3). The conceptually simple magnetization curve of the nearest-neighbor antiferromagnetic Heisenberg model on the square lattice will be resolved as a first such PFFRG application. The expected behavior of the model will be described in the following. The magnetization curve of the square-lattice Heisenberg model is already well studied [73, 72, 74, 75] and is known to be built by a ground state with a two-site unit cell. A schematic visualization of the continuous ground state evolution along the magnetization curve is shown as inset in Fig. 4.4. At $h \ll J$, the spins align antiferromagnetically and perpendicularly to the external magnetic field $\boldsymbol{h} = (0, 0, h)$. Since we apply the magnetic field along the z axis, the spins will order in the x-y plane at $h \ll J$. The spins then continuously cant towards the z axis as h increases in magnitude until they are ferromagnetically aligned at $h \geq 4J$, resulting in a saturated magnetization along the z axis of $M^z = 1/2$. In other words, the $\hat{S}_i^z$ spin components order ferromagnetically, whereas components $\hat{S}_i^x$ and $\hat{S}_i^y$ order antiferromagnetically throughout the magnetization curve. While M^z increases linearly with h for $h \in [0, 4J]$ in the classical model, being given by $M^z_{\mathrm{cl}} = \frac{h}{8J}$, a qualitative feature of the magnetization curve of the quantum model is an upward curvature that arises from a gradual suppression of zero-point fluctuations with increasing h [75].

Since the ground state breaks U(1) spin rotation symmetry about the z axis for $0 < h < 4J$, a seed field $\delta \boldsymbol{n}_i$ needs to be applied in addition to the global magnetic field h to access the magnetically ordered phase within PFFRG. We choose a staggered seed field perpendicular to the z axis, i.e., $\boldsymbol{n}_i \perp (0, 0, 1)$, in accordance with the antiferromagnetic arrangement of spin components in the x-y plane. The obtained PFFRG magnetization curve is shown in Fig. 4.4 along with data points previously obtained by qMC in Ref. [72]. The curve will be discussed in the following. The expected qualitative behavior of the magnetic ground state is successfully resolved by PFFRG along the full magnetization curve. An upward curvature is observed that, however, is less pronounced than predicted by qMC. This implied underestimation of quantum fluctuations by PFFRG had already been observed in Sec. 4.1 in the study of Heisenberg models at $h = 0$, where it leads to underestimated reductions of staggered magnetizations $M^{\Lambda\to 0}$ from their classical values of $M_{\mathrm{cl}} = 1/2$. In the Heisenberg model on the square lattice at $h = 0$, the resulting difference $M_{\mathrm{cl}} - M^{\Lambda\to 0}$ amounts to only 33% of the reduction predicted by qMC [64]. In comparison, the reduction of $M^{z,\Lambda\to 0}$ in the present magnetization curve from its classical value of $M^z_{\mathrm{cl}} = 1/4$ at $h = 2J$, expressed by $M^z_{\mathrm{cl}} - M^{z,\Lambda\to 0}$, amounts to 71% of the value predicted by qMC [72]. At small J/h, at which a model can be treated by perturbation theory, PFFRG results are expected to be more precise since the method is known to replicate perturbation theory up to second order in J/h [12]. Thus, the higher precision of $M^{\Lambda\to 0}$ at $h = 2J$ may be a consequence of the method already benefitting from this perturbative error control. In the same context, it is no surprise that PFFRG predicts the saturation of M^z at even larger $h/J \approx 4.0$ accurately. As an alternative confirmation of the magnetization curve's upper boundary, the spontaneously broken U(1) spin rotation symmetry of the magnetic ground state is observed to result in a flow breakdown at $h/J \leq 3.8$ in case no flow regularizing seed field is present.

4.3 Detection of magnetization plateaus

The previous application on the square-lattice Heisenberg model at finite h demonstrated that PFFRG can be applied in the study of magnetization curves. However, the studied magnetization curve was conceptually quite simple due to the absence of geometrical frustration in the underlying model. The curve was built by a classical magnetic order on two sublattices, with its only characteristic feature being an upward curvature caused by the gradual suppression of quantum fluctuations with increasing h. In the following, we transition to the study of magnetization curves of (mostly) geometrically frustrated models in order to investigate whether PFFRG is suited for the study of magnetization plateaus.

Magnetization plateaus are a phenomenon realized by frustrated quantum spin models in which quantum fluctuations create an energy gap that stabilizes a ground state with constant magnetization M^z over a finite interval in external magnetic field size h [1]. To study the detection of magnetization plateaus within PFFRG, the method will be applied to the antiferromagnetic dimer, the nearest-neighbor antiferromagnetic Heisenberg model on the three-dimensional pyrochlore lattice, and the nearest-neighbor antiferromagnetic XXZ model with interactions $J^{xx} = J^{yy} > 0$ and $J^{zz} > 0$ on the triangular lattice. The fundamentally different structures of plateau states in these models allow for a versatile study of the phenomenon. Note that two of the magnetization plateaus we study are special in the sense that they are found at zero magnetization and are built by paramagnetic states. Before the PFFRG magnetization curves are presented, the predicted magnetization behaviors of these models will be summarized first, with an emphasis on the magnetization plateaus. For our purposes, we will mostly neglect aspects of the magnetization curves that are not relevant to the study of the magnetization plateaus.

The antiferromagnetic dimer in a magnetic field, described by the analytically solvable model

$$\hat{\mathcal{H}} = J\hat{\boldsymbol{S}}_0 \cdot \hat{\boldsymbol{S}}_1 - h(\hat{S}_0^z + \hat{S}_1^z), \tag{4.6}$$

gives a simple realization of a magnetization plateau. In this model, the magnetization remains constant at $M^z = 0$ until an energy crossing of the singlet ground state and a triplet state with saturated magnetization $M^z = 1/2$ occurs at $h/J = 1$. It follows that the exact magnetization curve $M^z(h/J) = \theta(h/J - 1)/2$ can be described by a Heaviside step function $\theta(x)$ and the size of the plateau is given by the triplet gap. The PFFRG magnetization curve can be computed without the application of any seed field, since no ground state with spontaneously broken symmetries exists. Note that the magnetization curve is unaffected by the mapping onto a pseudo-fermion model.

In contrast to the dimer, the antiferromagnetic Heisenberg model on the pyrochlore lattice in a magnetic field is challenging to treat for many methods. Accordingly, the magnetization curve of the model is still under debate. Due to strong geometrical frustration enforced by the pyrochlore lattice structure, the $h = 0$ model assumes a quantum paramagnetic phase at $T = 0$. We refrain from a more detailed discussion of the $h = 0$ model at this point, since it will be treated in Chapter 5. The stability of the paramagnetic ground state under the application of a uniform magnetic field h manifests a magnetization plateau at $M^z = 0$. Different methods, such as DMRG [57] or a combination of exact diagonalization (ED) and vMC [56], have been applied to predict the plateau size, which corresponds to the triplet gap of the $h = 0$ model. The predicted sizes of both studies are consistent. DMRG predicts a triplet gap of size

$\Delta/J = 0.42(11)$ [57] and the combined ED and vMC study predicts a triplet gap of size $\Delta/J = 0.40(4)$ [56]. The DMRG study Ref. [57] further resolved the magnetization curve beyond the $M^z = 0$ plateau and predicts the existence of additional plateaus, most prominently at $M^z = 1/4$. Unfortunately, the PFFRG study of most predicted plateaus is hindered by the large magnetic unit cells that their underlying states are predicted to host [76, 57]. The amount of symmetries that the seed fields would have to break in order to achieve a flow regularization for these orders would result in too many required computational resources for the computation of PFFRG flows. To circumvent this issue, we will mostly restrict our study on the paramagnetic $M^z = 0$ plateau. Since the ground state of this plateau is paramagnetic, PFFRG flows computed in the h-dependent regime of the plateau do not experience any flow breakdowns even in the absence of seed fields.

The $M^z = 0$ plateaus of the above two models are built by quantum paramagnetic ground states with no classical analogue. In contrast, the magnetization plateau of the remaining model we consider, the antiferromagnetic XXZ model on the triangular lattice, is built by a dipolar magnetic order. Notably, the full magnetization curve of the model is built solely by magnetic orders with a three-site unit cell [58, 59]. It follows that PFFRG flows throughout the full magnetization curve can be regularized at moderate computational costs. In fact, PFFRG flows of all occurring magnetic orders can be regularized with only a single sublattice-dependent choice of seed field with $\delta\boldsymbol{n}_i = (1, 0, -1), (0, 1, 1), (0, 0, 0)$ depending on the sublattice. We will apply this seed field choice to compute the full magnetization curve via PFFRG. The plateau of the model is built by an "up-up-down" state in which spins are aligned colinear and parallel to the external magnetic field along the z axis. The ordered spins on two sublattices point along the magnetic field, whereas spins on the remaining sublattice point in the opposite direction, as shown in the inset of Fig. 4.6. Accordingly, the plateau is found at a magnetization of $M^z = 1/6$. Note that magnetic moments of the plateau state are reduced by quantum fluctuations. However, since this reduction is twice as large on the down spins as on the up spins, the plateau will still be located at $M^z = 1/6$ [1]. The width of the plateau in h depends on the ratio of interactions J^{xx}/J^{zz}. It is the largest for the Ising model at $J^{xx} = J^{yy} = 0$, where it covers the entire magnetization curve from $h = 0$ to saturation at $h_{\text{sat}} = 3(J^{zz} + J^{xx}/2)$. The plateau then becomes smaller with increasing J^{xx}/J^{zz} until it vanishes beyond the Heisenberg model at $J^{xx}/J^{zz} > 1$. Note that the plateau width is also expected to be reduced by the application of the finite seed field $\delta\boldsymbol{n}_i$. In this study, PFFRG is applied to the model with $J^{xx}/J^{zz} = 1/2$, which is expected to have a pronounced plateau even in presence of a finite δ. For this model, the DMRG study Ref. [59] predicts the plateau to be located at $h/J^{zz} \in [0.67(1), 2.63(1)]$.

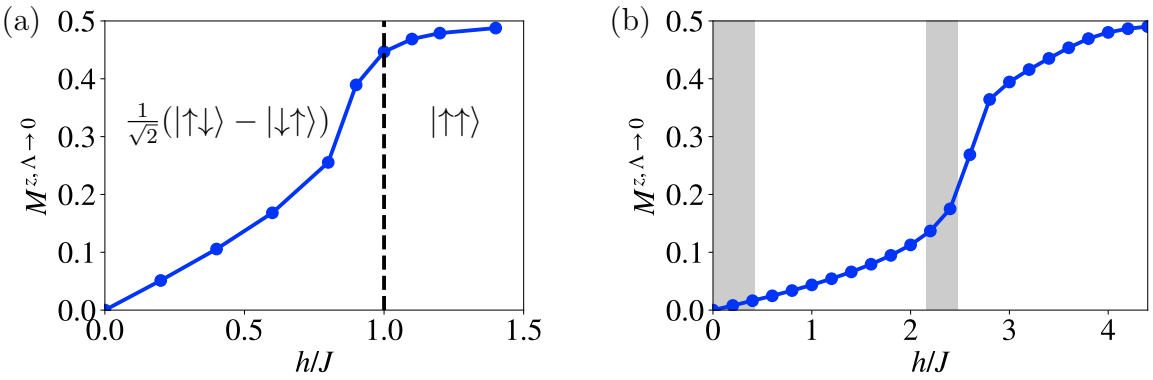

Figure 4.5: (a) PFFRG magnetization curve of the antiferromagnetic Heisenberg model on a dimer. The analytical position of the level crossing between a singlet ground state $\frac{1}{\sqrt{2}}(|\uparrow\downarrow\rangle - |\downarrow\uparrow\rangle)$ and a triplet ground state $|\uparrow\uparrow\rangle$ is indicated by a dashed vertical line. (b) PFFRG magnetization curve of the pyrochlore antiferromagnetic Heisenberg model in a magnetic field h. The magnetization $M^{z,\Lambda\to 0}$ is extrapolated to the cutoff-free limit for data points at any h/J, regardless of whether a flow exhibits a breakdown. Shaded regions correspond to DMRG predictions from Ref. [57] for the locations of the $M^z = 0$ and $M^z = 1/4$ magnetization plateaus.

Antiferromagnetic Heisenberg model on a dimer

We now continue by presenting the results for the considered models, starting with the dimer. Note that while the spin Hamiltonian of a dimer is easy to solve analytically, in the PFFRG framework the flow equations of the corresponding strongly interacting pseudo-fermion model are highly nontrivial and have to be solved analytically. The PFFRG magnetization process of an antiferromagnetic dimer is shown in Fig. 4.5(a). Starting from $h = 0$, the magnetization $M^{z,\Lambda\to 0}$ increases continuously and strictly monotonically with h. Accordingly, the analytically predicted $M^z = 0$ plateau at $h/J < 1$ or a sharp jump of the magnetization at $h/J = 1$ are not reproduced. However, the triplet gap is still indicated by the magnetization curve in the form of a steep increase of $M^{z,\Lambda\to 0}$ just below $h/J = 1$. While $M^{z,\Lambda\to 0} \approx 0.45$ is close to saturation at $h/J = 1$, it slowly converges towards $M^{z,\Lambda\to 0} = 1/2$ only at $h/J > 1$. In summary, while the $M^z = 0$ plateau is not reproduced in the PFFRG magnetization curve, the plateau size is still indicated by a steep increase of $M^{z,\Lambda\to 0}$ near the predicted plateau boundary.

Antiferromagnetic Heisenberg model on the pyrochlore lattice

Next, we continue with the discussion of the PFFRG magnetization curve of the antiferromagnetic Heisenberg model on the pyrochlore lattice. Most importantly, we are interested in the question whether PFFRG can be applied to resolve the $M^z = 0$ plateau.

In principle, the paramagnetic $M^z = 0$ plateau can be detected by two straightforward approaches. First, while the paramagnetic PFFRG flows located in the plateau should not exhibit a flow breakdown, flows at larger h beyond the plateau may transition to magnetic orders with spontaneously broken symmetries. These spontaneously broken symmetries should manifest flow breakdowns. By measuring the minimum h at which a flow breakdown occurs, an upper bound $h_{\max}$ for the $M^z = 0$ plateau can be determined. Second, the presence of the plateau should result in a constant magnetization of $M^{z,\Lambda\to 0} = 0$ across a finite range in h. Thus, the size of the plateau should be given by the magnetic field h/J at which $M^{z,\Lambda\to 0}$ becomes finite. As will be shown below, the PFFRG detection of the plateau will not be as straightforward as suggested above.

The full PFFRG magnetization curve of the Heisenberg model on the pyrochlore lattice is shown in Fig. 4.5(b). The predicted regions of the $M^z = 0$ and $M^z = 1/4$ plateaus are colored gray. $M^{z,\Lambda\to 0}$ is shown for each data point along the curve, beyond the predicted regime of the $M^z = 0$ plateau and regardless of whether a flow exhibits a breakdown. It follows that some data points are shown at an unphysical $\Lambda < \Lambda_c$. One reason for this choice of presentation is given by the difficulty in identifying the presence of flow breakdowns for this particular model. In fact, PFFRG flows show no unambiguous sign of a flow breakdown for the region $h/J \leq 2$. This region exceeds the triplet gap, predicted to be of size $\Delta/J = 0.42(11)$ by DMRG [57] and of size $\Delta/J = 0.40(4)$ by a combined ED and vMC study [56], by a multitude. Thus, magnetic orders may be located in this region, whose presence should generally enforce a flow breakdown. However, since no unambiguous flow breakdown can be detected, it follows that PFFRG is incapable to predict an upper limit for the triplet gap by measuring the magnetic field size h/J above which a flow breakdown occurs. Even if the paramagnetic $M^z = 0$ plateau cannot be detected indirectly by the appearance of a flow breakdown at the plateau boundary, one should still be able to detect a constant magnetization $M^{z,\Lambda\to 0} = 0$ across the plateau in principle. However, like in the magnetization curve of the antiferromagnetic dimer, $M^{z,\Lambda\to 0}$ is observed by PFFRG to increase strictly monotonically throughout the predicted region of the $M^z = 0$ plateau. Unlike the PFFRG magnetization curve of the antiferromagnetic dimer, the PFFRG magnetization curve of the pyrochlore Heisenberg model is featureless in the predicted region of the $M^z = 0$ plateau, such that no indication of the triplet gap size can be detected. In summary, PFFRG is unable to detect the $M^z = 0$ magnetization plateau of the Heisenberg model on the pyrochlore lattice via the model's magnetization curve.

Considering the full PFFRG magnetization curve, the found absence of a clear flow breakdown throughout most of the regime $0 < h/J < 4$ is unexpected, since magnetic orders with spontaneously broken symmetries are predicted by DMRG for most of the same regime [57]. The two scenarios below may offer explanations for the observation

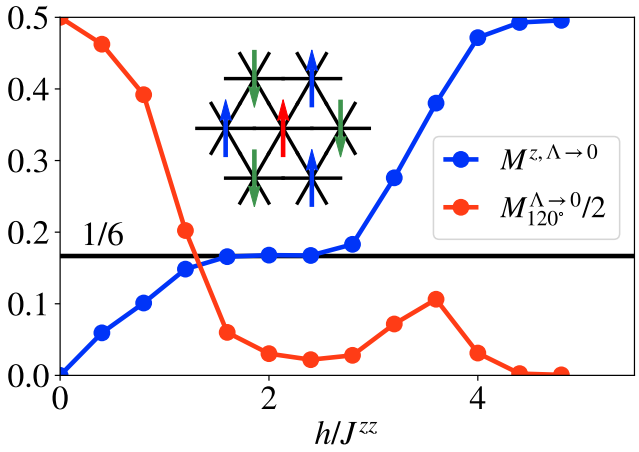

Figure 4.6: The dependencies of $M^{z,\Lambda\to 0}$ and $M^{\Lambda\to 0}_{120^\circ}$ [defined in Eq. (4.4)] on an external magnetic field h are considered for the XXZ model of Eq. (4.2) with interactions $J^{xx}/J^{zz} = J^{yy}/J^{zz} = 1/2$ on a triangular lattice. A seed field of size $\delta = 0.04J^{zz}$ is applied and the sublattice-dependent seed field orientation vectors are given by $\boldsymbol{n}_i = (1, 0, -1), (0, 1, 1), (0, 0, 0)$. The magnetization $M^z = 1/6$ of the colinear up-up-down plateau state, shown as an inset, is marked by a horizontal line.

of this apparent contradiction. As a first possible explanation, at magnetic field sizes h/J just above the triplet gap, quantum fluctuations and geometrical frustration could realize states that do not spontaneously break any symmetries of the Hamiltonian but still exhibit a finite magnetization. As a second explanation, many magnetization plateaus found by the DMRG study Ref. [57] are predicted to be built by ground states with large magnetic unit cells. However, the present PFFRG implementation only considers spin correlations of distances up to four nearest-neighbor spacings. The neglection of longer-range correlations could energetically favor states with smaller unit cells, or spontaneously broken symmetries of states with larger unit cells may not be correctly captured by the PFFRG flows, leading to stable flows instead. Interestingly, we do observe flow breakdowns to occur within the predicted region of the $M^z = 1/4$ magnetization plateau, most prominently at $h/J = 2.4$. In context of the above possible explanation of absent flow breakdowns, this observation would be explained by the fact that out of all predicted magnetically ordered plateaus, the $M^z = 1/4$ plateau is predicted to have the smallest magnetic unit cell. DMRG predicts the $M^z = 1/4$ state to be given by a colinear $\boldsymbol{q} = \boldsymbol{0}$ order with spins of three sublattices pointing up and spins of the remaining sublattice pointing down [57].

XXZ model on the triangular lattice

The PFFRG-based detection of magnetization plateaus was unsuccessful in the two models considered above. Before we try to understand the reason for this failure, we next consider the magnetization curve of the antiferromagnetic XXZ model on the triangular lattice with interactions $J^{xx}/J^{zz} = 1/2$. As will be shown, the detection of a magnetization plateau will be successful in this model at last. The full PFFRG magnetization curve is shown in Fig. 4.6. In addition to $M^{z,\Lambda\to 0}$, we consider the curve of $M^{\Lambda\to 0}_{120^\circ}/2$ as defined in Eq. (4.4). As a reminder, the latter observable assumes a value of $M^{\Lambda\to 0}_{120^\circ}/2 = 1/2$ for an ideal 120° order and assumes $M^{\Lambda\to 0}_{120^\circ}/2 = 0$ for a colinear order, such as the up-up-down state of the magnetization plateau (see inset of the figure) or the ferromagnetic state at saturated magnetization $M^{z,\Lambda\to 0} = 1/2$. As can be observed along the shown magnetization curve, PFFRG detects the predicted intermediate magnetization plateau at $M^z = 1/6$ in the region $1.6 \lesssim h/J^{zz} \lesssim 2.4$. The finite seed field of size $\delta = 0.04J^{zz}$ is expected to reduce the plateau in size. As such, the observed plateau region is consistent with the region $h/J^{zz} \in [0.67(1), 2.63(1)]$ predicted by the DMRG study Ref. [59]. The presence of a colinear plateau ground state is reflected by a local minimum of $M^{\Lambda\to 0}_{120^\circ}$ in the plateau region. However, due to a finite δ, a perfectly colinear state with $M^{\Lambda\to 0}_{120^\circ} = 0$ is not achieved by the plateau of the PFFRG magnetization curve.

Interpretation of results

In summary, PFFRG is not able to resolve the magnetization plateaus of the antiferromagnetic dimer and pyrochlore-lattice Heisenberg model. While the magnetization curve of a dimer still indicates the size of its plateau, no remnant of the $M^{z,\Lambda\to 0} = 0$ plateau is visible in the magnetization curve of the pyrochlore Heisenberg model. In contrast, the $M^z = 1/6$ magnetization plateau of the XXZ model on the triangular lattice is pronounced within PFFRG, even in presence of a large seed field of size $\delta = 0.04J^{zz}$. The reason why PFFRG reproduces the plateau of one model, while plateaus of other models are not captured, may be found in the structure of the respective plateau ground states, as will be explained in the following.

The plateau of the triangular-lattice XXZ model is built by a dipolar magnetic order. This type of order is known to be captured well within PFFRG [12]. On the other hand, the method is highly limited in the characterization of paramagnetic states due to the methodologically inherent truncation of flow equations. This is reflected by the fact that in absence of finite seed fields the spontaneous symmetry breaking of magnetic orders results in a flow breakdown, whereas the spontaneous symmetry breaking of

(paramagnetic) nematic states does not. The methodologically insufficient description of paramagnetic ground states suggests that their excitations may not be captured correctly as well. Importantly, an energy gap that results in the presence of a paramagnetic plateau at $M^z = 0$ may not be captured by PFFRG due to this methodological shortcoming, resulting in the absence of a magnetization plateau within PFFRG. In order to achieve a qualitative improvement in the description of paramagnetic ground states, and thus paramagnetic magnetization plateaus, a flow equation truncation scheme above the three-particle vertex or beyond may have to be applied. Such a truncation scheme has not been formulated for the PFFRG at this point. At last, note that the magnetically ordered plateau of the XXZ model is found at large h/J^{zz}, at which PFFRG is expected to give more precise results. In contrast, the studied plateaus of the remaining considered models are located near $h/J = 0$. It follows that, a priori, without considering the respective plateau states, one would expect the plateau of the XXZ model on the triangular lattice to be captured more precisely than the plateaus of the antiferromagnetic dimer and pyrochlore models located at smaller h/J^{zz}.

4.4 Discussion

A general PFFRG formulation was presented in the previous Chapter 3, which allows the treatment of spin models with spins coupled to finite magnetic fields. Based on this formulation, this chapter explored the methodological capabilities and limitations of the PFFRG in finite-field applications. To this end, the method extension has been applied to a variety of spin models, so that this chapter provides preliminary work in cartographing for which kinds of applications the extended method is best suited. While the present formulation of the PFFRG is in principle able to provide Λ flows for spin models with arbitrary terms linear or bilinear in spin operators, the phenomena that can occur in these models are captured by the method with varying success, as will be discussed in the following.

The successful regularization of flow breakdowns by the application of symmetry-breaking seed fields has been demonstrated for a variety of Heisenberg and XXZ models at zero and finite external magnetic fields h. The resulting smooth PFFRG flows allow for the study of $T = 0$ spin models within their magnetically ordered phases below the critical cutoff at $\Lambda < \Lambda_c$ and in the physically relevant cutoff-free limit at $\Lambda \to 0$. The implementation of seed fields (and magnetic fields in general) increases the computational costs necessary to evaluate PFFRG flows, since these fields break time-reversal symmetry, and, possibly, spin rotation and lattice symmetries of a model. The additional costs are particularly high in case continuous spin rotation symmetries are

broken (see Table 3.3). In this context, we emphasize that the resolution of magnetic orders without any continuous spin rotation symmetries and with a unit cell of multiple lattice sites has been found to be achievable at reasonable computational costs, as shown in this chapter for the Heisenberg and XXZ models on the triangular lattice. On the other hand, the magnetic orders that the method is able to resolve are limited by the amount of symmetries that individual magnetic orders spontaneously break, since each symmetry that a seed field has to break adds computational cost to the computation of a PFFRG flow. As a general rule of thumb, numerical PFFRG implementations that resolve magnetic orders with smaller magnetic unit cells are easier to construct and require less computational resources. To keep the computation of a regularized PFFRG flow efficient and numerically feasible, an applied seed field should only break the symmetries of a model that the magnetic order of the model spontaneously breaks. Importantly, this requires a priori knowledge of the ordering behavior of a model. In the magnetization curve of the pyrochlore Heisenberg model such knowledge was mostly absent, so that magnetic orders could not be resolved by the application of appropriate seed fields. However, even if the magnetic orders of the curve were known, their resolution by PFFRG may still be inaccessible with the currently available computational resources due to their large magnetic unit cells.

Regarding the quality of PFFRG results, a systematic overestimation of PFFRG magnetic order parameters has been observed and attributed to a mean-field bias of the Λ flow at $\Lambda \simeq \Lambda_c$. This bias is generated by the Hartree term of the self-energy and the RPA term of the two-particle vertex flow equation, which give the dominant contributions to the flow equations at Λ_c. Further investigation is required to find out whether the error generation at Λ_c can be reduced by the implementation of a multi-loop truncation scheme as implemented in Refs. [36] or [37]. On a positive note, spin arrangements of magnetic orders have been observed to be captured accurately by PFFRG and remain stable under different choices of seed fields, whose local orientations need not coincide with the local magnetization of a model's magnetic order, as has been shown for the Heisenberg model on the triangular lattice. Notably, a single seed field choice was sufficient to resolve all magnetic orders throughout the entire magnetization curve of the similar triangular lattice XXZ model.

At last, we discuss our results on magnetization curves. Full magnetization curves and their respective magnetic orders have been resolved by PFFRG on the square-lattice Heisenberg model and the triangular-lattice XXZ model. On the square lattice, a comparison of magnetizations with literature values revealed more accurate PFFRG results at higher magnetic field sizes. This result encourages the application of PFFRG to models with finite magnetic fields. Furthermore, the study of the triangular-lattice XXZ model demonstrated the successful resolution of the magnetization plateau at

$M^z = 1/6$. The computation of magnetization curves was less successful for the antiferromagnetic Heisenberg models on a dimer and on the pyrochlore lattice. The $M^z = 0$ magnetization plateaus of these models could not be reproduced by PFFRG. While the PFFRG magnetization curve of the antiferromagnetic dimer still allowed for an estimation of the plateau size, no sign of a plateau was found in the magnetization curve of the pyrochlore Heisenberg model. This suggests that the successful resolution of the $M^z = 1/6$ plateau of the triangular-lattice XXZ model may be caused by the presence of a magnetically ordered ground state. In contrast, the method appears to be highly limited in its ability to characterize paramagnetic ground states, as was found by the study of $M^z = 0$ plateaus. Thus, we expect the method to be better suited for the study of so-called 'classical' plateaus [1] with magnetically ordered ground states.

Chapter 5

Order-by-disorder, spin liquids, and nematic phases in nearest-neighbor spin models on the pyrochlore lattice

The previous chapters constitute the method development part of this thesis. In it, the PFFRG method was extended to treat spin models with broken TRS, and the resulting newly available method applications were explored along a variety of models with well-known behavior. In contrast, the next two chapters will apply the PFFRG method in collaboration with complementary techniques to study a selection of spin models of recent interest. These applications will not rely on the recent PFFRG extension for models with broken TRS. Instead, only models with TRS, for which the PFFRG is already a well-established method [12], will be considered. This chapter will set the focus on the study of nearest-neighbor spin models on the pyrochlore lattice.

Spin models on the pyrochlore lattice are a popular platform in the study of frustrated magnetism in three dimensions [77, 78, 4, 1]. The lattice is conceptually simple, being built by lattice sites arranged in corner-sharing tetrahedra, as shown in Fig. 5.1. This structure leads to strong geometrical frustration between nearest-neighbor interactions, enabling a multitude of interesting phenomena in nearest-neighbor models alone. Prominent among them is the classical spin-ice phase of the Ising antiferromagnet, which, for quantum spins, is known to transition into a U(1) QSL phase upon the perturbative inclusion of $\hat{S}_i^x \hat{S}_j^x + \hat{S}_i^y \hat{S}_j^y$ interactions (XY interactions) [4]. Still under debate is the extent of the QSL phase towards the regime of nonperturbative XY interaction sizes [56]. In particular, it is of interest whether the paramagnetic

ground state of the antiferromagnetic Heisenberg model is still located in the QSL phase [79, 48, 43, 80], and whether the QSL remains stable in the presence of other types of nearest-neighbor interactions allowed by the symmetries of pyrochlore compounds [49], such as Dzyaloshinskii-Moriya interactions (DMI). Both the properties of the ground state of the Heisenberg model and its stability under the presence of a finite DMI are treated in this chapter. Progress has been made in the study of the Heisenberg model ground state in recent years [56, 79, 48, 43, 80], suggesting the realization of a nematic phase in case of quantum spins. We treat the PFFRG perspective of this study in Sec. 5.1 by considering the ground state selections of the Heisenberg model for both the quantum cases $S = 1/2$ and $S = 1$, as done in our recent publications [48, 43], which apply PFFRG-based approaches, DMRG, and vMC.

A particular phenomenon of frustrated magnetism leads to the possibly nematic ground state selection of the pyrochlore Heisenberg antiferromagnet. In this model, strong geometrical frustration leads to an extensive classical ground state manifold. However, states within this manifold are generally not related by any symmetry of the model. A so-called *accidental* degeneracy is realized. It is this accidental degeneracy that allows certain states within this manifold to be preferably chosen by quantum fluctuations, possibly resulting in a nematic order. The thermal or quantum fluctuation-based transition into an ordered phase due to the preferential selection of certain states out of a larger classical ground state manifold is known under the term order-by-disorder (ObD) [5]. In spin models, this term is usually applied in the context of a magnetic order being selected out of a larger classical manifold. An in-depth study of the ObD phenomenon will be provided in Sec. 5.2, where we consider the general symmetry-constrained nearest-neighbor model on a pyrochlore lattice with a Heisenberg interaction J and a Dzyaloshinskii-Moriya (DM) interaction D, abbreviated as Heisenberg-DM model. The content of this section will follow along our publication Ref. [49]. Within the Heisenberg-DM model, the so-called Γ_5 phase, which hosts an accidentally degenerate classical ground state manifold, will emerge as a prime example of a subtle magnetic ObD selection. The magnetic order chosen out of the Γ_5 phase's one-dimensional classical ground state manifold may depend on both whether thermal, quantum, or both types of fluctuations are present. The subtleties of ObD selections will be further reflected by the observation that the ObD selection at critical temperature differs from that at zero temperature for some interaction regimes D/J. Note that the study of the Heisenberg-DM model will reveal the stability of the Heisenberg model's paramagnetic phase at $T = 0$ with respect to a finite DMI as well.

As a natural transition to the next Sec. 5.3, the study of the Heisenberg-DM model will reveal an additional paramagnetic phase in the ferromagnetic Heisenberg interaction regime $J < 0$. This phase is only realized for one set of interactions $D/J = 2$ in case

of classical spins, but it is stabilized over a finite range of interaction parameters by quantum fluctuations. In the classical model, it will be shown that the ground state manifold of the $D/J = 2$ model includes not only the extensive ground state manifold of the spin-ice phase, but also the classical ground state manifold of the previously mentioned Γ_5 phase (as well as an additional not yet introduced manifold). Interestingly, the thermal fluctuation-based competition between these manifolds will result in a temperature-driven crossover between two classical spin-liquid phases [71]. Furthermore, it turns out that the $D/J = 2$ model is relevant to so-called non-Kramers pyrochlore compounds and can be found on a critical point in between two quadrupolar magnetic phases and one dipolar paramagnetic phase (named in accordance with the symmetry properties of the effective spin components involved in these orders) in the general classical phase diagram for nearest-neighbor models of non-Kramers pyrochlores. Along an extended study of the $D/J = 2$ model, we will compute the $S = 1/2$ quantum version of this phase diagram and reveal the behavior of the $D/J = 2$ quantum model. The content of Sec. 5.3, which treats the classical and quantum $D/J = 2$ models and their surrounding non-Kramers phase diagrams, is covered by our recent publication Ref. [71]. Note that throughout the chapter, only nearest-neighbor models will be treated. Unless stated otherwise, interactions are assumed to be of this type.

The PFFRG method will be applied with the following specifications throughout the chapter. In Sec. 5.1 and 5.2, the self-energy and two-particle vertex are computed on exponential frequency grids with 64 sites for each frequency dependence. In Sec. 5.3, the exponential frequency grids consist of 2000 sites for the self-energy and of 64 sites for each transfer frequency of the two-particle vertex. The PFFRG flow equations are solved with Euler's method in Sec. 5.1 and 5.2, whereas they are solved by applying the implementation of Ref. [60] of an explicit embedded Runge-Kutta $(2, 3)$ method with an adaptive step size in Sec. 5.3. Spin correlations are given out over a maximum distance of five nearest-neighbor spacings in Sec. 5.1 and 5.2, and over a maximum distance of four nearest-neighbor spacings in Sec. 5.3. Correlations over longer distances are treated as zero. The smaller distance chosen in the latter section, for which the evaluation of PFFRG flows requires less computational resources, is explained by the computation of a two-dimensional phase diagram whose evaluation requires a lot of computational resources. PFFRG flows in Sec. 5.2.4 on explicit pyrochlore compounds are computed with the PFFRG specifications of Sec. 5.3, except for the difference that spin correlations are given out over a distance of five nearest-neighbor spacings.

5.1 Could the pyrochlore Heisenberg model host a nematic ground state? A PFFRG study on the $S = 1/2$ and $S = 1$ quantum models

The classical spin-ice phase, realized by the nearest-neighbor Ising model on the pyrochlore lattice, is *the* poster child of a three-dimensional classical spin liquid. Over the years, the phase has been studied extensively and is well understood at this point [81]. With $Ho_2Ti_2O_7$ and $Dy_2Ti_2O_7$, even two rare-earth Ti compounds have been found that realize a classical spin-ice phase on the pyrochlore lattice [81]. In contrast, the ground state of the conceptually similar Heisenberg antiferromagnet is still under debate for the quantum model, but an increasing number of arguments have been gathered in recent years [56, 79, 48, 43, 80] that support the picture of a lattice symmetry-breaking nematic ground state in the cases $S = 1/2$ or $S = 1$. The aim of this section is to study the state selection by quantum fluctuations within the classical ground state manifold of the pyrochlore Heisenberg model. For this purpose, the classical spin-ice phase will be introduced first in Sec. 5.1.1, and its transition to a U(1) QSL by the introduction of XY interactions will be touched on briefly. Afterwards, the current predictions of Refs. [56, 79, 48, 43, 80] on the ground-state selection of the Heisenberg model will be summarized in Sec. 5.1.2. A PFFRG-based perspective on the selection will be provided subsequently. It will cover the author's contributions to the recent publications Refs. [48] and [43], which treat the $S = 1/2$ and $S = 1$ models, respectively. It should be noted that the PFFRG approach presented in this section has limited validity in characterizing ground states when considered by itself. For complementary approaches that also apply a PFFRG-enhanced parton mean-field approach, vMC and DMRG, we refer to the original publications. Finally, a methodological discussion on the contribution of unphysical pseudo-fermion states to PFFRG ground states is given in Sec. 5.1.3.

5.1.1 A basic review of spin ice

The spin-ice phase will occur throughout the chapter and is relevant for understanding the classical ground state manifold of the antiferromagnetic Heisenberg model on the pyrochlore lattice. A brief introduction to the spin-ice phase will be provided in the following.

The pyrochlore lattice is a face-centered cubic lattice with a four-site unit cell. A more intuitive picture is gained by framing the lattice as being built by corner-sharing tetrahedra, with the lattice sites being positioned at the corners of the tetrahedra, as

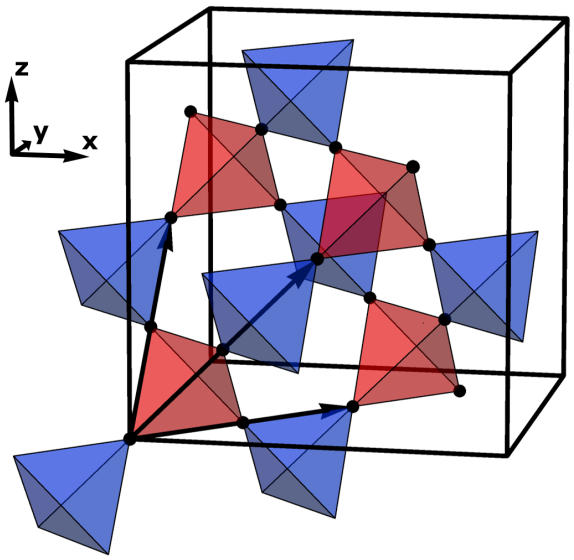

Figure 5.1: Visualization of the pyrochlore lattice. The lattice is built up from corner-sharing up and down tetrahedra, colored in red and blue respectively. The four sites of an up tetrahedron constitute the basis sites of the lattice, which is organised in a face-centered cubic (fcc) configuration. The corresponding primitive lattice vectors $\boldsymbol{a}_1 = (0,1,1)/2$, $\boldsymbol{a}_2 = (1,0,1)/2$ and $\boldsymbol{a}_3 = (1,1,0)/2$ are shown in black. The 16 sites and edges of the larger non-primitive simple cubic unit cell are highlighted in black as well.

shown in Fig. 5.1. The tetrahedra themselves are arranged in a bipartite diamond lattice. One can distinguish between up and down tetrahedra, colored red and blue, respectively, in the figure. Two lattice symmetries that we will consider in this section are the inversion symmetry about any lattice site and the C_3 rotation symmetry about an axis connecting any lattice site and the center of an adjacent tetrahedron.

We continue by considering pyrochlore spin models in which a single spin is placed on each lattice site. The classical spin-ice phase is realized in the antiferromagnetic Ising model, where spins are arranged along the site-dependent z axis pointing towards the center of the adjacent up (red) tetrahedron. The corner-sharing lattice structure allows to reformulate the Ising Hamiltonian as a sum over tetrahedra as

$$\begin{aligned}\mathcal{H} =& \sum_{\langle ij \rangle} S_i^z S_j^z \\ =& \frac{1}{2} \sum_t (S_{t0}^z + S_{t1}^z + S_{t2}^z + S_{t3}^z)^2 + C,\end{aligned} \tag{5.1}$$

with C being a constant and the index t labeling tetrahedra of the lattice. From this expression, it is apparent that the energy of the model is minimized by states in which the spins of each tetrahedron sum up to zero, i.e., $S_{t0}^z + S_{t1}^z + S_{t2}^z + S_{t3}^z = 0$ for each t. This constraint is fulfilled for states in which each two spins of a tetrahedron point

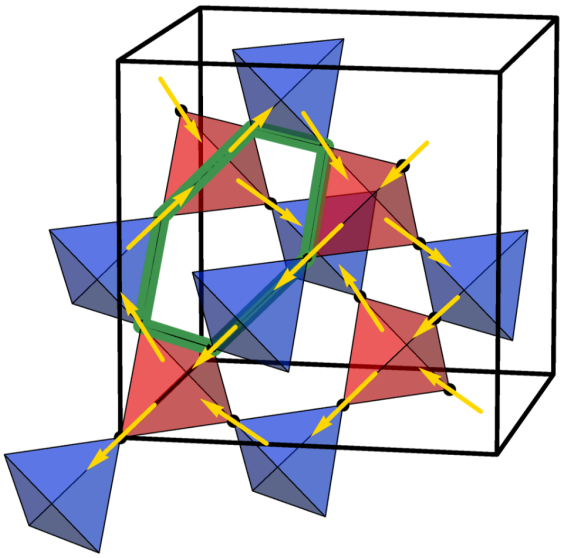

Figure 5.2: Example of a spin-ice configuration on the pyrochlore lattice. Up and down tetrahedra are colored in red and blue respectively. Classical spin vectors are shown in yellow and are oriented along the local z axis of the pyrochlore lattice, which points towards the center of the adjacent up (red) tetrahedron. A six-site hexagon, along which spins can be flipped without leaving the spin-ice manifold, is highlighted in green.

towards and away from its center (a cutout of such a state is shown in Fig. 5.2). This so-called ice rule owes its name to the fact that the resulting two-in two-out spin arrangements on single tetrahedra are analogous to the hydrogen atom arrangements found in the ambient-pressure structure of water ice [82]. The local ice rule constraint $S^z_{t0} + S^z_{t1} + S^z_{t2} + S^z_{t3} = 0$ allows for an extensive number of ground states, which prevents magnetic ordering down to the zero-temperature limit. This extensive ground state degeneracy is reflected in a $T = 0$ residual entropy of $S_P = N\ln(3/2)$, the Pauling entropy, which scales linearly with the system size N [78].

The spin-ice phase is considered a classical spin liquid and indeed contains fractionalized excitations, arguably the signature of spin liquids, in the form of magnetic monopoles. These are obtained in pairs by flipping a single spin, breaking the ice rule for the two adjacent tetrahedra in the process. Single defect tetrahedra can be moved around independently and without energy cost by flipping adjacent spins. In other words, we observe an initial spin-flip excitation being fractionalized into two deconfined defect tetrahedra, each interpreted as a magnetic monopole [78].

Besides the Pauling entropy, another experimental signature of classical spin ice are sharp features in the momentum dependence of the magnetic susceptibility that are of vanishing width, the so-called pinch points, as shown in Fig. 1 of Ref. [83]. They manifest as a direct consequence of the fulfillment of the ice rule. This rule implies

long-range correlations since neighboring lattice layers along the x, y, or z direction (as defined in Fig. 5.1) will realize exactly opposite magnetizations. In turn, the perfect correlations between lattice layers give rise to sharp features in the magnetic susceptibility [1]. An alternative view on pinch points is gained by considering the classical spin orientations as a site i dependent vector field $\boldsymbol{B}_i$ [78]. By coarse-graining the Ising model to a continuum theory with a continuous position vector $\boldsymbol{r}$, the ice rule transitions into the vector field restriction

$$\boldsymbol{\nabla} \cdot \boldsymbol{B}(\boldsymbol{r}) = 0, \tag{5.2}$$

reminiscent of the Gauss law in electromagnetism. In case $\boldsymbol{\nabla} \cdot \boldsymbol{B}(\boldsymbol{r}) \neq 0$, a broken ice rule is implied and magnetic monopole excitations emerge that act as sources of the emergent magnetic field $\boldsymbol{B}(\boldsymbol{r})$. The connection to electromagnetism can be extended by introducing the gauge field $\boldsymbol{A}(\boldsymbol{r})$ via

$$\boldsymbol{B}(\boldsymbol{r}) = \boldsymbol{\nabla} \times \boldsymbol{A}(\boldsymbol{r}), \tag{5.3}$$

which satisfies the Gauss law by construction. Many spin-ice configurations exist that lead to small magnetic field strengths $|\boldsymbol{B}|$, and fewer exist that lead to larger absolute sizes. This is captured effectively by the probability distribution

$$P(\boldsymbol{B}(\boldsymbol{r})) \propto e^{-\frac{\kappa}{2}\int_{\mathbb{R}^3} d\boldsymbol{r}|\boldsymbol{B}(\mathrm{r})|^2}, \tag{5.4}$$

with a constant κ [1]. Importantly, this distribution implies dipolar long-range correlations

$$\langle B^\mu(\boldsymbol{r}) B^\nu(\boldsymbol{0})\rangle \propto \frac{r^\mu r^\nu - |\boldsymbol{r}|^2\delta_{\mu\nu}}{|\boldsymbol{r}|^5}, \tag{5.5}$$

with $\mu, \nu \in \{x, y, z\}$. It is this dipolar correlation behavior that manifests pinch points in the magnetic susceptibility [83].

Quantum spin ice

It has been confirmed by several analytical and numerical approaches, including qMC [84], that classical spin ice transitions into a U(1) QSL once tunneling between classical spin-ice configurations is enabled by the perturbative introduction of quantum fluctuations in the form of XY interactions $\hat{S}_i^x \hat{S}_j^x + \hat{S}_i^y \hat{S}_j^y$ [4]. The tunneling processes become explicit in a perturbative expansion around the Ising model, with the simplest tunneling process between two spin-ice configurations corresponding to the local flipping of spins with alternating sign along a six-site hexagon of the lattice (see Fig. 5.2). The low-energy structure of the resulting quantum spin-ice phase is described by a U(1) lat-

tice gauge theory, which effectively realizes electromagnetism [4]. Thus, the emergent excitations of quantum spin ice include not only the magnetic monopoles of classical spin ice, but also electric monopoles and photon excitations[1]. While the monopole excitations are gapped, photon excitations are gapless and have a linear dispersion [4].

Relevant to the question posed by the title of this section, the antiferromagnetic Heisenberg model on the pyrochlore lattice, given by the Hamiltonian

$$\begin{aligned}\mathcal{H} =& J\sum_{\langle ij\rangle} \boldsymbol{S}_i \cdot \boldsymbol{S}_j \\ =& \frac{J}{2}\sum_t (\boldsymbol{S}_{t0}+\boldsymbol{S}_{t1}+\boldsymbol{S}_{t2}+\boldsymbol{S}_{t3})^2 + D,\end{aligned} \tag{5.6}$$

with D being a constant and $J > 0$, is a model that includes the spin-ice manifold within its classical ground state manifold. Instead of the Ising model's ice rule $S^z_{t0} + S^z_{t1} + S^z_{t2} + S^z_{t3} = 0$, the classical ground state manifold of the Heisenberg model is given by the states that satisfy $\boldsymbol{S}_{t0} + \boldsymbol{S}_{t1} + \boldsymbol{S}_{t2} + \boldsymbol{S}_{t3} = \boldsymbol{0}$ on each tetrahedron t of the lattice. On first sight, this higher-dimensional generalization of the ice rule raises the question of whether the ground state of the quantum model can be related to a quantum spin ice. However, although it is confirmed that the Heisenberg model remains paramagnetic down to $T = 0$ [83], ObD from quantum fluctuations could enforce other types of paramagnetic phases as well.

Revealing the nature of the ground state of the quantum model poses a challenge for many theoretical approaches. The interactions of the Heisenberg model are located far away from the classical Ising model. Therefore, a perturbative expansion around this limit is not justified. Due to geometrical frustration, the treatment of the model by qMC is prevented by the sign problem [1]. Furthermore, since the lattice is three-dimensional, the number of lattice sites that have to be treated increases quickly with the considered system size. The model is located in a methodological niche that is, however, accessible by PFFRG, a method well suited for the treatment of three-dimensional models with frustrated interactions.

[1]The existence of magnetic monopoles can in principle be incorporated into the standard theory of electromagnetism. However, even in case magnetic monopoles exist, it is questionable whether one would ever be able to observe any due to their large predicted mass comparable to the "kinetic energy of a charging rhinoceros" [85]. Note that the parameters of standard electromagnetism, and hence the relative energies of involved excitations, are different from those of the emergent electromagnetism of quantum spin ice [86].

5.1.2 Symmetry properties of the Heisenberg model ground states

Before we commence with the PFFRG study on the ground states of the $S = 1/2$ and $S = 1$ Heisenberg models, previously proposed nematic ground states of the quantum models will be briefly summarized in this paragraph. For the $S = 1/2$ model, a lattice inversion or combined inversion and C_3 symmetry-breaking ground state had been proposed on the basis of DMRG computations [79]. The same method finds enhanced tendencies towards the same scenarios of symmetry breaking in the $S = 1$ model [43]. The study of Ref. [48] applies vMC and a PFFRG-enhanced parton mean-field approach, which renormalizes mean-field solutions by taking into account vertex fluctuations captured by PFFRG. The study suggests inversion or combined inversion and C_3 symmetry breaking for the $S = 1/2$ model ground state as well. Another vMC and convolutional neural network study suggests a $S = 1/2$ model ground state with both broken inversion and C_3 lattice symmetry [56]. A more concrete ground state for both the $S = 1/2$ and $S = 1$ model, consistent with previously predicted scenarios of symmetry breaking, had been proposed in the more recent study of Ref. [80] in the form of an inversion and C_3 symmetry-breaking valence bond crystal with spin resonances along six-spin hexagons of the lattice. In summary, previous results point either to the scenario of a lattice inversion or combined inversion and C_3 symmetry breaking for the ground states of the $S = 1/2$ and $S = 1$ models.

We now apply PFFRG to investigate the Heisenberg model towards inversion, C_3, and combined C_3 and inversion symmetry breaking. More specifically, the PFFRG approach to study nematic orders described in Sec. 3.5.8 will be applied, in which Heisenberg interactions J of the $S = 1/2$ and $S = 1$ Heisenberg models will be strengthened ($J \to J + \delta$) and weakened ($J \to J - \delta$) by sizes $\delta \ll J$ along different symmetry-breaking patterns. Dimer response functions χ_D^Λ, defined as in Eq. (3.90), are computed for the perturbed models to measure the ground state responses towards different scenarios of symmetry breaking consistent with the respective perturbation patterns.

The applied inversion, C_3, and inversion and C_3 symmetry-breaking perturbation patterns are visualized in Fig. 5.3. Heisenberg interactions of bold bonds are strengthened, whereas interactions are weakened on the remaining bonds. Dimer response functions measure the difference between spin correlations χ_{ij}^Λ and χ_{kl}^Λ on two bonds $\langle i, j\rangle$ and $\langle k, l\rangle$ related by a lattice symmetry that is broken by an overlaying perturbation pattern. In presence of the perturbation pattern that breaks only inversion symmetry, $\chi_{D,i}^\Lambda$ is defined on two bonds related by lattice inversion symmetry [see Fig. 5.3(a)]. Thus, $\chi_{D,i}^\Lambda$ probes the response of the system towards sole inversion symmetry breaking. Sim-

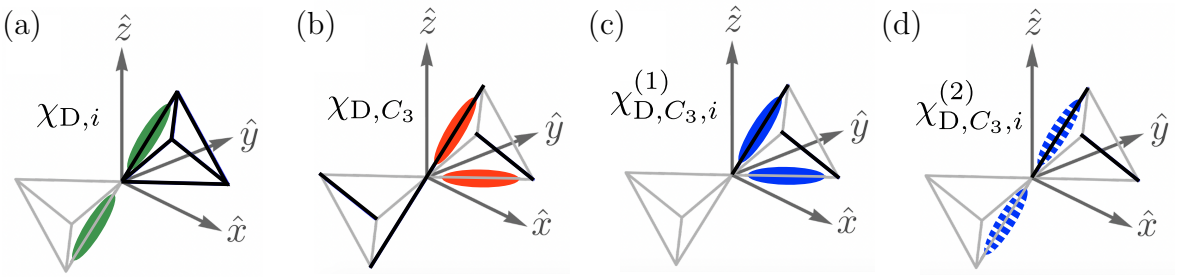

Figure 5.3: Specifications of dimer responses χ_D for perturbation patters applied in the study of the pyrochlore Heisenberg model ground state. Perturbation patterns are specified by showing them on the adjacent tetrahedra of a reference site, because the perturbations do not break translation symmetries of the lattice. Heisenberg interactions J on bold bonds are strengthened as $J \to J + \delta$, whereas they are weakened as $J \to J - \delta$ on the remaining bonds. Nearest-neighbor spin correlations on a pair of bonds related by a perturbatively broken lattice symmetry are considered for the computation of dimer responses. Those bonds are highlighted for each χ_D with the same color (and pattern) as the dimer response flow of equal χ_D in Fig. 5.4. The figure is replicated from Ref. [48].

ilarly, χ^{Λ}_{D,C_3} is defined on two bonds related by C_3 lattice symmetry in presence of a perturbation pattern that breaks only C_3 symmetry [see Fig. 5.3(b)]. In case two lattice symmetries are broken by a single perturbation pattern, two dimer response functions can be defined, each on a pair of bonds related by one of the broken symmetries. In our case, a perturbation is applied that breaks both inversion and C_3 symmetry. Large values of $\chi^{\Lambda,(1)}_{D,C_3,i}$ and $\chi^{\Lambda,(2)}_{D,C_3,i}$ then argue towards a ground state absent of both inversion and C_3 symmetry. While $\chi^{\Lambda,(1)}_{D,C_3,i}$ is defined on two bonds related by C_3 symmetry [see Fig. 5.3(c)], $\chi^{\Lambda,(2)}_{D,C_3,i}$ is defined on bonds related by inversion symmetry [see Fig. 5.3(d)].

The Λ flows of dimer responses are shown in Fig. 5.4 for both the $S = 1/2$ and $S = 1$ Heisenberg model. They mostly agree on a qualitative level between the cases $S = 1/2$ and $S = 1$. Interestingly, flows of the $S = 1$ model exhibit subtle signs of an instability at low cutoffs $\Lambda \approx 0.5$. However, recent DMRG and PMFRG results suggest that the $S = 1$ Heisenberg model is not magnetically ordered [87]. Since PFFRG predicts magnetic order for pyrochlore Heisenberg models with $S > 1$ that are still in the quantum regime of relatively small S [88], we interpret the observed feature not as a flow breakdown but as a consequence of a nearby critical point. The behavior of the χ^{Λ}_D flows allows to argue towards possible scenarios of symmetry breaking for the paramagnetic ground states. Not supported by PFFRG is the scenario of a ground state that only breaks inversion symmetry. This is reflected by the flows of $\chi^{\Lambda}_{D,i}$, along which $\chi^{\Lambda}_{D,i}$ decreases monotonically from its initial values of $\chi^{\Lambda\to\infty}_{D,i} = 1$ towards its final values $\chi^{\Lambda\to 0}_{D,i} \ll 1$. In contrast, the remaining response functions χ^{Λ}_{D,C_3}, $\chi^{\Lambda,(1)}_{D,C_3,i}$

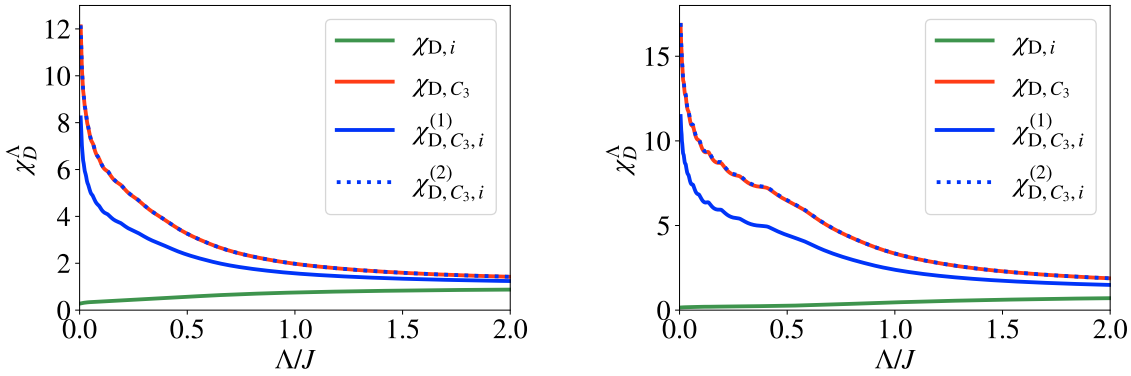

(a) $S = \frac{1}{2}$ (b) $S = 1$

Figure 5.4: PFFRG flows of dimer responses χ^{Λ}_D for the $S = 1/2$ and $S = 1$ antiferromagnetic Heisenberg models on the pyrochlore lattice. Dimer responses to different symmetry-breaking perturbation patterns were considered, which either break lattice inversion, C_3 or both symmetries of the Heisenberg models (see Fig. 5.3). The subfigures are replicated from Refs. [48] and [43].

and $\chi^{\Lambda,(2)}_{D,i,C_3}$ exhibit a large increase at small cutoffs $\Lambda \lesssim 1$ and reach large values of $\chi^{\Lambda}_D > 8$ at $\Lambda \to 0$. The largest values are achieved by χ^{Λ}_{D,C_3} and $\chi^{\Lambda,(1)}_{D,C_3,i}$. Note that values of both response functions are not exactly equal even though it visually appears to be the case in Fig. 5.4. The large values of $\chi^{\Lambda\to 0}_{D,C_3}$ suggest ground states that only break C_3 symmetry. Simultaneously, large values of $\chi^{\Lambda\to 0,(1)}_{D,C_3,i}$ and $\chi^{\Lambda\to 0,(2)}_{D,i,C_3}$ suggest that the ground states break both inversion and C_3 symmetry. Unfortunately, the method cannot distinguish by itself which of the two scenarios applies for the ground states of the $S = 1/2$ and $S = 1$ Heisenberg models. Note that the responses χ^{Λ}_{D,C_3}, $\chi^{\Lambda,(1)}_{D,C_3,i}$ and $\chi^{\Lambda,(2)}_{D,i,C_3}$ reach larger values in the cutoff-free limit $\Lambda \to 0$ for the $S = 1$ model than for the $S = 1/2$ model. This observation is in agreement with the enhanced symmetry breaking tendency of the $S = 1$ model found by DMRG in Ref. [43].

5.1.3 Unphysical states

The PFFRG method does not treat spin models directly, but the corresponding pseudo-fermion models, which hosts unphysical states. The above study of the ground states of the $S = 1/2$ and $S = 1$ Heisenberg models has so far neglected whether the presence of these unphysical states may affect measured values of χ^{Λ}_D. This question will be treated in the following, since in pseudo-fermion versions of quantum spin models, especially highly frustrated ones, it can occur that quantum fluctuations incorporate pseudo-fermion states of the unphysical Hilbert space sector into the ground state to some extent [35]. While the previous conclusions on the ground-state symmetry properties

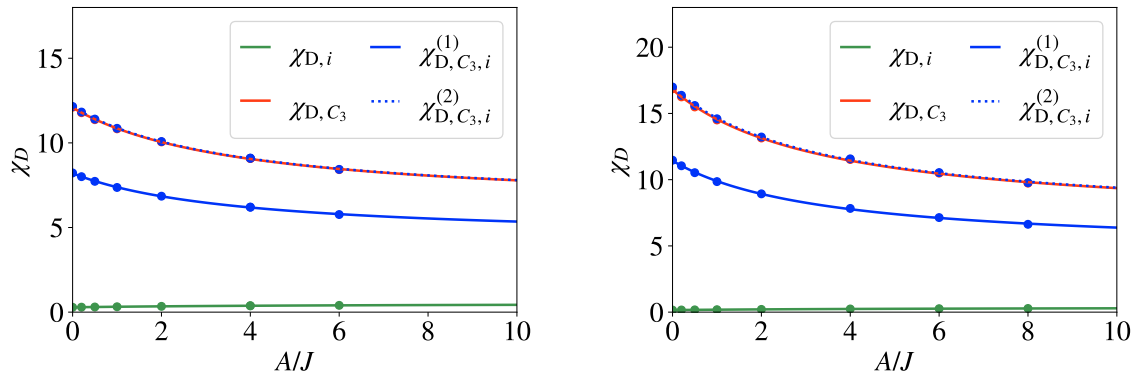

(a) $S = \frac{1}{2}$ (b) $S = 1$

Figure 5.5: Dependencies of dimer responses $\chi_D \equiv \chi_D^{\Lambda\to 0}$ of the $S = 1/2$ and $S = 1$ Heisenberg models on the level repulsion strength A/J, as defined in Eq. (5.7). The data points were fitted by the function (5.8). Fitted values of χ_D in the limit $A \to \infty$ are given in Table 5.1. Subfigure (b) is replicated from Ref. [43].

of Heisenberg models will remain unchanged, a quantitative correction of measured values χ_D^Λ will be observed. In PFFRG implementations of $S > 1/2$ models, the origin of unphysical states is twofold. On the one hand, the pseudo-fermion mapping (see Sec. 3.2) introduces two unphysical states with vanishing local spin $S = 0$ on each lattice site. On the other hand, the PFFRG treats models with spin numbers $S = M/2$ by placing M copies of $S = 1/2$ degrees of freedom on each lattice site [32]. This implementation of $S > 1/2$ models assumes that the M spin-1/2 quantum numbers are energetically favored to sum up to an effective $S = M/2$ spin on each site.

We investigate the influence of unphysical states on the measured dimer response functions by adding terms to the Hamiltonian that energetically reward maximum onsite spin numbers S. The new spin model is given by

$$\mathcal{H} = J \sum_{\langle ij \rangle} \hat{\boldsymbol{S}}_i \cdot \hat{\boldsymbol{S}}_j - A \sum_i \hat{\boldsymbol{S}}_i^2. \tag{5.7}$$

The dependence of each previously considered dimer response function in the cutoff-free limit $\chi_D \equiv \chi_D^{\Lambda\to 0}$ on the level repulsion strength $A > 0$ is shown in Fig. 5.5. We observe that the sizes of χ_D change significantly upon the inclusion of a finite A. Their dependence on A is found to be well fitted by the function

$$\chi_D(A/J) = \frac{a}{(A/J - b)} + c, \tag{5.8}$$

with fitting parameters a, b and c. Based on the observation that the data points are well captured by the fitting function, we use this function to estimate values of

	$A/J = 0$		$A/J \to \infty$	
χ_D	$S = \frac{1}{2}$	$S = 1$	$S = \frac{1}{2}$	$S = 1$
$\chi_{D,i}$	0.286	0.156	0.529(3)	0.378(2)
χ_{D,C_3}	12.1	16.9	6.1(2)	6.8(3)
$\chi^{(1)}_{D,C_3,i}$	8.2	11.5	4.3(1)	4.7(2)
$\chi^{(2)}_{D,C_3,i}$	12.2	17.0	6.1(2)	6.8(3)

Table 5.1: Dimer responses $\chi_D \equiv \chi_D^{\Lambda \to 0}$ in the absence of level-repulsion terms and in the large level-repulsion limit $A/J \to \infty$. Values for the case $A/J \to \infty$ are obtained by applying a non-linear least squares fit, using the fitting function of Eq. (5.8), to the data points of χ_D at different A/J, shown in Fig. 5.5. The table is replicated from Ref. [43].

the dimer response functions in the $A \to \infty$ limit, in which unphysical states do not contribute to the exact ground state of the pseudo-fermion Hamiltonian. Estimates of χ_D in the limit $A \to \infty$ are given in Table 5.1. Note that the results in the $A \to \infty$ limit should be treated with caution. While unphysical states do not contribute to the exact ground state in this limit, the flow equation truncation of the PFFRG may prevent a fulfillment of the strong constraint [given by Eq. (3.23)] even at $A \to \infty$. A similar effect is observed in Ref. [35], which instead aims to remove the contributions of unphysical states to thermodynamic averages by the application of the Popov-Fedotov trick.

In the limit $A \to \infty$, previously large dimer response functions of the $S = 1/2$ model with $A = 0$ are approximately halved. E.g., for the $S = 1/2$ model, dimer responses assume values of $\chi_{D,C_3} = 12.1$ at $A = 0$ and $\chi_{D,C_3} = 6.1(2)$ at $A \to \infty$ (reduction to 50% of the previous size). For the $S = 1$ model, the relative size reductions are even larger, likely due to the twofold origin of unphysical states. In case of the $S = 1$ model, we measure $\chi_{D,C_3} = 16.9$ at $A = 0$ and $\chi_{D,C_3} = 6.8(3)$ at $A \to \infty$ (reduction to 40% of the previous size). Nevertheless, dimer response functions are observed to remain much larger than 1 at $A \to \infty$ for both the $S = 1/2$ and $S = 1$ model if they already assume large values at $A = 0$. Likewise, $\chi_{D,i}$ remains small for the $S = 1/2$ and $S = 1$ models at $A \to \infty$. Hence, while the $A \to \infty$ dimer responses, which are closer to $\chi_D = 1$, reduce the significance of the previous PFFRG statement on the ground state symmetry properties, the conclusion of C_3, or combined inversion and C_3 symmetry-breaking ground states remains. The argument against the presence of ground states that only break lattice inversion symmetry remains as well. Furthermore, the deviation of dimer responses from $\chi_D = 1$ is still larger in the $S = 1$ model than in the $S = 1/2$ model, which is still in agreement with the DMRG result of an enhanced symmetry breaking in the $S = 1$ model [43].

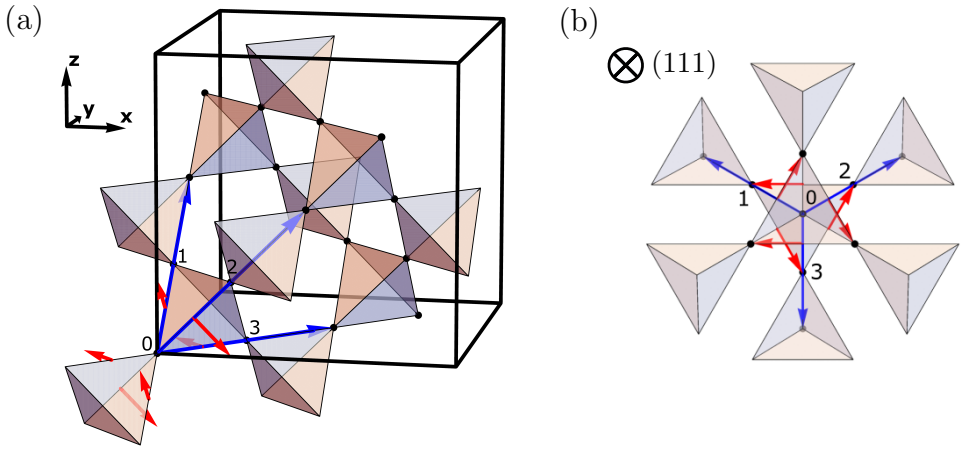

Figure 5.6: Depiction of the pyrochlore lattice. Corner-sharing tetrahedra, built up by nearest-neighbor bonds, are visualized. Primitive fcc lattice vectors are colored blue. The four basis sites are labeled. Red vectors that originate from bonds $\langle 0, j\rangle$ depict the orientations of the corresponding DMI vectors $\boldsymbol{D}_{0j}$ [see Eq. (5.9)] for a direct DMI. They are oriented coplanar in the (111) plane. (a) 16-site non-primitive simple cubic unit cell of the pyrochlore lattice. Sites within the unit cell are marked by black dots. Edges of the unit cell are depicted as black lines. (b) All six nearest neighbors of the reference site 0 and their adjacent tetrahedra are projected onto the (111) plane.

5.2 Order-by-disorder and suppression of magnetic order in the phase diagram of the pyrochlore magnet with Heisenberg and Dzyaloshinskii-Moriya interactions

We now go beyond the study of the previous section by considering not only a pyrochlore model with Heisenberg interactions, but additional DMI as well. The phase diagram of the model will be studied in detail, providing important insights on ObD selections within pyrochlore compounds and the stability of the Heisenberg model's paramagnetic ground state with respect to a finite DMI. The study of ObD will be performed in the so-called Γ_5 phase, in which the model selects a magnetic order within a one-dimensional ground state manifold of equal name [89]. Two orders within this manifold are observed to be selected by ObD, depending on the set of interactions, the temperature and whether quantum fluctuations are present: Either the so-called ψ_2 or ψ_3 order [49]. As will be explored in this section, the Γ_5 phase represents a paradigmatic example of the potential subtleties of ObD-driven selections. Furthermore, ObD selections within this phase are not only of theoretical relevance but also play a crucial role in the ground state selection of multiple pyrochlore compounds [77].

The Heisenberg-DM model studied in this section can be justified by considering the

models realizable by pyrochlore compounds. Importantly, not any kind of interaction can emerge in spin-model realizations of pyrochlore compounds. Instead, the realizable set of interactions is restricted by the symmetry properties of the lattice and the low-energy doublet on which an effective spin is defined for each lattice site. Four different types of interactions can occur between nearest neighbors if the spin doublet transforms as a magnetic dipole (or a pseudo-vector). They are given by a Heisenberg, Kitaev, Γ and DM interaction, with each being fully specified by a scalar prefactor in the general nearest-neighbor Hamiltonian [90] (the symmetry-based constraints on interactions will be treated further in Sec. 5.2.3). Note that the latter three interaction types are anisotropic under spin rotations. In this section, we will restrict ourselves to Heisenberg and DM interactions only, treating the Heisenberg-DM model

$$\hat{\mathcal{H}} = J \sum_{\langle ij \rangle} \hat{\boldsymbol{S}}_i \cdot \hat{\boldsymbol{S}}_j + \sum_{\langle ij \rangle} \boldsymbol{D}_{ij} \cdot (\hat{\boldsymbol{S}}_i \times \hat{\boldsymbol{S}}_j). \tag{5.9}$$

The orientations of DM vectors $\boldsymbol{D}_{ij}$ are fully constrained by the symmetry properties of the model, as will be derived in Sec. 5.2.3. The DM vector orientations are specified in Fig. 5.6. E.g., the DM vector $\boldsymbol{D}_{ij}$ for the bonds between sublattices $i = 0$ and $j = 1$ is given by $\boldsymbol{D}_{01} = D(0, -1, 1)$. It follows that the general parameterization of interactions in the Heisenberg-DM model is given by

$$\begin{aligned} J &= \cos(\theta), \\ D &= \sin(\theta), \end{aligned} \tag{5.10}$$

resulting in a one-dimensional phase diagram parameterized by θ. Even for this simplified model with only two interaction parameters, a rich phase diagram with multiple $T = 0$ paramagnetic phases and ObD-driven phases is obtained [49, 91, 71], including the aforementioned Γ_5 phase. From a material perspective, the consideration of a finite DMI over other types of anisotropic interactions is justified in that its size is of linear order in spin-orbit coupling in a perturbative expansion and, as such, the interaction is more relevant in the limit of small spin-orbit couplings than the Kitaev and Γ interactions, whose leading contributions are quadratic in a perturbative series [92].

We will go beyond the previous studies of the Heisenberg-DM model of Refs. [93, 94, 95] by considering both antiferromagnetic and ferromagnetic Heisenberg interactions, and by considering the $S = 1/2$ quantum model nonperturbatively beyond the large-S limit of linear spin-wave theory. Instead, the more sophisticated PFFRG method will be applied. In addition to PFFRG, multiple complementary methods will be applied as well to resolve the ObD selections in the Γ_5 phase for both the classical and quantum model in the zero and critical temperature limit.

To summarize, the Heisenberg-DM model on the pyrochlore lattice will allow us to study the stability of the paramagnetic phase surrounding the Heisenberg model and perform an extensive study on the subtleties of ObD in the Γ_5 phase. Furthermore, we will find an additional paramagnetic phase in the ferromagnetic regime $J < 0$, which is of finite extent in the phase diagram of the quantum model and will be of central importance in the following Sec. 5.3. The section will cover results of our publication Ref. [49] and will especially focus on the PFFRG perspective of the study. The main contributions of this thesis' author to Ref. [49] consist of the PFFRG-based study among other results such as the proof given in Sec. 5.2.4. In order to embed PFFRG results into the relevant context, results of the paper based on complementary methods (not produced by the author) will be replicated as well. Results of the study on the classical model, most importantly obtained by classical Monte Carlo (cMC), as well as linear spin-wave theory results, were achieved by Daniel Lozano-Gómez. High-temperature series expansion results were achieved by Rajiv R. P. Singh and Jaan Oitmaa. All authors of Ref. [49] contributed to interweaving the complementary results into a multifaceted publication.

The next subsections are organized as follows. An introduction on the phenomenon of thermal and quantum order-by-disorder will be provided in Sec. 5.2.1. Next, local and global coordinate systems of the pyrochlore lattice will be introduced in Sec. 5.2.2. As will be demonstrated later, for some purposes it will be more convenient to describe pyrochlore models in the local (site-dependent) coordinate system. The symmetry constraints on the spin model interactions are treated in Sec. 5.2.3. Importantly, the constraints will vary depending on the symmetry properties of effective spins realized by different classes of pyrochlore compounds. A classification scheme for ground state manifolds in pyrochlore nearest-neighbor spin models, previously formulated in Ref. [90], is given in Sec. 5.2.4. This scheme will provide the complete set of $T = 0$ classical phases that can occur in symmetry-constrained nearest-neighbor models on the pyrochlore lattice, and builds the theoretical foundation upon which fluctuation-based effects of state selection can be studied. Finally, Sec. 5.2.5 treats the results of Ref. [49]. To this end, the phase diagrams of both the classical and $S = 1/2$ Heisenberg-DM models will be provided and discussed in detail.

5.2.1 Thermal and quantum order-by-disorder

Because of its relevance to the Heisenberg-DM model, we discuss the phenomenon of ObD in this subsection as preparation for the study of the model. Previously, we studied the ground state of the antiferromagnetic Heisenberg model on the pyrochlore lattice. Although the interactions of the model are quite simple, unraveling its ground

state proved to be highly nontrivial, such that the exact nature of the state is still under debate. While the $S = 1/2$ Heisenberg model has long been treated as a U(1) spin liquid candidate, recent publications have gathered arguments in favor of the selection of a nematic order that breaks lattice symmetries (see Sec. 5.1 for a more in-depth discussion). The effect that drives the model to such an ordered state, even though its ground state manifold is extensive for classical spins, is called order-by-disorder. The term describes the scenario in which fluctuations, in this case of quantum origin, drive a model into a long-range order by favoring the selection of certain states out of a classically degenerate ground state manifold [5]. In this section, we are interested in the study of ObD that selects magnetically ordered ground states. In case the selection is driven by quantum fluctuations (quantum ObD), the fluctuations favor these states energetically. Closely related to quantum ObD is thermal ObD, in which thermal fluctuations entropically favor certain states of a classical ground state manifold over others. Thermal ObD selections can be intuitively understood as follows. All ground states of a classical model have an equal probability to be realized at $T = 0$. However, a small but finite $T > 0$ allows thermal fluctuations into energetically excited states that are close by. The thermal fluctuations into energetically excited states about a classical ground state configuration result in an additional entropy contribution associated with that respective ground state. It follows that a ground state with many low-lying excitations accessible by thermal fluctuations will be entropically favored in state selection. In short, the ground state selection at low temperatures depends not only on the ground state manifold but also on the close-by energy landscape surrounding it. The ObD effect leads to the seemingly paradoxical situation that while fluctuations may be necessary for a system to assume a long-range order, fluctuations that are too strong can have the opposite effect, causing the system to remain in a disordered phase.

Generally, ObD selections of a model need to be distinguished between different scenarios. While the thermal ObD selection near $T = 0$ may be straightforward to determine, it does not have to coincide with the selection at higher temperatures below the critical temperature T_c. In case a model is not classical, quantum and thermal ObD effects are intertwined. Quantum ObD transforms the energy landscape for classical states of a model, whereas thermal ObD acts on top of the new landscape[2]. The complex interplay between thermal and quantum fluctuations may complicate the ground state selection, as both types of fluctuations do not necessarily cooperate towards the selection of the same order [96]. In our study of the Heisenberg-DM model, one can broadly distinguish between four different cases for which ObD selections may differ. These are given by selections at infinitesimal temperature $T = 0^+$ or critical temperature $T \approx T_c$, and in presence or absence of quantum fluctuations. The classical model allows the

[2]Note that this is a simplified picture, as quantum fluctuations can also stabilize states without any classical analogue.

straightforward study of purely thermal ObD from the temperature of the phase transition T_c down to the zero-temperature limit by performing cMC simulations. State selections found near $T = 0$ can be solidified by applying low-temperature expansions about candidate spin configurations [49]. In the $S = 1/2$ quantum model, the study of ObD is methodologically more challenging. Predictions of the $T = 0$ ObD selections can be obtained by applying linear spin-wave theory. To determine the ObD selections at $T = T_c$, we apply both PFFRG and high-temperature series expansions (HTSE).

The selection within PFFRG is inferred from the magnetic susceptibility at the critical cutoff Λ_c. Strictly speaking, the cutoff does not correspond to a temperature. However, due to their similarities (see Sec. 3.5.4), we interpret the order selection at Λ_c as that of the quantum model at $T = T_c$, rather than at $T = 0$. As will be proven in Sec. 5.2.4, magnetic susceptibilities are only able to partially resolve the ground state selection within the ground state manifold of the Γ_5 phase. The necessary observables required to fully resolve state selections within the Γ_5 phase are not accessible within PFFRG due to the truncation of flow equations. However, HTSE will allow for a resolution of ObD state selections where the PFFRG fails by providing observables that are of up to sixth order in spin operators.

At last, we note that the strong geometrical frustration present in spin models on the pyrochlore lattice, realized by the arrangement of lattice sites in corner-sharing tetrahedra, provides ideal conditions for the realization of ObD. As a general property, frustration leads to accidental ground state degeneracies in classical spin models [1]. In case the classical ground state manifold is large, as is the case in the extensive manifold of the pyrochlore Ising model, any kind of magnetic order can be prevented down to $T = 0$, which may lead to the emergence of a spin-liquid phase at low temperatures. In case of a smaller ground state manifold, thermal or quantum fluctuations are more likely to drive a model into a magnetically ordered phase. ObD is the guiding principle in the selection of this symmetry-breaking ground state. Thus, the presence of frustration enables the ObD phenomenon by creating accidental degeneracies.

5.2.2 Local and global coordinate systems

While spin models are often expressed in a global site-independent coordinate system, the choice of coordinates is free in principle. On the pyrochlore lattice, it is often advantageous to assume a local site-dependent coordinate system. E.g., many relevant magnetic orders of this section simplify if they are expressed in the local coordinate system. This includes the spin configurations of the Γ_5 manifold, which correspond to ferromagnetic arrangements in the local x-y plane. The sublattice-dependent basis

vectors of the local coordinate system are given by [97]

$$\begin{aligned}
\boldsymbol{x}_0 &= \frac{1}{\sqrt{6}}\begin{pmatrix}-2\\1\\1\end{pmatrix}, \quad \boldsymbol{y}_0 = \frac{1}{\sqrt{2}}\begin{pmatrix}0\\-1\\1\end{pmatrix}, \quad \boldsymbol{z}_0 = \frac{1}{\sqrt{3}}\begin{pmatrix}1\\1\\1\end{pmatrix}, \\
\boldsymbol{x}_1 &= \frac{1}{\sqrt{6}}\begin{pmatrix}-2\\-1\\-1\end{pmatrix}, \quad \boldsymbol{y}_1 = \frac{1}{\sqrt{2}}\begin{pmatrix}0\\1\\-1\end{pmatrix}, \quad \boldsymbol{z}_1 = \frac{1}{\sqrt{3}}\begin{pmatrix}-1\\1\\1\end{pmatrix}, \\
\boldsymbol{x}_2 &= \frac{1}{\sqrt{6}}\begin{pmatrix}2\\1\\-1\end{pmatrix}, \quad \boldsymbol{y}_2 = \frac{1}{\sqrt{2}}\begin{pmatrix}0\\-1\\-1\end{pmatrix}, \quad \boldsymbol{z}_2 = \frac{1}{\sqrt{3}}\begin{pmatrix}1\\-1\\1\end{pmatrix}, \\
\boldsymbol{x}_3 &= \frac{1}{\sqrt{6}}\begin{pmatrix}2\\-1\\1\end{pmatrix}, \quad \boldsymbol{y}_3 = \frac{1}{\sqrt{2}}\begin{pmatrix}0\\1\\1\end{pmatrix}, \quad \boldsymbol{z}_3 = \frac{1}{\sqrt{3}}\begin{pmatrix}1\\1\\-1\end{pmatrix}.
\end{aligned} \tag{5.11}$$

The sublattices are defined in Fig. 5.6. The local z-axis vector $\boldsymbol{z}_i$ is oriented towards (away from) the center of the adjacent up (down) tetrahedra, previously introduced in Fig. 5.1. Importantly, the full set of local z axis vectors $\boldsymbol{z}_i$ remains invariant under the application of spin model symmetries in pyrochlore compounds, whereas the full set of local x and y axis vectors, given by $\boldsymbol{x}_i$ and $\boldsymbol{y}_i$, generally transforms under the application of symmetries. It will be shown in the following subsection that in the local coordinate system pyrochlore compounds can realize interactions $\hat{S}_i^z \hat{S}_j^z$ of the Ising model given by Eq. (5.1), as well as a continuous interpolation between the Ising and Heisenberg models in the form of an XXZ model with interactions $\alpha(\hat{S}_i^x \hat{S}_j^x + \hat{S}_i^y \hat{S}_j^y) + \hat{S}_i^z \hat{S}_j^z$ (with $\alpha \in \mathbb{R}$). In contrast, symmetry properties of pyrochlore compounds do not allow for a realization of the Ising model in the global coordinate system. Instead, a $\hat{S}_i^z \hat{S}_j^z$ interaction on a nearest-neighbor bond $\langle i, j\rangle$ implies Kitaev interactions $\hat{S}_i^\mu \hat{S}_j^\mu$, with bond-dependent $\mu \in \{x, y, z\}$, on the full lattice if the model is expressed in the global coordinate system. Note that while the Heisenberg model in the global coordinate system can be realized by pyrochlore compounds with small spin-orbit coupling, a Heisenberg model in the local coordinate system implies strong spin-orbit coupling, since the Heisenberg interactions in the local coordinate system become strongly anisotropic if they are expressed in the global coordinate system.

5.2.3 Symmetry-constrained nearest-neighbor models

We now introduce the symmetry-constrained nearest-neighbor spin models realized by pyrochlore compounds, restricting ourselves to bilinear spin interactions only. The

Heisenberg-DM model represents a simplification of these models, which have additional interaction types. The introduced models will further be relevant in Sec. 5.3 when models of non-Kramers pyrochlores are considered. Note that the spin models considered here are to be understood as low-energy effective models of Mott-insulating pyrochlore compounds. As such, the spin models and the spin operators themselves, with the latter being built from local low-energy doublets, have to reflect symmetry properties of the compounds on which they are based. For simplicity in notation, spin components will be formulated as being classical in this subsection, i.e., they are given by scalars S^μ instead of quantum operators $\hat{S}^\mu$.

Underlying the existence of many symmetry-allowed interactions in effective spin models is spin-orbit coupling. As the name suggests, spin-orbit coupling couples spin degrees of freedom to real-space orientations and thereby allows for the emergence of anisotropic interactions in effective spin models. Vice versa, if no spin-orbit coupling is present, spin degrees of freedom are not coupled to real space. As a consequence, they can only interact through isotropic Heisenberg interactions $J_{ij}\boldsymbol{S}_i\boldsymbol{S}_j$ in this case. In the presence of spin-orbit coupling, the scalar J_{ij}, quantifying the isotropic Heisenberg interactions, is promoted to a 3×3 matrix $\boldsymbol{J}_{ij}$. The resulting unconstrained nearest-neighbor Hamiltonian is then given by

$$\mathcal{H} = \sum_{\langle ij \rangle} \boldsymbol{S}_i^T \boldsymbol{J}_{ij} \boldsymbol{S}_j. \tag{5.12}$$

Symmetry transformations of a model constrain the interaction matrices $\boldsymbol{J}_{ij}$. Starting from unconstrained interaction matrices $\boldsymbol{J}_{ij}$, we will argue in the following how symmetries constrain $\boldsymbol{J}_{ij}$ in pyrochlore compounds. The sublattice and lattice vector conventions specified in Fig. 5.6 will be used.

Trivially, we know that interactions $\boldsymbol{J}_{ij}$ and $\boldsymbol{J}_{kl}$ of different bonds $\langle i, j \rangle$ and $\langle k, l \rangle$ can be related to each other by finding a symmetry transformation that maps $\langle i, j \rangle$ onto $\langle k, l \rangle$. E.g., such a symmetry may be given by a lattice translation. In case of the pyrochlore lattice, lattice symmetries allow all nearest-neighbor bonds to be mapped onto one another. It follows that one $\boldsymbol{J}_{ij}$ of a single bond $\langle i, j \rangle$ specifies all interactions of the full nearest-neighbor model[3,4].

The general form of $\boldsymbol{J}_{ij}$ on a single bond $\langle i, j \rangle$ in particular can be constrained by

[3] Likewise, all second-nearest-neighbor bonds can be mapped onto one another under the application of lattice symmetries. Hence, all their interactions are implied as well by giving $\boldsymbol{J}_{ij}$ for only a single bond. For third nearest neighbors, however, there exist two symmetry-inequivalent types of bonds. It follows that there exist two independent third-nearest-neighbor interaction matrices $\boldsymbol{J}_{ij}$ [98].

[4] Note that we consider spin models on ideal pyrochlore lattices. This case is not to be confused with that of the similar breathing pyrochlore lattice, in which up and down tetrahedra are not related by symmetries and exhibit different nearest-neighbor interactions as a consequence [98].

applying symmetry transformations that map the bond $\langle i,j\rangle$ onto itself, provided that the symmetry transformations involve nontrivial spin transformations. The transformations may apply a combination of lattice rotation, inversion, reflection or translation symmetries. Importantly, since we are considering the case in which spin components are coupled to real-space orientations via spin-orbit coupling, lattice symmetry operations generally transform not only real-space coordinates but spin components as well. The manner in which the spin components transform depends on the symmetry properties of the underlying doublets on which the effective spins are defined. Depending on the pyrochlore compound, different components S^μ of an effective-spin vector $\boldsymbol{S}$ may even exhibit different transformation properties [77].

In the following, we will first assume the case that the spins transform as magnetic dipoles, i.e., as pseudo-vectors. If a global SO(3) real-space rotation given by the matrix $\boldsymbol{U}$ is applied, then a spin transforms as $\boldsymbol{S}_i \to \boldsymbol{U}\boldsymbol{S}_i$. A comparison with Eq. (5.12) reveals that the spin transformation can always be recast as an interaction matrix transformation $\boldsymbol{J}_{ij} \to \boldsymbol{U}^T\boldsymbol{J}_{ij}\boldsymbol{U}$ instead. In short, the strategy in deriving the general form of $\boldsymbol{J}_{ij}$ for a bond $\langle i,j\rangle$ is to first identify all M symmetry operations that map the bond $\langle i,j\rangle$ onto itself, then gathering the rotation matrices $\boldsymbol{U}_k$, with $k = 1,\ldots,M$, associated with these operations, and then solving the set of constraints $\boldsymbol{J}_{ij} = \boldsymbol{U}_k^T\boldsymbol{J}_{ij}\boldsymbol{U}_k$. E.g., in case of no spin-orbit coupling, the model exhibits a global SO(3) spin rotation symmetry, since spin degrees of freedom are not coupled to real space. Trivially, this pure spin rotation symmetry operation leaves all lattice bonds invariant and can thus be applied to constrain $\boldsymbol{J}_{ij}$. Requiring $\boldsymbol{J}_{ij}$ to be invariant under any transformation $\boldsymbol{J}_{ij} \to \boldsymbol{U}^T\boldsymbol{J}_{ij}\boldsymbol{U}$, with $\boldsymbol{U}$ being an arbitrary SO(3) spin rotation matrix, implies a pure Heisenberg interaction $\boldsymbol{J}_{ij} = J_{ij}\mathbb{1}$.

In the general case of dipolar spins on a pyrochlore lattice, the symmetry-constrained $\boldsymbol{J}_{ij}$ for nearest neighbors contains four different types of interactions. We first state the explicit matrix expressions and explain them afterwards. In the global coordinate system, the interaction matrices $\boldsymbol{J}_{ij}$, coupling spins between sublattices i and j (see Fig. 5.6), are given by

$$\boldsymbol{J}_{01} = \begin{pmatrix} J+K & D & D \\ -D & J & \Gamma \\ -D & \Gamma & J \end{pmatrix}, \quad \boldsymbol{J}_{02} = \begin{pmatrix} J & -D & \Gamma \\ D & J+K & D \\ \Gamma & -D & J \end{pmatrix}, \quad \boldsymbol{J}_{03} = \begin{pmatrix} J & \Gamma & -D \\ \Gamma & J & -D \\ D & D & J+K \end{pmatrix},$$
$$\boldsymbol{J}_{12} = \begin{pmatrix} J & -\Gamma & D \\ -\Gamma & J & -D \\ -D & D & J+K \end{pmatrix}, \boldsymbol{J}_{23} = \begin{pmatrix} J+K & -D & D \\ D & J & -\Gamma \\ -D & -\Gamma & J \end{pmatrix}, \boldsymbol{J}_{31} = \begin{pmatrix} J & -D & -\Gamma \\ D & J+K & -D \\ -\Gamma & D & J \end{pmatrix}, \tag{5.13}$$

with J, K, D, Γ being scalars (or a pseudoscalar in the case of D) that quantify the Heisenberg, Kitaev, Dzyaloshinskii-Moriya, and Γ interactions, respectively [97, 90]. Note that the interactions of bonds depend only on the sublattices involved and not on whether the bonds lie on an up or down tetrahedron. Hence, we only specify $\boldsymbol{J}_{ij}$ for 6 of the 12 nearest-neighbor bonds unequal by translation symmetries. Also, note that the order of sublattice indices in $\boldsymbol{J}_{ij}$ matters due to the antisymmetric matrix entries $\pm D$ that correspond to a DMI. The interaction matrices satisfy $J_{ij}^{\mu\nu} = J_{ji}^{\nu\mu}$.

The relations between the interaction matrices on different bonds are understood from symmetry operations as follows. Nearest-neighbor bonds $\langle 0,1\rangle$, $\langle 0,2\rangle$ and $\langle 0,3\rangle$ of an up tetrahedron are mapped onto one another by applying the C_3 lattice rotation symmetry about the [111] axis going through the 0 sublattice. This symmetry operation relates the respective matrices $\boldsymbol{J}_{01}$, $\boldsymbol{J}_{02}$ and $\boldsymbol{J}_{03}$. Since the spins transform as magnetic dipoles, the C_3 symmetry operation cyclically permutes spin components S^μ (or, similarly, interaction matrix components $J_{ij}^{\mu\nu}$). Likewise, the bonds $\langle 1,2\rangle$, $\langle 2,3\rangle$ and $\langle 3,1\rangle$ of an up tetrahedron are mapped onto one another by applying the same C_3 rotation symmetry, relating the matrices $\boldsymbol{J}_{12}$, $\boldsymbol{J}_{23}$ and $\boldsymbol{J}_{31}$ in the process. Finally, the $\langle 0,1\rangle$ and $\langle 3,2\rangle$ bonds of a tetrahedron are mapped onto one another by a C_2 rotation about the global z axis, with the axis going through the midpoints of the $\langle 1,2\rangle$ and $\langle 0,3\rangle$ bonds on the same tetrahedron. Such a rotation leaves S^z unaffected and changes the sign of the remaining spin components ($S^x \to -S^x$ and $S^y \to -S^y$). Bonds of up and down tetrahedra are mapped onto one another by inversion symmetry with respect to a lattice site. Inversion symmetry leaves the spins (pseudo-vectors) unaffected. Thus, we have related the interaction matrices $\boldsymbol{J}_{ij}$ of all bonds $\langle i,j\rangle$ unequal by translation symmetries.

Symmetry restrictions on the DMI

While we have so far only stated the most general symmetry-constrained interactions $\boldsymbol{J}_{ij}$ and related their expressions for different $\langle i,j\rangle$ to symmetry operations, we will now further consider the constrained $\boldsymbol{J}_{ij}$ for a single bond. Since we are interested in studying the Heisenberg-DM model, we consider how the DMI is constrained in particular. The DMI corresponds to the anisotropic component of $\boldsymbol{J}_{ij}$ that is antisymmetric under the exchange of spins ($i \leftrightarrow j$ leads to $D \leftrightarrow -D$ in $\boldsymbol{J}_{ij}$) [92]. If we consider only a finite DMI and set the remaining interactions to zero, a general unconstrained

interaction matrix is given by

$$\boldsymbol{J}_{\mathrm{DMI,ij}} = \begin{pmatrix} 0 & D_{ij}^z & -D_{ij}^y \\ -D_{ij}^z & 0 & D_{ij}^x \\ D_{ij}^y & -D_{ij}^x & 0 \end{pmatrix}. \tag{5.14}$$

Due to its property of being antisymmetric, any DMI can always be expressed by a vector $\boldsymbol{D}_{ij}$, such that the interaction reads as

$$\boldsymbol{S}_i^T \boldsymbol{J}_{\mathrm{DMI,ij}} \boldsymbol{S}_j = \boldsymbol{D}_{ij} \cdot (\boldsymbol{S}_i \times \boldsymbol{S}_j). \tag{5.15}$$

In our case, symmetries fully restrict the orientations of $\boldsymbol{D}_{ij}$ to those specified in Fig. 5.6. The restrictions can be derived from pyrochlore reflection symmetries, as done in Ref. [93], by applying so-called Moriya's rules [92]. Alternatively, rotation and inversion symmetries can be applied to constrain the form of $\boldsymbol{D}_{ij}$ as follows. By employing inversion symmetry and a C_2 symmetry about the $[0\bar{1}1]$ axis passing through the sublattice 0, the $\langle 0,1\rangle$ nearest-neighbor bond maps onto itself. Spin components S_i^y and S_i^z permute under this operation. The DMI matrix $\boldsymbol{J}_{\mathrm{DMI,01}}$ of Eq. (5.14) has to remain invariant under the corresponding permutations of matrix entries (e.g., $J_{\mathrm{DMI,01}}^{xy} = J_{\mathrm{DMI,01}}^{xz}$ implies $D_{01}^z = -D_{01}^y$, and $J_{\mathrm{DMI,01}}^{yz} = J_{\mathrm{DMI,01}}^{zy}$ implies $D_{01}^x = 0$). It follows that the DM vector is fixed as $\boldsymbol{D}_{01} = D(0,-1,1)$. One can distinguish between the two cases of a so-called direct and indirect DMI, corresponding to the cases $D > 0$ and $D < 0$ respectively. Each can lead to vastly different ordering behavior [93], as will be seen in the phase diagram of the Heisenberg-DM model.

Effective spin realizations in pyrochlore compounds

In the previous discussion on the symmetry-constrained interactions, we assumed that spin components transform as magnetic dipoles. However, this is often not the case in spin models realized by pyrochlore compounds [77]. Here, we give an overview on three different effective-spin realizations found in pyrochlores. To better distinguish the differences between realizable interactions for these different classes of pyrochlores, we express their symmetry-constrained spin models in the local coordinate system. In this local frame, the general nearest-neighbor model for dipolar spins is given by [97]

$$\begin{aligned} \mathcal{H} = \sum_{\langle ij \rangle} & J^{zz} S_i^z S_j^z - J^{\pm}(S_i^+ S_j^- + S_i^- S_j^+) \\ & + J^{\pm\pm}(\gamma_{ij} S_i^+ S_j^+ + \gamma_{ij}^* S_i^- S_j^-) \\ & + J^{z\pm}[S_i^z(\zeta_{ij} S_j^+ + \zeta_{ij}^* S_j^-) + i \leftrightarrow j], \end{aligned} \tag{5.16}$$

with

$$\boldsymbol{\zeta} = \begin{pmatrix} 0 & -1 & e^{i\pi/3} & e^{-i\pi/3} \\ -1 & 0 & e^{-i\pi/3} & e^{i\pi/3} \\ e^{i\pi/3} & e^{-i\pi/3} & 0 & -1 \\ e^{-i\pi/3} & e^{i\pi/3} & -1 & 0 \end{pmatrix}, \qquad \boldsymbol{\gamma} = -\boldsymbol{\zeta}^*. \tag{5.17}$$

The matrix entries ζ_{ij} are determined by the sublattices of lattice sites i and j. The interactions of the local and global frame are related by

$$\begin{aligned} J^{zz} &= -\frac{1}{3}[J - K + 2(\Gamma + 2D)], \\ J^{\pm} &= \frac{1}{6}(J - K - \Gamma - 2D), \\ J^{\pm\pm} &= \frac{1}{6}[2J + K - 2(\Gamma + D)], \\ J^{z\pm} &= \frac{1}{3\sqrt{2}}(2J + K + \Gamma - D). \end{aligned} \tag{5.18}$$

While pyrochlore compounds like $Er_2Ti_2O_7$ or $Yb_2Ti_2O_7$, with effective spins transforming as dipoles, realize Hamiltonians of the form shown in Eq. (5.16), other classes of compounds enforce simplified versions [77].

In compounds such as $Ce_2Zr_2O_7$ [99] and $Nd_2Zr_2O_7$ [100], spins are built from dipolar-octupolar doublets. While, in the local coordinate system, spin components S^x and S^z behave as components of a magnetic dipole, S^y transforms like a component of a magnetic octupole tensor under the application of lattice symmetries (or, alternatively formulated, $S^{\pm}$ behave as components of an octupole tensor) [101]. These transformation properties lead to different symmetry constraints on the interactions compared to the case of purely dipolar spins, such that the most general nearest-neighbor Hamiltonian for dipolar-octupolar pyrochlores is given by

$$\mathcal{H}_{\mathrm{DO}} = \sum_{\langle ij \rangle} J^{xx} S_i^x S_j^x + J^{yy} S_i^y S_j^y + J^{zz} S_i^z S_j^z + J^{xz}(S_i^x S_j^z + S_i^z S_j^x) \tag{5.19}$$

in the local coordinate system. Note that the interactions are equal on each nearest-neighbor bond. An additional spin rotation by an angle of $\theta = \arctan[2J^{xz}/(J^{xx} - J^{zz})]/2$ to new spin components

$$\begin{aligned} S_i^{\tilde{x}} &= \cos(\theta)\mathrm{S_i^x} + \sin(\theta)\mathrm{S_i^z}, \\ S_i^{\tilde{y}} &= S_i^y, \\ S_i^{\tilde{z}} &= \cos(\theta)\mathrm{S_i^z} - \sin(\theta)\mathrm{S_i^x} \end{aligned} \tag{5.20}$$

allows to eliminate the J^{xz} interaction term, simplifying the Hamiltonian to a XYZ model in the process [102]. The actual effective spin properties in dipolar-octupolar compounds are actually even a little bit more intricate. While the spin component S^x transforms as a magnetic dipole under the application of lattice symmetries, it does not have a finite magnetic dipole moment, i.e., it has a g factor of $g^{xx} = 0$. To leading order, S^x actually only contributes to the magnetic octupole moment operator in a multipole expansion that is projected onto the Hilbert space of the low-energy doublet on which the effective spin is defined [103, 104]. Since both the S^x and S^y components do not possess a finite g factor, neutrons, to leading order, only scatter along the local S^z component.

Another class of pyrochlore compounds realizes non-Kramers doublets and will be treated in Sec. 5.3. In such compounds, spin components S^x and S^y transform as components of a magnetic quadrupole moment, whereas the remaining S^z component transforms as a the component of a magnetic dipole [77]. It follows from these particular properties that $S^{\pm}$ is even under time reversal, whereas S^z is odd. As a direct consequence, the $J^{z\pm}$ interaction in Eq. (5.16) has to vanish by the enforcement of time-reversal symmetry. Apart from a vanishing $J^{z\pm} = 0$, the symmetry-constrained Hamiltonian of these so-called non-Kramers pyrochlores is given by Eq. (5.16). Like for dipolar-octupolar compounds, the g tensor of an effective spin in non-Kramers compounds has a finite entry only for the local z spin component [77]. It follows that only this component is scattered upon in neutron scattering experiments.

Material perspective

Even considering only interactions bilinear in spin operators, the symmetry-constrained Hamiltonian for dipolar spins on the pyrochlore lattice, given by Eq. (5.12), allows for three types of different anisotropic interactions, fully specified by the parameters K, Γ and D. Our aim is not only to consider anisotropic interactions in the perturbative limit $K, \Gamma, D \ll J$ but, in context of the Heisenberg-DM model, to uncover the full phase diagram spanned by Heisenberg and DM interactions J and D. How justified is the study of this model over the full regime of D/J in the context of experimentally available pyrochlore compounds? Some considerations on this question are given in the following.

As mentioned previously, anisotropic interactions are realized by a finite spin-orbit coupling. In the perturbative limit of small spin-orbit coupling, it had been shown in Ref. [92] that anisotropic interactions $J_{ij}^{\mu\nu}$ bilinear in spin operators and odd under spin exchange ($J_{ij}^{\mu\nu} = -J_{ji}^{\mu\nu}$), known as DMI, scale linearly with the size of spin-orbit

coupling. In contrast, anisotropic interactions that are invariant under spin exchange ($J_{ij}^{\mu\nu} = J_{ji}^{\mu\nu}$), such as Kitaev or Γ terms, scale quadratically. Hence, the consideration of a finite DMI over other types of anisotropic interactions is justified in the case of small spin-orbit coupling.

Since the size of spin-orbit coupling in an atom scales quartically with its nuclear charge [105], the perturbative limit $D \ll J$ can be overcome by compounds that feature magnetic ions of heavier elements. In these systems, the picture of small anisotropic interactions in the background of an isotropic Heisenberg model generally does not hold, and effective spin models throughout the entire interaction parameter space D/J can be realized in principle. Note that the consideration of a finite DMI over a Kitaev or Γ interaction is no longer justified from a material perspective if the perturbative picture with $K, \Gamma, D \ll J$ has already broken down due to strong spin-orbit coupling.

The perturbative picture of a small D/J can be applied to pyrochlore compounds based on 3d transition metals as magnetic ions [106, 107]. In contrast, rare-earth pyrochlore systems with magnetic ions based on heavier 4f transition metals are able to realize strong anisotropic interactions. Some examples of rare-earth compounds that are argued to realize effective $S = 1/2$ models are given by $Er_2Ti_2O_7$ [108], $Er_2Sn_2O_7$ [109], $Yb_2Ge_2O_7$ [110] and $Yb_2Ti_2O_7$ [111]. See Ref. [77] for a comprehensive review on the low-energy physics of rare-earth pyrochlores.

5.2.4 Irreducible-representation-based decomposition of states

After having introduced the symmetry-constrained spin model on the pyrochlore lattice given by Eqs. (5.12)-(5.13), we can now study its low-energy behavior. As a first step, it will be useful to describe the structure of the model's classical ground state manifolds. Generally, determining the classical ground state manifold of a frustrated spin model is nontrivial. In case of a nearest-neighbor spin model on the pyrochlore lattice, the problem can be solved elegantly by applying concepts of group theory, as shown in Ref. [90]. In this subsection, we will follow along the proposed decomposition of the $\boldsymbol{q} = \boldsymbol{0}$ state space, formulated in Ref. [90], that classifies manifolds with respect to irreducible representations (irreps) of the tetrahedral point group. At a later point, we will apply the scheme for the Heisenberg-DM model. The presented decomposition of manifolds will provide the foundation for more advanced studies that investigate the effects of thermal and quantum fluctuations on state selections.

The first simplification in the description of ground state manifolds consists of the proof that the classical nearest-neighbor model on the pyrochlore lattice given by Eq. (5.12) always possesses a $\boldsymbol{q} = \boldsymbol{0}$ ground state, i.e., a ground state with a four-site unit

cell containing only the spins of a single up tetrahedron. This property simplifies the problem of finding ground states on the pyrochlore lattice to that of finding ground states on a single tetrahedron, and is a prerequisite for the ground state description via irreps of the tetrahedral point group. While the proof for the existence of $\boldsymbol{q} = \boldsymbol{0}$ ground states is only valid for classical spins, we will only observe $\boldsymbol{q} = \boldsymbol{0}$ ground states in later applications on the quantum model as well. Therefore, an irrep decomposition of states is the appropriate framework to study both the classical and quantum model. The proof of Ref. [90] for the existence of $\boldsymbol{q} = \boldsymbol{0}$ ground states goes as follows: The pyrochlore lattice is built by *corner-sharing* tetrahedra, with up and down tetrahedra building a bipartite lattice. Since the tetrahedra are corner-sharing, if each tetrahedron itself is simultaneously in a ground state configuration, so is the full lattice. One can now find a four-site ground state configuration for a single up tetrahedron and configure the spins on every up tetrahedron of the lattice (i.e, every spin of the lattice) in this configuration. This results in a spin configuration of the lattice in which all up tetrahedra are in their ground state. It can be proven that all down tetrahedra are then in a ground state configuration as well by the argument that the lattice inversion symmetry maps each up on a down tetrahedron and vice versa while leaving interactions and spin configurations invariant. Thus, the whole lattice is in a ground state, which proves that a classical $\boldsymbol{q} = \boldsymbol{0}$ ground state always exists.

Next, one can consider the interaction-dependent ground state manifolds on a single tetrahedron. Importantly, classically degenerate state manifolds on a single tetrahedron t can be characterized by different real order parameters $\boldsymbol{m}_{\Psi,t}$ that transform with nontrivial irreps Ψ of the tetrahedral point group [90]. This is implied by a rewriting of the full lattice Hamiltonian given by Eq. (5.12) in terms of $\boldsymbol{m}_{\Psi,t}$, as will be shown below. The order parameters $\boldsymbol{m}_{\Psi,t}$ are built from linear combinations of spin components S_i^μ, involving each site i on a tetrahedron t, and will be specified later. The full lattice Hamiltonian, rewritten in terms of $\boldsymbol{m}_{\Psi,t}$, is given by [90]

$$\mathcal{H} = \sum_t a_{A_2} m_{A_2,t}^2 + a_E \boldsymbol{m}_{E,t}^2 + a_{T_2} \boldsymbol{m}_{T_2,t}^2 + a_{T_{1||}} \boldsymbol{m}_{T_{1||},t}^2 + a_{T_{1\perp},t} \boldsymbol{m}_{T_{1\perp},t}^2 + a_{T_{1||\perp}} \boldsymbol{m}_{T_{1||},t} \cdot \boldsymbol{m}_{T_{1\perp},t}. \tag{5.21}$$

The sum goes over all up and down tetrahedra t of the lattice. Note that the T_1 irrep appears in the two different order parameters $\boldsymbol{m}_{T_{1||},t}$ and $\boldsymbol{m}_{T_{1\perp},t}$. The parameters a_Ψ corresponding to the energies associated with different irreps Ψ are given by

$$\begin{aligned} a_{A_2} &= -J + K - 2(\Gamma + 2D), & a_E &= -J + K + \Gamma + 2D, \\ a_{T_2} &= -J - K + \Gamma - 2D, & a_{T_{1||}} &= 3J + K, \\ a_{T_{1\perp}} &= -J - K - \Gamma + 2D, & a_{T_{1||\perp}} &= -\sqrt{8}\Gamma. \end{aligned} \tag{5.22}$$

Alternatively, expressed in terms of the interactions of the local coordinate system, they are given by

$$\begin{aligned}
a_{A_2} &= 3J^{zz}, \\
a_E &= -6J^{\pm}, \\
a_{T_2} &= 2(J^{\pm} - 2J^{\pm\pm}), \\
a_{T_{1||}} &= \frac{1}{3}(-J^{zz} + 4J^{\pm} + 8J^{\pm\pm} + 8\sqrt{2}J^{z\pm}), \\
a_{T_{1\perp}} &= \frac{2}{3}(-J^{zz} + J^{\pm} + 2J^{\pm\pm} - 4\sqrt{2}J^{z\pm}), \\
a_{T_{1||\perp}} &= -\frac{\sqrt{8}}{3}(-J^{zz} - 2J^{\pm} - 4J^{\pm\pm} + 2\sqrt{2}J^{z\pm}).
\end{aligned} \tag{5.23}$$

In the Heisenberg-DM model, $a_{T_{1||\perp}}$ vanishes since $\Gamma = 0$. Otherwise, the last interaction term in $\mathcal{H}$, which mixes between the two different order parameters $\boldsymbol{m}_{T_{1||},t}$ and $\boldsymbol{m}_{T_{1\perp},t}$, can always be eliminated by performing the substitution

$$\begin{aligned}
\boldsymbol{m}_{T_{1,A},t} &= \cos(\alpha)\boldsymbol{m}_{T_{1||},t} - \sin(\alpha)\boldsymbol{m}_{T_{1\perp},,t}, \\
\boldsymbol{m}_{T_{1,B},t} &= \sin(\alpha)\boldsymbol{m}_{T_{1||},t} + \cos(\alpha)\boldsymbol{m}_{T_{1\perp},t},
\end{aligned} \tag{5.24}$$

with

$$\alpha = \frac{1}{2}\arctan\left(\frac{\sqrt{8}\Gamma}{4J + 2K + \Gamma - 2D}\right). \tag{5.25}$$

Afterwards, we are left with a Hamiltonian that contains only terms quadratic in a single irrep order parameter and is given by

$$\mathcal{H} = \sum_t a_{A_2} m_{A_2,t}^2 + a_E \boldsymbol{m}_{E,t}^2 + a_{T_2}\boldsymbol{m}_{T_2,t}^2 + a_{T_{1,A}}\boldsymbol{m}_{T_{1,A},t}^2 + a_{T_{1,B}}\boldsymbol{m}_{T_{1,B},t}^2. \tag{5.26}$$

The $\boldsymbol{q} = \boldsymbol{0}$ ground state manifold can be determined straightforwardly from this formulation of the spin model by expressing the spin length constraint in terms of $\boldsymbol{m}_\Psi$. The constraint is given by

$$m_{A_2,t}^2 + \boldsymbol{m}_{E,t}^2 + \boldsymbol{m}_{T_2,t}^2 + \boldsymbol{m}_{T_{1,A},t}^2 + \boldsymbol{m}_{1,B,t}^2 = 1 \tag{5.27}$$

on a tetrahedron t. It is now apparent how to identify the classical $\boldsymbol{q} = \boldsymbol{0}$ ground state manifolds of the Hamiltonian given by Eq. (5.26). The combination of Eq. (5.26) and Eq. (5.27) reveals that the ground state manifold is given by the states that maximize the absolute order parameters $|\boldsymbol{m}_{\Psi,t}|$ with the minimum corresponding prefactor a_Ψ, where $\Psi \in \{A_2, E, T_2, T_{1,A}, T_{1,B}\}$.

Since tetrahedra of the lattice are corner sharing, specifying the ground state configuration that maximizes $|\boldsymbol{m}_{\Psi,t}|$ of a minimum a_Ψ for a single tetrahedron t restricts the

ground state configurations that the adjacent tetrahedra can assume. In case only a single minimum irrep parameter a_Ψ exists, the system usually has no tiling degrees of freedom in the sense that specifying the ground state configuration of a single tetrahedron uniquely specifies the ground state of the full lattice model. The ground state degeneracy on a single tetrahedron is then equal to the ground state degeneracy of the full lattice. However, in case multiple a_Ψ of minimum value exist, there may exist a degree of freedom for the ground state configuration of the lattice that allows the tiling of tetrahedra with different ground state configurations throughout the lattice [90] (similar to the previous situation of spin ice, where there exist six ground state configurations on a single tetrahedron, but an extensive ground state manifold on the full lattice). Examples of nontrivial ground state tilings will emerge in Sec. 5.3.

Order parameters and ground state manifolds

We now present the irrep order parameters $\boldsymbol{m}_\Psi$ and the classical states that maximize them. The irrep order parameters, defined on a tetrahedron t and formulated as in Ref. [39], are given in the global coordinate system by

$$\begin{aligned}
m_{A_2,t} &= \frac{1}{2}\sum_{i\in t} \boldsymbol{z}_i \cdot \boldsymbol{S}_{ti}, \\
\boldsymbol{m}_{E,t} &\coloneqq \begin{pmatrix} m_{\psi_2} \\ m_{\psi_3} \end{pmatrix} = \frac{1}{2}\sum_{i\in t} \begin{pmatrix} \boldsymbol{x}_i \cdot \boldsymbol{S}_{ti} \\ \boldsymbol{y}_i \cdot \boldsymbol{S}_{ti} \end{pmatrix}, \\
\boldsymbol{m}_{T_2,t} &= \frac{\sqrt{3}}{2\sqrt{2}}\sum_{i\in t} \begin{pmatrix} (\boldsymbol{z}_i \times \boldsymbol{S}_{ti})^x \\ (\boldsymbol{z}_i \times \boldsymbol{S}_{ti})^y \\ (\boldsymbol{z}_i \times \boldsymbol{S}_{ti})^z \end{pmatrix}, \\
\boldsymbol{m}_{T_{1\parallel},t} &= \frac{1}{2}\sum_{i\in t} \begin{pmatrix} S^x_{ti} \\ S^y_{ti} \\ S^z_{ti} \end{pmatrix}, \\
\boldsymbol{m}_{T_{1\perp},t} &= \frac{\sqrt{3}}{2}\sum_{i\in t} \begin{pmatrix} z_i^x \boldsymbol{v}_i^{yz} \cdot \boldsymbol{S}_{ti} \\ z_i^y \boldsymbol{v}_i^{xz} \cdot \boldsymbol{S}_{ti} \\ z_i^z \boldsymbol{v}_i^{xy} \cdot \boldsymbol{S}_{ti} \end{pmatrix},
\end{aligned} \tag{5.28}$$

with the sums going over the sublattice sites $i \in \{0,1,2,3\}$ of the tetrahedron t. Note that we have defined order parameters m_{ψ_2} and m_{ψ_3}, which will become relevant at a later point, in the second line. $\boldsymbol{x}_i$, $\boldsymbol{y}_i$ and $\boldsymbol{z}_i$ correspond to normalized vectors along the site-dependent axes of the local coordinate system and are defined in Eq. (5.11). $\boldsymbol{v}_i^{\mu\nu}$, with $\mu,\nu \in \{x,y,z\}$, are normalized bond vectors on an up tetrahedron and point from a site of sublattice i towards the nearest neighbor lying in the same μ-ν plane.

They are given by

$$\begin{aligned}
\boldsymbol{v}_0^{xy} &= -\boldsymbol{v}_3^{xy} = \frac{1}{\sqrt{2}}\begin{pmatrix}1\\1\\0\end{pmatrix}, \qquad \boldsymbol{v}_2^{xy} = -\boldsymbol{v}_1^{xy} = \frac{1}{\sqrt{2}}\begin{pmatrix}-1\\1\\0\end{pmatrix}, \\
\boldsymbol{v}_0^{xz} &= -\boldsymbol{v}_2^{xz} = \frac{1}{\sqrt{2}}\begin{pmatrix}1\\0\\1\end{pmatrix}, \qquad \boldsymbol{v}_3^{xz} = -\boldsymbol{v}_1^{xz} = \frac{1}{\sqrt{2}}\begin{pmatrix}-1\\0\\1\end{pmatrix}, \\
\boldsymbol{v}_0^{yz} &= -\boldsymbol{v}_1^{yz} = \frac{1}{\sqrt{2}}\begin{pmatrix}0\\1\\1\end{pmatrix}, \qquad \boldsymbol{v}_3^{yz} = -\boldsymbol{v}_2^{yz} = \frac{1}{\sqrt{2}}\begin{pmatrix}0\\-1\\1\end{pmatrix}.
\end{aligned} \tag{5.29}$$

From Eq. (5.28), the interpretation of some manifolds of irreps Ψ, built by spin configurations that maximize $\boldsymbol{m}_{\Psi,t}$, becomes straightforward. Their respective spin arrangements will be summarized in the following. The manifolds of irreps A_2 and E are built by ferromagnetic spin arrangements in the local coordinate system. m_{A_2} is maximized by a pair of states related by TRS for which spins are ordered along the local z axis. Because this axis points towards (away from) the center of adjacent up (down) tetrahedra, the resulting $\boldsymbol{q} = \boldsymbol{0}$ order, shown in Fig. 5.9(a), is fittingly called all-in all-out (AIAO) order [90]. In the E irrep manifold, spins are ordered ferromagnetically in the local x-y plane, with the corresponding one-dimensional manifold being referred to as Γ_5 manifold [90]. While the Γ_5 manifold is partially accidental, note that all orders within it break TRS and C_3 symmetry. It follows that each Γ_5 state is part of a set of six degenerate states, all lying within the Γ_5 manifold, that are mapped onto one another by applying symmetries of the spin model. Within the degenerate Γ_5 manifold, the so-called ψ_2 and ψ_3 states are observed to be chosen by ObD selections [90, 89]. Their corresponding order parameters are denoted as m_{ψ_2} and m_{ψ_3} in Eq. (5.28). These orders are shown along the Γ_5 manifold in Figs. 5.9(c)-(d). The ψ_2 and ψ_3 orders include states with spins oriented along the local x axis for the ψ_2 and along the local y axis for the ψ_3 order, and they include states with spins oriented along directions that are equal by symmetries of the model. In the global coordinate system, all six states of the ψ_3 phase are coplanar. Spins of these states are arranged in either the global x-y, y-z or z-x plane, with pairs of spins being perpendicular to each other and spins of a single pair being antiferromagnetically aligned [see Fig. 5.9(d)]. In contrast, the ψ_2 phase does not involve coplanar spin arrangements in the global coordinate system. Moving on to the next irrep, the T_2 irrep order parameter is maximized by so-called Palmer-Chalker states, in which spins assume coplanar arrangements in the global coordinate system as well [90]. These states are obtained from ψ_3 states by flipping colinear pairs of spins on two sublattices. Palmer-Chalker states will not play

a role in the ground state selection of the Heisenberg-DM model. Not yet discussed are the states of the order parameters $\boldsymbol{m}_{T_{1\parallel},t}$ and $\boldsymbol{m}_{T_{1\perp},t}$, which are associated with the T_1 irrep. Of these order parameters, states of the $T_{1||}$ phase are easily understood, since they correspond to any ferromagnetic ordering in the global coordinate system. At last, $T_{1\perp}$ states arrange spins to be coplanar and oriented along bonds of a tetrahedron. E.g., Fig. 5.9(b) shows a spin configuration that contributes only to the last row of the order parameter $\boldsymbol{m}_{T_{1\perp},t}$. The corresponding phase will be referred to as $T_{1\perp}$ order.

For models with a finite $a_{T_{1||\perp}}$ in Eq. (5.21), the case $\alpha = -\arctan(\frac{1}{\sqrt{2}})$ [see Eq. (5.25)], given under the condition for interactions

$$2J + K + \Gamma - D = 0, \tag{5.30}$$

or, equivalently,

$$J^{z\pm} = 0, \tag{5.31}$$

is worth pointing out. The restriction $J^{z\pm} = 0$ implies that this scenario is always given for non-Kramers pyrochlore compounds. In this case, the aforementioned transformation given by Eq. (5.24) of irrep order parameters $\boldsymbol{m}_{T_{1||},t}$ and $\boldsymbol{m}_{T_{1\perp},t}$, which results in the new pair of order parameters $\boldsymbol{m}_{T_{1,A},t}$ and $\boldsymbol{m}_{T_{1,B},t}$, has to be applied to obtain a Hamiltonian that is of the easily solvable form given by Eq. (5.26). In the special case $J^{z\pm} = 0$, $T_{1,B}$ will be renamed as T_1^{Ice}, since its manifold is then equal to the spin-ice manifold. The corresponding order parameter in the local coordinate system, with local spin z components $S^z_{i,l} = \boldsymbol{z}_i \cdot \boldsymbol{S}_i$, is given by

$$\begin{aligned}\boldsymbol{m}_{T_1^{\mathrm{Ice}},t} = \frac{1}{2}\big(&- S^z_{t0,l} - S^z_{t1,l} + S^z_{t2,l} + S^z_{t3,l},\\ &- S^z_{t0,l} + S^z_{t1,l} - S^z_{t2,l} + S^z_{t3,l},\\ &- S^z_{t0,l} + S^z_{t1,l} + S^z_{t2,l} - S^z_{t3,l}\big).\end{aligned} \tag{5.32}$$

For the same case $J^{z\pm} = 0$, we rename $T_{1,A}$ as T_1^{xy}, since its order parameter is then maximized by orders in the local x-y plane. The order parameter is obtained from $\boldsymbol{m}_{T_2,t}$ by performing a spin rotation of $\pi/2$ about the local z axis, denoted by the operator $\boldsymbol{U}_i$. Hence, it is given by

$$\boldsymbol{m}_{T_1^{xy},t} = \frac{\sqrt{3}}{2\sqrt{2}} \sum_{i\in t} \begin{pmatrix} (\boldsymbol{z}_i \times \boldsymbol{U}_i^{-1} \boldsymbol{S}_{ti} \boldsymbol{U}_i)^x \\ (\boldsymbol{z}_i \times \boldsymbol{U}_i^{-1} \boldsymbol{S}_{ti} \boldsymbol{U}_i)^y \\ (\boldsymbol{z}_i \times \boldsymbol{U}_i^{-1} \boldsymbol{S}_{ti} \boldsymbol{U}_i)^z \end{pmatrix}. \tag{5.33}$$

Application to the Heisenberg-DM model

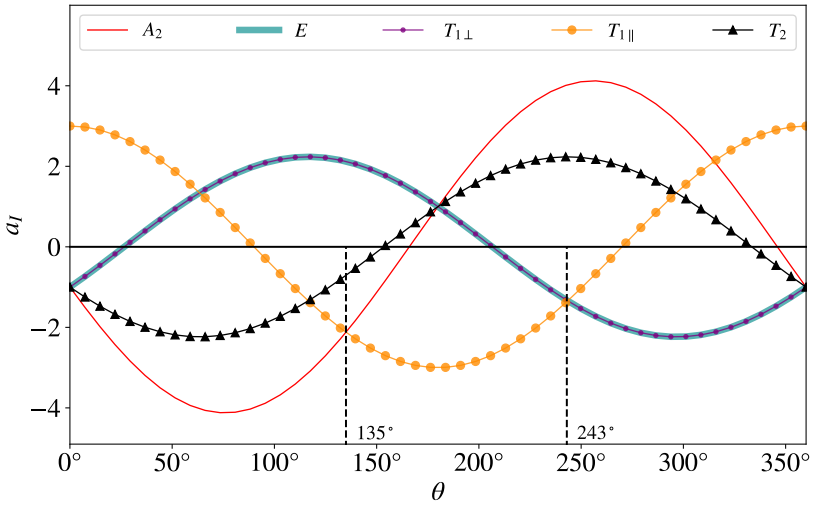

Figure 5.7: Irreducible representation's energy parameter (IEP) a_I as a function of θ. Note that the critical angles $\theta = 135°, 243°$ for the phase boundaries between the AIAO and the colinear ferromagnet (FM), and the latter with the Γ_5 phase, correspond to the ratios $D/J = -1$ and 2, respectively. Note also that the a_I for the E and $T_{1\perp}$ irreps are degenerate for all values of θ (purple dots and blue line are overlapping). The figure and its caption are replicated from Ref. [49].

The irrep-based decomposition of classical manifolds will now be applied to the Heisenberg-DM model and its $T = 0$ classical phase diagram will be discussed. The irrep-dependent energies a_Ψ of the Heisenberg-DM model are shown along the classical $T = 0$ phase diagram in Fig. 5.7, with the interactions parameterized by an angle θ as in Eq. 5.10. Irrep parameters a_Ψ of minimum value determine the ground state manifolds of the classical model. This leads to different phases depending on θ. It can be observed that the T_2 manifold is irrelevant for the question of ground state selection, except at the Heisenberg model. Three different ground state regimes of finite extent exist. Their boundaries are located at $D/J = 0, -1, 2$ (or, alternatively, $\theta \approx 0°, 135°, 243°$), with $J > 0$ at the former boundary and $J < 0$ at the latter two boundaries.

The model assumes an AIAO order in the A_2 phase, which extends over the finite range $\theta \in (0°, 135°)$ in presence of a direct DMI $D > 0$. In the region $\theta \in (135°, 243°)$ surrounding the ferromagnetic model at $\theta = 180°$, a $T_{1||}$ phase is chosen, corresponding to ferromagnetic order. As a consequence of a finite anisotropic DMI at $\theta \neq 180°$, different choices of the global spin orientation for ferromagnetic order are generally not related by a rotation symmetry, as is the case for a pure Heisenberg model. It follows that, while ferromagnetic states of all spin orientations share the same classical energy, ObD will favor certain orientations. In fact, as shown in the recent publication Ref. [91], the selection of a ferromagnetic order in the Heisenberg-DM model is special in the sense that all ferromagnetic product states are still exact eigenstates of the quantum

model, even in the presence of a finite DMI.

In the presence of an indirect DMI, the E and $T_{1\perp}$ manifolds build the classical ground state manifold in the region $\theta \in (243°, 360°)$. We will refer to the manifold of this phase as Γ_5/copl manifold, as will be rationalized in the following. All states of the manifold break the C_3 lattice symmetry and TRS. Therefore, they group up into sets of six symmetry-related states. The Γ_5/copl manifold consists of the one-dimensional Γ_5 manifold and three disconnected one-dimensional manifolds with coplanar spin arrangements in the global coordinate system. The latter coplanar manifolds are each connected to the Γ_5 manifold and are mapped onto each other by the C_3 lattice symmetry. In contrast, the Γ_5 manifold as a whole does not transform under application of the C_3 lattice symmetry. However, the states within it do. The coplanar manifolds interpolate between states of the E and $T_{1\perp}$ irreps. Starting from a ψ_3 or $T_{1\perp}$ state, the coplanar manifolds are covered by global spin rotations about the x, y and z axes of the global coordinate system. Depending on the state, the axis of rotation depends on whether the spins are oriented in the y-z, z-x or x-y plane, respectively; see Figs. 5.9(b)-(d), which indicate one such manifold in purple. In contrast, the Γ_5 manifold, shown in turquoise, is covered by rotations about the local z axis. Later, we will observe that fluctuations only select states of the Γ_5 manifold out of the larger Γ_5/copl manifold. For this reason, the phase will be referred to as Γ_5 phase.

Order parameter susceptibility

From the classical $T = 0$ phase diagram we conclude that the ground state selections in both the ferromagnetic and Γ_5 phase are governed by ObD. In this thesis, we will only treat the state selection in the Γ_5 phase and refer to Ref. [91] for a study on the ObD selection in the ferromagnetic phase. Without considering the methodological feasibility, the most straightforward approach to determine the ground state selections within the Γ_5 manifold would be to consider the expectation values of the irrep order parameters $\boldsymbol{m}_{\psi_2}$ and $\boldsymbol{m}_{\psi_3}$ at temperatures $T < T_c$. Such an approach was not possible by PFFRG at the time when the study of the Heisenberg-DM model was performed[5], and is not possible by HTSE, since both methods consider the system only for cutoffs or temperatures above the phase transition, i.e., at cutoffs or temperatures where the

[5]Note that this study was done before the PFFRG extension to models that break time-reversal symmetry was formulated. In principle, the magnetic orders found by PFFRG can also be resolved by considering the expectation values of the order parameters of the different irreps. However, such an approach would include some hurdles. Symmetry-breaking seed-field perturbations would have to be included in the model, increasing the computational complexity of solving the flow equations and increasing the sophistication of the numerical PFFRG implementation in the process. Additionally, the seed field perturbations would ideally have to be applied such that they do not energetically favor any of the candidate orders.

order parameters are not finite.

Magnetic susceptibilities provide an alternative route to study magnetic phases and can be computed at $T > T_c$ (or $\Lambda > \Lambda_c$) to determine the magnetic phases assumed by the system at $T = T_c$ (or $\Lambda = \Lambda_c$). However, susceptibility peak patterns of different magnetic orders are not unique. This is also the case in the Heisenberg-DM model, in which only $\boldsymbol{q} = \boldsymbol{0}$ orders are selected. E.g., the AIAO and Γ_5/copl orders share the same peak positions in the susceptibility $\chi^{\mu\mu}(\boldsymbol{q})$, with $\mu = x, y, z$. Note that the symmetry properties of the model allow different $\mu\nu$ components of $\chi^{\mu\nu}(\boldsymbol{q})$ to be related. All diagonal components $\chi^{\mu\mu}$ can be mapped onto one another by the C_3 symmetry that cyclically permutes μ, and all individual off-diagonal components $\chi^{\mu\nu}$ with $\mu \neq \nu$ are related by C_2 and C_3 lattice symmetries.

To better distinguish magnetic orders by their susceptibilities, we apply PFFRG to compute static order parameter susceptibilities defined by

$$\bar{\chi}_\psi = \frac{1}{N} \sum_{ij} \sum_{\mu\nu} n^\mu_{\psi,i} \bar{\chi}^{\mu\nu}_{ij} n^\nu_{\psi,i}, \tag{5.34}$$

in which N is the number of lattice sites and $n^\mu_{\psi,i}$ is the μ component of a normalized vector $\boldsymbol{n}_{\psi,i}$ that corresponds to the orientation of a spin on site i in the given spin configuration ψ. The $T = 0$ static susceptibility $\bar{\chi}^{\mu\nu}_{ij}$ is defined as in Eq. (3.63). The static order parameter susceptibility $\bar{\chi}_\psi$ allows for a straightforward distinction between different orders ψ, often in cases where $\chi^{\mu\mu}(\boldsymbol{q})$ fails to distinguish magnetic orders. However, we will show later in this subsection that symmetry-based arguments lead to the property that $\bar{\chi}_\psi$ cannot distinguish orders within the Γ_5 and $T_{1||}$ manifold, respectively. Such a distinction requires observables of higher than quadratic order in spin operators. In fact, HTSE require sixth-order cumulants C_6 to resolve which magnetic orders are selected in the Γ_5 phase [49]. The cumulants are defined as

$$C_{6,\psi} \equiv \langle \hat{M}^6_\psi \rangle - 15 \langle \hat{M}^4_\psi \rangle \langle \hat{M}^2_\psi \rangle + 30 \langle \hat{M}^2_\psi \rangle^3, \tag{5.35}$$

with

$$\hat{M}_\psi = \sum_i \boldsymbol{n}_{\psi,i} \cdot \hat{\boldsymbol{S}}_i. \tag{5.36}$$

The computation of $C_{6,\psi}$ is not possible by PFFRG, which only allows the computation of observables that are linear or quadratic in spin operators. Consequently, PFFRG will not be able to resolve all ObD selections of the Heisenberg-DM model.

Symmetry constraints on the order parameter susceptibility

It will now be proven that two-spin observables cannot resolve the ObD selection within the Γ_5 manifold and the ObD selection of the $T_{1||}$ ferromagnetic phase, i.e., each $\bar{\chi}_\psi$ of a Γ_5 order is equal and each $\bar{\chi}_\psi$ of a $T_{1||}$ ferromagnetic order is equal, respectively. To this end, spin correlations $\boldsymbol{\chi}_{ij}$ will be written as 3×3 matrices obtained by multiplying a spin column vector $\boldsymbol{S}_i$ with a spin row vector $\boldsymbol{S}_j^T$. The correlation matrices are given by

$$\boldsymbol{\chi}_{ij} = \frac{\langle \boldsymbol{S}_i \boldsymbol{S}_j^T \rangle - \langle \boldsymbol{S}_i \rangle \langle \boldsymbol{S}_j^T \rangle}{T}. \tag{5.37}$$

For the derivation of equal order parameter suceptibilities within the Γ_5 manifold, the spins are given in the local coordinate system. The susceptibility matrix is obtained from $\boldsymbol{\chi}_{ij}$ by a Fourier transform

$$\boldsymbol{\chi}(\boldsymbol{q}) = \frac{1}{N} \sum_{ij} e^{i\boldsymbol{q}\cdot(\boldsymbol{r}_i - \boldsymbol{r}_j)} \boldsymbol{\chi}_{ij}, \tag{5.38}$$

where the sum indices i and j go over all pyrochlore lattice sites with real-space position vectors $\boldsymbol{r}_i$ and $\boldsymbol{r}_j$. We remember that states of the Γ_5 manifold, such as ψ_2 and ψ_3 states are ferromagnetic in the local coordinate system. To compute their order parameter susceptibilities we set $\boldsymbol{q} = \boldsymbol{0}$ and define $\boldsymbol{\chi}$ as

$$\boldsymbol{\chi} \coloneqq \boldsymbol{\chi}(\boldsymbol{q} = \boldsymbol{0}) = \frac{1}{N} \sum_{ij} \boldsymbol{\chi}_{ij}. \tag{5.39}$$

For the ψ_2 and ψ_3 orders, spins are directed along the local x and y axis, respectively. It follows that their order parameter susceptibilities are given by susceptibility matrix entries in the local coordinate system. More precisely, $\chi_{\psi_2} = \chi^{xx}$ and $\chi_{\psi_3} = \chi^{yy}$.

To show that these entries are in fact equal, we employ symmetry properties of $\boldsymbol{\chi}$. It can be seen from Eq. (5.37) that the correlation matrix obeys $\boldsymbol{\chi}_{ij} = \boldsymbol{\chi}_{ji}^T$. Applying this relation in Eq. (5.39) leads to $\boldsymbol{\chi} = \boldsymbol{\chi}^T$. It follows that $\boldsymbol{\chi}$ has the general form

$$\boldsymbol{\chi} = \begin{pmatrix} A & D & E \\ D & B & F \\ E & F & C \end{pmatrix}, \tag{5.40}$$

with $A, B, C, D, E, F \in \mathbb{R}$. Symmetries of the model can be applied to restrict the general form of $\boldsymbol{\chi}$ even further. Applying a lattice rotation symmetry changes site indices $ij \to kl$ and rotates spins via a rotation matrix $\boldsymbol{R}$. In $\boldsymbol{\chi}$, the rotation of spins is expressed by the transformation $\boldsymbol{\chi} \to \boldsymbol{R}^T \boldsymbol{\chi} \boldsymbol{R}$. If this transformation corresponds to a symmetry of the Hamiltonian of Eq. (5.12) that is not spontaneously broken, $\boldsymbol{\chi}$ has

to fulfill

$$\boldsymbol{\chi} = \boldsymbol{R}^T \boldsymbol{\chi} \boldsymbol{R}. \tag{5.41}$$

For the C_3 lattice rotation symmetry, $\boldsymbol{R}$ corresponds to a 120° rotation about the local z axis. It follows from Eqs. (5.40) and (5.41) that $\boldsymbol{\chi}$ is restricted to the form

$$\boldsymbol{\chi} = \begin{pmatrix} A & 0 & 0 \\ 0 & A & 0 \\ 0 & 0 & C \end{pmatrix}. \tag{5.42}$$

Thus, the equivalence $\chi_{\psi_2} = \chi_{\psi_3} = \chi^{xx} = \chi^{yy} = A$ is proven. In fact, the restricted form of $\boldsymbol{\chi}$ implies the same order parameter susceptibility for any ferromagnetic order in the local x-y plane, i.e., for any order of the Γ_5 manifold.

The proof of equal order parameter susceptibilities for any $T_{1||}$ ferromagnetic state is carried out analogously. Instead of expressing the susceptibility matrix $\boldsymbol{\chi}$ in the local coordinate system, the global coordinate system is chosen. In this case, C_3 and C_2 lattice symmetries enforce $\boldsymbol{\chi} \propto \mathbb{1}A$, with A being a constant. It follows that the order parameter susceptibility of a ferromagnetic order along $\boldsymbol{n}$, with $\boldsymbol{n}$ being normalized, is given by

$$\chi_{\mathrm{FM}}(\boldsymbol{n}) = \boldsymbol{n}^T \boldsymbol{\chi} \boldsymbol{n} = A, \tag{5.43}$$

Consequently, $\chi_{\mathrm{FM}}(\boldsymbol{n})$ does not depend on the spin orientation $\boldsymbol{n}$.

Examples: Flows of order parameter susceptibilities on effective models of pyrochlore compounds $Er_2Ti_2O_7$ and $Er_2Sn_2O_7$

We now demonstrate that the order parameter susceptibility $\bar{\chi}_\psi$ is well suited for the identification of magnetic orders in pyrochlore nearest-neighbor models. For this purpose, we consider effective spin models of the well-studied rare-earth pyrochlores $Er_2Ti_2O_7$ and $Er_2Sn_2O_7$.

$Er_2Ti_2O_7$ is a rare-earth compound that is known to assume a Γ_5 order [108]. A spin Hamiltonian with interactions $\{J_{zz}, J_\pm, J_{z\pm}, J_{\pm\pm}\} = \{-2.5 \pm 1.8, 6.5 \pm 0.75, -0.88 \pm 1.5, 4.2 \pm 0.5\} \cdot 10^{-2}$ meV was proposed in Ref. [108] by fitting spin wave spectra measured by inelastic neutron scattering measurements. The second rare-earth compound $Er_2Sn_2O_7$ assumes a Palmer-Chalker magnetic order [109]. By fitting interactions of the model on the basis of inelastic neutron scattering experiments and the measured critical temperature, a nearest-neighbor model with interactions $\{J_{zz}, J_\pm, J_{z\pm}, J_{\pm\pm}\} = \{0.0006667, 0.02317, 0.0004714, 0.07183\}$ meV had been proposed for this compound [109].

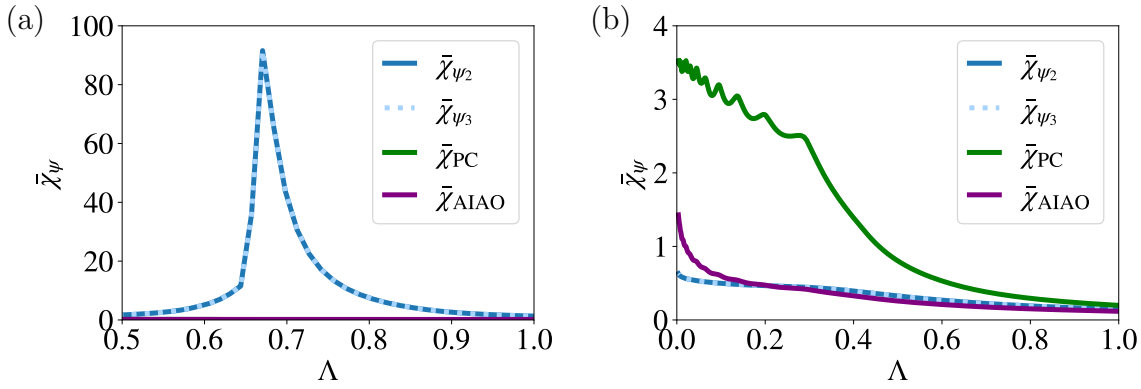

Figure 5.8: PFFRG flows of order parameter susceptibilities $\bar{\chi}_\psi$ [see Eq. (5.34)] that are obtained for effective models of rare-earth pyrochlore compounds $Er_2Ti_2O_7$ and $Er_2Sn_2O_7$. Cutoffs are given in units of the respective Heisenberg interaction J. For each considered irrep manifold, $\bar{\chi}_\psi$ is given for one or two representative states. ψ_2 and ψ_3 states represent the Γ_5 (E) manifold, AIAO states represent the A_2 manifold, and Palmer-Chalker (PC) states represent the T_2 manifold. (a) PFFRG flow of the $Er_2Ti_2O_7$ model with interactions $\{J_{zz}, J_\pm, J_{z\pm}, J_{\pm\pm}\} = \{-2.5\pm1.8, 6.5\pm0.75, -0.88\pm 1.5, 4.2\pm0.5\}\cdot10^{-2}$ meV [108]. (b) PFFRG flow of the $Er_2Sn_2O_7$ model with interactions $\{J_{zz}, J_\pm, J_{z\pm}, J_{\pm\pm}\} = \{0.0006667, 0.02317, 0.0004714, 0.07183\}$ meV [109].

To determine the ground state selections of these models within PFFRG, we compute the static order parameter susceptibilities $\bar{\chi}_\psi$ for states ψ that are representative of different irrep manifolds. For simplicity, the irrelevant flows of $\bar{\chi}_{T_{1,A}}$ and $\bar{\chi}_{T_{1,B}}$ will not be shown. Order parameter susceptibility flows for the spin models of both compounds are shown in Fig. 5.8. The chosen magnetic phases can be unambiguously determined from the dominant $\bar{\chi}_\psi$ at $\Lambda = \Lambda_c$. While the flow of $Er_2Ti_2O_7$, shown in Fig. 5.8(a), exhibits a magnetic phase transition into a Γ_5 phase, the flow of $Er_2Sn_2O_7$, shown in Fig. 5.8(b), transitions into a Palmer-Chalker (T_2) phase. Note that the flows of $\bar{\chi}_{\psi_3}$ and $\bar{\chi}_{\psi_2}$ are equal as a consequence of the model's C_3 symmetry, as was proven above.

5.2.5 Phase diagrams of the classical and quantum models

We are now in a position to discuss the phase diagram of the Heisenberg-DM model under consideration of thermal and quantum fluctuations. The full phase diagram is shown in Fig. 5.9(e). It is shown for the classical model at $T = 0$ and at $T = T_c$, with results obtained by cMC, and for the $S = 1/2$ quantum model at $T = 0$ solved by PFFRG. For the study of ObD selections, additional methods will be applied. In the following, we will first discuss the phase diagram of the classical model. Results on the quantum model will be discussed subsequently.

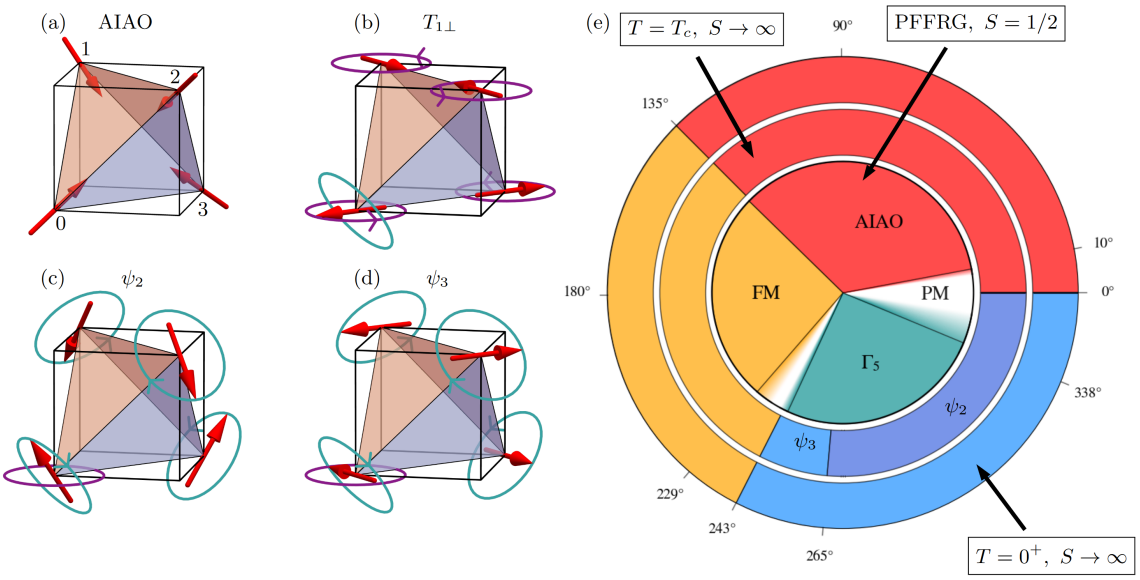

Figure 5.9: (a)-(d) Magnetic $\boldsymbol{q} = \boldsymbol{0}$ orders for the Hamiltonian in Eq. (5.9), illustrated for one "up" tetrahedron, where the turquoise (purple) rings in panels (b)-(d) indicate spin rotations about axes in the local (global) coordinate frame to construct the spin states defined by the Γ_5 manifold (coplanar manifold). Note that only one out of three coplanar manifolds is shown by the purple rings which is, in the present case, obtained by rotating an x-y-coplanar ψ_3 spin state [red arrows in panel (d)] or a $T_{1\perp}$ spin state [red arrows in panel (b)] about the perpendicular global $\boldsymbol{z}$ (cubic [001]) axis. In a similar way, the other two coplanar manifolds are defined in the global x-z and y-z planes, respectively. In panels (b)-(d), the two rings corresponding to the Γ_5 (turquoise) and coplanar (purple) manifolds illustrate how these two manifolds only intersect at a ψ_3 spin configuration. This already suggests the importance that ψ_3 states will play, through thermal and quantum fluctuations, in systems defined by interaction parameters that put them in a regime of competing Γ_5 and $T_{1\perp}$ orders. (e) Phase diagram of the $S = 1/2$ Hamiltonian in Eq. (5.9) parameterized by θ with $J = \cos(\theta)$ and $D = \sin(\theta)$. Here, the outermost ring illustrates the $T = 0^+$ order as observed in classical Monte Carlo ($S \to \infty$), the middle ring represents the selected state at $T = T_c$ for the classical model ($S \to \infty$), and the inner circle represents the $T = 0$ quantum phase diagram as obtained by the pseudo-fermion functional renormalization group (PFFRG, $S = 1/2$). The white regions in the inner (PFFRG $S = 1/2$) circle correspond to regions where the PFFRG method identifies an absence of conventional long-range magnetic order at $T = 0$. The figure and its caption are replicated from Ref. [49].

Classical model

The $T = 0$ paramagnetic phases of the classical model are of no extend. They are located at the pure Heisenberg model at $D = 0$ ($\theta = 0$), and in between the ferromagnetic and Γ_5 phases at $D/J = 2$ ($\theta \approx 243°$) in presence of an indirect DMI $D < 0$. In contrast to the Heisenberg model, the paramagnetic model at $D/J = 2$ is less explored. This may be partly due to the fact that previous studies of the Heisenberg-DM model

to Ref. [49] did not treat the latter paramagnetic phase, as they only considered the case of an antiferromagnetic Heisenberg interaction $J > 0$ [93, 94, 95]. Note that the model at $D/J = 2$ fulfills $J_{ij}^{z\pm} = 0$. It follows that it is relevant for non-Kramers pyrochlore compounds, in which the restriction $J_{ij}^{z\pm} = 0$ is always enforced by symmetries of the spin doublet.

While the absence of magnetic order in the Heisenberg model, already treated in Sec. 5.1, is expected due to an extensive classical ground state manifold, the cause of the absence of magnetic order at $D/J = 2$ is less apparent at first. The ground state decomposition in terms of different irreps gives insight into this observed behavior. As shown in Fig. 5.7, the ground state manifold of the model at $D/J = 2$ is given by the irrep manifolds of E, $T_{||}$ and $T_{\perp}$ (and states that interpolate between them). Because the extensive spin-ice manifold is captured by a local order parameter $\boldsymbol{m}_{T_1^{\mathrm{Ice}},t}$ [see Eq. (5.32)] that is obtained from a superposition of the $T_{||}$ and $T_{\perp}$ order parameters, the spin-ice manifold contributes to the ground state manifold of the $D/J = 2$ model. However, the situation of the $D/J = 2$ model is more sophisticated than in the Ising model (i.e., in classical spin ice), since additional manifolds to T_1^{Ice} compete for the fluctuation-based ground state selection. This leads to highly nontrivial finite-temperature and quantum behaviors of the model. Furthermore, an understanding of the ground state manifold of the $D/J = 2$ model is complicated by the fact that the various ground state configurations on a single tetrahedron allow for nontrivial degrees of freedom in tiling tetrahedra with different ground state configurations across the lattice. The $D/J = 2$ model and its vicinity in interaction parameter space will be treated in further detail in Sec. 5.3.

We continue with a discussion of the magnetically ordered phases. The positions of classical phase boundaries between magnetic phases at $T = 0^+$ and $T = T_c$ are unchanged from the boundary positions of the fluctuation-free phase diagram of Fig. 5.7. Regarding the bulk of magnetic phases, cMC allows the study of ObD selections in the Γ_5 and ferromagnetic phases. For an in-depth treatment of the state selection in the ferromagnetic phase, we refer to Ref. [91]. The ObD selection of the Γ_5 phase is found to depend on both the temperature and interactions parameterized by θ. A cMC-based plot on the Γ_5 phase over temperature T and interactions θ, shown in Fig. 5.10, reveals the classical ObD selection. At $T \approx T_c$, the ψ_3 phase is found to persist in the region $\theta \in (243°, 265°)$, whereas ψ_2 extends over the region $\theta \in [265°, 360°)$. In the $T = 0^+$ limit, only the ψ_3 order is selected by thermal fluctuations. The latter result is further corroborated by larger entropy contributions associated with ψ_3 compared to ψ_2, as is found by classical low-temperature expansions about the respective states [49]. Since the results on the phase diagram of the classical model are not based on contributions of the author, we will leave the discussion of the classical phase diagram at this point

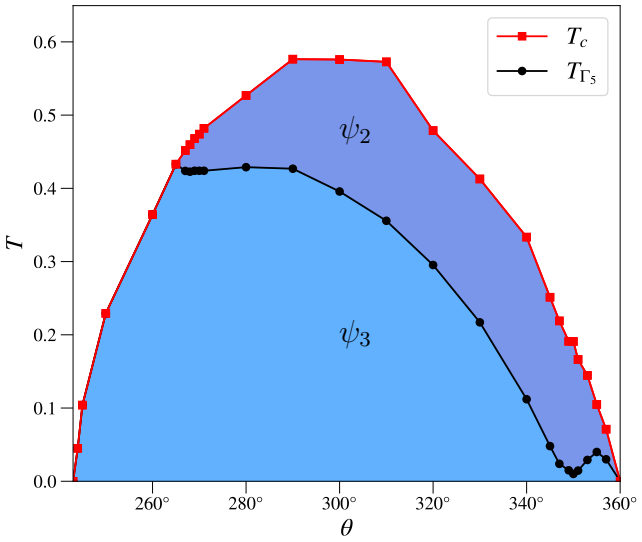

Figure 5.10: Temperature-dependent classical phase diagram for the Γ_5 phase, which is obtained by cMC and illustrates the selection between the ψ_2 and ψ_3 ordering as a function of θ. The figure is replicated from Ref. [49] and the caption is amended.

and move on to the quantum model. Further details on the ObD selections of the classical model are given in Refs. [49, 91].

Quantum model

The $T = 0$ phase diagram of the quantum model is computed via PFFRG and shown in Fig. 5.9(e). Inherent to the PFFRG is an uncertainty in the classification of a magnetic flow breakdowns. Especially at phase boundaries between paramagnetic and magnetically ordered phases, flow breakdowns can be subtle, such that an unambiguous identification of a breakdown is not always possible. We visualize the widths of these regions of uncertainty in the phase diagram by continuous color gradients across phase boundaries.

Neglecting subtle ObD selections, the phases that appear in the quantum-model phase diagram do not differ from those found in the classical phase diagram. However, phase boundaries are shifted and paramagnetic phases are now stabilized over a finite extent in θ. In the following, we first consider PFFRG results on a representative selection of models at fixed θ across each of the occurring phases. For these models, the flows of the maximum static susceptibility $\bar{\chi}^{zz}_{\text{max}}$ and susceptibilities $\bar{\chi}^{zz}(\boldsymbol{q})$ at fixed Λ, either in the $\Lambda \to 0$ limit for paramagnetic flows or at $\Lambda \approx \Lambda_c$ just above a flow breakdown, are shown in Fig. 5.11. The flows of $\bar{\chi}^{zz}_{\text{max}}$ in particular are shown in Fig. 5.11(a). The flows of the paramagnetic phases at $\theta = 0°$ and $\theta = 238°$ remain smooth at any Λ. Subtle oscillatory features at small $\Lambda < 0.5$ in the flow at $\theta = 238°$ are numerical

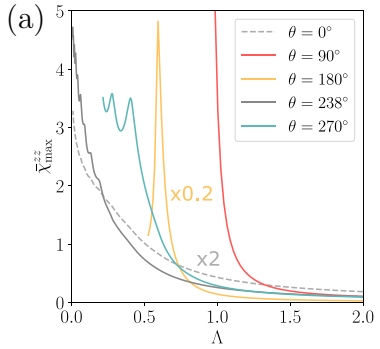

PFFRG flows of $\bar{\chi}^{zz}_{\max}$ for different θ

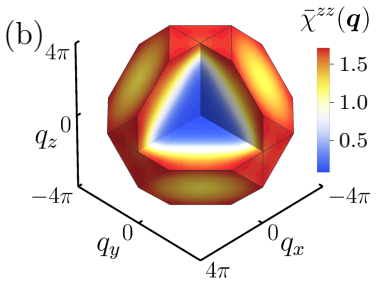

$\theta = 0°$, antiferromagnetic interaction

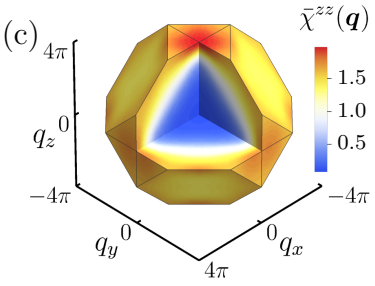

$\theta = 356°$

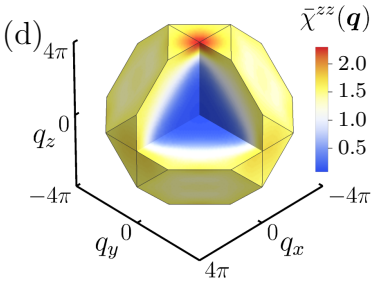

$\theta = 4°$

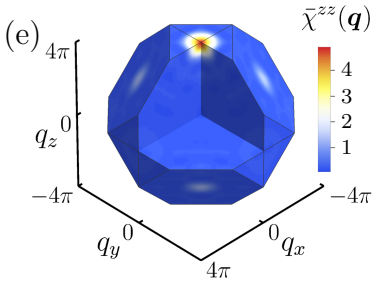

$\theta = 90°$, direct DMI

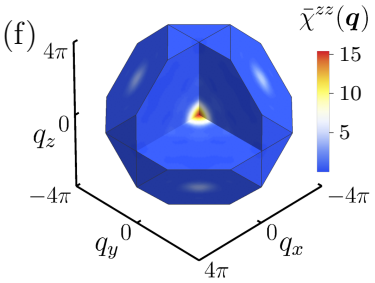

$\theta = 180°$, ferromagnetic interaction

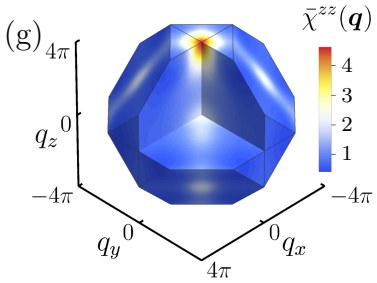

$\theta = 238°$, ferromagnetic and indirect DM interaction

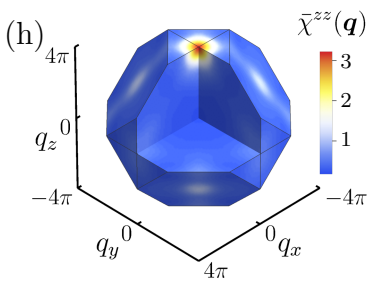

$\theta = 270°$, indirect DMI

Figure 5.11: (a) Selected PFFRG flows of the maximum susceptibility $\bar{\chi}^{zz}_{\max}$ and (b)-(h) examples for momentum resolved susceptibilities $\bar{\chi}^{zz}(\boldsymbol{q})$ over the extended Brillouin zone at the flow breakdown for magnetically ordered phases [i.e., for (e), (f), (h)] or in the low-Λ limit for nonmagnetic flows [i.e., for (b), (c), (d), (g)]. The figure and its caption are replicated from Ref. [49].

artifacts on top of a smooth flow and are caused by a combined application of a sharp frequency cutoff and a vertex frequency discretization in our PFFRG implementation [36]. Magnetic ordering in the ferromagnetic or Γ_5 phase results in a flow breakdown, as is observed in the flows shown at $\theta = 180°$ and $\theta = 270°$ respectively. Interestingly, the magnetic phase transition in the flow shown within the AIAO phase at $\theta = 90°$ realizes an actual divergence of $\bar{\chi}^{zz}_{\max}$ instead of a flow breakdown.

The magnetic Bragg peaks that emerge at the magnetic phase transitions are shown

for all magnetic phases of the phase diagram. They can be observed in the static susceptibilities $\bar{\chi}^{zz}(\boldsymbol{q})$ of the models at $\theta = 90°, 180°$ and $270°$, shown in Figs. 5.11(e), (f) and (h). AIAO and Γ_5 orders, which are both of $\boldsymbol{q} = \boldsymbol{0}$ type, share the same peak positions in $\bar{\chi}^{zz}(\boldsymbol{q})$, with the dominant peak being located at $\boldsymbol{q} = (0, 0, 4\pi)$. It follows that for the present model $\bar{\chi}^{zz}(\boldsymbol{q})$ is insufficiently suited for the characterization of magnetic phases. An unambiguous distinction between the magnetic orders of the AIAO and Γ_5 phases can be achieved by considering order parameter susceptibilities, given by Eq. (5.34), of the respective irrep manifolds. Susceptibilities of the paramagnetic phases are shown in Figs. 5.11(b)-(d) and 5.11(g) at $\theta = 0°, \theta = \pm 4°$ and $238°$. In these phases, strongly fluctuating ground states give rise to broad features across the extended Brillouin zone.

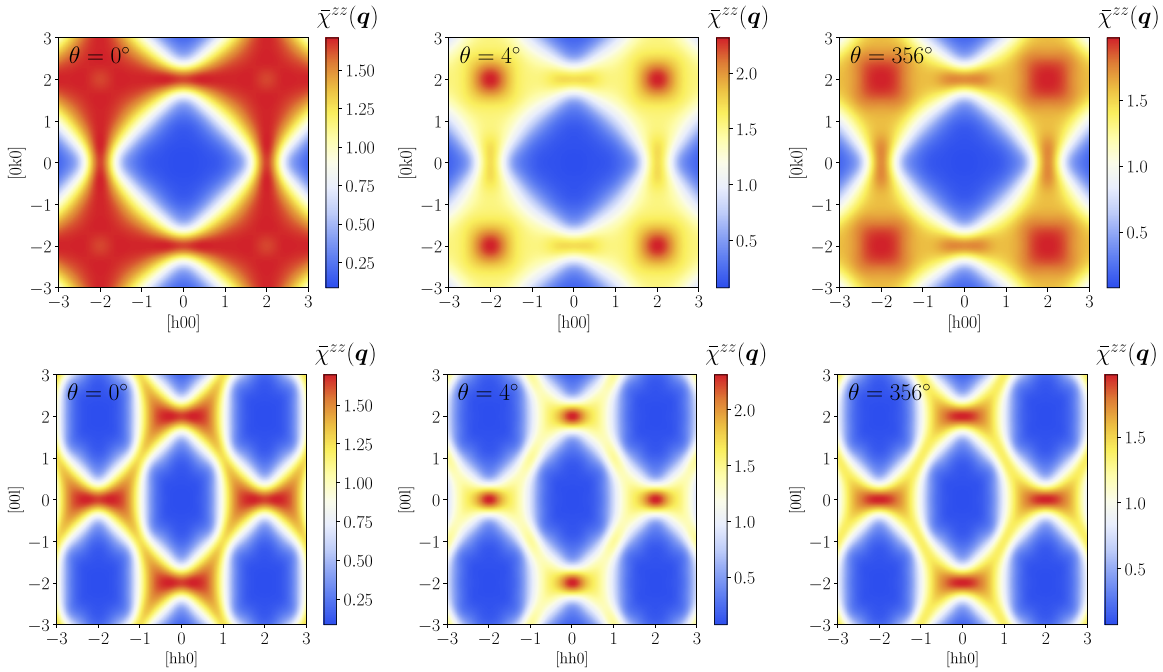

Figure 5.12: Static zz susceptibility, as defined in Eq. (3.65), of the pure and DMI-perturbed Heisenberg antiferromagnet, obtained from PFFRG in the low-cutoff limit. The $[hk0]$ and $[hhl]$ planes are shown in the upper and lower rows, respectively. The figure and its caption are replicated from Ref. [49].

We now continue with more advanced discussions on the individual phases of the $S = 1/2$ Heisenberg-DM model, focusing first on the paramagnetic regimes of the phase diagram. Quantum fluctuations stabilize the previously paramagnetic points of the classical phase diagram at $\theta = 0°$ and $\theta = 243°$ over finite regions in θ. We first discuss the paramagnetic phase surrounding the Heisenberg model. It is found to remain stable in presence of both small direct and indirect DMI within a regime $-9° \lesssim \theta \lesssim 8°$. Slightly smaller direct than indirect DMI are required to enforce a magnetic phase transition. In the static susceptibility $\bar{\chi}^{zz}(\boldsymbol{q})$ of the paramagnetic phase near the Heisenberg model, shown in Figs. 5.11(b)-(d) at $\theta = 0°$ and $\theta = \pm 4°$,

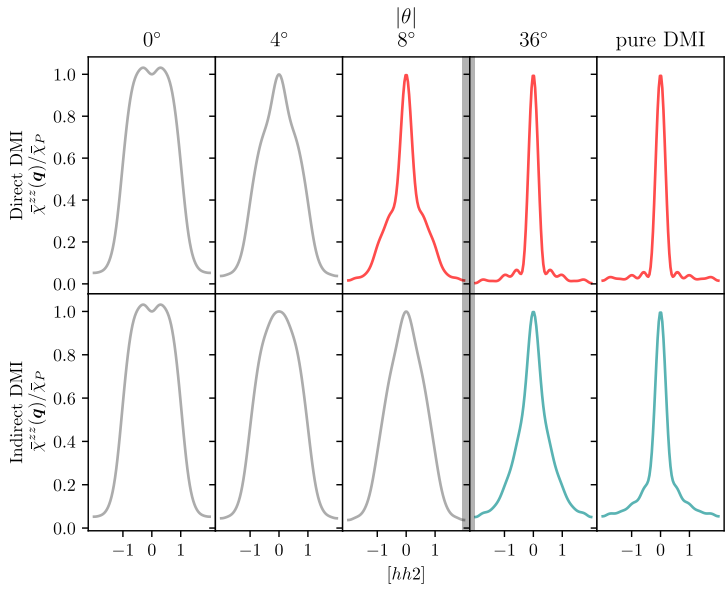

Figure 5.13: Normalized line shape of the static zz susceptibility along $[hh2]$, i.e., across the pinch point/peak $\bar{\chi}_P$ at $hkl = 002$. From left to right, starting from a pure antiferromagnetic Heisenberg model, the evolution of the line shape with increasing absolute DMI is shown. The transitions between paramagnetic and ordered phases are highlighted by bold vertical lines. The figure and its caption are replicated from Ref. [49].

it is observed that the introduction of a finite DMI redistributes weight towards the dominant Bragg peak position $\boldsymbol{q} = (0, 0, 4\pi)$ of the magnetic order that is approached in the phase diagram. This process is visible even still within the paramagnetic phase of the phase diagram. To better characterize the weight redistribution processes, one- and two-dimensional cross sections of $\bar{\chi}^{zz}(\boldsymbol{q})$ are shown in Figs. 5.12 and 5.13. The static susceptibility across the $[hk0]$ and $[hhl]$ planes is shown in Fig. 5.12, whereas Fig. 5.13 considers $\bar{\chi}^{zz}(\boldsymbol{q})$ along $[hh2]$, centered around the broadened pinch point feature of the Heisenberg model at $\boldsymbol{q} = (0, 0, 4\pi)$.

First, we note the observation of features similar to pinch points, which are a characteristic feature of spin ice [1], in the $[hh\ell]$ plane of the model $\theta = 0°$, shown in Fig. 5.12. In contrast to exact pinch points, the observed features are broadened along $[00h]$, which is expected due to the following argument. A perfect fulfillment of the ice rule should result in the presence of pinch points with vanishing width along $[00h]$. This is the case for the Ising model at $T = 0$. Similar to the ice rule, the ground state manifold of the classical Heisenberg model is characterized by a higher-dimensional generalization of the ice rule where the spin vectors on a tetrahedron t have to sum up to the zero vector, i.e., $\boldsymbol{S}_{t0} + \boldsymbol{S}_{t1} + \boldsymbol{S}_{t2} + \boldsymbol{S}_{t3} = \boldsymbol{0}$. This constraint includes the ice rule of the Ising model $S^z_{t0} + S^z_{t1} + S^z_{t2} + S^z_{t3} = 0$. However, while ground states of the classical Heisenberg model fulfill the ice rule exactly, ground states of the quantum model do not, due to

the fact that the sum of spin z components over a tetrahedron $\hat{S}^z_{t0}+\hat{S}^z_{t1}+\hat{S}^z_{t2}+\hat{S}^z_{t3}$ does not commute with the full Hamiltonian $\mathcal{H}$, i.e., states that fulfill the ice rule are not eigenstates of the Heisenberg model. Thus, $\langle(\hat{S}^z_{t0}+\hat{S}^z_{t1}+\hat{S}^z_{t2}+\hat{S}^z_{t3})^2\rangle > 0$ for the $S = 1/2$ Heisenberg model, which results in the presence of broadened pinch points, as is observed in Fig. 5.12. The susceptibility pattern of the Heisenberg model is observed to deform even further away from exhibiting pinch-point features upon the introduction of a finite DMI, as observed in Fig. 5.12 as well. Note that the susceptibility patterns at $\theta = \pm 4$ hint towards the previously observed higher stability of the paramagnetic phase towards the introduction of an indirect rather than a direct DMI, since for an equal absolute $|D/J|$ a direct DMI results in a larger weight redistribution towards $\boldsymbol{q} = (0, 0, 4\pi)$ than an indirect DMI does. Another perspective on the pinch point deformation upon the introduction of a finite DMI is given by Fig. 5.13, which shows the normalized line shapes of $\bar{\chi}^{zz}$ along $[hh2]$ for models about $\theta = 0°$. In agreement with Ref. [88], we observe a small local minimum within the broadened pinch point at $hkl = 002$ for the Heisenberg model at $\theta = 0$. As $|\theta|$ increases, the line shape deforms slightly differently depending on whether a direct or indirect DMI is present. Small kink-like features become visible next to the maximum of $\bar{\chi}^{zz}$ in presence of a direct DMI. These features are missing in case of a finite indirect DMI.

Leaving the paramagnetic phase around the Heisenberg model behind us, we now consider the second paramagnetic region of the phase diagram, which is found near the model $D/J = 2$ (or $\theta \approx 243°$) and extends mostly in the direction of the ferromagnetic model (towards smaller θ). PFFRG finds that the paramagnetic phase occupies the region $237° \lesssim \theta \lesssim 241.5°$. Note that the regions of uncertainty across the phase boundaries include the $D/J = 2$ model at $\theta \approx 243$, which is paramagnetic for classical spins. It is relevant to the location of the phase boundary between paramagnetic and Γ_5 phases that in the general phase diagram for non-Kramers pyrochlore compounds, which also includes the $D/J = 2$ model and is treated in Sec. 5.3, we will observe that quantum fluctuations shift the previously classical boundary of the Γ_5 phase such that the Γ_5-ordered region is extended. This observation suggests that the region of the Γ_5 phase is extended by quantum fluctuations in the Heisenberg-DM model as well, and consequently includes the $D/J = 2$ model. Taking a closer look at the static susceptibility within the paramagnetic phase at $\theta = 238°$, shown in Fig. 5.11(g), we find a feature reminiscent of the dominant Bragg peak displayed by the Γ_5 phase. However, the smooth PFFRG flow of $\bar{\chi}^{zz}_{\text{max}}$ for equal $\theta = 238°$, shown in Fig. 5.11(a), indeed reaffirms the paramagnetic nature of the phase.

The magnetically ordered phases of the phase diagram will be discussed next. The phase boundary between AIAO and ferromagnetic order is the only boundary between two magnetically ordered phases. Its position is given by $\theta \approx 136°$ at which the AIAO

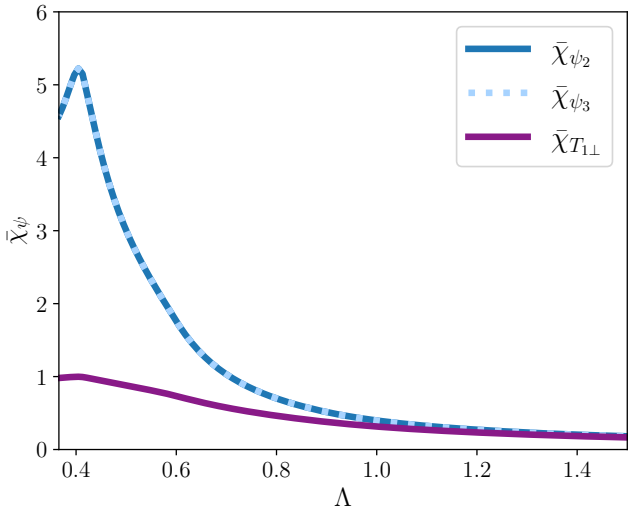

Figure 5.14: PFFRG flows of the order parameter susceptibility $\bar{\chi}_\psi$ for ψ_2, ψ_3 and $T_{1\perp}$ orders in the pure indirect DMI limit at $\theta = 270°$. Note that the curves for $\bar{\chi}_{\psi_2}$ and $\bar{\chi}_{\psi_3}$ lie on top of each other, see text for details. The kink at $\Lambda \approx 0.4$ signals a flow breakdown associated with magnetic long-range order. The figure and its caption are replicated from Ref. [49].

and FM order parameter susceptibilities are of equal size at the critical cutoff. It follows that quantum fluctuations shift the previously classical boundary from $\theta \approx 135°$ towards a slightly larger θ.

ObD selection

The Γ_5 phase is the remaining phase to be discussed. The ObD selection of the Γ_5 phase at T_c is studied by both PFFRG and HTSE. First, PFFRG is applied to resolve that ObD selects a magnetic order in the Γ_5 submanifold out of the larger Γ_5/copl classical ground state manifold. Since PFFRG cannot resolve the ObD selection within the Γ_5 manifold, as previously proven in Sec. 5.2.4, HTSE is applied to reveal the magnetic order chosen out of the Γ_5 manifold instead. While PFFRG does not strictly consider the quantum model at finite temperature, the cutoff Λ effectively acts as a temperature. Hence, the PFFRG ObD selection at $\Lambda = \Lambda_c$ is rather to be interpreted as the selection of the quantum model at $T = T_c$ than as the selection at $T = 0$. As will be observed by PFFRG, the ObD selection of the Γ_5 manifold out of the larger Γ_5/copl manifold is unambiguous, such that subtle differences in the description of the Heisenberg-DM model in terms of Λ or T are not expected to affect this partially resolved ObD selection.

To study the ObD selection with PFFRG, we represent the Γ_5/copl ground state manifold by three states and compute their respective order parameter susceptibility flows. The states are given by a ψ_2, ψ_3 and $T_{1\perp}$ state. The full Γ_5/copl manifold can be re-

constructed from these states (and symmetry-equivalent states) as follows. Within the Γ_5 manifold, any state, with classical spin orientations $\boldsymbol{S}_i^{\Gamma_5}(\alpha)$ on site i, can be characterized by a single angle α, because the manifold is one-dimensional. These states can be built from ψ_2 and ψ_3 states with spin orientations $\boldsymbol{S}_i^{\psi_2} = \boldsymbol{x}_i$ and $\boldsymbol{S}_i^{\psi_3} = \boldsymbol{y}_i$ by linear combination such that

$$\boldsymbol{S}_i^{\Gamma_5}(\alpha) = \sin(\alpha)\boldsymbol{S}_i^{\psi_2} + \cos(\alpha)\boldsymbol{S}_i^{\psi_3}. \tag{5.44}$$

Analogously, the coplanar manifold within the x-y plane is fully covered by linear combinations of $T_{1\perp}$ and ψ_3 states with spin orientations $\boldsymbol{S}_i^{T_{1\perp}}$ and $\boldsymbol{S}_i^{\psi_3}$ that are oriented in the x-y plane. States of this manifold that are oriented in the x-y plane are given by

$$\boldsymbol{S}_i^{\mathrm{copl}}(\alpha) = \sin(\alpha)\boldsymbol{S}_i^{T_{1\perp}} + \cos(\alpha)\boldsymbol{S}_i^{\psi_3}. \tag{5.45}$$

See Figs. 5.9(b)-(d) for the visualizations of the magnetic orders and manifolds given by $\boldsymbol{S}_i^{\psi_2}$, $\boldsymbol{S}_i^{\psi_3}$, $\boldsymbol{S}_i^{T_{1\perp}}$, $\boldsymbol{S}_i^{\Gamma_5}(\alpha)$ and $\boldsymbol{S}_i^{\mathrm{copl}}(\alpha)$.

The order parameter flows of the model at $\theta = 270°$ with an indirect DMI and no Heisenberg interaction are shown in Fig. 5.14. The ObD selection of this model is representative of the selection found throughout the full Γ_5 phase. The shown PFFRG flows confirm that symmetries enforce the order parameter susceptibilities of ψ_2 and ψ_3 states to be equal, as previously proven analytically. However, PFFRG distinguishes between states of the coplanar manifold, represented by $T_{1\perp}$ order, and of the Γ_5 manifold, represented by ψ_2 (ψ_3) order. The flow of $\bar{\chi}_{\psi_2}$ ($\bar{\chi}_{\psi_3}$) is dominant over the flow of $\bar{\chi}_{T_{1\perp}}$. Thus, it is clear that ObD favors a state selection within the Γ_5 manifold. Although not shown explicitly, this selection choice is found throughout the entire appropriately named Γ_5 phase.

As shown in more detail in Ref. [49], HTSE is applied to further specify the ObD selection of the $S = 1/2$ model within the Γ_5 manifold. For this purpose, temperature-dependent sixth-order cumulants C_{6,ψ_2} and C_{6,ψ_3} of the ψ_2 and ψ_3 orders [see Eq. (5.35)] are computed within Padé approximation. Their temperature-dependent differences $C_{6,\psi_2} - C_{6,\psi_3}$ are then computed to find out which order is chosen by the model. As the temperature is lowered from above the magnetic phase transition, the absolute difference of cumulants quickly increases in magnitude at some temperature $T > T_c$. Whether this increase occurs towards positive or negative values of $C_{6,\psi_2} - C_{6,\psi_3}$ indicates the phase selected by ObD. Computations are performed at angle differences of $\Delta\theta = 10°$. The method finds ψ_3 order to be favored at $\theta = 250°$ and $260°$. For this range in θ, the same order is selected in the classical model at $T = T_c$. From $\theta = 270°$ up to $\theta = 300°$, HTSE finds ψ_2 order, which is again consistent with the classical ObD selection at $T = T_c$. The favored selection at the remaining measured points of

$\theta = 310°$ and $320°$ is inconclusive. We conclude that the ObD selections of the quantum model at $T = T_c$ are mostly equal to the selections of the classical model. It is unclear whether there is a perfect agreement, because HTSE results become inconclusive at θ near the Heisenberg model. However, even for models near the Heisenberg limit we can still state that both the quantum and classical model select orders within the Γ_5 manifold.

For the ObD selection study of the quantum model at $T = 0^+$, linear spin-wave theory is applied to compute energy corrections to the ψ_2 and ψ_3 states. We keep the discussion on spin-wave results brief and refer to Ref. [49] for further information. In the region $\theta \in [344°, 352°]$ of the Γ_5 phase, the ObD selection remains inconclusive due to θ-dependent oscillations of high frequencies in the zero-energy dependencies of the ψ_2 and ψ_3 orders. These oscillations are inherent to the model and are not caused by numerical imprecision. Interestingly, the location of the inconclusive region coincides with the local temperature minimum of the classical ψ_2-ψ_3 boundary in Fig. 5.10. Throughout the remaining conclusive region of the Γ_5 phase, linear spin-wave theory finds that ψ_3 order is energetically favored by the quantum model at $T = 0^+$. This ObD selection is, like the selection at $T = T_c$, in agreement with the selection of the classical model.

5.3 Entropically-driven spin liquid to spin liquid transition in the phase diagram of non-Kramers pyrochlores

The above study of the Heisenberg-DM model revealed a $T = 0$ paramagnetic phase realized by the ferromagnetic model at $D/J = 2$, which is stabilized over a finite extent in the $T = 0$ phase diagram upon the inclusion of quantum fluctuations. Similar to the pure Heisenberg model, the $D/J = 2$ model was found to realize an extensive classical ground state manifold; however, its complete ground state manifold is composed by different irrep manifolds. The classical ground state manifold of the Heisenberg model is built by the manifolds of irreps E, T_2 and A_2. Imposing that the order parameters $\boldsymbol{m}_\Psi$ of the remaining irreps Ψ vanish leads to the classical constraint that the sums of spin vectors $\boldsymbol{S}_i$ over any tetrahedron t vanish, i.e., $\boldsymbol{S}_{t0} + \boldsymbol{S}_{t1} + \boldsymbol{S}_{t2} + \boldsymbol{S}_{t3} = \boldsymbol{0}$ for sites $i = 0, 1, 2, 3$ of any tetrahedron. In contrast, the classical ground state manifold of the $D/J = 2$ model is built by the manifolds of E, T_1^{Ice} and T_1^{xy} (or E, $T_{1||}$ and $T_{1\perp}$). While the T_1^{Ice} manifold contains all spin-ice states, with spins oriented along the local z axis, states within the manifolds of E and T_1^{xy} orient spins in the local x-y

plane. In addition to states that lie in single manifolds of $\Psi = E$, T_1^{Ice} or T_1^{xy}, the full ground state manifold of the $D/J = 2$ model further allows for mixed states that include finite $\boldsymbol{m}_{\Psi,t}$ for $\Psi = E$, T_1^{Ice} and T_1^{xy} simultaneously, and different tetrahedra t of the lattice can be tiled in different ground state configurations. Taking all these degrees of freedom into consideration, the structure of the full ground state manifold of the $D/J = 2$ model becomes highly nontrivial.

It is an aim of this section to unravel the structure of the ground state manifold of the $D/J = 2$ model to some degree and to understand the low-temperature behavior of the model. It will be shown that the classical $D/J = 2$ model is entropically driven to undergo a temperature-dependent spin liquid to spin liquid transition at low temperature T^*. While the spin liquid at $T > T^*$ is governed by fluctuations in the E, T_1^{xy} and T_1^{Ice} manifolds, states in the E and T_1^{xy} manifolds depopulate at $T < T^*$ such that a spin-ice phase is realized in the limit $T \to 0^+$. The phenomenology of the spin liquid to spin liquid crossover will be understood by formulating the spin model as an effective theory of competing rank-1 and rank-2 gauge fields [71], with the rank-1 gauge field dominating at $T < T^*$ and a combined rank-1 and rank-2 gauge field being active in the $T > T^*$ spin-liquid phase.

In addition to the classical $D/J = 2$ model, the quantum $S = 1/2$ model will be studied as well. In the quantum model, we will find hints that the $D/J = 2$ model assumes a magnetically ordered Γ_5 phase instead. To better understand this observation, the general phase diagram for nearest-neighbor models of non-Kramers pyrochlores, which includes the $D/J = 2$ model, will be computed. The study of this phase diagram is the second major subject of this section. In the quantum phase diagram, classical phase boundaries will be shifted. As a result, the spin model that is phenomenologically most similar to the classical $D/J = 2$ model will be found at different interaction strengths. The quantum model analogue to the classical $D/J = 2$ model will be found to realize a paramagnetic ground state that is most similar to the $T > T^*$ spin-liquid phase of the classical $D/J = 2$ model.

In non-Kramers pyrochlore systems, states of the T_1^{Ice} manifold involve only the spin components S_i^z of the local coordinate system, which transform as dipolar components, whereas states of the E and T_1^{xy} manifolds involve only spin components S_i^x and S_i^y, which transform as quadrupolar components. Since one ground state manifold of the $D/J = 2$ model (the manifold of T_1^{Ice}) is associated with dipolar order and the remaining two ground state manifolds (the manifolds of E and T_1^{xy}) are associated with quadrupolar orders (here, "dipolar" and "quadrupolar" denote the symmetry properties of the spin components involved), the $D/J = 2$ model will be referred to as dipolar-quadrupolar-quadrupolar (DQQ) model in the context of non-Kramers py-

rochlore systems.

The content of this section follows along with our recent publication of Ref. [71] and is organized as follows. We begin by treating the low-temperature behavior of the classical DQQ model in Sec. 5.3.1. Afterwards, we broaden the scope of the study by considering the classical and quantum phase diagrams for the general nearest-neighbor model of non-Kramers pyrochlore compounds. First, the classical phase diagram will be treated in Sec. 5.3.2. Then, the phase diagram of the $S = 1/2$ quantum model will be resolved in Sec. 5.3.3. The latter section will treat the quantum DQQ model as well. We refer to Ref. [71] for a more detailed treatment of the classical and quantum DQQ models. While the paper of Ref. [71] was created in close collaboration, the author of this thesis mainly contributed to the quantum perspective on the DQQ model provided by PFFRG, and to the understanding of degrees of freedom in the classical ground state manifold of the DQQ model. The main contributions to the paper were made by Daniel Lozano-Gómez, who was the main contributor to the classical perspective on the DQQ model and derived the coarse-grained effective description of the DQQ model. High-temperature series expansion results were provided by Jaan Oitmaa and Rajiv R. P. Singh. For further information on contributions, we refer to the section "Author contributions" in Ref. [71]. Corresponding to the contributions of this thesis' author to Ref. [71], this section will rather focus on the quantum behavior of the DQQ model and the non-Kramers phase diagram. In contrast, some aspects of the classical DQQ model that are treated in Ref. [71] will be omitted. In this section, energies of the DQQ model will be given in units of the Heisenberg interaction $|J|$.

5.3.1 The classical DQQ model

The classical DQQ model will be considered in the following. For this purpose, cMC results of Ref. [71] will be replicated and discussed. We are interested in the behavior of the model at low temperatures within the nontrivial paramagnetic regime, i.e., within the regimes of classical spin liquids. For these temperatures, the manifolds of the irreps A_2 and T_2, which do not contribute to the classical ground state manifold, are mostly depopulated. Consequently, we only need to consider the populations of (ground state) manifolds associated with T_1^{Ice}, T_1^{xy} and E.

We first try to understand the selection mechanism between the two classical spin-liquid phases found at low temperatures. The transition between the spin-liquid phases can be observed in the temperature-dependent specific heat C of the DQQ model, obtained by cMC and shown in Fig. 5.15(b). In this plot, the transition manifests in a bump at $T^* \sim 0.03$. Further insight on the transition is gained by considering the temperature-

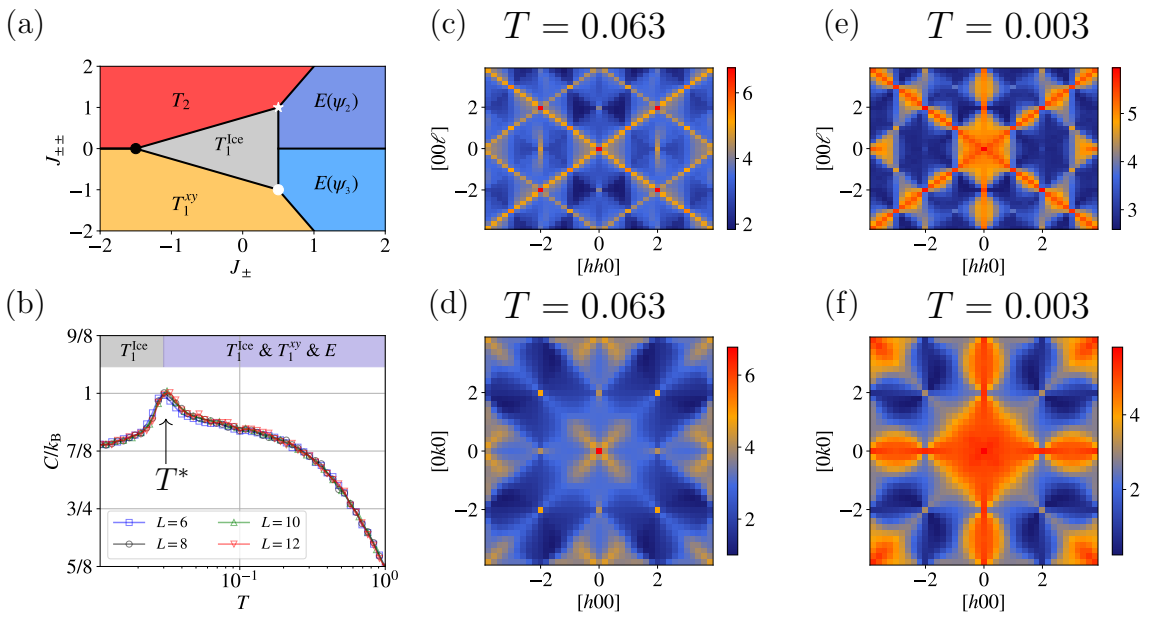

Figure 5.15: (a) Non-Kramers phase diagram with $J^{zz} = 3$ where the DQQ model corresponds to the white dot at the boundary between the classical T_1^{xy}, $E(\psi_3)$, and T_1^{Ice} phases. (b) Specific heat of the DQQ model obtained from Monte Carlo simulations for various system sizes where a bump at a temperature $T^* \sim 0.03$ in the specific heat that signals a crossover between an intermediate-temperature and a low-temperature regime, further discussed in the main text, is observed. This crossover is characterized by an entropically driven depopulation of the E and T_1^{xy} irrep modes. Spin structure factors in the $[hh\ell]$ (c) and $[hk0]$ (d) planes for a temperature just above the crossover temperature T^*. Spin structure factors in the $[hh\ell]$ (e) and $[hk0]$ (f) planes for a temperature below the crossover temperature T^*. The figure and its caption are replicated from Ref. [71].

dependent selection of irrep manifolds by giving out $\langle \boldsymbol{m}_{\Psi,t} \rangle$ for all irreps Ψ. Such a plot is given in Ref. [71] and yields the following insights. While at temperatures above T^*, the classical model selects states throughout manifolds of all ground state irreps (with $|\langle \boldsymbol{m}_{T_1^{\mathrm{Ice}},t} \rangle|$, $|\langle \boldsymbol{m}_{T_1^{xy},t} \rangle|$ and $|\langle \boldsymbol{m}_{E,t} \rangle|$ being of equal orders of magnitude), T_1^{xy} and E manifolds begin to depopulate with decreasing temperature at $T \sim T^*$, and at $T < T^*$ the spin-ice manifold of T_1^{Ice} governs state selection ($|\langle \boldsymbol{m}_{T_1^{\mathrm{Ice}},t} \rangle| \gg |\langle \boldsymbol{m}_{T_1^{xy},t} \rangle|, |\langle \boldsymbol{m}_{E,t} \rangle|$), with a pure spin-ice phase being realized in the limit $T \to 0^+$ [71]. The selection of the T_1^{Ice} manifold at low temperatures is explained by the presence of soft modes about pure spin-ice configurations. Such modes are not found about randomly selected states of the remaining ground state manifold, as confirmed by classical low-temperature expansions on states sampled by the iterative minimization method [71]. The presence and ratio of soft modes about pure spin-ice states is further confirmed by the specific heat C at $T \to 0^+$. In this temperature limit, cMC finds $C/k_B \approx 7/8$, which implies that 1/4 of the modes about pure spin-ice states are of quartic order whereas the remaining modes are of quadratic order (see Ref. [112]).

Next, we consider the phenomenology of both spin-liquid phases by discussing SFs of the DQQ model given by Eqs. (3.67)-(3.68). SFs of cMC in the $[hh\ell]$ and $[hk0]$ planes are shown in Figs. 5.15(c)-(f). They are computed with an isotropic g factor of $\boldsymbol{g} = \mathbb{1}$ and are shown both in the spin-liquid phase at $T > T^*$ ($T = 0.063$) and the spin-liquid phase at $T < T^*$ ($T = 0.003$). We will refer to SFs with an isotropic g factor as spin SFs. Note that these SFs are not representative of non-Kramers compounds, which fulfill $g^{xx} = g^{yy} = 0$ in the local coordinate system. It is apparent from the Figs. 5.15(c)-(f) that the respective SFs of the two spin-liquid phases exhibit vastly different features. The SF of the spin-liquid phase at $T < T^*$ reproduces the scattering pattern found in spin ice, including twofold pinch points [78]. The $T > T^*$ spin SF of the other spin-liquid phase exhibits twofold pinch points as well, e.g., at $hh\ell = 220$ and 002. However, additional features are present as well that hint at the presence of processes that cannot be described by pure spin-ice physics. These features are given by pinch lines (i.e., one-dimensional extensions of pinch points, see Ref. [113]), which can be observed along the [111] and $[1\bar{1}\bar{1}]$ directions, and fourfold pinch points, which are visible in the $[hk0]$ plane at $hk0 = 000$.

As was shown in Sec. 5.1.1, twofold pinch points can be understood as emerging from the fulfillment of a Gauss law, formulated for a rank-1 tensor field $\boldsymbol{B}(\boldsymbol{r})$ analogous to the magnetic field of electromagnetism. The Gauss law is fulfilled by construction by introducing a rank-1 gauge field $\boldsymbol{A}(\boldsymbol{r})$ via $\boldsymbol{B}(\boldsymbol{r}) = \nabla \times \boldsymbol{A}(\boldsymbol{r})$, which is analogous to an electromagnetic potential. Similarly, fourfold pinch points are associated with an emergent rank-2 gauge field and the corresponding generalization of the Gauss law [114, 113]. In context of the DQQ model, the observed twofold and fourfold pinch-point features of the spin SFs can be understood by formulating an effective long-wavelength theory for the DQQ model in the spirit of Refs. [114, 113]. One arrives at a theory of the form

$$\begin{aligned}\mathcal{H} &= E_0 + \frac{3}{16}\int d^3\boldsymbol{q}\left(|\boldsymbol{q}\cdot\boldsymbol{B}^{\mathrm{Ice}}|^2 + |\boldsymbol{q}\cdot\mathcal{M}^{xy}|^2\right)\\ &\quad + \lambda\int d^3\boldsymbol{q}\left(|\boldsymbol{B}^{\mathrm{Ice}}|^2 + \mathrm{tr}\left[(\mathcal{M}^{xy})^T\mathcal{M}^{xy}\right]\right) + O(\boldsymbol{q}^4),\end{aligned} \tag{5.46}$$

with the rank-1 tensor field $\boldsymbol{B}^{\mathrm{Ice}}$ and the rank-2 tensor field $\mathcal{M}^{xy}$ (see Ref. [71] for further information on their properties). The first term E_0 gives the ground state energy of the model, the second term enforces a Gauss laws for the tensor fields $\boldsymbol{B}^{\mathrm{Ice}}$ and $\mathcal{M}^{xy}$ in the limit $T \to 0$, and the third term corresponds to the soft spin-length constraint, where the spin length on each site is fulfilled only on average. The fields of different ranks represent different irreps, since $\boldsymbol{B}^{\mathrm{Ice}}$ is given by the order parameter of spin ice ($\boldsymbol{B}^{\mathbf{Ice}} = \boldsymbol{m}^{\mathrm{Ice}}_{T_1}$), and $\mathcal{M}^{xy}$ contains only components of order parameters $\boldsymbol{m}_E$ and $\boldsymbol{m}^{xy}_{T_1}$. It follows that while the former field describes the dipolar spin components

S_i^z in a non-Kramers model, the latter involves the quadrupolar components S_i^x and S_i^y (expressed in the local coordinate system). Note that $\boldsymbol{B}^{\mathrm{Ice}}$ and $\mathcal{M}^{xy}$ only couple via the spin length constraint.

It follows from the effective description of the DQQ model given by Eq. (5.46) that the intermediate-temperature spin-liquid phase at $T > T^*$ is to be understood as a phase described by competing emergent rank-1 and rank-2 gauge fields. These manifest themselves in the spin SF in the form of twofold and fourfold pinch points, respectively. Note that the effective model of Eq. (5.46) only captures the paramagnetic phase at $T > T^*$. At $T < T^*$, fourfold pinch points vanish and the quadrupolar spin components become fully irrelevant at $T \to 0^+$, as a spin-ice phase emerges in this limit [71].

Neutron structure factor

Above, the different natures of spin-liquid phases of the DQQ model became apparent in the spin SF patterns of Figs. 5.15(c)-(d). However, the DQQ model is primarily relevant to non-Kramers pyrochlores. For these systems, spin SFs, which assume isotropic g tensors $\boldsymbol{g} = \mathbb{1}$, are inaccessible by experiments. Instead, non-Kramers pyrochlore systems exhibit an anistropic g tensor that is only finite along the spin z components of the local coordinate system. We set this g tensor component as $g^{zz} = 1$. The corresponding non-Kramers SFs with $g^{xx} = g^{yy} = 0$ and $g^{zz} = 1$ will be referred to as neutron SFs. Such SFs are shown for the DQQ model in Fig. 5.16, where they are obtained by cMC. It can be observed that both the neutron SFs within the spin-liquid phase at $T > T^*$ and $T < T^*$ exhibit the characteristic pattern of a spin-ice phase. This is a direct consequence of the anisotropic g tensor. The neutron SFs capture only the rank-1 gauge field $\boldsymbol{B}^{\mathrm{Ice}}$, which is described by the dipolar spin components S_i^z with finite $g^{zz} = 1$, and not the rank-2 gauge field $\mathcal{M}^{xy}$, which is described by the quadrupolar spin components S_i^x and S_i^y with vanishing $g^{xx} = g^{yy} = 0$. Because the coarse-grained theory of Eq. (5.46) represents an effective description of spin ice if a vanishing $\mathcal{M}^{xy} = 0$ is considered, spin-ice SF patterns are obtained as a consequence in the neutron SFs, which do not capture $\mathcal{M}^{xy}$. However, a deviation from the pure spin-ice SF pattern is found in the $[hh\ell]$ plane of the non-spin-flip channel. Here, SFs of both spin-liquid phases exhibit a periodic variation of weight, with the positions of maxima coinciding between the SFs of both phases. In contrast, the ideal spin-ice phase of the Ising model exhibits a flat non-spin-flip neutron SF in the $[hh\ell]$ plane [45].

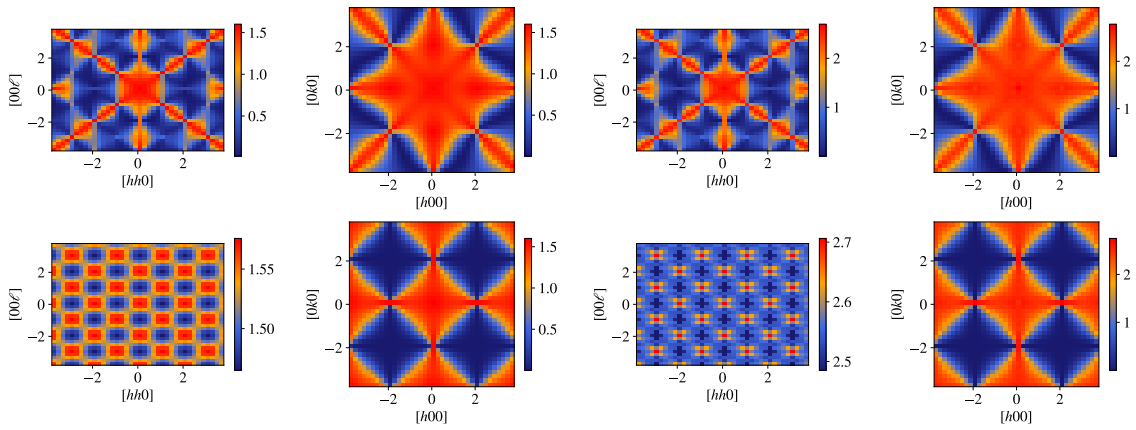

(a) $T > T^*$ (b) $T < T^*$

Figure 5.16: Polarized neutron structure factors for the DQQ model above T^* (a) at $T = 0.063J$ and below (b) at $T = 0.003J$. In each panel, the left plot corresponds to the $[hh\ell]$ plane and the right plot to the $[hk0]$ plane where the first row is the spin-flip channel and the second row corresponds to the non-spin-flip channel. These structure factors were obtained for a system size $L = 10$. The figure and its caption are replicated from Ref. [71].

Ground state degrees of freedom

In the following, we aim to gain a better understanding of the classical ground state manifold of the DQQ model and the spin degrees of freedom within it. We already know that $\boldsymbol{q} = \boldsymbol{0}$ ground state configurations of the DQQ model are obtained by tiling the lattice with a configuration on a tetrahedron that contributes only to order parameters $\boldsymbol{m}_{T_1^{\text{Ice}},t}$, $\boldsymbol{m}_{T_1^{xy},t}$ and $\boldsymbol{m}_{E,t}$. However, the degeneracy $a_{T^{\text{Ice}}} = a_{T_1^{xy}} = a_E$ of the DQQ model allows for lattice ground states that tile tetrahedra with different spin configurations as well. In order to describe the full classical ground state manifold of the DQQ model, all possible tiling degrees of freedom have to be known. Here, we will explore tiling degrees of freedom in the DQQ model and, more explicitly, demonstrate how degeneracies of ground states on a single tetrahedron can lead to subextensive degeneracies in the lattice model. Two examples of lattice configurations that mix between multiple irrep manifolds by having different ground state configurations on different tetrahedra will be given.

It had previously been shown in Ref. [90] that for pyrochlore lattice models an at least subextensive ground state manifold follows from the degeneracy of two $\boldsymbol{q} = \boldsymbol{0}$ ground state configurations with coinciding spin orientations on one or more sublattice sites. The corresponding degrees of freedom in tiling the lattice with tetrahedra of different ground state configurations are summarized by the so-called "Lego-brick" rules [90], which will only partially be repeated here. If the spin orientations of two $\boldsymbol{q} = \boldsymbol{0}$ ground state configurations coincide on one sublattice, then, starting from one of the two

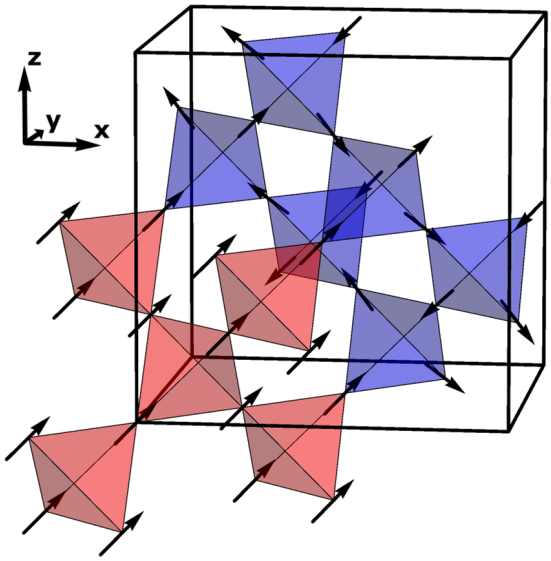

Figure 5.17: Visualization of a (111) domain wall in a classical ground state configuration of the DQQ model. The domain wall is positioned in a lattice plane whose sites build a triangular lattice and is enclosed by a ferromagnetic (with $\boldsymbol{S}_i \parallel (111)$) and a spin-ice configuration with shown spin orientations $\boldsymbol{S}_i$ on site i. Tetrahedra of both configurations are colored red and blue, respectively.

$\boldsymbol{q} = \boldsymbol{0}$ spin arrangements, there exists a degree of freedom that consists of changing the spin configurations throughout a kagome plane of the pyrochlore lattice[6]. It follows that there exists a degeneracy of at least $\mathcal{O}(2^L)$, with L being the linear size of the lattice. The degree of freedom is illustrated in Fig. 5.17, which shows a ground state configuration of the DQQ model. A (111) domain wall is shown in between a spin-ice (blue) and a ferromagnetic (red) region. Both spin-ice and ferromagnetic configurations are ground states of the classical DQQ model, since spin-ice configurations build the manifold of T_1^{Ice}, and ferromagnetic configurations build the manifold of $T_{1||}$. The domain wall does not have a finite energy cost, because all adjacent tetrahedra are in a ground state configuration. It is located in a triangular lattice (111) plane of the pyrochlore lattice and can be moved without energy cost by changing the spin configurations throughout a full adjacent kagome plane such that a plane of tetrahedra changes either from a ferromagnetic to spin-ice ground state configuration or vice versa.

A degeneracy of higher order is implied if two $\boldsymbol{q} = \boldsymbol{0}$ ground state configurations coincide on two sublattices. In this case, a degeneracy of at least $\mathcal{O}(2^{L^2})$ exists. Degrees of freedom now consist of changing spin configurations along a 1D line throughout the lattice. In the DQQ model there exists a special case of such a degree of freedom that is continuous, as will be shown in the following. A subset of $\boldsymbol{q} = \boldsymbol{0}$ ground

[6]Note that the pyrochlore lattice can be considered as being built by alternating triangular and kagome lattice planes.

state configurations of the DQQ model are specified by two continuous angles α and β that each determine the spin orientations on only two sublattices. The sublattice i dependent spin vectors $\boldsymbol{S}_i$ for these configurations are given by

$$\begin{aligned}\boldsymbol{S}_0 &= \big(\cos(\beta), 0, \sin(\beta)\big),\\ \boldsymbol{S}_1 &= \big(\cos(\beta), 0, -\sin(\beta)\big),\\ \boldsymbol{S}_2 &= \big(\cos(\alpha), 0, \sin(\alpha)\big),\\ \boldsymbol{S}_3 &= \big(\cos(\alpha), 0, -\sin(\alpha)\big).\end{aligned} \tag{5.47}$$

in the local coordinate system. Except for certain angles, the configuration contributes to all irrep order parameters $\boldsymbol{m}_{T_1^{\mathrm{Ice}},t}$, $\boldsymbol{m}_{T_1^{xy},t}$, and $\boldsymbol{m}_{E,t}$. Three exceptions are given by a pure spin-ice configuration, obtained by setting $\alpha = \beta = \pi/2$, ψ_2 order, obtained in case $\alpha = \beta = 0$, and a pure T_1^{xy} state, obtained for $\alpha = 0$ and $\beta = \pi$. Configurations of Eq. (5.47) are shown in Fig. 5.18 along a line of tetrahedra for two choices of angles α and β. A continuous degree of freedom exists that corresponds to rotating spins of sublattices 2 and 3 (shown in red) along a 1D line. The axis of rotation is oriented along the local y axis and has opposite sign for sublattices 2 and 3. In addition to providing a continuous degree of freedom along a 1D line, the spin configurations of Eq. (5.47) are an example of classical ground state configurations in the DQQ model that mix between different irrep order parameters.

Note that different spin-ice configurations of T_1^{Ice} can themselves coincide on two different sites of a tetrahedron and, thus implying a degree of freedom in tiling tetrahedra of different ground state configurations on the pyrochlore lattice. Notably, the spin-ice configurations represent a special case in which the tiling degree of freedom is local and extensive, resulting in the spin-ice physics already covered in Sec. 5.1.1.

5.3.2 Classical phase diagram of non-Kramers pyrochlore models

It was mentioned earlier that the DQQ model can be realized by non-Kramers pyrochlore systems. In this context, the general phase diagram of nearest-neighbor models of non-Kramers pyrochlores will be computed. Here, we first consider the classical phase diagram. Afterwards, the quantum case will be considered, which will be useful for interpreting the behavior of the $S = 1/2$ DQQ model as well.

As argued in Sec. 5.2.3, the general nearest-neighbor spin model of non-Kramers

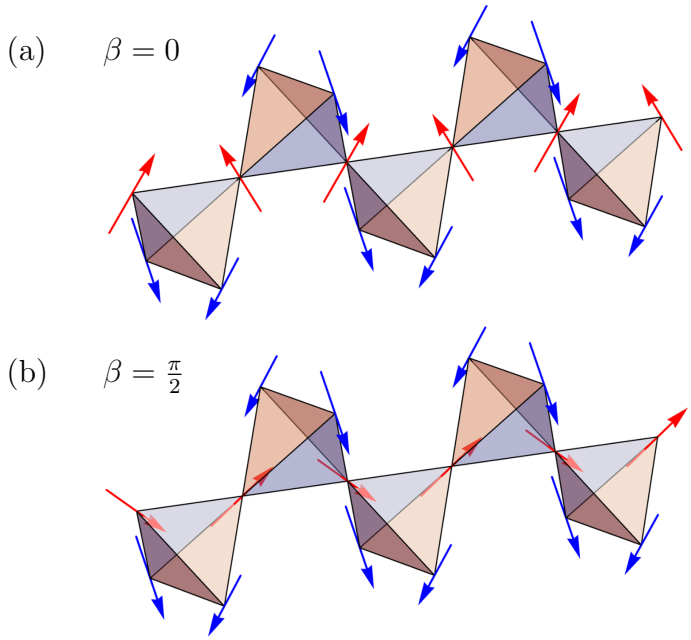

Figure 5.18: The ground state spin configuration of Eq. (5.47) is shown for fixed $\beta = 0$ and $\beta = \pi/2$, with α staying constant at $\alpha = 0$. Spins on sublattices 0 and 1 (2 and 3) are shown in blue (red). The figure and its caption are replicated from Ref. [71].

pyrochlores is given in the local coordinate system by

$$\mathcal{H} = \sum_{\langle ij \rangle} J^{zz} S_i^z S_j^z - J^{\pm}(S_i^+ S_j^- + S_i^- S_j^+) + J^{\pm\pm}(\gamma_{ij} S_i^+ S_j^+ + \gamma_{ij}^* S_i^- S_j^-)], \tag{5.48}$$

with γ_{ij} being defined in Eq. (5.17). From the dependence on three interaction parameters J^{zz}, $J^{\pm}$ and $J^{\pm\pm}$ follows a two-dimensional phase diagram, which we choose to compute at a constant $J^{zz} = 3$. The classical phase diagram at $T = 0^+$ is shown in Fig. 5.15(a) and will be summarized in the following[7]. The phase diagram contains extended phases characterized by the irreps T_2, T_1^{xy}, T_1^{Ice} and E. The E phase, which has a Γ_5 classical ground state manifold, is found to realize a different ObD selection depending on the sign of $J^{\pm\pm}$. A ψ_2 order is selected for $J^{\pm\pm} > 0$, whereas a ψ_3 order is selected for $J^{\pm\pm} < 0$.

Surrounding the Ising model at $J^{\pm} = J^{\pm\pm} = 0$ is a paramagnetic region of triangular shape that corresponds to a spin-ice phase with ground state irrep T_1^{Ice}. Each corner of the triangle is adjacent to three distinct phases characterized by different irreps. Each model of a single corner is treated in this chapter. The left corner (black dot) at $\{J^{zz}, J^{\pm}, J^{\pm\pm}\} = \{3, -1.5, 0\}$ realizes the antiferromagnetic Heisenberg model. How-

[7]Note that the notation for interactions in Fig. 5.15(a) is slightly different, because the figure is replicated from Ref. [71]

ever, note that this Heisenberg model is defined in the local coordinate system and corresponds to a model with highly anisotropic interactions of $\{J, K, \Gamma, D\} = \{-3, 6, 0, 0\}$ in the global coordinate system. Conversely, the Heisenberg model with interactions $\{J, K, \Gamma, D\} = \{3, 0, 0, 0\}$ in the global coordinate system realizes the interactions $\{J^{zz}, J^{\pm}, J^{\pm\pm}, J^{z\pm}\} = \{-1, 0.5, \sqrt{2}, 1\}$ in the local coordinate system, which cannot be realized by non-Kramers models due to $J^{z\pm} \neq 0$. Thus, the Heisenberg model in the non-Kramers phase diagram is not the same Heisenberg model realized by the Heisenberg-DM model. The lower right corner of the triangle, corresponding to the local interactions $\{J^{zz}, J^{\pm}, J^{\pm\pm}\} = \{3, 0.5, -1\}$, gives the DQQ model. The model of the upper right corner is dual to the DQQ model and is referred to as DQQ* model. The duality transformation between the two models is given by a spin rotation of an angle $\pi/2$ about the local z axis, which maps $J^{\pm\pm} \to -J^{\pm\pm}$ and leaves the remaining interactions invariant. Under this transformation, each the T_1^{xy} and T_2 manifolds, and the ψ_2 and ψ_3 states exchange. The duality transformation implies that all information on the complete phase diagram is already included in the restricted case $J^{\pm\pm} < 0$. Actually, a subtle fourth triple point at which three phases meet is caused by ObD and is found for the XXZ model at $\{J^{zz}, J^{\pm}, J^{\pm\pm}\} = \{3, 0, 0.5\}$ in between the T_1^{Ice}, ψ_2 and ψ_3 phases. We will mostly neglect this particular point in our study.

5.3.3 Quantum phase diagram of non-Kramers pyrochlore models

We now continue with the study of the phase diagram of the $S = 1/2$ quantum model for non-Kramers pyrochlores, which will be computed by PFFRG and further complemented by HTSE results. An emphasis will be put on the vicinity of the DQQ model. While it was shown earlier that the classical DQQ model hosts emergent competing gauge fields of different ranks, which lead to an entropically-driven spin liquid to spin liquid transition, it is still unanswered at this point whether the quantum model exhibits the same behavior in state selection. Before addressing this question with the help of the phase diagram, we consider features of the wider non-Kramers phase diagram first.

The $S = 1/2$ non-Kramers phase diagram at $T = 0$, determined by PFFRG, is shown in Fig. 5.19(a). We begin by briefly discussing technical details of its computation. Its content will be discussed afterwards. The computed phase diagram covers most of the lower half ($J^{\pm\pm} \leq 0$) of the classical phase diagram shown in Fig. 5.15(a). Phase boundaries of the upper half ($J^{\pm\pm} > 0$) follow directly from the previously introduced duality transformation that relates models with different signs of $J^{\pm\pm}$. Like in the classical phase diagram, the J^{zz} interaction is kept constant at $J^{zz} = 3$, whereas

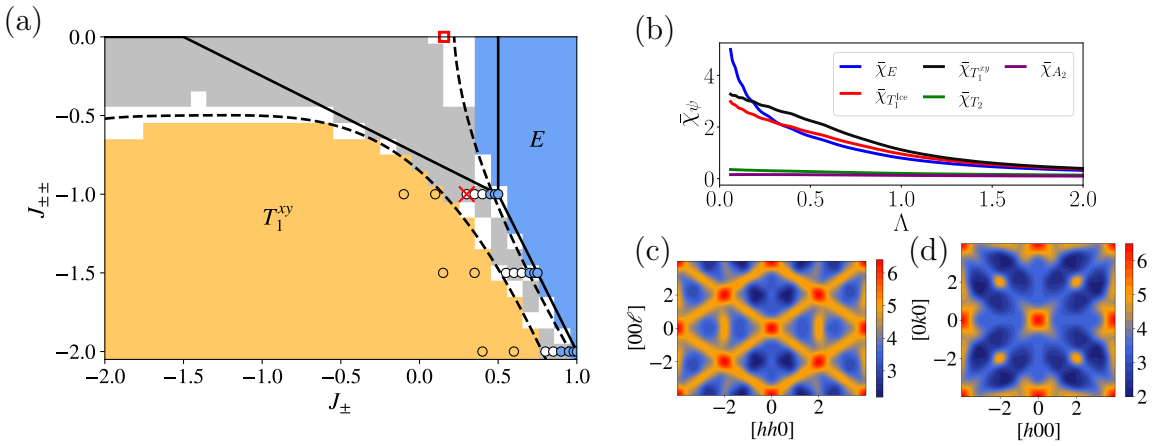

Figure 5.19: (a) PFFRG phase diagram of the spin-1/2 non-Kramers pyrochlore model at $T = 0$ with fixed $J^{zz} = 3$ where the gray region denotes an absence of magnetic long-range order, the yellow and blue regions correspond to the $\boldsymbol{q} = \boldsymbol{0}$ quadrupolar orders T_1^{xy} and E, respectively, and the white regions are of uncertain magnetic behavior. As a guide to the eye, the approximate quantum phase boundaries from PFFRG are indicated by dashed lines. Solid black lines mark the classical phase boundaries. HTSE results are shown as points, whose colors correspond to the order parameter susceptibility dominating in a calculation up to order $(1/T)^8$. The phase boundary between quantum spin-ice and magnetic E phases, as previously determined by quantum Monte Carlo on the unfrustrated $J_{\pm\pm} = 0$-line (the so-called XXZ model) is marked by a red square [84]. (b) Order parameter susceptibilities $\bar{\chi}_\psi$ from PFFRG at $T = 0$ as a function of the renormalization group parameter Λ for the quantum spin-1/2 model with interactions $\{J_{zz}, J_\pm, J_{\pm\pm}\} = \{3.0, 0.3, -1.0\}$, marked by a red cross in the phase diagram in (a). (c), (d) Static (zero frequency) spin structure factors from PFFRG at $T = 0$ for the same model as in (b) within the $[hh\ell]$ and $[hk0]$ planes in the low-cutoff limit $\Lambda \to 0$. The figure and its caption are replicated from Ref. [71].

$J^{\pm\pm} \leq 0$ and $J^\pm$ are varied. For each model with given interaction values, the presence of magnetic order is determined by identifying whether the PFFRG susceptibility flow exhibits a breakdown. This criterion leaves room for ambiguity in phase classification near phase boundaries of the phase diagram due to subtle flow breakdowns. It follows that the phase diagram exhibits regions in which the presence of magnetic order is uncertain. These regions are shown in white. Like in Sec. 5.2, phases are identified by the irrep-dependent order parameter susceptibility of maximum size at the flow breakdown or in the low cutoff limit if no flow breakdown is present. The internal structure of the quantum paramagnetic region will be mostly neglected in this study. I.e., we will generally not attempt to distinguish paramagnetic regions with different underlying phases. While the paramagnetic phase is expected to be described by a quantum spin ice near the Ising model [84], other paramagnetic phases are likely to be realized further away, as was shown in Sec. 5.1 for the Heisenberg model. Alternative paramagnetic phases are especially expected in paramagnetic regions where the spin-ice manifold does not contribute to the classical ground state manifold. We restrict

the characterization of paramagnetic regimes to the description of competition between irrep manifolds, quantified by order parameter susceptibilities, and to the computation of SFs. While order parameter susceptibilities do not strictly measure the contribution of particular states or irrep manifolds to quantum paramagnetic ground states, we will interpret the sizes of order parameter susceptibilities as roughly reflecting the involvement of their respective irrep manifolds in the state selection of a considered paramagnetic phase.

The quantum-model phase diagram of Fig. 5.19(a) is summarized as follows. Like in the classical phase diagram, we observe three distinct connected regions for the case $J^{\pm\pm} \leq 0$. They correspond to a quantum paramagnetic phase, and magnetically ordered E and T_1^{xy} phases. A quantum fluctuation-based shift of classical phase boundaries is observed. The E phase extends beyond its classical boundary. In contrast, the T_1^{xy}-ordered region shrinks in size. Newly positioned phase boundaries allow for a paramagnetic corridor to emerge in between the E and T_1^{xy} phases. The corridor is connected to the paramagnetic region surrounding the spin-ice model. Similarly, the boundary of the previously classical paramagnetic region extends from the Heisenberg model at $\{J^{zz}, J^{\pm}, J^{\pm\pm}\} = \{3, -1.5, 0\}$ towards smaller $J^{\pm}$ upon the inclusion of quantum fluctuations, resulting in an even wider paramagnetic corridor along $J^{\pm\pm} = 0$ in between the T_1^{xy} and T_2 phases. A comparison between PFFRG and qMC results is feasible for the XXZ model ($J^{\pm\pm} = 0$) at $J^{\pm} > 0$. In agreement with PFFRG, a shift of the phase boundary between the paramagnetic and E-ordered regions towards smaller $J^{\pm} > 0$ is observed within qMC [84]. The qMC phase boundary at $J^{\pm} = 0.156$ is marked in the PFFRG phase diagram by a red square. It falls into the uncertain region. PFFRG results on the XXZ model will be discussed further at a later point.

HTSE results complement the phase diagram of the quantum model in Fig. 5.19(a) and state dominant ordering tendencies across the E-T_1^{xy} phase boundary at $J^{\pm\pm} = -1.0$, -1.5 and -2.0. Small circles of corresponding coloring show which order parameter susceptibility is dominant at temperatures above an approached phase transition for each considered model with given interactions. The results argue towards a phase boundary shift towards smaller $J^{\pm\pm}$ in comparison to the classical position. This observation is supported by the phase boundaries found by PFFRG. Within the paramagnetic corridor predicted by PFFRG, HTSE finds interaction intervals where neither order parameter susceptibility of a candidate magnetic phase is found to grow substantially with decreasing temperature. This observation further hints at the existence of the paramagnetic corridor.

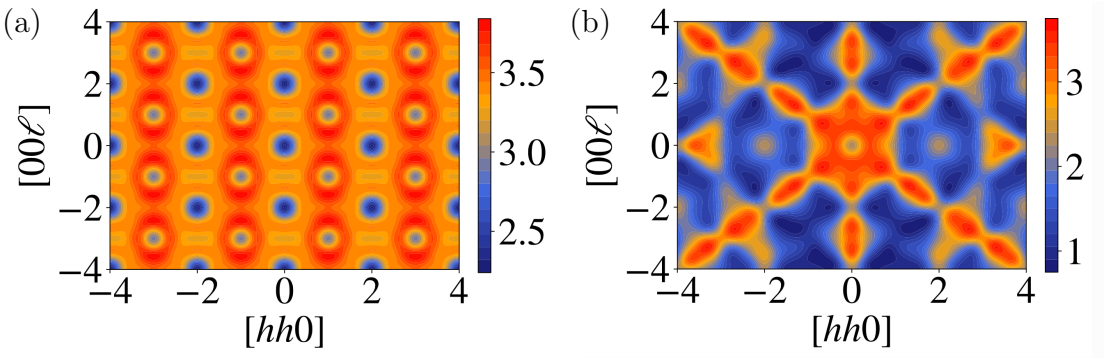

Figure 5.20: Static neutron SFs computed by PFFRG for the model $\{J_{zz}, J_{\pm}, J_{\pm\pm}\} = \{3.0, 0.1, 0\}$ in the low-cutoff limit, shown for the (a) non-spin-flip channel and (b) spin-flip channel.

Quantum XXZ model

We now shed some light on the XXZ model ($J_{\pm\pm} = 0$), which is included in the non-Kramers phase diagram of Fig. 5.19. The expected behavior of the XXZ model will be summarized first. Afterwards, we investigate the behavior observed by PFFRG and highlight the PFFRG SF in the predicted quantum spin-ice phase near the Ising model.

The XXZ model is known to realize a quantum spin-ice phase if $|J^{\pm}|/J^{zz}$ is sufficiently small. For a ferromagnetic $J^{\pm} > 0$, the $S = 1/2$ model is treatable by qMC, which finds that, for the case $T = 0$, the model undergoes a phase transition from the quantum spin-ice to the E phase at $J^{\pm} \approx 0.156$ in case $J^{zz} = 3$ [84]. This phase boundary differs from its position for the classical model, which is found at $J^{\pm} = 0.5$. Fig. 5.19 shows that PFFRG reproduces the phase boundary shift towards smaller $J^{\pm}$. The boundary found by qMC lies in the uncertain region of the PFFRG phase diagram. For $J^{\pm} < 0$, the paramagnetic region of the $S = 1/2$ XXZ model extends beyond the Heisenberg model. However, as argued in Sec. 5.1, the $S = 1/2$ (and $S = 1$) paramagnetic ground state of the Heisenberg model (found at $\{J_{zz}, J_{\pm}, J_{\pm\pm}\} = \{3, -1.5, 0\}$) is believed to assume a nematic order. This implies a phase transition in the phase diagram at $-1.5 < J_{\pm} < 0$ for $J_{zz} = 3$ between the quantum spin-ice phase near the Ising model and the nematic phase of the Heisenberg model if no additional paramagnetic phase is found in between the two phases.

Next, we consider the spin SF in the quantum spin-ice phase. While the ground state of the Ising model, which realizes a classical spin ice, possesses sharp pinch-point features in its SF, it is nontrivial how the inclusion of quantum fluctuations, which allow for tunneling processes between different spin-ice configurations, affects these features. Importantly, quantum spin ice has photon excitations, which are gapless (unlike the electric and magnetic monopole excitations) and are expected to affect the SF at low

temperatures. It is argued in Ref. [115] that the gaplessness of photon excitations at the $\boldsymbol{q}$ locations of pinch points causes the pinch points in the spin-flip channel of the equal-time spin SF to vanish at $T = 0$ (however, note that they are predicted to reemerge at finite temperatures). Furthermore, photon excitations are gapless at $\boldsymbol{q} = \boldsymbol{0}$. As a consequence, the intensity in the spin-flip channel of the equal-time spin SF is predicted to vanish linearly with T at $\boldsymbol{q} = \boldsymbol{0}$.

The static PFFRG spin SF for a model in the quantum spin-ice regime at $\{J_{zz}, J_{\pm}, J_{\pm\pm}\} = \{3.0, 0.1, 0\}$ is shown in Fig. 5.20 in both the spin-flip and non-spin-flip channel. Note that the predictions of Ref. [115] were made for the equal-time spin SF, whereas we show the static SF instead[8]. A priori, it is not clear which predicted features of the equal-time SF are expected to remain in the static SF. Interestingly, we observe a local minimum in the spin-flip channel at $\boldsymbol{q} = \boldsymbol{0}$, which is also predicted in the equal-time SF. However, the intensity does not vanish completely at $\boldsymbol{q} = \boldsymbol{0}$, like it is predicted in the $T = 0$ equal-time SF. Similarly, a vanishing of pinch points is partially reproduced, e.g., at $\boldsymbol{q} = (1, 1, 1)$ and $(0, 0, 2)$. Note that the PFFRG computation of the SF only includes maximum correlation distances of four nearest-neighbor spacings, since the corresponding model was evaluated as part of the non-Kramers phase diagram. As a consequence of this approximation and additional numerical approximations, such as the truncation of flow equations, details in the present PFFRG SF should be taken with a grain of salt, especially in the context that PFFRG is not able to reproduce sharp pinch points in the Ising model as well (not shown). In order to unravel which observed features of the SF are a consequence of numerical approximations, an advanced study would be necessary that investigates the effects of each individual approximation on the SF. Such an investigation is beyond the scope of this study.

Regarding the non-spin flip channel of the model $\{J_{zz}, J_{\pm}, J_{\pm\pm}\} = \{3.0, 0.1, 0\}$, shown in Fig. 5.20(a), we note that the observed pattern of local minima is reminiscent of the non-spin-flip channel pattern observed in the qMC study of the XXZ model in Ref. [84], with minima being located at the same positions. However, we observe the subtle difference that at these positions there exist two types of alternating local minima in the PFFRG SF, which exhibit different widths and minimum values (e.g., at $hhl = 002$ and $hhl = 111$). This is in contrast to Ref. [84], where all local minima, except the minimum at $\boldsymbol{q} = \boldsymbol{0}$, appear to have the same shape.

[8]The PFFRG is formulated in frequency space, so that generally static SFs are given out. For the given numerical implementation, a Fourier transform to an equal-time SF had not been implemented.

The $S = 1/2$ DQQ model

Previous observations in the phase diagram of the quantum model will now aid in the following discussion of the $S = 1/2$ DQQ model. The $S = 1/2$ DQQ model, with $\{J^{zz}, J_{\pm}, J^{\pm\pm}\} = \{3, 0.5, -1\}$, is located in a region of uncertainty in the PFFRG phase diagram of Fig. 5.19(a). A dominant E order parameter susceptibility and the previously discussed shift of phase boundaries in the quantum model suggest the scenario in which the model orders magnetically into an E phase. A good qualitative agreement with the SFs of the classical DQQ model in the $T > T^*$ phase is obtained by considering a quantum model with reduced $J^{\pm}$ instead, which is deeper within the paramagnetic corridor of the phase diagram and near the point $\{J^{zz}, J_{\pm}, J^{\pm\pm}\} = \{3.0, 0.3, -1.0\}$ (marked by a red cross in the phase diagram). The order parameter susceptibility flows and spin SFs of this model are shown in Figs. 5.19(b)-(d). Note that the plot uses a slightly different notation for order parameter susceptibilities $\bar{\chi}_{\Psi}$ from the previous notation $\bar{\chi}_{\psi}$ used in the study of the Heisenberg-DM model. $\bar{\chi}_{\Psi}$ is now labeled by the irrep Ψ it represents instead of a spin configuration ψ (within the irrep Ψ manifold) for which $\bar{\chi}_{\Psi}$ is computed. One observes that $\bar{\chi}_{\Psi}$ of each classical ground state irrep is of comparable size in the low cutoff limit[9]. The $T = 0$ PFFRG spin SF exhibits patterns with a close resemblance to those found in the SF of the classical DQQ model at $T > T^*$. In contrast, the $T = 0^+$ spin-ice SF of the classical DQQ model is not reproduced at all in the quantum-model phase diagram near the DQQ model. This suggests that the $T = 0$ quantum model with $\{J^{zz}, J_{\pm}, J^{\pm\pm}\} = \{3.0, 0.3, -1.0\}$ rather realizes a quantum analogue to the combined rank-1 rank-2 spin-liquid phase of the classical DQQ model, rather than a phase similar to a spin ice. It is known that the quantum XXZ model realizes a quantum spin-ice phase for interactions close to the Ising model [84]. Since the full paramagnetic region of the phase diagram is connected, a QSL to QSL transition may still be achieved by moving along the quantum-model phase diagram from the Ising model towards the $\{J^{zz}, J_{\pm}, J^{\pm\pm}\} = \{3.0, 0.3, -1.0\}$ model.

We show the static neutron SF of the model $\{J^{zz}, J_{\pm}, J^{\pm\pm}\} = \{3.0, 0.3, -1.0\}$ in Fig. 5.21. Since neutrons scatter only on the spin z components of the local coordinate system, a spin-ice-like pattern is obtained similar to that observed in the classical DQQ model shown in Fig. 5.16. However, some subtle differences are visible. At scattering vectors $[hh\ell] = [000]$, $[002]$ and symmetry-related points, a slight local decrease of intensity is visible in the spin-flip channel. Furthermore, we observe broadened pinch points. Although broadened pinch points are expected, because the ice rule is not

[9]Note that a $\boldsymbol{q} = \boldsymbol{0}$ spin-ice configuration was chosen for the computation of $\bar{\chi}_{T_1^{\mathrm{Ice}}}$. Hence, the order parameter susceptibility is not representative of the full spin-ice manifold. I.e., there may exist $\boldsymbol{q} \neq \boldsymbol{0}$ spin-ice configurations with order parameter susceptibilities of larger values.

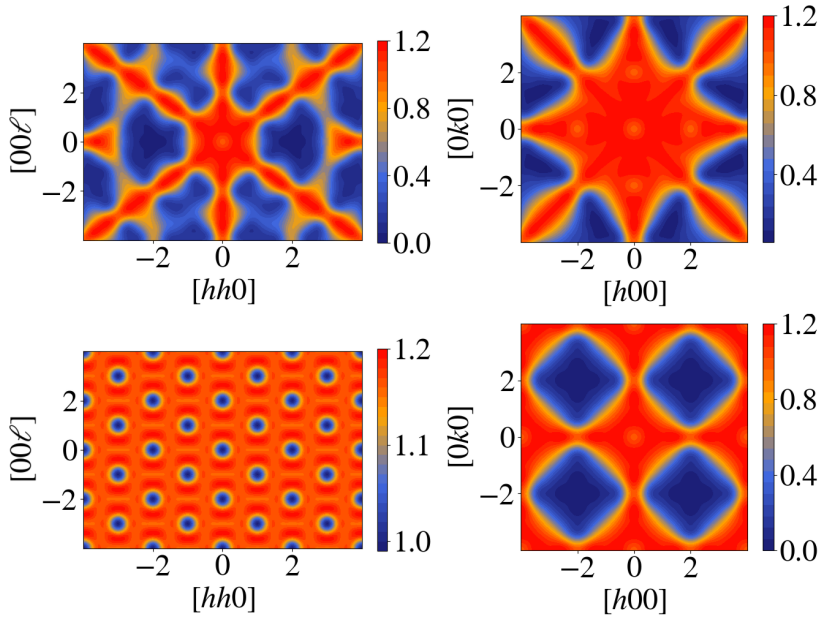

Figure 5.21: Static neutron SFs computed by PFFRG for the model $\{J_{zz}, J_{\pm}, J_{\pm\pm}\} = \{3.0, 0.3, -1.0\}$ in the low-cutoff limit. The first and second rows correspond to the spin-flip and non-spin-flip channels respectively. The figure and its caption are replicated from Ref. [71].

fulfilled by the ground state of the quantum model, we note that broadened pinch points can also arise from numerical approximations involved within PFFRG. Finally, a qualitatively different pattern than in the classical DQQ model is obtained in the $[hh\ell]$ plane of the non-spin-flip channel. The observed pattern is reminiscent of the pattern obtained by qMC in the quantum spin-ice phase of the XXZ model (see Fig. 3(a) in Ref. [84]).

To obtain a better picture of the evolution of SFs across the phase diagram, we plot spin SFs in the quantum paramagnetic and uncertain regions near the quantum DQQ model in Fig. 5.22. We point out that we did not claim that the SF of the model $\{J^{zz}, J_{\pm}, J^{\pm\pm}\} = \{3.0, 0.3, -1.0\}$ exhibits the best qualitative agreement with the SF of the classical DQQ model at $T > T^*$. Instead, it was only stated that a good agreement is obtained in a region near this model. E.g., SFs of the models with interactions $\{J^{zz}, J^{\pm}, J^{\pm\pm}\} = \{3.0, 0.3, -0.9\}$ and $\{J^{zz}, J^{\pm}, J^{\pm\pm}\} = \{3.0, 0.4, -1.1\}$ show close resemblance to SFs of the classical DQQ model as well.

Experimental relevance of the DQQ model

We end the treatment of the DQQ model with a discussion on its experimental relevance. As was mentioned earlier, the DQQ model can be realized by non-Kramers pyrochlore compounds. The a priori chance of finding a non-Kramers compound that

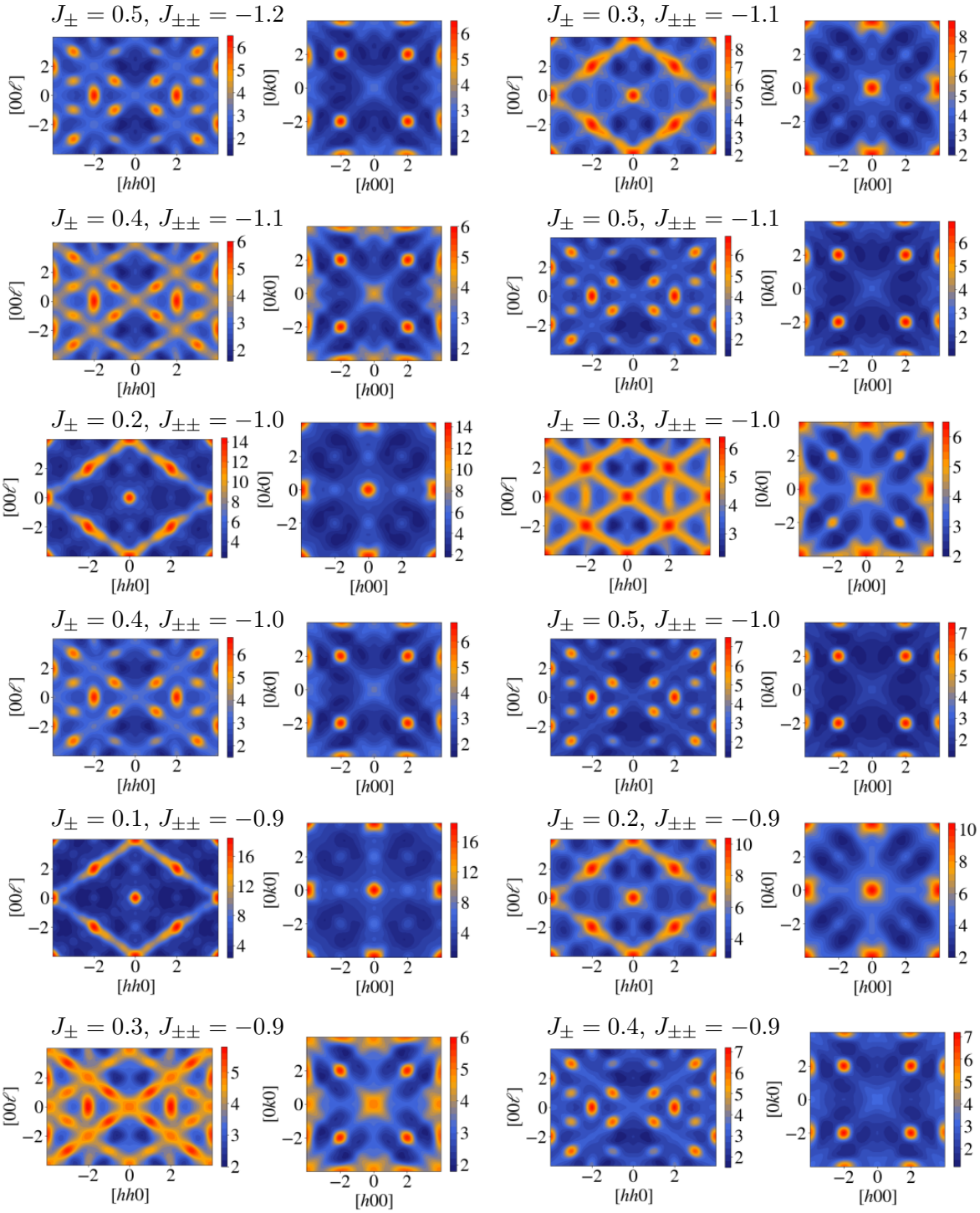

Figure 5.22: Static spin SFs computed by PFFRG in the low-cutoff limit. Different interactions with constant $J_{zz} \equiv 3$, and within the paramagnetic regime of the quantum-model phase diagram Fig. 5.19(a) near the DQQ model are considered. The figure and its caption are replicated from Ref. [71].

approximately realizes the DQQ model is greater than for compounds with fully dipolar spins, since nearest-neighbor models of non-Kramers compounds are restricted by symmetries to have one interaction less ($J^{z\pm} = 0$). In fact, the previously studied non-Kramers pyrochlore system $Tb_2Ti_2O_7$ might be a candidate material for the realization

of a rank-1 rank-2 spin liquid, since it was predicted to be described by a model found in the vicinity of the DQQ* model [116].

However, even if a system is found that is proposed to be well described by the DQQ or DQQ* model, it is unclear at this point how to experimentally capture the underlying physics of its possible rank-1 rank-2 spin liquid phase. The anisotropic g tensor of non-Kramers systems allows only for the rank-1 gauge field (the spin-ice component) to be detected by neutron scattering. Meanwhile, the rank-2 gauge field of the spin liquid remains hidden. At this point, to the best of the author's knowledge, a strategy to experimentally reveal the presence of a rank-2 spin liquid that is realized by the local x and y spin components of a non-Kramers compound has yet to be proposed.

5.4 Discussion

The pyrochlore lattice represents a prominent platform for the study of frustrated magnetism [117]. In this chapter, we restricted ourselves to nearest-neighbor spin models on this lattice and have investigated their various properties. On the basis of the symmetry-constrained models realized by pyrochlore compounds, classical and quantum phase diagrams of the Heisenberg-DM model and of non-Kramers pyrochlore systems were computed and discussed in detail. Due to geometrical frustration, many occurring phases were characterized by classically degenerate ground state manifolds. As such, an underlying theme throughout the chapter was the ObD selection within these manifolds driven by the presence of quantum or thermal fluctuations. Particular attention was paid to models within the phase diagrams that are positioned on classical phase boundaries and realize extensive classical ground state manifolds as a consequence. More specifically, these models are given by the Heisenberg and DQQ models, in which ObD fails to realize magnetically ordered phases. We use this opportunity at the end of the chapter to summarize and discuss its most important results.

We first discuss insights on the studied phase diagrams in general, then phases found within the phase diagrams, and at last the Heisenberg and DQQ models in particular. Phase diagrams were resolved both for the classical and $S = 1/2$ quantum models. Classical phase boundaries were found to be shifted by quantum fluctuations. Generally, paramagnetic regimes were of larger extent in the quantum models. E.g., while paramagnetic phases of the Heisenberg-DM model, found near the Heisenberg and DQQ ($D/J = 2$) models, were of no finite extent in the $T = 0$ classical phase diagram, they were stabilized over a finite region in the phase diagram of the quantum model. However, not every model that is paramagnetic for classical spins remained paramagnetic for quantum spins. This was best observed in the non-Kramers phase diagram.

Here, the E phase extends in the phase diagram of the quantum model beyond its classical phase boundary towards the neighboring paramagnetic regime with a classical spin-ice ground state manifold. This behavior was independently confirmed by qMC for the XXZ model [84]. An unexpected observation regarding the paramagnetic regime is the emergence of paramagnetic corridors in the $S = 1/2$ non-Kramers phase diagram in between the E and T_1^{xy}, and T_1^{xy} and T_2 phases. Note that the classical models on the corresponding classical boundaries are magnetically ordered at $T = 0$ for the considered interaction ranges of the computed phase diagram (except at the tricritical end points of the phase boundaries) [71].

The Γ_5 phase of the Heisenberg-DM model was found to be a prime example to demonstrate the potential subtleties of ObD selections. The ObD selection between ψ_2 and ψ_3 orders out of the Γ_5/copl manifold was found to depend on both the interactions of the model and the temperature. With respect to the latter parameter, a different selection was found at zero and critical temperatures across most of the Γ_5-ordered region in the phase diagram of the Heisenberg-DM model. In the quantum model, the resolution of the ObD selection was methodologically challenging. PFFRG was able to only partially resolve the state selection of the Γ_5 phase due to equal order parameter susceptibilities for all orders of the Γ_5 manifold. Note that the property of equal order parameter susceptibilities is expected to hinder the identification of the state selection in neutron scattering experiments as well. To determine the ObD selection of the quantum model within the Γ_5 manifold, HTSE was applied. Remarkably, ObD selections were found to mostly coincide between the classical and quantum models. Beyond the Γ_5 phase, we point out that the ferromagnetic phase of the Heisenberg-DM model realizes an interesting case of ObD as well, since accidentally degenerate ferromagnetic product states are exact ground states of the Heisenberg-DM quantum model. As such, this phase allows the study of ObD in a quantum model on a state without quantum zero-point fluctuations. The ObD selections in the ferromagnetic phase of the Heisenberg-DM model are studied in Ref. [91].

With the Heisenberg and DQQ models, two particular models with given interactions have been studied in more detail in this chapter. The Heisenberg and DQQ models were realized in the phase diagrams of both the Heisenberg-DM model and non-Kramers pyrochlore models. Furthermore, both the Heisenberg and DQQ models remain nonmagnetic down to $T = 0$ due to their extensive classical ground state manifolds, and exhibit nontrivial fluctuation-based state selections within their respective ground state manifold. We first studied the Heisenberg model, which is more prominent in previous studies of spin models on the pyrochlore lattice (see Sec. 5.1). In agreement with growing evidence from the literature, we argued in a PFFRG study that the ground states of the $S = 1/2$ and $S = 1$ models realize nematic orders that either break lattice

C_3 or both C_3 and inversion symmetry. Unlike the Heisenberg model, the DQQ model has previously been neglected in the literature. For classical spins, the DQQ model was revealed to possess a spin liquid to spin liquid transition in its temperature dependence. In the quantum model, phase boundaries of the $T = 0$ non-Kramers phase diagram are shifted compared to the classical boundaries such that the quantum model analogue to the classical DQQ model was found at different interactions $\{J^{zz}, J^{\pm}, J^{\pm\pm}\}$. This quantum version of the DQQ model was found to realize a phase that closely resembles the intermediate-temperature spin-liquid phase of the classical DQQ model, which is described by a combined rank-1 rank-2 gauge field, in its spin SF.

Chapter 6

$K_2Ni_2(SO_4)_3$ and the tetra-trillium-lattice Heisenberg model as a novel three-dimensional platform of frustrated magnetism

The spin models on the pyrochlore lattice studied in the previous chapter provided insights on state selection mechanisms found in the field of highly frustrated magnetism and were of relevance to experimentally studied spin compounds. However, there of course exist many alternative lattice platforms for the study of frustrated magnetism as well. We will now move beyond pyrochlore lattice applications and study frustrated magnetism on the three-dimensional tetra-trillium lattice instead. Unlike in applications of the previous chapter, we will restrict ourselves to Heisenberg models only. However, the competition between Heisenberg interactions will not be restricted to nearest-neighbor bonds only, but will include interactions between further neighbors as well.

Spin models on the interconnected trillium or tetra-trillium lattice, often realized by langbeinite compounds [118], have recently received attention due to their relevance in understanding the low-temperature behavior of the novel spin liquid candidates $K_2Ni_2(SO_4)_3$ [13, 119, 118] and $KSrFe_2(PO_4)_3$ [120]. Out of these systems, this chapter will treat the $K_2Ni_2(SO_4)_3$ compound. It has been synthesized as both powder and crystal sample, and has been found experimentally to exhibit a highly dynamical state down to low temperatures. While the compound exhibits weak magnetic order near $T = 0$, it can even be driven into a paramagnetic state by applying an external magnetic field [13]. The compound is found by density functional theory (DFT) to be

described by a $S = 1$ Heisenberg model with many competing Heisenberg interactions spanning from first- to fifth-nearest neighbors. Such a model is well suited to be treated by the PFFRG method, in which further-neighbor interactions are straightforwardly implemented by adjusting the initial conditions of the PFFRG flow in the infinite cutoff limit.

An aim of this chapter is to theoretically understand the experimentally found low-temperature behavior of $K_2Ni_2(SO_4)_3$. To this end, we will follow along our recent publication Ref. [118], which builds on our previous study Ref. [13] and applies PFFRG, cMC, inelastic neutron scattering (INS) and DFT in a complementary approach to reveal the magnetic order of $K_2Ni_2(SO_4)_3$. The author of this thesis contributed with the PFFRG perspective of these publications. Hence, this chapter will emphasize the PFFRG aspects of the study. The found low-temperature behavior will suggest that the spin model of $K_2Ni_2(SO_4)_3$ lies in proximity to a $T = 0$ paramagnetic phase. In this context, we will show that the two-dimensional $T = 0$ phase diagram built by the dominant Heisenberg interactions of $K_2Ni_2(SO_4)_3$ hosts a paramagnetic region of large extent for the quantum models with $S = 1/2$ and $S = 1$. Interestingly, the effective spin model of $K_2Ni_2(SO_4)_3$, obtained by DFT, lies in proximity to the paramagnetic region, contextualizing the magnetic order found experimentally in the compound. Furthermore, the considered parameter space of the phase diagram is assumed to be relevant for a wide variety of langbeinite compounds [118]. Thus, the discovery of the large $T = 0$ paramagnetic region opens up a promising new direction in the research of quantum spin-liquid phases.

The chapter is organized as follows. The trillium and tetra-trillium lattices, and the Heisenberg models that they realize, are introduced first in Sec. 6.1. Afterwards, we present the study of $K_2Ni_2(SO_4)_3$ in Sec. 6.2, which argues along the contents of the publications of Refs. [13] and [118], to which the author contributed with the PFFRG perspective. Thus, PFFRG results are treated in detail, whereas we refer to the publications for further information and discussion on experimental results and aspects of the classical models. In Sec. 6.3, we consider Heisenberg models on the tetra-trillium lattice more generally and study the $S = 1/2$ and $S = 1$ reduced phase diagrams that consider only the three dominant Heisenberg interactions of the DFT model of $K_2Ni_2(SO_4)_3$. Finally, a discussion of the chapter is provided in Sec. 6.4.

In this chapter, the PFFRG will be applied with the following specifications: The self-energy and the two-particle vertex are discretized on frequency grids, with frequencies being exponentially distributed about the zero frequency. The frequency grid of the self-energy contains 1000 positive frequencies, and the frequency grid of the two-particle vertex contains 32 positive frequencies for each of its three transfer frequency

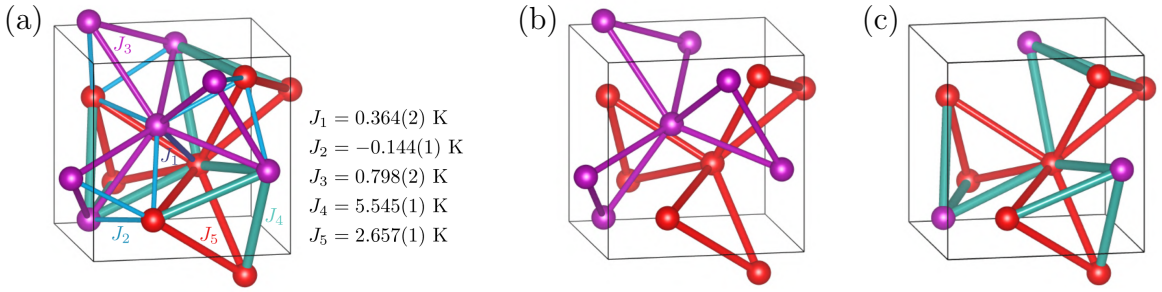

Figure 6.1: Crystal and magnetic structure of $K_2Ni_2(SO_4)_3$. (a) Two trillium lattices of Ni^{2+} ions in $K_2Ni_2(SO_4)_3$ with the five nearest-neighbour couplings calculated by DFT energy mappings. (b) J_3 and J_5 form two independent trillium lattices. (c) J_4 couples each ion from one trillium lattice to the nearest triangle of the second trillium lattice. For $J_4 = J_5$, magnetic ions form a network of corner-shared tetrahedra based on a trillium lattice, a tetra-trillium lattice. The figure and its caption are replicated from Ref. [118].

arguments. Spin correlations will be neglected if they exceed distances of three underlying cubic lattice constants of the tetra-trillium lattice. Hence, the two-particle vertex is given out for 1842 lattice vectors, or 622 vectors unrelated by lattice symmetries. For the computation of the J_3-J_4-J_5 model phase diagram, correlations are already neglected for distances above two cubic lattice constants, which implies 186 vectors unrelated by symmetry. An explicit embedded Runge-Kutta (2, 3) method with adaptive step size is applied to solve the flow equations. For this purpose, the Runge-Kutta implementation of Ref. [60] is used.

6.1 Trillium and tetra-trillium lattices

The magnetic lattice of the compound $K_2Ni_2(SO_4)_3$ is given by two interconnected trillium lattices [13] that can alternatively be framed as a so-called tetra-trillium lattice [119]. In this section, our aim is to introduce these lattices before studying the physics of $K_2Ni_2(SO_4)_3$ and of Heisenberg models on the tetra-trillium lattice in general. The trillium lattice is a three-dimensional lattice built by corner-sharing triangles of lattice sites [121], with each lattice site being shared by three triangles, as shown in Fig. 6.1(b). Lattice sites are arranged in a simple cubic lattice structure with a 4-site unit

cell. The sublattice vectors $\boldsymbol{b}_i$ depend on a real parameter u and are given by

$$\begin{aligned}\boldsymbol{b}_0 =&(u,u,u),\\ \boldsymbol{b}_1 =&(\frac{a}{2}+u,\frac{a}{2}-u,a-u),\\ \boldsymbol{b}_2 =&(a-u,\frac{a}{2}+u,\frac{a}{2}-u),\\ \boldsymbol{b}_3 =&(\frac{a}{2}-u,a-u,\frac{a}{2}+u),\end{aligned} \tag{6.1}$$

with a being the lattice constant of the simple cubic lattice. Note that the lattice constant of $K_2Ni_2(SO_4)_3$ is given by $a = 9.81866(12)\mathring{A}$ at $T = 100K$ [13]. Since u is a real parameter, the extended Brillouin zone of the lattice is generally of infinite extent. This is the case for $K_2Ni_2(SO_4)_3$ as well, for which $u_1 \approx 0.33554$ and $u_2 \approx 0.59454$. Trillium lattice symmetries consist of a C_3 rotation about the [111] axis and a screw symmetry that applies a C_2 rotation about [001] followed by a translation by $(a/2, 0, a/2)$. It follows from these symmetries that all lattice sites and bonds J_3 or J_5 in Fig. 6.1(b) can be mapped onto one another by applying lattice symmetries.

The tetra-trillium lattice is obtained from the trillium lattice by upgrading its triangles to tetrahedra. This is achieved by adding a single lattice site to each triangle, as shown in Fig. 6.1(c). Newly added sites are shown in purple, whereas bonds and sites of the previous trillium lattice are shown in red. The tetrahedra become visible by considering the turquoise bonds between newly added sites and sites of the trillium lattice. It is visible in Fig. 6.1(c) that the tetrahedra are corner-sharing. In total, the change from trillium to tetra-trillium lattice amounts to four additional sites added per cubic unit cell. Note that the additional purple sites are not located on any vertices between tetrahedra of the tetra-trillium lattice, but instead are connected via turquoise bonds only to sites of a single triangle of the previous trillium lattice. Since the newly added turquoise bonds are not related to the bonds of the previous trillium lattice by any symmetry, they are expected to generally carry different interactions in spin models. In compounds, the length of turquoise bonds will generally differ from the length of red bonds (bonds within the trillium lattice) as well. It follows that tetra-trillium realizations are expected to possess irregular tetrahedra. Note that as an alternative to the framing of the tetra-trillium lattice as being built by corner-sharing tetrahedra, the tetra-trillium lattice can be understood as two interconnected trillium lattices with different lattice parameters u, as shown in Fig. 6.1(b).

We can now relate the trillium and tetra-trillium lattices to the magnetic lattice structure found in $K_2Ni_2(SO_4)_3$, which is shown in Fig. 6.1(a) and contains first- to fifth-nearest-neighbor bonds with Heisenberg interactions J_1 to J_5. The third (purple) and fifth-nearest-neighbor (red) bonds of $K_2Ni_2(SO_4)_3$ correspond to the bonds within each

of its trillium lattices that build corner-sharing triangles. The fourth-nearest-neighbor bonds (turquoise) partially build up the tetrahedra of the tetra-trillium lattice [as shown in Fig. 6.1(c)], connect both trillium lattices and build a bipartite lattice structure if considered by themselves. A comparison between Figs. 6.1(a) and 6.1(c) reveals that a model of corner-sharing tetrahedra on the tetra-trillium lattice is obtained from a spin model of $K_2Ni_2(SO_4)_3$ by only considering finite interactions J_4 and J_5 between fourth- and fifth-nearest neighbors. At last, the first- and second-nearest-neighbor bonds of $K_2Ni_2(SO_4)_3$ connect sites between its two trillium lattices.

Before introducing effective spin models of $K_2Ni_2(SO_4)_3$ in more detail, we draw a connection to Heisenberg models on the previously studied pyrochlore lattice. A connecting feature that enforces geometrical frustration on each the pyrochlore, trillium, and tetra-trillium lattice is that spin models on each of these lattices can realize corner-sharing clusters of interacting spins. These clusters represent tetrahedra on the pyrochlore and tetra-trillium lattices, and triangles on the trillium lattice. In such corner-sharing structures, the conditions for classical ground state configurations of Heisenberg models are straightforward, as explained in the following. For simplicity, one can consider a nearest-neighbor antiferromagnetic Heisenberg model given by

$$\mathcal{H} = J \sum_{\langle ij \rangle} \boldsymbol{S}_i \cdot \boldsymbol{S}_j, \tag{6.2}$$

with $J > 0$, in which spins interact only within corner-sharing clusters c of nearest neighbors, i.e., each spin $\boldsymbol{S}_i$ of a cluster c interacts with each remaining spin $\boldsymbol{S}_j$ of the same cluster, and two clusters c and c' can share at most one spin. In this case, the Hamiltonian can be rewritten as

$$\mathcal{H} = \frac{J}{2} \sum_c (\sum_{i \in c} \boldsymbol{S}_i)^2 + D, \tag{6.3}$$

with D being a constant [1]. A Hamiltonian of this form already occurred in Eq. (5.6) of the last chapter in context of the Heisenberg model on the pyrochlore lattice, where the summation index labels tetrahedra of the lattice. It is apparent from Eq. (6.3) that the classical ground state manifold of $\mathcal{H}$ is given by the states that fulfill the constraint $(\sum_{i \in c} \boldsymbol{S}_i)^2 = 0$ on each cluster c of the lattice. In case of the pyrochlore Heisenberg model, the resulting classical ground state manifold is extensive (see Chapter 5). The extensivity follows from a local ground state degree of freedom that conserves $(\sum_{i \in c} \boldsymbol{S}_i)^2$ and, for the classical spin-ice submanifold, consists of flipping six spins of a hexagon loop along their local z axis. The corner-sharing tetrahedra of the tetra-trillium lattice build pentagon instead of hexagon loops. Because of the odd number of sites in these loops, an analogous local degree of freedom that maps between

two classical ground states does not exist. However, it has been confirmed that a local operation exists on the tetra-trillium lattice that flips spins on a larger motif involving 18 spins and preserves $(\sum_{i\in c} \boldsymbol{S}_i)^2$ on each tetrahedron [118]. An extensive classical ground state manifold follows for Heisenberg models of corner-sharing tetrahedra on the tetra-trillium lattice as well, which are consequently absent of magnetic order for both classical and quantum spins down to $T = 0$.

6.1.1 Spin models of $K_2Ni_2(SO_4)_3$

A brief overview on the proposed spin models of $K_2Ni_2(SO_4)_3$ is provided in the following. Two DFT Heisenberg models have been proposed. The chronologically first model, proposed in Ref. [13], is based on the crystal structure of the compound at room temperature. Later, the model was refined in Ref. [118] by considering the crystal structure at $T = 100K$, which was measured by single-crystal x-ray diffraction. The latter $S = 1$ Heisenberg model is shown in Fig. 6.1. Ni^{2+} sites are the magnetic ions of the lattice. Five different Heisenberg interactions have been identified, which are labeled from J_1 to J_5 and correspond to first to fifth-nearest-neighbor interactions. The interactions are given by $\{J_1, J_2, J_3, J_4, J_5\} = \{0.364(2), -0.144(1), 0.798(2), 5.545(1), 2.657(1)\}K$ for the DFT model that applies the crystal structure at $T = 100K$. Note that the interactions J_4 and J_5 are dominant, followed by J_3. This will justify the neglection of J_1 and J_2 in the later studied phase diagram of the J_3-J_4-J_5 model.

As mentioned earlier, the Heisenberg model of corner-sharing tetrahedra on the tetra-trillium lattice, visualized in Fig. 6.1(c), is obtained by the simplification $J_1 = J_2 = J_3 = 0$. The suggestion that the magnetic behavior of $K_2Ni_2(SO_4)_3$ is well described by such a model was made in Ref. [119], which estimated the interactions of $K_2Ni_2(SO_4)_3$ based on single-crystal INS data fitted by calculations based on the self-consistent Gaussian approximation (SCGA). The corresponding model is given by $\{J_1, J_2, J_3, J_4, J_5\} = \{-0.3(3), 0.0(2), 0.1(2), 5.5(3), 3.0(2)\}K$. Due to small J_1, J_2 and J_3, this model suggests that the spin physics of $K_2Ni_2(SO_4)_3$ is well described by a model of corner-sharing tetrahedra on the tetra-trillium lattice.

Depending on whether the DFT- or SCGA-based spin model is believed to better describe the low-temperature behavior of $K_2Ni_2(SO_4)_3$, the physics of the compound can be framed as being described by different limiting cases. The $100K$ DFT model suggests to frame the compound as being described by a simplified J_3-J_4-J_5 model that describes two separate trillium lattices with interactions J_3 and J_5 that are coupled by a finite interaction J_4. The previous studies of Refs. [121, 122] found a variant of 120° order as the ground state in the case of two noninteracting trillium lattices, i.e.,

in the case $J_4 = 0$. The introduction of a finite J_4 geometrically frustrates the system by coupling both trillium lattices. However, the system becomes unfrustrated in the limit $J_4 \to \infty$ as a bipartite lattice with an antiferromagnetically ordered ground state is realized in this limit.

The SCGA-based spin model of Ref. [119] suggests a different framing of $K_2Ni_2(SO_4)_3$. This model is well approximated by a J_4-J_5 model instead that describes a tetra-trillium system built from corner-sharing tetrahedra, which suggests to draw a connection to the antiferromagnetic Heisenberg model on the pyrochlore lattice. However, while the corner-sharing arrangements of spins in the tetra-trillium and pyrochlore Heisenberg models result in paramagnetic phases at $T = 0$ for both models, the organizations of tetrahedra on the tetra-trillium and pyrochlore lattices are different and should lead to different paramagnetic ground states as a consequence. As explained in Sec. 3.5.8 of the last chapter, the spin liquid of the classical pyrochlore Heisenberg model exhibits characteristic pinch points in its SF. These pinch points are a signature of the fulfillment of the ice rule, which implies a spin-ice phase with algebraically decaying correlations on the pyrochlore lattice [123]. In contrast, the SF of the classical tetra-trillium-lattice Heisenberg model does not exhibit any pinch points and it is argued in Ref. [118] that the non-bipartite organization of tetrahedra in the tetra-trillium lattice could lead to the realization of a Z_2 spin liquid with exponentially decaying correlations.

In the following study of $K_2Ni_2(SO_4)_3$, we will generally consider its DFT model. Especially in the context that a Heisenberg model of the compound requires the fitting of five Heisenberg interactions J_1 to J_5, an ab initio DFT approach appears to be more suitable for the determination of an effective spin model than the fitting of interactions via SCGA from INS data.

6.2 The quantum spin liquid candidate $K_2Ni_2(SO_4)_3$

The previously established DFT spin model of $K_2Ni_2(SO_4)_3$ will now be investigated in a combined PFFRG, cMC and INS study to reveal the low-temperature behavior of $K_2Ni_2(SO_4)_3$. As a starting point, we first briefly summarize the low-temperature phenomenology of the compound from an experimental perspective, which reflects the highly frustrated nature of the compound and suggests its proximity to a spin-liquid phase. $K_2Ni_2(SO_4)_3$ assumes a weak magnetic order at $T_N \approx 1.1K$, which releases only 1% of the system's entropy [13]. Furthermore, within the magnetically ordered phase at temperatures well below T_N, the compound retains a continuum of featureless spin excitations in its energy spectrum for constant momenta [119, 13, 118]. Such a feature is often observed in magnetically ordered compounds proximate to predicted

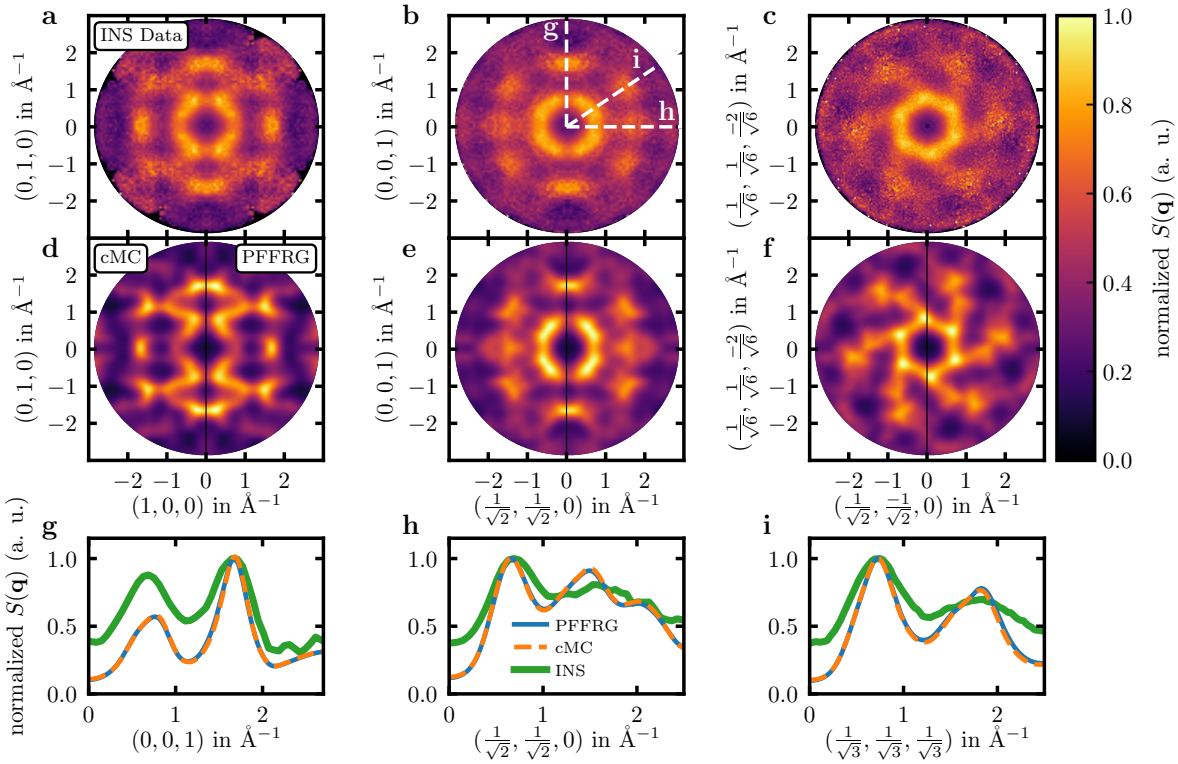

Figure 6.2: Comparison of experimental and theoretical spin structure factors. Spin structure factor along different planes in reciprocal space. (a)-(c) correspond to the experimental data obtained by INS at $T = 2\ K$ with the incident energy $E_i = 5.0\,\text{meV}$, integrated in the range $0.5\,\text{meV}$ and $1.0\,\text{meV}$. (d)-(f) are results of cMC calculations at $T = 0.35\ J_4$ ($T = 1.94\text{K}$) (left half) and PFFRG calculations for $\Lambda_c = 0.58\ J_4 (\Lambda_c = 3.22\text{K})$ (right half), using the form factor of Ni^{2+} ions. (g)-(i) display line cuts along three principal directions indicated by white dashed lines in the panel (b). The figure and its caption are replicated from Ref. [118].

spin-liquid phases [124, 125, 126], in which the continuum of excitations is caused by the pairwise excitations of spinon quasiparticles. These excitations are in contrast to the single magnon excitations with sharp dispersions that are usually found in magnetically ordered states. The proximity of $K_2Ni_2(SO_4)_3$ to a spin-liquid regime is further corroborated by the observation that the application of an external magnetic field B drives the system from a magnetically ordered into a field-induced paramagnetic phase at $B \gtrsim 4T$ [13]. Regarding the magnetic order of the compound at $T < T_N$, weak magnetic Bragg peaks at $T = 0.01$ are observed to be located at $hkl = \frac{1}{3}00$, $\frac{1}{3}\frac{1}{3}0$ and $\frac{1}{3}\frac{1}{3}\frac{1}{3}$ [13, 119]. These positions would be consistent with a large $L^3 = (3a)^3$ magnetic unit cell. Note that a magnetic unit cell with a width of $L = 3a$ would contain 216 lattice sites.

With the above experimental features of $K_2Ni_2(SO_4)_3$ being established, we now aim to understand the behavior of the compound in a combined experimental and theoretical effort. The first major objective of our study is to determine the magnetic order of $K_2Ni_2(SO_4)_3$. This will be achieved on the basis of its single crystal INS SF and by applying PFFRG and cMC to the $S = 1$ and classical DFT model, respectively. To achieve a better comparison between numerical and experimental results, the magnetic form factor of Ni^{2+} ions will be applied in the computation of SFs $S(\boldsymbol{q}) = \sum_{\mu=x,y,z} \chi^{\mu\mu}(\boldsymbol{q})$ obtained by PFFRG and cMC. The form factor causes $S(\boldsymbol{q})$ to slowly fall off with increasing $|\boldsymbol{q}|$ [127]. Note that the shown SFs obtained by PFFRG will be static, whereas cMC results show equal-time SFs. The equal-time SF obtained by INS $S_{\text{exp}}(\boldsymbol{q})$, measured above the ordering temperature at $T = 2K$, is approximated by integrating the measured frequency-dependent SF $S_{\text{exp}}(\boldsymbol{q}, \omega)$ over a finite frequency interval, i.e.,

$$S_{\text{exp}}(\boldsymbol{q}) = \int_{\omega_1}^{\omega_2} d\omega S_{\text{exp}}(\boldsymbol{q}, \omega). \tag{6.4}$$

The lower integration limit $\omega_1 \sim 0.5meV$ is set at the range in ω above which coherent scattering is obtained, and the upper integration limit $\omega_2 \sim 1meV$ is fixed such that the signal-to-noise ratio is maximized [118].

Based on the SFs obtained by INS, PFFRG and cMC, the magnetic order of $K_2Ni_2(SO_4)_3$ will be inferred by the following argument. A good fit between the PFFRG and INS SFs will suggest that the DFT model captures the low-temperature physics of the compound well. Although PFFRG is able to confirm the magnetic phase transition of $K_2Ni_2(SO_4)_3$, as is implied by the presence of a flow breakdown, it is unable to determine the underlying magnetic order from the SF. A good fit between PFFRG and cMC SFs will be used as an argument to suggest that a quantum-to-classical correspondence is realized in the DFT model. This correspondence describes the phenomenon where the behavior of a quantum model at a finite temperature is well captured by the clas-

sical model at a rescaled temperature [128]. In order to suggest this correspondence, the PFFRG frequency cutoff will be interpreted as an effective temperature. Under the assumption that the quantum-to-classical correspondence holds, the cMC results on the classical model can be utilized to infer the magnetic order of the $S = 1$ quantum model and, by extension, of $K_2Ni_2(SO_4)_3$.

The INS SF in the paramagnetic phase at $T = 2K$ is shown in the (001), $(1\bar{1}0)$ ($[hk0]$, $[hhl]$) and (111) planes in Figs. 6.2(a)-(c). For comparison, SFs of the $S = 1$ and classical DFT models, obtained by PFFRG at the critical cutoff $\Lambda_c = 3.22K$ and by cMC at $T = 1.94K$, are shown in equal planes in Figs. 6.2(d)-(f). The cMC temperature is chosen such that the best agreement with the PFFRG SF is achieved. Intensities of cMC and PFFRG SFs are rescaled globally to give equal values if they are integrated over $\boldsymbol{q}$. The patterns of PFFRG and cMC SFs are found to be in excellent agreement, with no qualitative differences being visible. The SFs exhibit broad features across momentum space, and a spiral-galaxy-like pattern, with arms emerging from the corners of a hexagonal shape, emerges in the (111) plane. The agreement between PFFRG and cMC SFs is further highlighted by considering their intensities along [100], [110] and [111] cuts in momentum space, as done in Figs. 6.2(g)-(i). We interpret the almost identical SFs of PFFRG and cMC as the realization of a quantum-to-classical correspondence in the DFT model, i.e., the behavior of the $S = 1$ quantum model at a finite frequency cutoff, which effectively acts as a temperature, is well captured by the classical model at finite temperatures. Thus, we are justified to infer the magnetic order of the quantum model from cMC simulations. A comparison between INS and PFFRG/cMC SFs reveals matching patterns as well, which suggests that the DFT model captures the low-energy physics of $K_2Ni_2(SO_4)_3$ well. Together with the quantum-to-classical correspondence, this enables the application of cMC to infer the magnetic order of $K_2Ni_2(SO_4)_3$.

Although the agreement between the shown SFs of different methods is good, we point out some differences found between the numerical and INS SFs as well, which are best described along the one-dimensional cuts of Figs. 6.2(g)-(i). In these plots, subtle features of the INS SF at large $|\boldsymbol{q}| > 1\mathring{A}^1$ are not captured along the directions [100] and [110]. Furthermore, relative intensities of the prominent peaks are different in INS and PFFRG/cMC SFs, and the INS SF features are generally broader than those found in the PFFRG/cMC SFs. However, some deviations between the INS and cMC (PFFRG) SFs are expected even if the DFT model captures the magnetic behavior of the compound well. Factors that may lead to deviations are that the temperature (cutoff) at which the cMC (PFFRG) SF was obtained was not fitted for a best agreement with the INS SF, and that the applied magnetic form factor may not correctly capture the SF intensity falloff. Additionally, there are some experimental limitations involved.

E.g., the INS SF can only be measured and thus integrated over a finite energy range instead of over all energies, as would be required for the computation of the equal-time SF.

Now that cMC has been established to capture well the low-temperature behavior of $K_2Ni_2(SO_4)_3$, the magnetic order of the compound can be determined via cMC as a reasonable next step. For this purpose, cMC was applied in Ref. [118] for different system sizes L^3 with periodic boundary conditions. In the low-temperature limit, minimum and equal ground state energies were obtained for $L = 3an$, with $n \in \mathbb{N}$. In the corresponding ground state, spins are oriented in angles close to 120°, and a comparison of INS with cMC SFs shows an agreement in Bragg peak positions. Thus, the low-temperature magnetic phase of $K_2Ni_2(SO_4)_3$ is identified to realize a variant of 120° order with a cubic magnetic unit cell of width $L = 3a$. Note that the realized magnetic order of cMC is found to be sensitive with respect to varying Heisenberg interaction strengths of the model. E.g., the SCGA model of Ref. [119] leads to a $L = 5n$ magnetic unit cell in cMC [118]. However, such a magnetic order does not reproduce the experimentally observed Bragg peak positions.

Comparison of DFT and SCGA-based models

As mentioned earlier, different spin models have been proposed to describe the magnetic behavior of $K_2Ni_2(SO_4)_3$. In the following, their predictions will be compared from a PFFRG perspective. Fig. 6.3 shows PFFRG SF flows for all proposed models of $K_2Ni_2(SO_4)_3$ in addition to the flow of the tetra-trillium Heisenberg model with interactions $J_1 = J_2 = J_3 = 0$ and $J_4 = J_5 > 0$. The models of $K_2Ni_2(SO_4)_3$ are given by the two DFT models, obtained from the $K_2Ni_2(SO_4)_3$ lattice structure at room temperature (DFT-1 model) [13] and $T = 100$ (DFT-2 model) [118], and the model obtained by fitting INS data by SCGA [119]. All $K_2Ni_2(SO_4)_3$ models exhibit a clear flow breakdown at $\Lambda_c/J_4 \sim 0.5$ that signifies the onset of magnetic order. Due to their

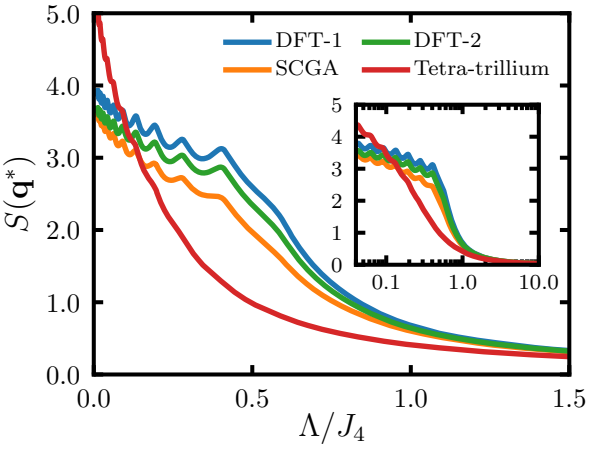

Figure 6.3: PFFRG flows for different $S = 1$ models. For each case, $\mathbf{q}^*$ corresponds to the point in reciprocal space for which the highest value of the spin structure factor is observed. DFT-1 labels the DFT room temperature model while DFT-2 corresponds to the $T = 100$K model. The figure and its caption are replicated from Ref. [118].

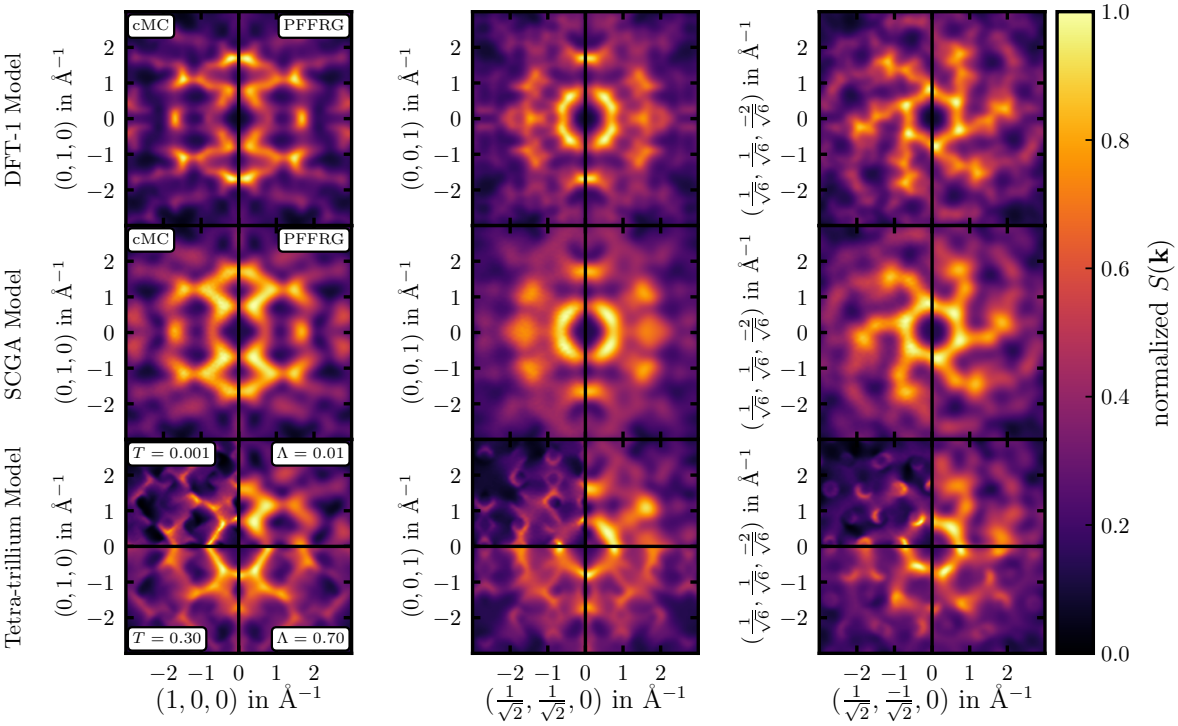

Figure 6.4: Spin structure factors obtained with cMC (left parts) and PFFRG (right parts). The first two lines correspond to DFT-1 [13] and SCGA models [119]; and calculations are at $T = 0.3J_4$ for cMC and at the breaking point of the flow for PFFRG. The bottom row corresponds to the tetra-trillium lattice, and temperatures and Λ-cutoffs are indicated in the panels. The figure and its caption are replicated from Ref. [118].

large magnetic unit cells, the magnetic orders cannot be fully characterized by PFFRG alone. However, they can be characterized by cMC. Unlike the flows of the models of $K_2Ni_2(SO_4)_3$, the flow of the tetra-trillium antiferromagnet does not show any sign of magnetic order, which implies a quantum paramagnetic regime in interaction parameter space near the models of $K_2Ni_2(SO_4)_3$.

PFFRG and cMC SFs of the DFT-1 and SCGA models, i.e., of the models that we had neglected in the above study of $K_2Ni_2(SO_4)_3$, are shown at critical cutoff and corresponding temperature in Fig. 6.4. From the comparison with the SFs of Fig. 6.2, it can be seen that the SF patterns realized by the DFT-1 and SCGA models are similar to those of the INS SF. However, the SFs of these models do not provide a notably better match to the INS SF than the SF of the DFT-2 model does. Although all considered models realize SFs similar to that observed by INS, we still believe the DFT-2 model to provide the best low-temperature description of $K_2Ni_2(SO_4)_3$ for the following reasons. Since the fitted interaction parameters of the SCGA-based model are based on the phenomenology of the INS SF, the model is obtained in ignorance of the underlying mechanisms that determine the interactions. In contrast, the DFT models are based on ab initio calculations that make use of the compound's crystal structure. Of the

DFT models, the DFT-2 model is obtained from the crystal structure of $K_2Ni_2(SO_4)_3$ at lower temperatures. At last, we note that the DFT-2 model reproduces the magnetic Bragg peaks measured by neutron diffraction, while the $L = 5n$ order realized by the SCGA model does not [118].

6.3 The tetra-trillium Heisenberg model

Inspired by various hints towards the existence of a QSL phase near the $S = 1$ model of $K_2Ni_2(SO_4)_3$, we next consider the vicinity of the model in interaction parameter space. Since the DFT model is dominated by the interactions J_3, J_4 and J_5, we neglect the remaining interactions and study the phase diagram of the J_3-J_4-J_5 model. A reasonable starting point about which to center the phase diagram would be the tetra-trillium antiferromagnet with $J_3 = 0$ and $J_4 = J_5 > 0$. As implied by its smooth PFFRG flow, shown in Fig. 6.3, the $S = 1$ model does not order magnetically. This is explained by the extensive classical ground state manifold of the model, which follows from the tetra-trillium lattice bond structure of corner-sharing tetrahedra. Accordingly, the model does not order for classical and $S = 1/2$ spins as well [118]. The following discussion on the phase diagram of the J_3-J_4-J_5 model will first focus on the conceptually simpler tetra-trillium Heisenberg model with $J_3 = 0$ and $J_4 = J_5 > 0$ before features of the wider phase diagram are considered.

SFs of the $S = 1$ and classical tetra-trillium Heisenberg models, obtained by cMC and PFFRG, are shown in the last row of Fig. 6.4. Four scenarios are considered, those being the $S = 1$ model in the small cutoff limit $\Lambda = 0.01J_4$ and at intermediate cutoffs $\Lambda = 0.70J_4$, and the classical model near zero temperature at $T = 0.001J_4$ and at intermediate temperatures $T = 0.3J_4$. In the case of intermediate cutoffs and temperatures, the figure demonstrates the presence of a quantum-to-classical correspondence in the tetra-trillium Heisenberg model, as is signified by the matching SF patterns between the classical and quantum models. However, as T and Λ decrease, quantum fluctuations take on a larger role in the state selection of the $S = 1$ model, and qualitative differences between SFs of the classical and quantum models emerge. The observed SF pattern of the $S = 1$ model at $\Lambda = 0.01$ is not reproduced by the thermal fluctuations of the classical model at any temperature [118]. Thus, the quantum-to-classical correspondence breaks down at smaller temperatures $T < 0.3J_4$. The differing features between SFs of the classical and quantum models near $T = 0$ and $\Lambda = 0$, respectively, suggest that the ground state of the $S = 1$ model originates from the quantum properties of the model, such that a state with a similar SF cannot be reproduced by the classical model. Thus, the tetra-trillium Heisenberg model may realize a QSL

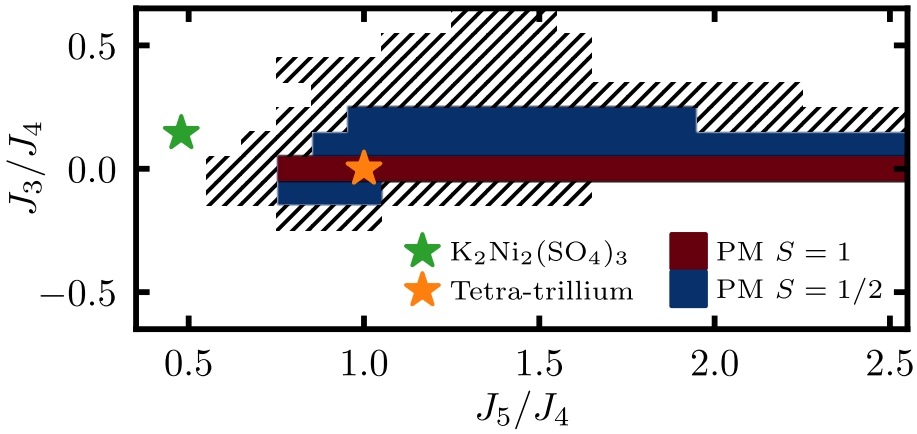

Figure 6.5: The 'island of liquidity' around the tetra-trillium lattice. PFFRG paramagnetic region of the $S = 1/2$ (red+blue) and $S = 1$ (red) J_3-J_4-J_5 model. The dashed part indicates the region where the existence of a flow breakdown is hard to determine for the $S = 1/2$ model. Green and orange stars indicate the DFT model for $K_2Ni_2(SO_4)_3$ and the tetra-trillium lattice limit, respectively. The figure and its caption are replicated from Ref. [118].

that is stabilized by local tunneling processes between different classical ground state configurations. Note that an incapability of the quantum-to-classical correspondence to persist down to the zero-temperature limit has been observed in Ref. [128] as well. The recent paper of Ref. [129] provides an explanation on why quantum-to-classical correspondences generally break down at low temperatures (or cutoffs). By using spin diagrammatic perturbation theory to expand the static magnetic susceptibility in J/T (with J being a Heisenberg interaction), it was shown that up to and including order $1/T^3$ the static magnetic susceptibility of a finite-S quantum model is equal to the classical $S \to \infty$ susceptibility of the same model at a rescaled temperature. It follows that quantum-to-classical correspondences generally break down at an order of $1/T^4$.

6.3.1 $T = 0$ phase diagram of the tetra-trillium J_3-J_4-J_5 model

We now consider the wider $T = 0$ phase diagram about the tetra-trillium Heisenberg model of corner-sharing tetrahedra. The $S = 1/2$ and $S = 1$ phase diagram of the J_3-J_4-J_5 model is shown in Fig. 6.5. It includes the tetra-trillium Heisenberg model at $J_3 = 0$ and $J_5/J_4 = 1$, and a version of the $K_2Ni_2(SO_4)_3$ DFT model with approximated interactions $J_1 = J_2 = 0$. As discussed earlier, the model at $J_3 = 0$ and $J_5/J_4 = 1$ is located in a quantum paramagnetic regime. Especially in case $S = 1/2$ this regime is found to be of large extent in the parameter space considered here. Furthermore, flow breakdowns are found to be very subtle for models with $J_3 > 0$ and for this regime emerge only slowly over wide parameter regimes as one moves across the phase diagram

from a paramagnetic to a magnetically ordered phase. This behavior results in a large region in which the existence of a flow breakdown is uncertain. This region is marked as dashed in Fig. 6.5.

A strong dependence of the paramagnetic region on the spin length S is observed. The $S = 1/2$ model remains paramagnetic for finite and mostly positive J_3. In the case $S = 1$, relevant to $K_2Ni_2(SO_4)_3$, the paramagnetic region is greatly reduced in size, such that even small sizes $|J_3/J_4| = 0.1$ lead to magnetic instabilities. Uncertainties of the PFFRG method make it difficult to resolve the size of the paramagnetic region for smaller perturbations of sizes $|J_3/J_4| < 0.1$. For the classical phase diagram, cMC confirms that magnetic order sets in for any finite J_3 [118]. In contrast to the quantum models, the classical spin model remains paramagnetic only upon varying J_5/J_4 about the tetra-trillium point at $\{J_3, J_4, J_5\} = \{0, 1, 1\}$, which is marked by an orange star. On this line of the classical phase diagram, a magnetic phase boundary is found at $0.3 < J_5/J_4 < 0.4$, which exceeds the paramagnetic regions of both the $S = 1/2$ and $S = 1$ models. The position of the boundary can be explained as follows [118]. Rewriting the J_4-J_5 model of corner-sharing tetrahedra as done in Eq. (6.3) leads to the local constraint for classical ground states given by

$$\frac{J_4}{J_5}\boldsymbol{S}_{t0} + \boldsymbol{S}_{t1} + \boldsymbol{S}_{t2} + \boldsymbol{S}_{t3} = \boldsymbol{0}, \tag{6.5}$$

with $\boldsymbol{S}_{ti}$ being a spin on site $i \in \{0, 1, 2, 3\}$ of a tetrahedron t of the lattice. The spins $\boldsymbol{S}_{t0}$ interact only with spins of a single tetrahedron (via the interaction J_4), whereas $\boldsymbol{S}_{t1}$, $\boldsymbol{S}_{t2}$, and $\boldsymbol{S}_{t3}$ are located on sites shared by three tetrahedra. The constraint of Eq. (6.5) cannot be fulfilled anymore for $J_5/J_4 < 1/3$. In this case, ground states of the model are given by states that minimize $|J_4/J_5\boldsymbol{S}_{t0} + \boldsymbol{S}_{t1} + \boldsymbol{S}_{t2} + \boldsymbol{S}_{t3}|$ instead, which results in the magnetic order that fulfills $\boldsymbol{S}_{t0} = -\boldsymbol{S}_{t1} = -\boldsymbol{S}_{t2} = -\boldsymbol{S}_{t3}$ for any t. This magnetic order corresponds to an antiferromagnetic order where spins within the individual trillium lattices are ferromagnetically ordered, but with an opposite orientation depending on the trillium lattice. Starting from $\{J_3, J_4, J_5\} = \{0, 1, 1\}$ again and moving in direction towards the Heisenberg model of the pure trillium lattice at $J_5/J_4 \to \infty$, no magnetic order is observed by cMC at least up to $J_5/J_4 = 3.5$, which approximately corresponds to the region in which PFFRG finds that the $S = 1$ model enters a magnetic order. For the $S = 1/2$ model, the paramagnetic region is found to extend to even larger but finite values of J_5/J_4 [118].

At last, we consider the DFT model of $K_2Ni_2(SO_4)_3$ in the phase diagram, where it is marked by a green star. It is positioned in a magnetically ordered region and has a clear flow breakdown. Simultaneously, the model is located relatively close to the paramagnetic regime, which contextualizes the experimental features of a weak

magnetic order [13]. From experiments, we further know that the compound can be driven into a paramagnetic phase by the application of an external magnetic field [13]. This suggests that the paramagnetic regime of the phase diagram may increase in size if an external magnetic field is applied, until the regime includes the DFT model at intermediate field sizes. Going forward, the magnetic field dependence of the paramagnetic region could in principle be studied by the recent PFFRG extension that enables the treatment of finite magnetic fields [39]. Moreover, if more compounds are realized that are well described within the phase diagram, it will be of interest to observe their response to finite magnetic fields.

As a closing remark, we note that the phase diagram considered here is of interest to compounds of the langbeinite family, which realize interconnected trillium lattices [13]. Because PFFRG has found a paramagnetic regime of large extent in the phase diagram of the J_3-J_4-J_5 model on the same lattice, which is expected to further increase in size if a finite external magnetic field is applied, the present study establishes spin models realized by langbeinite compounds as a promising platform for the future search and study of QSL phases.

6.4 Discussion

In this chapter, we considered the magnetism of systems on interconnected trillium lattices that can also be framed as a tetra-trillium lattice. In particular, we were interested in providing a theoretical explanation for the experimentally observed low-temperature behavior of $K_2Ni_2(SO_4)_3$, which shows signs of strong frustration.

In the study of $K_2Ni_2(SO_4)_3$, an effective DFT spin Hamiltonian with $S = 1$, based on the structure of the compound at $T = 100K$, was proposed to describe the compound well. The validity of the model was corroborated by a good agreement between experimental and theoretical observations, e.g., in the INS and PFFRG SFs. Furthermore, SFs obtained by PFFRG and cMC of the $S = 1$ and classical DFT models were observed to exhibit a striking agreement as well, suggesting the presence of a quantum-to-classical correspondence between the $S = 1$ and classical DFT models. This correspondence was utilized to determine the magnetic order of $K_2Ni_2(SO_4)_3$ by cMC. The order was revealed to be a near-120° order with a 216-site magnetic unit cell.

The phase diagram of the J_3-J_4-J_5 model on the interconnected trillium lattice was considered to contextualize the weak magnetic order and the proximate spin liquid behavior of $K_2Ni_2(SO_4)_3$. Importantly, an extended paramagnetic regime was found

about the tetra-trillium Heisenberg model with interactions $J_3 = 0$ and $J_5/J_4 = 1$, for which the spatial structure of the interactions simplifies to a network of corner-sharing tetrahedra. The extent of the paramagnetic region was found to depend strongly on the spin length S, being especially large at a minimum $S = 1/2$. On the other hand, the region becomes one-dimensional in case of classical spins, where it persists only for $J_3 = 0$. The $T = 0$ paramagnetic regimes of the $S = 1/2$ and $S = 1$ models were found to be in the vicinity of the DFT model of $K_2Ni_2(SO_4)_3$, contextualizing the experimentally observed proximate spin liquid behavior of the compound. Going forward and beyond the study of $K_2Ni_2(SO_4)_3$, a new direction in the search of spin-liquid phases in three dimensions has been opened up by the location of a large paramagnetic region in the phase diagram of the J_3-J_4-J_5 model, especially in the context that the J_3-J_4-J_5 model is relevant to compounds of the langbeinite family [13]. Many such compounds are yet unexplored with respect to their magnetic behavior [13], leaving much territory still to uncover in the field of langbeinite magnetism.

In conclusion, the study of this chapter has not only explained the low-temperature behavior of $K_2Ni_2(SO_4)_3$, but also suggested langbeinite compounds as a novel platform for the future study of frustrated magnetism. Nevertheless, open questions still remain regarding $K_2Ni_2(SO_4)_3$ and the J_3-J_4-J_5 phase diagram. Future studies may attempt to further characterize paramagnetic phases in the J_3-J_4-J_5 phase diagram or the field-induced paramagnetic phase of $K_2Ni_2(SO_4)_3$ at intermediate magnetic fields, e.g., by proposing spin-liquid ground states with specified gauge fields. Furthermore, we have so far restricted our theoretical study to models with zero external magnetic fields. A more versatile interweaving of theoretical and experimental descriptions of $K_2Ni_2(SO_4)_3$ may be achieved by extending the PFFRG and cMC study to the finite-field behavior of the compound in the future.

Chapter 7

Conclusion

The development and applications of the pseudo-fermion functional renormalization group are a major theme threading throughout this thesis. In the first part of the thesis, given by the Chapters 2-4, an emphasis had been put on the introduction and development of the method. The main methodological advancement consists of a PFFRG formulation for spin models with broken time-reversal symmetry that enables both the study of previously inaccessible models with finite magnetic fields as well as of previously accessible models within their magnetically ordered phases. After the extended PFFRG method was introduced, these newly accessible PFFRG applications were subsequently explored along a large variety of spin models. In the second part of the thesis, given by the Chapters 5-6, PFFRG was applied in order to answer recent questions in the research of frustrated magnetism. In this context, insights were gained on the behavior of nearest-neighbor spin models on the pyrochlore lattice and of Heisenberg models on the tetra-trillium lattice, including the density functional theory model of the spin-liquid candidate $K_2Ni_2(SO_4)_3$. From a methodological standpoint, these applications served as a showcase of PFFRG use cases as well, revealing different aspects of the method in the process. As such, the conclusion of this thesis is well suited to reflect on the PFFRG method in general and its prospective role among other methods in the study of spin models. The following discussion will first be centered on methodological aspects of the thesis. Afterwards, the focus will be shifted to the physical insights gained throughout this work.

Prior to this thesis, the PFFRG method was already well developed and established, as shown by the recent review Ref. [12]. The method extension provided by this work, and not covered in the previous review, presents an efficient formulation of pseudo-fermion vertices and flow equations for spin models with broken time-reversal symmetry. The capability thereby gained to treat such models has profound implications. While previous PFFRG applications were restricted to spin models with only terms bilinear in spin

operators, the new formulation allows for the additional treatment of site-dependent terms linear in spin operators, which are often realized in experiments by the coupling to an external magnetic field. Since magnetic fields pose a prominent and easily accessible parameter in experimental studies, further possibilities for the integration of the PFFRG in collaborative efforts with experiments emerge. Furthermore, the now accessible study of phenomena at finite magnetic fields, such as magnetization plateaus or field-induced paramagnetic phases, represents promising future applications. In addition to these new applications, the extended method allows for a different paradigm in the study of magnetic phases. In previous applications, the presence of magnetic order in spin models has been determined by a breakdown in the flow of the cutoff-dependent magnetic susceptibility [12]. The magnetic order was then further specified by the study of the magnetic susceptibility above the critical cutoff. The now accessible application of symmetry-breaking magnetic seed fields allows for the regularization of flow breakdowns [51, 50]. The resulting flows can be continued into magnetically ordered phases and down to the cutoff-free limit. It follows that a detection of magnetic phases via finite order parameters and a direct study of magnetically ordered phases at $T = 0$ is enabled.

While the finite-field PFFRG applications are promising, the exploratory study of Chapter 4 finds that the accuracy of PFFRG results in these new applications is of varying degree and highlights the limitations of the method in the study of magnetic phases at zero cutoff. Nearest-neighbor Heisenberg models on the square, honeycomb, and triangular lattice suggest that magnetic orders are reproduced accurately on a qualitative level, whereas sizes of magnetic order parameters are systematically overestimated. More accurate quantitative results may only be achieved by the implementation of more sophisticated and numerically expensive truncation schemes for flow equations. Applications at finite magnetic fields reveal that the magnetization plateau of the triangular-lattice XXZ model is resolved consistently with literature results. However, predicted plateaus are absent in the antiferromagnetic Heisenberg models on a dimer and pyrochlore lattice. These results suggest that the method is more accurate for models with dipolar ordered ground states. This methodological shortcoming is again rooted in the methodologically inherent truncation of flow equations. Overall, we assess that further study would still be beneficial to better interpret PFFRG results within magnetic phases and to better understand which properties of a model favor an accurate PFFRG description of its ground state.

Spin models without magnetic fields were treated in Chapters 5 and 6. The capability of PFFRG to treat three-dimensional and highly frustrated models with many competing interactions was demonstrated for a selection of nearest-neighbor spin models on the pyrochlore lattice and Heisenberg models on the tetra-trillium lattice. In particular,

PFFRG was applied to compute the phase diagrams of the J_3-J_4-J_5 Heisenberg model on the tetra-trillium lattice and of the general nearest-neighbor model for non-Kramers pyrochlores. Since PFFRG flows of the same model with different interaction parameter sizes are computed by merely changing the initial conditions of the vertex flows at infinite cutoff, phase diagrams can be computed straightforwardly in absence of a priori knowledge on their realized phases. Together with the capability of the method to treat three-dimensional and highly frustrated models, the method is thus particularly suited for these applications.

Complementary application of different numerical methods with PFFRG has been demonstrated for different spin models. E.g., the versatility of PFFRG in the treatment of frustrated and complex spin models allows for close collaboration with experimental studies. In our case, density functional theory was applied to the experimentally studied compound $K_2Ni_2(SO_4)_3$ to obtain an effective spin model treatable by PFFRG. The same strategy had already been successfully applied in previous studies [130, 98, 131] and is promising for future studies on compounds as well. The study of $K_2Ni_2(SO_4)_3$ further revealed a quantum-to-classical correspondence for its effective spin model via the structure factors obtained by classical Monte Carlo and PFFRG at finite temperatures and cutoffs, respectively. The correspondence was utilized to reveal the magnetic order of the $S = 1$ model with classical Monte Carlo by proxy. In the Heisenberg-DM and non-Kramers model on the pyrochlore lattice, a collaborative study was performed by employing PFFRG, high-temperature series expansions and classical Monte Carlo, among other methods. PFFRG predictions on phase boundaries were further corroborated by high-temperature series expansion results. In the magnetically ordered Γ_5 phase, PFFRG was able to partially resolve a quantum order-by-disorder selection. The final selection within the remaining classical Γ_5 submanifold was resolved by high-temperature series expansions. A comparison between the ground state selections in PFFRG and high-temperature series expansions with classical Monte Carlo allowed a comparative study of both the classical and quantum order-by-disorder selections at near-zero and critical temperature.

We now move from the conclusion on methodological aspects of the thesis and shift the focus to the contributions provided in the field of frustrated magnetism. Although spin models on the pyrochlore lattice have experienced much popularity as a platform of frustrated magnetism in the last decades [117, 77], many of their properties still remain under debate or underexplored. For the nearest-neighbor Heisenberg model, we advanced the debate on the $S = 1/2$ model ground state by providing further arguments for the previously claimed ground state [79, 56] that either breaks C_3, or C_3 and inversion lattice symmetries. Furthermore, it was shown that PFFRG suggests an enhanced symmetry breaking in the $S = 1$ model in comparison to the case $S = 1/2$. The

obtained results on the ground states have been published in Refs. [48, 43]. Beyond the Heisenberg model, the nearest-neighbor model with both Heisenberg and anisotropic Dzyaloshinskii-Moriya interactions was considered. While the quantum model had been studied previously in Refs. [93, 94, 95], these publications only considered the case of an antiferromagnetic Heisenberg interaction and applied either a perturbative large-S or mean-field approximation. In a joint study with complementary methods, treated in this thesis and published in Ref. [49], we resolved the full phase diagram of the quantum model with PFFRG. In particular, the Γ_5 phase of the model was found to host subtle order-by-disorder selections. Fluctuations were found to select different magnetic orders within the classically degenerate Γ_5 manifold depending on the interactions and whether the temperature is set near zero or at critical temperature. Interestingly, order-by-disorder selections of the classical and quantum models were found to be in good agreement, which is not always the case [96]. By including ferromagnetic Heisenberg interactions in the phase diagram of the quantum model, an extended paramagnetic regime was revealed in addition to the paramagnetic regime centered around the antiferromagnetic Heisenberg model. Further study investigated a classical spin model within this regime, the dipolar-quadrupolar-quadrupolar (DQQ) model, that remains paramagnetic down to $T = 0$ and exhibits an entropically-driven spin liquid to spin liquid transition under the variation of temperature. These properties are enabled by an extensive ground state manifold, which includes the spin-ice manifold. The DQQ model may be relevant to future experimental studies of spin liquid to spin liquid transitions since it can be realized by non-Kramers pyrochlores in principle. However, in the analogous $S = 1/2$ quantum model, PFFRG suggests that only the intermediate-temperature spin-liquid phase is realized. A PFFRG phase diagram, complemented by high-temperature series expansion results, for the general nearest-neighbor Hamiltonian of non-Kramers pyrochlores embedded the DQQ model within a larger paramagnetic regime. The phase diagram may guide a future search for compounds near the DQQ model or contextualize magnetic behavior of other non-Kramers pyrochlore compounds. Insights on the classical DQQ model and the $S = 1/2$ phase diagram of non-Kramers pyrochlores were published in Ref. [71], where the author mostly contributed with PFFRG results for quantum models.

Inspired by the preceding studies on the tetra-trillium compound $K_2Ni_2(SO_4)_3$ given by Refs. [13, 119], the $S = 1/2$ and $S = 1$ phase diagrams of the J_3-J_4-J_5 Heisenberg model on the tetra-trillium lattice were computed by PFFRG. A large so far unexplored paramagnetic region was found within the phase diagrams. Since the J_3-J_4-J_5 model is of high relevance to langbeinite compounds, this finding establishes langbeinite compounds as a promising future platform for the search and study of three-dimensional spin-liquid realizations. The DFT model of $K_2Ni_2(SO_4)_3$ was found by PFFRG to be

magnetically ordered but located near the paramagnetic regime. This finding contextualized the experimentally observed unstable magnetic order of $K_2Ni_2(SO_4)_3$ under the application of an external magnetic field [13]. A collaborative study that applied PFFRG, classical Monte Carlo, and inelastic neutron scattering advanced the understanding of the compound by revealing its underlying magnetic order to be given by a near-120° order with a 216-site magnetic unit cell. Findings on $K_2Ni_2(SO_4)_3$ and the J_3-J_4-J_5 Heisenberg model are published in Refs. [13, 118]. We conclude that this thesis not only advances the study of frustrated magnetism on pyrochlore and tetra-trillium systems, but also suggests future directions in their research and provides new methodological approaches to their study through the further development of the PFFRG method.

Appendix A

PFFRG flow equations for a general Heisenberg model

The PFFRG flow equations for a general spin model with terms linear and bilinear in spin operators are given in Eqs. (3.55)-(3.56). Treatable spin models may not contain any continuous spin rotation symmetries or time-reversal symmetry. By assuming such symmetries, the flow equations simplify. An often considered case is that of a Heisenberg model, i.e, a model with a global SU(2) spin rotation symmetry and time-reversal symmetry. Due to its relevancy, we show simplified flow equations for a general Heisenberg model in the following. Symmetry-imposed simplifications of the self-energy $\Sigma(1'|1)$ and two-particle vertex $\Gamma(1',2'|1,2)$ structures in their spin argument dependencies have already been given in Table 3.2. It follows from the SU(2) symmetry that $\Gamma(1',2'|1,2)$ contains only two finite and independent components $\Gamma^{\rho\varphi}$, in whose notation we have neglected the frequency and site arguments for simplicity. These are given by $\Gamma^d = \Gamma^{00}$ and $\Gamma^s = \Gamma^{xx} = \Gamma^{yy} = \Gamma^{zz}$. Because of time-reversal symmetry, $\Sigma(1'|1)$ contains only one finite component $\Sigma^{\rho=0}$. The simplified flow equations are obtained by inserting these restrictions into the general flow equations, given in Eqs. (3.55)-(3.56).

For a Heisenberg model, the self-energy flow equation is given by

$$\frac{d}{d\Lambda}\Sigma_i^{0,\Lambda}(\omega) = \frac{1}{2\pi}\int_{\mathbb{R}} d\omega' \Big\{ -2\sum_j \Gamma_{ij}^{d,\Lambda}(\omega_1+\omega', 0, \omega_1-\omega')\mathcal{S}_j^{0,\Lambda}(\omega') \\ + [3\Gamma_{ii}^{s,\Lambda}(\omega+\omega', \omega-\omega', 0) + \Gamma_{ii}^{d,\Lambda}(\omega+\omega', \omega-\omega', 0)]\mathcal{S}_i^{0,\Lambda}(\omega')\Big\}, \tag{A.1}$$

and the two-particle vertex flow equations are given by

$$
\begin{aligned}
&\frac{d}{d\Lambda}\Gamma^{d,\Lambda}_{i_1i_2}(s,t,u) = \frac{1}{2\pi}\int_{\mathbb{R}} d\omega' \\
&\Big\{ -[3\Gamma^{s,\Lambda}_{i_1i_2}(s,-\omega'-\omega_{2'},\omega_{1'}+\omega')\Gamma^{s,\Lambda}_{i_1i_2}(s,\omega_2+\omega',\omega_1+\omega') \\
&\quad + \Gamma^{d,\Lambda}_{i_1i_2}(s,-\omega'-\omega_{2'},\omega_{1'}+\omega')\Gamma^{d,\Lambda}_{i_1i_2}(s,\omega_2+\omega',\omega_1+\omega')]\Pi^{00,\Lambda}_{i_1i_2}(s+\omega',\omega') \\
&-2\sum_j \Gamma^{d,\Lambda}_{i_1j}(\omega_{1'}+\omega',t,\omega_1-\omega')\Gamma^{d,\Lambda}_{ji_2}(\omega_2+\omega',t,-\omega_{2'}+\omega')\Pi^{00,\Lambda}_{jj}(t+\omega',\omega') \\
&+[3\Gamma^{d,\Lambda}_{i_1i_2}(\omega_{1'}+\omega',t,\omega_1-\omega')\Gamma^{s,\Lambda}_{i_2i_2}(\omega_2+\omega',-\omega_{2'}+\omega',t) \\
&\quad + \Gamma^{d,\Lambda}_{i_1i_2}(\omega_{1'}+\omega',t,\omega_1-\omega')\Gamma^{d,\Lambda}_{i_2i_2}(\omega_2+\omega',-\omega_{2'}+\omega',t)]\Pi^{00,\Lambda}_{i_2i_2}(t+\omega',\omega') \\
&+[3\Gamma^{s,\Lambda}_{i_1i_1}(\omega_{1'}+\omega',\omega_1-\omega',t)\Gamma^{d,\Lambda}_{i_1i_2}(\omega_2+\omega',t,-\omega_{2'}+\omega') \\
&\quad + \Gamma^{d,\Lambda}_{i_1i_1}(\omega_{1'}+\omega',\omega_1-\omega',t)\Gamma^{d,\Lambda}_{i_1i_2}(\omega_2+\omega',t,-\omega_{2'}+\omega')]\Pi^{00,\Lambda}_{i_1i_1}(t+\omega',\omega') \\
&+[3\Gamma^{s,\Lambda}_{i_1i_2}(\omega_{2'}-\omega',-\omega_1-\omega',u)\Gamma^{s,\Lambda}_{i_1i_2}(\omega_2-\omega',\omega_{1'}+\omega',u) \\
&\quad + \Gamma^{d,\Lambda}_{i_1i_2}(\omega_{2'}-\omega',-\omega_1-\omega',u)\Gamma^{d,\Lambda}_{i_1i_2}(\omega_2-\omega',\omega_{1'}+\omega',u)]\Pi^{00,\Lambda}_{i_2i_1}(u+\omega',\omega')\Big\},
\end{aligned}
$$

$$
\begin{aligned}
&\frac{d}{d\Lambda}\Gamma^{s,\Lambda}_{i_1i_2}(s,t,u) = \frac{1}{2\pi}\int_{\mathbb{R}} d\omega' \\
&\Big\{[+2\Gamma^{s,\Lambda}_{i_1i_2}(s,-\omega'-\omega_{2'},\omega_{1'}+\omega')\Gamma^{s,\Lambda}_{i_1i_2}(s,\omega_2+\omega',\omega_1+\omega') \\
&\quad - \Gamma^{s,\Lambda}_{i_1i_2}(s,-\omega'-\omega_{2'},\omega_{1'}+\omega')\Gamma^{d,\Lambda}_{i_1i_2}(s,\omega_2+\omega',\omega_1+\omega') \\
&\quad - \Gamma^{d,\Lambda}_{i_1i_2}(s,-\omega'-\omega_{2'},\omega_{1'}+\omega')\Gamma^{s,\Lambda}_{i_1i_2}(s,\omega_2+\omega',\omega_1+\omega')]\Pi^{00,\Lambda}_{i_1i_2}(s+\omega',\omega') \\
&-2\sum_j \Gamma^{s,\Lambda}_{i_1j}(\omega_{1'}+\omega',t,\omega_1-\omega')\Gamma^{s,\Lambda}_{ji_2}(\omega_2+\omega',t,-\omega_{2'}+\omega')\Pi^{00,\Lambda}_{jj}(t+\omega',\omega') \\
&+[\Gamma^{s,\Lambda}_{i_1i_2}(\omega_{1'}+\omega',t,\omega_1-\omega')\Gamma^{d,\Lambda}_{i_2i_2}(\omega_2+\omega',-\omega_{2'}+\omega',t) \\
&\quad - \Gamma^{s,\Lambda}_{i_1i_2}(\omega_{1'}+\omega',t,\omega_1-\omega')\Gamma^{s,\Lambda}_{i_2i_2}(\omega_2+\omega',-\omega_{2'}+\omega',t)]\Pi^{00,\Lambda}_{i_2i_2}(t+\omega',\omega') \\
&+[\Gamma^{d,\Lambda}_{i_1i_1}(\omega_{1'}+\omega',\omega_1-\omega',t)\Gamma^{s,\Lambda}_{i_1i_2}(\omega_2+\omega',t,-\omega_{2'}+\omega') \\
&\quad - \Gamma^{s,\Lambda}_{i_1i_1}(\omega_{1'}+\omega',\omega_1-\omega',t)\Gamma^{s,\Lambda}_{i_1i_2}(\omega_2+\omega',t,-\omega_{2'}+\omega')]\Pi^{00,\Lambda}_{i_1i_1}(t+\omega',\omega')] \\
&+[2\Gamma^{s,\Lambda}_{i_1i_2}(\omega_{2'}-\omega',-\omega_1-\omega',u)\Gamma^{s,\Lambda}_{i_1i_2}(\omega_2-\omega',\omega_{1'}+\omega',u) \\
&\quad + \Gamma^{s,\Lambda}_{i_1i_2}(\omega_{2'}-\omega',-\omega_1-\omega',u)\Gamma^{d,\Lambda}_{i_1i_2}(\omega_2-\omega',\omega_{1'}+\omega',u) \\
&\quad + \Gamma^{d,\Lambda}_{i_1i_2}(\omega_{2'}-\omega',-\omega_1-\omega',u)\Gamma^{s,\Lambda}_{i_1i_2}(\omega_2-\omega',\omega_{1'}+\omega',u)]\Pi^{00,\Lambda}_{i_2i_1}(u+\omega',\omega')\Big\},
\end{aligned}
\tag{A.2}
$$

$$
\text{with}\quad \Pi^{00,\Lambda}_{i_3,i_4}(\omega_3,\omega_4) = G^{0,\Lambda}_{i_3}(\omega_3)\tilde{\mathcal{S}}^{0,\Lambda}_{i_4}(\omega_4) + G^{0,\Lambda}_{i_4}(\omega_4)\tilde{\mathcal{S}}^{0,\Lambda}_{i_3}(\omega_3).
$$

In addition to the flow equations, expressions for observables simplify if a Heisenberg model is treated. Since the pure Heisenberg model fulfills time-reversal symmetry, its magnetization vanishes. Furthermore, SU(2) spin rotation symmetry imposes that spin correlations are only finite for diagonal components $\chi^{xx} = \chi^{yy} = \chi^{zz}$. By inserting the

simplified vertex structures into the general expression for spin correlations, given by Eq. (3.64), one obtains the simplified expression for spin correlations. These are given by

$$\begin{aligned}\chi_{ij}^{zz}(\omega) = &-\frac{1}{4\pi}\delta_{ij}\int_{\mathbb{R}} d\omega' G_i^0(\omega')G_i^0(\omega+\omega') \\ &-\frac{1}{8\pi^2}\int_{\mathbb{R}^2} d\omega' d\omega'' G_i^0(\omega')G_j^0(\omega+\omega'')G_i^0(\omega+\omega')G_j^0(\omega'')\times \\ &\big\{2\Gamma_{ij}^s(\omega+\omega'+\omega'',\omega,\omega'-\omega'') \\ &\quad+\delta_{ij}[\Gamma_{ii}^s(\omega+\omega'+\omega'',\omega'-\omega'',\omega)-\Gamma_{ii}^d(\omega+\omega'+\omega'',\omega'-\omega'',\omega)]\big\}.\end{aligned}$$

Bibliography

[1] Claudine Lacroix, Philippe Mendels, and Frédéric Mila. *Introduction to Frustrated Magnetism: Materials, Experiments, Theory*. Springer Series in Solid-State Sciences, 2011.

[2] J. Richter and J. Schulenburg. The spin-1/2 J_1-J_2 Heisenberg antiferromagnet on the square lattice: Exact diagonalization for N=40 spins. *The European Physical Journal B*, 73(1):117–124, Jan 2010.

[3] Alexei Kitaev. Anyons in an exactly solved model and beyond. *Annals of Physics*, 321(1):2–111, 2006.

[4] M. J. P. Gingras and P. A. McClarty. Quantum spin ice: a search for gapless quantum spin liquids in pyrochlore magnets. *Reports on Progress in Physics*, 77(5):056501, May 2014.

[5] J. Villain, R. Bidaux, J.-P. Carton, and R. Conte. Order as an effect of disorder. *Journal de Physique*, 41:1263–1272, 1980.

[6] Ryogo Kubo. The Spin-Wave Theory of Antiferromagnetics. *Phys. Rev.*, 87:568–580, Aug 1952.

[7] J.H.P. Colpa. Diagonalization of the quadratic boson hamiltonian. *Physica A: Statistical Mechanics and its Applications*, 93(3):327–353, 1978.

[8] Román Orús. Tensor networks for complex quantum systems. *Nature Reviews Physics*, 1(9):538–550, September 2019.

[9] J. Ignacio Cirac, David Pérez-García, Norbert Schuch, and Frank Verstraete. Matrix product states and projected entangled pair states: Concepts, symmetries, theorems. *Rev. Mod. Phys.*, 93:045003, Dec 2021.

[10] Wolfgang von der Linden. A quantum Monte Carlo approach to many-body physics. *Physics Reports*, 220(2):53–162, 1992.

[11] Johannes Reuther and Peter Wölfle. J_1-J_2 frustrated two-dimensional Heisenberg model: Random phase approximation and functional renormalization group. *Phys. Rev. B*, 81:144410, Apr 2010.

[12] Tobias Müller, Dominik Kiese, Nils Niggemann, Björn Sbierski, Johannes Reuther, Simon Trebst, Ronny Thomale, and Yasir Iqbal. Pseudo-fermion functional renormalization group for spin models, 2023. arXiv:2307.10359 [cond-mat.str-el].

[13] Ivica Živković, Virgile Favre, Catalina Salazar Mejia, Harald O. Jeschke, Arnaud Magrez, Bhupen Dabholkar, Vincent Noculak, Rafael S. Freitas, Minki Jeong, Nagabhushan G. Hegde, Luc Testa, Peter Babkevich, Yixi Su, Pascal Manuel, Hubertus Luetkens, Christopher Baines, Peter J. Baker, Jochen Wosnitza, Oksana Zaharko, Yasir Iqbal, Johannes Reuther, and Henrik M. Rønnow. Magnetic Field Induced Quantum Spin Liquid in the Two Coupled Trillium Lattices of $K_2Ni_2(SO_4)_3$. *Phys. Rev. Lett.*, 127:157204, Oct 2021.

[14] J.J. Sakurai and Jim Napolitano. *Modern Quantum Mechanics Third Edition*. Cambridge University Press, 2021.

[15] J. Bardeen, L. N. Cooper, and J. R. Schrieffer. Theory of Superconductivity. *Phys. Rev.*, 108:1175–1204, Dec 1957.

[16] Walter Metzner, Manfred Salmhofer, Carsten Honerkamp, Volker Meden, and Kurt Schönhammer. Functional renormalization group approach to correlated fermion systems. *Rev. Mod. Phys.*, 84:299–352, Mar 2012.

[17] John W. Negele and Henri Orland. *Quantum Many-particle Systems (Advanced Books Classics)*. Westview Press, 1998.

[18] Alexander L. Fetter and John Dirk Walecka. *Quantum theory of many-particle systems*. Dover Publications Inc., 1971.

[19] Fabian B Kugler and Jan von Delft. Derivation of exact flow equations from the self-consistent parquet relations. *New J. Phys.*, 20(12):123029, 2018.

[20] Mark Srednicki. *Quantum Field Theory*. Cambridge: Cambridge University Press, 2007.

[21] Kambis Veschgini and Manfred Salmhofer. Schwinger-Dyson renormalization group. *Phys. Rev. B*, 88:155131, Oct 2013.

[22] David Senechal, Andre-Marie Tremblay, and Claude Bourbonnais. *Theoretical methods for strongly correlated electrons*. Springer, 2004.

[23] S. X. Yang, H. Fotso, J. Liu, T. A. Maier, K. Tomko, E. F. D'Azevedo, R. T. Scalettar, T. Pruschke, and M. Jarrell. Parquet approximation for the 4×4 Hubbard cluster. *Phys. Rev. E*, 80:046706, Oct 2009.

[24] Ka-Ming Tam, H. Fotso, S.-X. Yang, Tae-Woo Lee, J. Moreno, J. Ramanujam, and M. Jarrell. Solving the parquet equations for the Hubbard model beyond weak coupling. *Phys. Rev. E*, 87:013311, Jan 2013.

[25] Wei-jie Fu. QCD at finite temperature and density within the fRG approach: an overview. *Communications in Theoretical Physics*, 74(9):097304, Sep 2022.

[26] G. Camacho, C. Klöckner, D. M. Kennes, and C. Karrasch. Review of recent developments of the functional renormalization group for systems out of equilibrium. *The European Physical Journal B*, 95(12):195, December 2022.

[27] Nils Niggemann, Björn Sbierski, and Johannes Reuther. Frustrated quantum spins at finite temperature: Pseudo-Majorana functional renormalization group approach. *Phys. Rev. B*, 103:104431, Mar 2021.

[28] Nils Niggemann, Johannes Reuther, and Björn Sbierski. Quantitative functional renormalization for three-dimensional quantum Heisenberg models. *SciPost Phys.*, 12:156, 2022.

[29] Raphael Goll, Dmytro Tarasevych, Jan Krieg, and Peter Kopietz. Spin functional renormalization group for quantum Heisenberg ferromagnets: Magnetization and magnon damping in two dimensions. *Phys. Rev. B*, 100:174424, Nov 2019.

[30] Jan Krieg and Peter Kopietz. Exact renormalization group for quantum spin systems. *Phys. Rev. B*, 99:060403, Feb 2019.

[31] Finn Lasse Buessen, Vincent Noculak, Simon Trebst, and Johannes Reuther. Functional renormalization group for frustrated magnets with nondiagonal spin interactions. *Phys. Rev. B*, 100:125164, Sep 2019.

[32] M. L. Baez and J. Reuther. Numerical treatment of spin systems with unrestricted spin length S: A functional renormalization group study. *Phys. Rev. B*, 96:045144, Jul 2017.

[33] Finn Lasse Buessen, Dietrich Roscher, Sebastian Diehl, and Simon Trebst. Functional renormalization group approach to SU(N) Heisenberg models: Real-space renormalization group at arbitrary N. *Phys. Rev. B*, 97:064415, Feb 2018.

[34] Dietrich Roscher, Finn Lasse Buessen, Michael M. Scherer, Simon Trebst, and Sebastian Diehl. Functional renormalization group approach to SU(N) Heisenberg

models: Momentum-space renormalization group for the large-N limit. *Phys. Rev. B*, 97:064416, Feb 2018.

[35] Benedikt Schneider, Dominik Kiese, and Björn Sbierski. Taming pseudofermion functional renormalization for quantum spins: Finite temperatures and the Popov-Fedotov trick. *Phys. Rev. B*, 106:235113, Dec 2022.

[36] Dominik Kiese, Tobias Müller, Yasir Iqbal, Ronny Thomale, and Simon Trebst. Multiloop functional renormalization group approach to quantum spin systems. *Phys. Rev. Research*, 4:023185, Jun 2022.

[37] Julian Thoenniss, Marc K. Ritter, Fabian B. Kugler, Jan von Delft, and Matthias Punk. Multiloop pseudofermion functional renormalization for quantum spin systems: Application to the spin-$\frac{1}{2}$ kagome Heisenberg model, 2020. arXiv:2011.01268 [cond-mat.str-el].

[38] Marc K. Ritter, Dominik Kiese, Tobias Müller, Fabian B. Kugler, Ronny Thomale, Simon Trebst, and Jan von Delft. Benchmark calculations of multiloop pseudofermion fRG. *The European Physical Journal B*, 95(7):102, July 2022.

[39] Vincent Noculak and Johannes Reuther. Pseudo-fermion functional renormalization group with magnetic fields. *Phys. Rev. B*, 109:174414, May 2024.

[40] Fabian B. Kugler and Jan von Delft. Multiloop functional renormalization group for general models. *Phys. Rev. B*, 97:035162, Jan 2018.

[41] Yi Zhou, Kazushi Kanoda, and Tai-Kai Ng. Quantum spin liquid states. *Rev. Mod. Phys.*, 89:025003, Apr 2017.

[42] Ian Affleck, Z. Zou, T. Hsu, and P. W. Anderson. SU(2) gauge symmetry of the large-U limit of the Hubbard model. *Phys. Rev. B*, 38:745–747, Jul 1988.

[43] Imre Hagymási, Vincent Noculak, and Johannes Reuther. Enhanced symmetry-breaking tendencies in the $S = 1$ pyrochlore antiferromagnet. *Phys. Rev. B*, 106:235137, Dec 2022.

[44] Sergei V Maleev. Polarized neutron scattering in magnets. *Physics-Uspekhi*, 45(6):569, Jun 2002.

[45] K. T. K. Chung, J. S. K. Goh, A. Mukherjee, W. Jin, D. Lozano-Gómez, and M. J. P. Gingras. Probing Flat Band Physics in Spin Ice Systems via Polarized Neutron Scattering. *Phys. Rev. Lett.*, 128:107201, Mar 2022.

[46] Max Hering and Johannes Reuther. Functional renormalization group analysis of Dzyaloshinsky-Moriya and Heisenberg spin interactions on the kagome lattice. *Phys. Rev. B*, 95:054418, Feb 2017.

[47] Johannes Reuther. *Frustrated Quantum Heisenberg Antiferromagnets: Functional Renormalization-Group Approach in Auxiliary-Fermion Representation.* PhD thesis, 2011.

[48] Max Hering, Vincent Noculak, Francesco Ferrari, Yasir Iqbal, and Johannes Reuther. Dimerization tendencies of the pyrochlore Heisenberg antiferromagnet: A functional renormalization group perspective. *Phys. Rev. B*, 105:054426, Feb 2022.

[49] Vincent Noculak, Daniel Lozano-Gómez, Jaan Oitmaa, Rajiv R. P. Singh, Yasir Iqbal, Michel J. P. Gingras, and Johannes Reuther. Classical and quantum phases of the pyrochlore $S = \frac{1}{2}$ magnet with Heisenberg and Dzyaloshinskii-Moriya interactions. *Phys. Rev. B*, 107:214414, Jun 2023.

[50] Manfred Salmhofer, Carsten Honerkamp, Walter Metzner, and Oliver Lauscher. Renormalization Group Flows into Phases with Broken Symmetry. *Progress of Theoretical Physics*, 112(6):943–970, 12 2004.

[51] R. Gersch, C. Honerkamp, D. Rohe, and W. Metzner. Fermionic renormalization group flow into phases with broken discrete symmetry: charge-density wave mean-field model. *Eur. Phys. J. B*, 48:060403, 2005.

[52] Yasir Iqbal, Pratyay Ghosh, Rajesh Narayanan, Brijesh Kumar, Johannes Reuther, and Ronny Thomale. Intertwined nematic orders in a frustrated ferromagnet. *Phys. Rev. B*, 94:224403, Dec 2016.

[53] Luca Capriotti, Federico Becca, Alberto Parola, and Sandro Sorella. Resonating Valence Bond Wave Functions for Strongly Frustrated Spin Systems. *Phys. Rev. Lett.*, 87:097201, Aug 2001.

[54] Steven R. White and Ian Affleck. Dimerization and incommensurate spiral spin correlations in the zigzag spin chain: Analogies to the Kondo lattice. *Phys. Rev. B*, 54:9862–9869, Oct 1996.

[55] Hiroaki Kusunose. Self-Consistent Fluctuation Theory for Strongly Correlated Electron Systems. *Journal of the Physical Society of Japan*, 79(9):094707, 2010.

[56] Nikita Astrakhantsev, Tom Westerhout, Apoorv Tiwari, Kenny Choo, Ao Chen, Mark H. Fischer, Giuseppe Carleo, and Titus Neupert. Broken-Symmetry

Ground States of the Heisenberg Model on the Pyrochlore Lattice. *Phys. Rev. X*, 11:041021, Oct 2021.

[57] Imre Hagymási, Robin Schäfer, Roderich Moessner, and David J. Luitz. Magnetization process and ordering of the $S = \frac{1}{2}$ pyrochlore Heisenberg antiferromagnet in a magnetic field. *Phys. Rev. B*, 106:L060411, Aug 2022.

[58] Daisuke Yamamoto, Giacomo Marmorini, and Ippei Danshita. Quantum Phase Diagram of the Triangular-Lattice XXZ Model in a Magnetic Field. *Phys. Rev. Lett.*, 112:127203, Mar 2014.

[59] Daniel Sellmann, Xue-Feng Zhang, and Sebastian Eggert. Phase diagram of the antiferromagnetic XXZ model on the triangular lattice. *Phys. Rev. B*, 91:081104, Feb 2015.

[60] Mark Galassi, Jim Davies, James Theiler, Brian Gough, Gerard Jungman, Patrick Alken, Michael Booth, and Fabrice Rossi. *GNU Scientific Library Reference Manual (3rd Ed.)*. Network Theory Ltd., 2009.

[61] Vincent Noculak. PFFRG.cpp. GitHub repository. `https://github.com/VincentNoculak/PFFRG.cpp`, 2024.

[62] Gordon Baym and Leo P. Kadanoff. Conservation Laws and Correlation Functions. *Phys. Rev.*, 124:287–299, Oct 1961.

[63] Gordon Baym. Self-Consistent Approximations in Many-Body Systems. *Phys. Rev.*, 127:1391–1401, Aug 1962.

[64] Karl J. Runge. Quantum Monte Carlo calculation of the long-range order in the Heisenberg antiferromagnet. *Phys. Rev. B*, 45:7229–7236, Apr 1992.

[65] J. D. Reger, J. A. Riera, and A. P. Young. Monte Carlo simulations of the spin-1/2 Heisenberg antiferromagnet in two dimensions. *Journal of Physics: Condensed Matter*, 1(10):1855, Mar 1989.

[66] Steven R. White and A. L. Chernyshev. Neél Order in Square and Triangular Lattice Heisenberg Models. *Phys. Rev. Lett.*, 99:127004, Sep 2007.

[67] Jiale Huang and Xiangjian Qian and Mingpu Qin. On the magnetization of the 120° order of the spin-1/2 triangular lattice Heisenberg model: a DMRG revisited. *Journal of Physics: Condensed Matter*, 36(18):185602, Feb 2024.

[68] Luca Capriotti, Adolfo E. Trumper, and Sandro Sorella. Long-Range Néel Order in the Triangular Heisenberg Model. *Phys. Rev. Lett.*, 82:3899–3902, May 1999.

[69] Johannes Reuther, Ronny Thomale, and Simon Trebst. Finite-temperature phase diagram of the Heisenberg-Kitaev model. *Phys. Rev. B*, 84:100406, Sep 2011.

[70] Ahmet Keleş and Erhai Zhao. Rise and fall of plaquette order in the Shastry-Sutherland magnet revealed by pseudofermion functional renormalization group. *Phys. Rev. B*, 105:L041115, Jan 2022.

[71] Daniel Lozano-Gómez, Vincent Noculak, Jaan Oitmaa, Rajiv R. P. Singh, Yasir Iqbal, Johannes Reuther, and Michel J. P. Gingras. Competing gauge fields and entropically driven spin liquid to spin liquid transition in non-Kramers pyrochlores. *Proceedings of the National Academy of Sciences*, 121(36):e2403487121, Aug 2024.

[72] Anders W. Sandvik. Stochastic series expansion method with operator-loop update. *Phys. Rev. B*, 59:R14157–R14160, Jun 1999.

[73] A. Honecker, J. Schulenburg, and J. Richter. Magnetization plateaus in frustrated antiferromagnetic quantum spin models. *J. Phys.: Condens. Matter*, 16:749, 2004.

[74] M. S. Yang and K. H. Mütter. The two dimensional antiferromagnetic Heisenberg model in the presence of an external field. *Zeitschrift für Physik B Condensed Matter*, 104:117–123, 1997.

[75] M. E. Zhitomirsky and T. Nikuni. Magnetization curve of a square-lattice Heisenberg antiferromagnet. *Phys. Rev. B*, 57:5013–5016, Mar 1998.

[76] Santanu Pal and Siddhartha Lal. Magnetization plateaus of the quantum pyrochlore Heisenberg antiferromagnet. *Phys. Rev. B*, 100:104421, Sep 2019.

[77] Jeffrey G. Rau and Michel J.P. Gingras. Frustrated Quantum Rare-Earth Pyrochlores. *Annual Review of Condensed Matter Physics*, 10(1):357–386, 2019.

[78] C. Castelnovo, R. Moessner, and S.L. Sondhi. Spin Ice, Fractionalization, and Topological Order. *Annual Review of Condensed Matter Physics*, 3(1):35–55, 2012.

[79] Imre Hagymási, Robin Schäfer, Roderich Moessner, and David J. Luitz. Possible Inversion Symmetry Breaking in the $S = 1/2$ Pyrochlore Heisenberg Magnet. *Phys. Rev. Lett.*, 126:117204, Mar 2021.

[80] Robin Schäfer, Benedikt Placke, Owen Benton, and Roderich Moessner. Abundance of Hard-Hexagon Crystals in the Quantum Pyrochlore Antiferromagnet. *Phys. Rev. Lett.*, 131:096702, Aug 2023.

[81] Steven T Bramwell and Mark J Harris. The history of spin ice. *Journal of Physics: Condensed Matter*, 32(37):374010, Jun 2020.

[82] L. Pauling. The Structure and Entropy of Ice and of Other Crystals with Some Randomness of Atomic Arrangement. *J. Am. Chem. Soc.*, 57:2680–84, 1935.

[83] S. V. Isakov, K. Gregor, R. Moessner, and S. L. Sondhi. Dipolar Spin Correlations in Classical Pyrochlore Magnets. *Phys. Rev. Lett.*, 93:167204, Oct 2004.

[84] Yasuyuki Kato and Shigeki Onoda. Numerical Evidence of Quantum Melting of Spin Ice: Quantum-to-Classical Crossover. *Phys. Rev. Lett.*, 115:077202, Aug 2015.

[85] J Preskill. Magnetic Monopoles. *Annual Review of Nuclear and Particle Science*, 34(1):461–530, 1984.

[86] Salvatore D. Pace, Siddhardh C. Morampudi, Roderich Moessner, and Chris R. Laumann. Emergent Fine Structure Constant of Quantum Spin Ice Is Large. *Phys. Rev. Lett.*, 127:117205, Sep 2021.

[87] Imre Hagymási, Nils Niggemann, and Johannes Reuther. Phase diagram of the antiferromagnetic J_1-J_2 spin-1 pyrochlore Heisenberg model, 2024. arXiv:2405.12745 [cond-mat.str-el].

[88] Yasir Iqbal, Tobias Müller, Pratyay Ghosh, Michel J. P. Gingras, Harald O. Jeschke, Stephan Rachel, Johannes Reuther, and Ronny Thomale. Quantum and Classical Phases of the Pyrochlore Heisenberg Model with Competing Interactions. *Phys. Rev. X*, 9:011005, Jan 2019.

[89] Anson W. C. Wong, Zhihao Hao, and Michel J. P. Gingras. Ground state phase diagram of generic XY pyrochlore magnets with quantum fluctuations. *Phys. Rev. B*, 88:144402, Oct 2013.

[90] Han Yan, Owen Benton, Ludovic Jaubert, and Nic Shannon. Theory of multiple-phase competition in pyrochlore magnets with anisotropic exchange with application to $Yb_2Ti_2O_7, Er_2Ti_2O_7$, and $Er_2Sn_2O_7$. *Phys. Rev. B*, 95:094422, Mar 2017.

[91] Alexander Hickey, Daniel Lozano-Gómez, and Michel J. P. Gingras. Order-by-disorder without quantum zero-point fluctuations in the pyrochlore Heisenberg ferromagnet with Dzyaloshinskii-Moriya interactions, 2024. arXiv:2403.02391 [cond-mat.str-el].

[92] Tôru Moriya. Anisotropic Superexchange Interaction and Weak Ferromagnetism. *Phys. Rev.*, 120:91–98, Oct 1960.

[93] Maged Elhajal, Benjamin Canals, Raimon Sunyer, and Claudine Lacroix. Ordering in the pyrochlore antiferromagnet due to Dzyaloshinsky-Moriya interactions. *Phys. Rev. B*, 71:094420, Mar 2005.

[94] B. Canals, M. Elhajal, and C. Lacroix. Ising-like order by disorder in the pyrochlore antiferromagnet with Dzyaloshinskii-Moriya interactions. *Phys. Rev. B*, 78:214431, Dec 2008.

[95] Gia-Wei Chern. Pyrochlore antiferromagnet with antisymmetric exchange interactions: critical behavior and order from disorder, 2010. arXiv:1008.3038 [cond-mat.str-el].

[96] R. Schick, T. Ziman, and M. E. Zhitomirsky. Quantum versus thermal fluctuations in the fcc antiferromagnet: Alternative routes to order by disorder. *Phys. Rev. B*, 102:220405, Dec 2020.

[97] Kate A. Ross, Lucile Savary, Bruce D. Gaulin, and Leon Balents. Quantum Excitations in Quantum Spin Ice. *Phys. Rev. X*, 1:021002, Oct 2011.

[98] Pratyay Ghosh, Yasir Iqbal, Tobias Müller, Ravi T. Ponnaganti, Ronny Thomale, Rajesh Narayanan, Johannes Reuther, Michel J. P. Gingras, and Harald O. Jeschke. Breathing chromium spinels: a showcase for a variety of pyrochlore Heisenberg Hamiltonians. *npj Quantum Materials*, 4(1):63, December 2019.

[99] E. M. Smith, O. Benton, D. R. Yahne, B. Placke, R. Schäfer, J. Gaudet, J. Dudemaine, A. Fitterman, J. Beare, A. R. Wildes, S. Bhattacharya, T. DeLazzer, C. R. C. Buhariwalla, N. P. Butch, R. Movshovich, J. D. Garrett, C. A. Marjerrison, J. P. Clancy, E. Kermarrec, G. M. Luke, A. D. Bianchi, K. A. Ross, and B. D. Gaulin. Case for a $U(1)_\pi$ Quantum Spin Liquid Ground State in the Dipole-Octupole Pyrochlore $Ce_2Zr_2O_7$. *Phys. Rev. X*, 12:021015, Apr 2022.

[100] J. Xu, Owen Benton, V. K. Anand, A. T. M. N. Islam, T. Guidi, G. Ehlers, E. Feng, Y. Su, A. Sakai, P. Gegenwart, and B. Lake. Anisotropic exchange Hamiltonian, magnetic phase diagram, and domain inversion of $Nd_2Zr_2O_7$. *Phys. Rev. B*, 99:144420, Apr 2019.

[101] Yi-Ping Huang, Gang Chen, and Michael Hermele. Quantum Spin Ices and Topological Phases from Dipolar-Octupolar Doublets on the Pyrochlore Lattice. *Phys. Rev. Lett.*, 112:167203, Apr 2014.

[102] Owen Benton. Quantum origins of moment fragmentation in $Nd_2Zr_2O_7$. *Phys. Rev. B*, 94:104430, Sep 2016.

[103] E. M. Smith, O. Benton, D. R. Yahne, B. Placke, R. Schäfer, J. Gaudet, J. Dudemaine, A. Fitterman, J. Beare, A. R. Wildes, S. Bhattacharya, T. DeLazzer, C. R. C. Buhariwalla, N. P. Butch, R. Movshovich, J. D. Garrett, C. A. Marjerrison, J. P. Clancy, E. Kermarrec, G. M. Luke, A. D. Bianchi, K. A. Ross, and B. D. Gaulin. Reply to "Comment on: 'Case for a $U(1)_\pi$ Quantum Spin Liquid Ground State in the Dipole-Octupole Pyrochlore $Ce_2Zr_2O_7$' ", 2022. arXiv:2209.14956 [cond-mat.str-el].

[104] Félix Desrochers and Yong Baek Kim. Spectroscopic Signatures of Fractionalization in Octupolar Quantum Spin Ice. *Phys. Rev. Lett.*, 132:066502, Feb 2024.

[105] Franz Schwabl. *Quantum Mechanics*. Springer, 4 edition, 2007.

[106] Azam Sadeghi, Mojtaba Alaei, Farhad Shahbazi, and Michel J. P. Gingras. Spin Hamiltonian, order out of a Coulomb phase, and pseudocriticality in the frustrated pyrochlore Heisenberg antiferromagnet FeF_3. *Phys. Rev. B*, 91:140407, Apr 2015.

[107] Kira Riedl, Daniel Guterding, Harald O. Jeschke, Michel J. P. Gingras, and Roser Valentí. Ab initio determination of spin Hamiltonians with anisotropic exchange interactions: The case of the pyrochlore ferromagnet $Lu_2V_2O_7$. *Phys. Rev. B*, 94:014410, Jul 2016.

[108] Lucile Savary, Kate A. Ross, Bruce D. Gaulin, Jacob P. C. Ruff, and Leon Balents. Order by Quantum Disorder in $Er_2Ti_2O_7$. *Phys. Rev. Lett.*, 109:167201, Oct 2012.

[109] D. R. Yahne, D. Pereira, L. D. C. Jaubert, L. D. Sanjeewa, M. Powell, J. W. Kolis, Guangyong Xu, M. Enjalran, M. J. P. Gingras, and K. A. Ross. Understanding Reentrance in Frustrated Magnets: The Case of the $Er_2Sn_2O_7$ Pyrochlore. *Phys. Rev. Lett.*, 127:277206, Dec 2021.

[110] C. L. Sarkis, J. G. Rau, L. D. Sanjeewa, M. Powell, J. Kolis, J. Marbey, S. Hill, J. A. Rodriguez-Rivera, H. S. Nair, D. R. Yahne, S. Säubert, M. J. P. Gingras, and K. A. Ross. Unravelling competing microscopic interactions at a phase boundary: A single-crystal study of the metastable antiferromagnetic pyrochlore $Yb_2Ge_2O_7$. *Phys. Rev. B*, 102:134418, Oct 2020.

[111] Allen Scheie, Jonas Kindervater, Shu Zhang, Hitesh J. Changlani, Gabriele Sala, Georg Ehlers, Andre Heinemann, Gregory S. Tucker, Seyed M. Koohpayeh, and Collin Broholm. Multiphase magnetism in $Yb_2Ti_2O_7$. *Proceedings of the National Academy of Sciences*, 117(44):27245–27254, 2020.

[112] R. Moessner and J. T. Chalker. Low-temperature properties of classical geometrically frustrated antiferromagnets. *Phys. Rev. B*, 58:12049–12062, Nov 1998.

[113] Owen Benton, L.D.C. Jaubert, Han Yan, and Nic Shannon. A spin-liquid with pinch-line singularities on the pyrochlore lattice. *Nature Communications*, 7(1):11572, May 2016.

[114] Han Yan, Owen Benton, L. D. C. Jaubert, and Nic Shannon. Rank–2 $U(1)$ Spin Liquid on the Breathing Pyrochlore Lattice. *Phys. Rev. Lett.*, 124:127203, Mar 2020.

[115] Owen Benton, Olga Sikora, and Nic Shannon. Seeing the light: Experimental signatures of emergent electromagnetism in a quantum spin ice. *Phys. Rev. B*, 86:075154, Aug 2012.

[116] H. Takatsu, S. Onoda, S. Kittaka, A. Kasahara, Y. Kono, T. Sakakibara, Y. Kato, B. Fåk, J. Ollivier, J. W. Lynn, T. Taniguchi, M. Wakita, and H. Kadowaki. Quadrupole Order in the Frustrated Pyrochlore $Tb_{2+x}Ti_{2-x}O_{7+y}$. *Phys. Rev. Lett.*, 116:217201, May 2016.

[117] Jason S. Gardner, Michel J. P. Gingras, and John E. Greedan. Magnetic pyrochlore oxides. *Rev. Mod. Phys.*, 82:53–107, Jan 2010.

[118] Matías G. Gonzalez, Vincent Noculak, Aman Sharma, Virgile Favre, Jian-Rui Soh, Arnaud Magrez, Robert Bewley, Harald O. Jeschke, Johannes Reuther, Henrik M. Rønnow, Yasir Iqbal, and Ivica Živković. Dynamics of $K_2Ni_2(SO_4)_3$ governed by proximity to a 3D spin liquid model. *Nature Communications*, 15(1):7191, Aug 2024.

[119] Weiliang Yao, Qing Huang, Tao Xie, Andrey Podlesnyak, Alexander Brassington, Chengkun Xing, Ranuri S. Dissanayaka Mudiyanselage, Haozhe Wang, Weiwei Xie, Shengzhi Zhang, Minseong Lee, Vivien S. Zapf, Xiaojian Bai, D. Alan Tennant, Jian Liu, and Haidong Zhou. Continuous Spin Excitations in the Three-Dimensional Frustrated Magnet $K_2Ni_2(SO_4)_3$. *Phys. Rev. Lett.*, 131:146701, Oct 2023.

[120] K. Boya, K. Nam, K. Kargeti, A. Jain, R. Kumar, S. K. Panda, S. M. Yusuf, P. L. Paulose, U. K. Voma, E. Kermarrec, Kee Hoon Kim, and B. Koteswararao. Signatures of spin-liquid state in a 3D frustrated lattice compound KSrFe2(PO4)3 with S = 5/2. *APL Materials*, 10(10):101103, Oct 2022.

[121] John M. Hopkinson and Hae-Young Kee. Geometric frustration inherent to the trillium lattice, a sublattice of the B20 structure. *Phys. Rev. B*, 74:224441, Dec 2006.

[122] Sergei V. Isakov, John M. Hopkinson, and Hae-Young Kee. Fate of partial order on trillium and distorted windmill lattices. *Phys. Rev. B*, 78:014404, Jul 2008.

[123] C. L. Henley. Power-law spin correlations in pyrochlore antiferromagnets. *Phys. Rev. B*, 71:014424, Jan 2005.

[124] I. Rousochatzakis, S. Kourtis, J. Knolle, R. Moessner, and N. B. Perkins. Quantum spin liquid at finite temperature: Proximate dynamics and persistent typicality. *Phys. Rev. B*, 100:045117, Jul 2019.

[125] A. O. Scheie, E. A. Ghioldi, J. Xing, J. A. M. Paddison, N. E. Sherman, M. Dupont, L. D. Sanjeewa, Sangyun Lee, A. J. Woods, D. Abernathy, D. M. Pajerowski, T. J. Williams, Shang-Shun Zhang, L. O. Manuel, A. E. Trumper, C. D. Pemmaraju, A. S. Sefat, D. S. Parker, T. P. Devereaux, R. Movshovich, J. E. Moore, C. D. Batista, and D. A. Tennant. Proximate spin liquid and fractionalization in the triangular antiferromagnet KYbSe2. *Nature Physics*, 20(1):74–81, Jan 2024.

[126] Luke J. Sandilands, Yao Tian, Kemp W. Plumb, Young-June Kim, and Kenneth S. Burch. Scattering Continuum and Possible Fractionalized Excitations in $\alpha-RuCl_3$. *Phys. Rev. Lett.*, 114:147201, Apr 2015.

[127] David L. Price and Felix Fernandez-Alonso. Chapter 1 - An Introduction to Neutron Scattering. In Felix Fernandez-Alonso and David L. Price, editors, *Neutron Scattering – Fundamentals*, volume 44 of *Experimental Methods in the Physical Sciences*, pages 1–136. Academic Press, 2013.

[128] Tao Wang, Xiansheng Cai, Kun Chen, Nikolay V. Prokof'ev, and Boris V. Svistunov. Quantum-to-classical correspondence in two-dimensional Heisenberg models. *Phys. Rev. B*, 101:035132, Jan 2020.

[129] Benedikt Schneider and Björn Sbierski. Taming spin susceptibilities in frustrated quantum magnets: Mean-field form and approximate nature of the quantum-to-classical correspondence, 2024. arXiv:2407.09401 [cond-mat.str-el].

[130] Yasir Iqbal, Tobias Müller, Harald O. Jeschke, Ronny Thomale, and Johannes Reuther. Stability of the spiral spin liquid in $MnSc_2S_4$. *Phys. Rev. B*, 98:064427, Aug 2018.

[131] Shravani Chillal, Yasir Iqbal, Harald O. Jeschke, Jose A. Rodriguez-Rivera, Robert Bewley, Pascal Manuel, Dmitry Khalyavin, Paul Steffens, Ronny Thomale, A. T. M. Nazmul Islam, Johannes Reuther, and Bella Lake. Evidence for a three-dimensional quantum spin liquid in PbCuTe2O6. *Nature Communications*, 11(1):2348, May 2020.

[132] Bennett, Loris and Melchers, Bernd and Proppe, Boris. Curta: A General-purpose High-Performance Computer at ZEDAT, Freie Universität Berlin, 2020.

Acknowledgements

First of all, I would like to thank my supervisor Johannes Reuther. He gave me the opportunity to work on many interesting projects, and was always receptive to open and fruitful discussions. It has been a pleasure to work with him.

Next, I would like to thank the group members of AG Reuther, and more generally the members of the AG Reuther group seminar, for providing an open and friendly environment that allowed for insightful and enjoyable discourse.

Throughout the thesis, I was able to participate in a wide range of interesting research projects. These projects were collaborative efforts and each had its own unique character. I found it very inspiring to experience the different work styles and approaches of the people involved. In particular, it was always intriguing to hear the different perspectives on the same physical problems. This thesis would not have been possible without the contributions of all the collaborators involved. Among them, I would like to thank in particular Daniel Lozano-Gómez, Matías G. Gonzalez, Max Hering, Imre Hagymási, Ivica Živković, Michel J. P. Gingras, Yasir Iqbal, Rajiv R. P. Singh and Johannes Reuther (in no particular order) for our collaboration. In addition to my collaborators, I would also like to thank Nils Niggemann and Björn Sbierski for useful discussions and comments.

I would like to thank for being given access to high-performance computing (HPC) clusters, whose computational resources enabled the PFFRG computations of this thesis. The first cluster I used was the tron cluster service at the Department of Physics, Freie Universität Berlin, which I would like to thank for computing time. In addition, I would like to thank the HPC service of FUB-IT [132], Freie Universität Berlin, for computing time. Furthermore, I gratefully acknowledge the computing time provided on the high-performance computer Noctua 2 at the NHR Center PC2. This is funded by the Federal Ministry of Education and Research and the state governments participating on the basis of the resolutions of the GWK for the national high-performance computing at universities (www.nhr-verein.de/unsere-partner). The computations on Noctua 2 were performed using computing resources under project "hpc-prf-pm2frg".

Finally, I would also like to thank Yasir Iqbal for providing access to his personal computing cluster.

At last, I would like to thank the Helmholtz-Zentrum Berlin (HZB) for funding me throughout the work on my thesis. I this context, I would like to thank the people of HZB who helped me with work-related organizational matters, in particular Marie Haltod and Cornelia Reuper.

Declaration of authorship

Name: Noculak
First name: Vincent

I declare to the Freie Universität Berlin that I have completed the submitted dissertation independently and without the use of sources and aids other than those indicated. The present thesis is free of plagiarism. I have marked as such all statements that are taken literally or in content from other writings. This dissertation has not been submitted in the same or similar form in any previous doctoral procedure.

I agree to have my thesis examined by a plagiarism examination software.

Place, Date	Signature